

# **Molecular analysis of the SNARE complex formation machinery and the impact of SNAREopathic mutations**

Inaugural-Dissertation

to obtain the academic degree  
Doctor rerum naturalium (Dr. rer. nat.)

submitted to the Department of Biology, Chemistry, Pharmacy  
of Freie Universität Berlin

by

**Xiao Jakob Schmitt**

Berlin, 2024



The work for this thesis was conducted from October 2018 to September 2024 under the supervision of Prof. Dr. Christian Freund at the Institute for Chemistry and Biochemistry, Freie Universität Berlin, Germany.

1<sup>st</sup> reviewer: Prof. Dr. Christian Freund  
Freie Universität Berlin  
Institute for Chemistry and Biochemistry  
Thielallee 63, 14195 Berlin, Germany

2<sup>nd</sup> reviewer: Prof. Dr. Kevin Pagel  
Freie Universität Berlin  
Institute for Chemistry and Biochemistry  
Altensteinstraße 23A, 14195 Berlin, Germany

Date of Defense: **16.12.2024**

### Acknowledgements

Honestly, if you had asked me years ago whether I could make it to become a Doctor rerum naturalium, I would have never believed I could. I remember it like it was yesterday - my family and I were staying at my grandmother's house in China, discussing the future. I was toying with the idea of trying to become a doctoral student. I had always loved chemistry, especially bioorganic chemistry, even back in school, and thought, why not pursue it? However, my mother told me it would require a lot of effort and much more studying than I was doing at the time, giving me the impression that I might not be able to make it. Yet, the thought stayed with me, along with my mother's words. When it came time to decide what to study, I had almost completely buried the idea of becoming a doctoral student and opted for a teaching degree in chemistry and biology at university. Despite putting this wish aside, I kept taking steps to keep the possibility alive. Looking back at my CV, I see many instances where I went the extra mile to leave the door open to a doctoral program. And when the opportunity finally came - luckily at the right time and place - I seized it. And now, here I am.

However, all the effort and hardships are only half the story, as one also needs the luck to find the right people who will support, guide, and keep you on track. I was fortunate to find such people, and I would like to express my deep gratitude here.

First and foremost, I want to thank my supervisor, **Prof. Dr. Christian Freund**, for giving me the opportunity to work on such a fantastic research project. I could not have wished for a better one, as neurobiochemistry has always been my favorite subject, both in school and university. I am very grateful and happy that he gave me the chance to start as a doctoral student in his group, which cannot be taken for granted, especially since I came from a different academic background with a teaching degree. His guidance throughout the project was invaluable, with great new ideas and inputs, while also respecting and evaluating my own ideas for the project. I always felt I was in good hands.

I would also like to thank **Prof. Dr. Kevin Pagel**, who is serving as my second reviewer and has had a significant impact on me during my undergraduate studies. I owe him much for the great bachelor's and master's projects, as well as my work as a student assistant in his group, which laid the foundation for my scientific career and for this thesis.

Further thanks go to my collaboration partners, **Dr. Wietske van der Ent** and **Prof. Dr. Camila Esguerra** from the University of Oslo, as well as **Dr. Agata Witkowska** from the FMP Berlin, for the productive cooperation and for taking the time to engage in scientific discussions. I would like to extend special thanks to the students I had the pleasure of working with during this project: **Andrea Ramos Silva**, **Thomas Alexander Kratz**, **Yana Ostrovska**, and **Anastasios Reklos**. Their ideas and dedicated work significantly advanced the project. A very special thanks goes to **Tamina J. Werk**, whose contributions had a major positive impact on this work. It was a great joy working with all of you, and wonderful friendships have come out of it.

I would also like to thank the entire AG Freund: the former members **Dr. Esam T. Abualrous**, **Dr. Eliot Morrison**, **Dr. Christoph Weise**, **Dr. Miriam Bertazzon**, **Dr. Tatjana Wegner**,



## Acknowledgements

---

**Dr. Huan Lan**, and **Dr. Nirdosh Dadwal**, who were always great mentors and guides, and especially **Dr. Fabian Gerth**, through whose collaborative project I joined the group and who supported me scientifically during my early weeks.

Special thanks to the current members **Steffen Dähn** and **Dr. Almudena Hurtado-Pico** for handling all the orders and lab organization, and **Frank Kuppler** for his constant helpfulness and the scientific and non-scientific chats. I also want to thank **Dr. Miguel Alvaro-Benito**, **Eva Brencher**, and **Alexandra Mitlehner**, from whom I learned both small and significant things. Special thanks also to **Dr. Jana Sticht**, **Dr. Benno Kuroпка**, and **Andor Kristen**, whose expertise in NMR, mass spectrometry, and programming, respectively, was indispensable in so many experiments. I would also like to thank our associate postdoc, **Dr. Alexander Schendzielorz**, who was always available to help with his great experience.

Further thanks goes to **Nicole Holton** from the AG Wahl for her patient help with the numerous ITC measurements. I am also grateful to **MoloX GmbH** for allowing me to use their French Press.

Thanks as well to the **ERANet NEURON Consortium** for facilitating networking and scientific exchange, with special recognition to **Prof. Dr. Ruud F. Toonen**. My additional thanks go to **Prof. Dr. Fan Liu** and **Heike Stephanowitz**, who were key in helping establish the XL-MS method in our lab, and to the **SFB-958**.

Last but not least, I want to thank my **family** and **friends**, who have always supported and encouraged me unconditionally. They have been my constant support outside the lab, a source of new energy, and a safe haven I could always rely on. Especially my siblings, **Ben** and **Pia**, and most of all, you, **Katja**, as my partner. You have stood by my side throughout this significant, long, and formative time, always having my back and allowing me to focus. I could always, 100%, rely on you. A lot of time has passed during this work, and sadly, I have lost some family members along the way. However, new family members have also come into my life, and you, Katja, gave me the most precious gift of all: **Emilia Yulan**.

Thank you.



# Declaration of Authorship

I hereby declare that I alone am responsible for the content of my doctoral dissertation and that I have only used the sources or references cited in the dissertation.

Xiao Jakob Schmitt

# I. Table of Contents

II. List of Abbreviations .....	IX
III. Abstract.....	XII
III. Zusammenfassung.....	XIII
1. Introduction.....	1
1.1. Mechanisms of fast and reliable neurotransmission.....	1
1.2. Molecular mechanisms of synaptic vesicle docking, priming and fusion.....	3
1.3. The SNARE complex: driving force of synaptic vesicle fusion .....	5
1.4. Syntaxin-1: central hub of the SNARE complex .....	7
1.5. Molecular mechanisms and functions of Synaptosome-associated protein 25 kDa .....	10
1.6. Synaptobrevin-2: essential v-SNARE in synaptic transmission.....	12
1.7. Mammalian uncoordinated 18-1: templating the SNARE complex for synaptic vesicle fusion .....	14
1.7. Mammalian uncoordinated 13-1: catalyzing synaptic vesicle Fusion.....	18
1.8. Integrating the mechanisms of SNARE-mediated vesicle fusion .....	21
1.9. SNAREopathies: disorders of the synaptic vesicle fusion machinery .....	22
1.9.1. Stx1B mutations translate into SNAREopathic neurological disorders.....	25
2. Aim.....	29
3. Materials and Methods.....	30
3.1. Materials .....	30
3.1.1. Devices and consumables.....	30
3.1.2. Standard Chemicals .....	31
3.1.3. Isotopes .....	32
3.1.4. Enzymes .....	32
3.1.5. Oligonucleotides .....	32
3.1.6. Constructs.....	34
3.1.7. Bacterial strains .....	35
3.1.8. Growth media .....	35
3.1.9. Standard buffers, dyes and other solutions.....	36
3.2. Molecular biology methods.....	36
3.2.1. Molecular cloning.....	36
3.2.2. Site-directed mutagenesis .....	37
3.3. Protein biochemistry methods.....	38
3.3.1. Protein expression .....	38
3.3.2. Protein purification .....	39
3.3.3. SDS-PAGE.....	43
3.3.4. Bicinchoninic acid (BCA) assay.....	43
3.3.5. SNARE complex formation assay .....	44

# Table of Contents

3.3.6. Tryptic in-gel digestion.....	44
3.3.7. SNARE lipid vesicle preparation.....	45
3.3.8. GST pull-down assay of Munc18-1 <i>via</i> Stx1B wild-type and mutants .....	46
3.3.9. Western blot.....	46
3.4. Biophysical methods.....	47
3.4.1. Circular dichroism (CD) spectroscopy.....	47
3.4.2. Vesicle fusion assay – lipid mixing fluorescence detection.....	49
3.4.3. Isothermal titration calorimetry (ITC).....	50
3.4.4. Nuclear magnetic resonance (NMR) spectroscopy.....	52
3.4.5. Cross-linking mass spectrometry (XL-MS).....	55
3.5. Biological Methods .....	62
3.5.1. Zebrafish maintenance and breeding.....	62
3.5.2. Generating transient transgenic zebrafish .....	63
3.5.3. Tectal field recordings.....	63
3.5.4. Touch response recording .....	63
4. Results.....	64
4.1. E210K and L221P mutations affect helicity but not thermal stability of Stx1B .....	64
4.2. Stx1B <sup>L221P</sup> diminishes stability and helicity of the SNARE complex .....	65
4.3. FRET-based Vesicle fusion assay using $\Delta$ N-SNARE complexes to study the effects of Stx1B E210K and L221P mutations .....	67
4.3.1. Stx1B L221P mutation significantly impairs vesicle membrane fusion .....	67
4.3.2. Differential effects Stx1B E210K and L221P mutations on vesicle membrane fusion kinetics .....	70
4.4. Characterizing the interaction of Stx1B <sup>E210K</sup> and Stx1B <sup>L221P</sup> with Munc18-1.....	73
4.4.1. Stx1B <sup>E210K</sup> and Stx1B <sup>L221P</sup> show reduced affinity to Munc18-1, rescued by Stx1B <sup>E210K,K82E</sup> .....	73
4.4.2. Only K82E mutation compensates for Stx1B <sup>E210K</sup> -induced Munc18-1 interaction deficits, but not a neighboring K83E mutation.....	76
4.5. <i>In vivo</i> expression of human Stx1B patient variants in zebrafish .....	79
4.5.1. Expression of human Stx1B patient variants leads to epileptiform activity in wild-type zebrafish larvae.....	79
4.5.2. Human Stx1B <sup>WT</sup> , Stx1B <sup>L221P</sup> and Stx1B <sup>E210K,K82E</sup> partially rescue zebrafish Stx1B-null larvae .....	83
4.6. NMR characterization of the Syb2 binding to the Munc13-MUN domain .....	86
4.6.1. C-terminal JMD of Syb2 responsible for binding to Munc13-MUN .....	86
4.6.2. Tryptophane residues of Syb2 C-terminal JMD critical for Munc13-MUN interaction .	91
4.6.3. The C-terminal JMD of Syb2 shows weak binding to Munc18-1 .....	95
4.7. Structural analysis of the SNARE complex formation machinery <i>via</i> XL-MS .....	99
4.7.1. Detailed workflow of cross-linking mass spectrometry using the bottom-up approach .....	100
4.7.2. DSSO and DSBU: choosing, analyzing, and evaluating cross-linkers .....	103

# Table of Contents

---

4.7.3. XL-MS reveals interaction sites between C-terminus and SNARE motif of Syb2 and Munc13-MUN.....	108
4.7.4. Syb2 SNARE motif aligns to domain 3a binding groove and domain 1 of Munc18-1	111
4.7.5. Cross-links indicate conformational changes in the binding sites between Munc18-1 and Stx1B mutants.....	118
5. Discussion .....	124
5.1. Advances in understanding the molecular mechanism of the SNARE complex formation machinery and the role of Stx1B E210K and L221P SNAREopathic mutations.....	124
5.2. Evaluating the molecular impact of Stx1B <sup>E210K</sup> and Stx1B <sup>L221P</sup> mutations on the SNARE complex formation machinery .....	125
5.4. The Critical Role of the K82-E210 Salt Bridge in Stx1B's Binding to Munc18-1 .....	128
5.5. Evaluating the functional integration and the impact of Stx1B mutants in zebrafish models .....	130
5.3. Functional impacts of Stx1B mutations on SNARE complex formation and membrane fusion .....	135
5.6. Insights and limits of investigating the interaction of Syb2 and Munc13-MUN <i>via</i> NMR..	139
5.7. Unveiling protein interaction networks and structural dynamics: Insights from cross-linking mass spectrometry .....	142
6. Outlook .....	151
7. Appendix.....	152
8. References .....	181
IV. List of Publications .....	XVI
V. Curriculum Vitae.....	XVII

## II. List of Abbreviations

2YT	Double Yeast Tryptone
Abs	Absence seizure/epilepsy
ACN	Acetonitrile
ALS	Amyotrophic lateral sclerosis
AS	Atonic seizures
C-terminus	Carbonly-terminus
CaMb	Calmodulin-binding region
CATCHR	Complexes associated with tethering containing helical rods
CAZ	Cytomatrix of the active zone
CD	Circular dichroism
CID	Collision-induced dissociation
CPS	Complex partial seizures
DPC	Dodecylphosphocholine
dpf	days post-fertilization
DSBU	disuccinimidyl dibutyric urea
DSSO	Disuccinimidyl sulfoxide
EEG	Electroencephalogram
EM	Electron microscopy
EPR	Electron paramagnetic resonance
EPSC	Excitatory postsynaptic current
ETD	Electron transfer dissociation
FDR	False discovery rate
FID	Free induction decay
FRET	Fluorescence resonance energy transfer
GGE	Genetic generalized epilepsy
GPS	Generalized polyspikes
GTCS	Generalized tonic–clonic seizures
HCD	High-energy collisional dissociation
HSQC	Heteronuclear single-quantum correlation
IDP	Intrinsically disordered protein
InDel	Insertion/deletion
INEPT	Insensitive nuclei enhanced by polarization transfer
IPTG	Isopropyl- $\beta$ -D-1-thiogalactopyranoside
ITC	Isothermal titration calorimetry
JMD	Juxtamembrane domain
$K_D$	Dissociation constant
KKEE	KK82-83EE

## List of Abbreviations

---

L-CPL	Left circularly polarized light
LB	Lysogeny Broth
LC-MS	Liquid chromatography-mass spectrometry
LFP	Local field potential
MGF	Mascot generic format
mIPSC	Mini-inhibitory postsynaptic current
MS <sup>3</sup>	Tandem mass spectrometry with additional step of fragmentation
MS/MS	Tandem mass spectrometry
MST	Microscale thermophoresis
Munc13-1	Mammalian uncoordinated 13-1
Munc18-1	Mammalian uncoordinated 18-1
Myo	Myoclonic epilepsy
m/z	mass-to-charge
N-terminus	Amino-terminus
NHS	N-hydroxysuccinimide
nmd	Nonsense-mediated decay
NMR	Nuclear magnetic resonance
NSF	<i>N</i> -ethylmaleimide sensitive factor
OG	$\beta$ -D-glucopyranoside
PC	L- $\alpha$ -phosphatidylcholine
PCR	Polymerase chain reaction
PE	L- $\alpha$ -phosphatidylethanolamine
pIDDT	Predicted local distance difference test
PIP <sub>2</sub>	Phosphatidylinositol 4,5-bisphosphate
PIP <sub>3</sub>	Phosphatidylinositol 3,4,5-triphosphate
PPM	Parts per million
PPR	Paired-pulse ratio
PS	L- $\alpha$ -phosphatidylserine
Pvr	Vesicular release probability
R-CPL	Right circularly polarized light
RF	Radio frequency
RRP	Readily-releasable pool
RT	Room temperature
SDA	Sulfosuccinimidyl 2-( <i>m</i> -azido- <i>o</i> -nitrobenzamido)ethyl-1,3'-dithiopropionate
SDM	Site-directed mutagenesis
SDS-PAGE	Sodium dodecyl sulfate-polyacrylamide gel electrophoresis
SM	Sec1/Munc18-like family
S/N	Signal-to-noise
SNAP	Soluble NSF attachment receptor



## List of Abbreviations

---

SNAP-25	Synaptosome-associated protein 25kDa
SNARE	Soluble <i>N</i> -ethylmaleimide-sensitive-factor attachment receptor
$\alpha$ -SNAP	$\alpha$ -soluble NSF-attachment protein
SUV	Small unilamellar vesicel
SV	Synaptic vesicle
Stx1	Syntaxin-1
Stx1A	Syntaxin-1A
Stx1B	Syntaxin-1B
Stxbp1	Syntaxin-binding protein 1
Syb2	Synaptobrevin-2
T <sub>M</sub>	Melting temperature
TMR	Transmembrane region
t-SNARE	Target membrane-associated SNARE
Unc13A	Unc-13 homolog A
v-SNARE	Vesicle membrane-associated SNARE
VAMP-2	Vesicle-Associated Membrane Protein 2
WT	Wild-type
XL	Cross-link
XL-MS	Cross-linking mass spectrometry

### III. Abstract

Neurotransmitter release *via* synaptic vesicle fusion is essential for fast and reliable neurotransmission in chemical synapses. This process is mediated by the soluble *N*-ethylmaleimide-sensitive factor attachment protein receptor (SNARE) complex, composed of Syntaxin-1 (Stx1), Synaptobrevin-2 (Syb2), and Synaptosome-associated protein 25 kDa (SNAP-25), and is further orchestrated by key regulator proteins such as Munc18-1 and Munc13-1. Mutations in SNARE and regulatory proteins are associated with a group of neurological disorders known as SNAREopathies, which present with a range of phenotypes from cognitive impairments to epilepsy.

In this work, we investigate the molecular impact of two clinically significant mutations in Syntaxin-1B (Stx1B), E210K and L221P, both of which are associated with distinct epilepsy phenotypes. Despite their clinical relevance, the molecular mechanisms by which these mutations disrupt proper neurotransmission have remained unclear. Our findings reveal that the Stx1B<sup>E210K</sup> mutant primarily affect the interaction to Munc18-1. The mutation introduces charge repulsion between the H<sub>abc</sub> domain and the SNARE motif of Stx1B, altering the conformation and significantly reducing its binding affinity to Munc18-1. This alteration can be rescued by charge reversion of the opposing K82 side chain in the H<sub>abc</sub> domain (Stx1B<sup>E210K,K82E</sup>), restoring interaction almost to wild-type level. In contrast, the L221P mutation directly compromises the structural integrity of the SNARE motif in Stx1B. The substitution of proline affects the helicity of Stx1B, SNARE complex stability and significantly reducing the efficiency and velocity of liposome fusion *in vitro*. The distinct molecular effects of these two mutations demonstrate how specific alterations within the same SNARE motif can lead to diverse pathophysiological outcomes.

*In vivo* experiments, performed in collaboration with the University of Oslo, using zebrafish models expressing human Stx1B wild-type and mutant constructs display an increased number and duration of seizure events in the mutants, as measured by local field potential recordings. Additionally, the E210K mutant exhibits an impaired touch response. Importantly, both the seizure activity and the altered touch response by Stx1B<sup>E210K</sup> were rescued in zebrafish expressing the charge-reversion rescue mutant Stx1B<sup>E210K,K82E</sup>, which partially restored normal local field potential patterns and behavioral responses. These results suggest that the molecular alterations in SNARE complex formation and function are directly linked to the epileptic phenotypes observed *in vivo*.

Additionally, we investigate the interaction of Syb2 with its regulatory partners, Munc18-1 and the MUN domain of Munc13-1, which are crucial for aligning and stabilizing the SNARE motifs of Stx1 and Syb2, ensuring proper SNARE complex assembly. Our findings confirm that Syb2's juxtamembrane domain (JMD) binds to the C-terminal region of the MUN domain of Munc13-1, with both tryptophan residues in the JMD acting as anchor points. Additionally, cross-linking mass spectrometry revealed that the SNARE motif of Syb2 aligns with the concave side of the MUN domain, and an additional binding site for Syb2 was identified in domain 1 of Munc18-1.

### III. Zusammenfassung

Die Freisetzung von Neurotransmittern durch synaptische Vesikelfusion ist entscheidend für eine schnelle und zuverlässige Neurotransmission in chemischen Synapsen. Dieser Prozess wird durch den löslichen N-ethylmaleimide-sensitive factor attachment protein receptor (SNARE)-Komplex vermittelt, bestehend aus Syntaxin-1 (Stx1), Synaptobrevin-2 (Syb2) und dem Synaptosome-associated protein 25 kDa (SNAP-25). Die Bildung des SNARE-Komplexes wird von Regulatorproteinen wie Munc18-1 und Munc13-1 gesteuert. Mutationen in SNARE- und Regulatorproteinen sind mit einer Gruppe neurologischer Erkrankungen verbunden, die als SNAREopathien bekannt sind und von kognitiven Beeinträchtigungen bis hin zu Epilepsie reichen. In dieser Arbeit untersuchen wir die molekularen Auswirkungen der klinisch relevanten Syntaxin-1B (Stx1B)-Mutationen E210K und L221P, die mit unterschiedlichen Epilepsie-Phänotypen assoziiert sind. Trotz ihrer klinischen Bedeutung sind die molekularen Mechanismen, durch die diese Mutationen die korrekte Neurotransmission stören, bislang unklar geblieben. Unsere Ergebnisse zeigen, dass die Stx1B<sup>E210K</sup>-Mutante hauptsächlich die Interaktion mit Munc18-1 stört. Die Mutation verursacht eine Ladungsabstoßung zwischen der H<sub>abc</sub>-Domäne und dem SNARE-Motiv, was die Konformation verändert und die Bindungsaffinität zu Munc18-1 signifikant reduziert. Diese Beeinträchtigung kann durch eine Ladungsumkehr der gegenüberliegenden K82-Seitenkette (Stx1B<sup>E210K,K82E</sup>) nahezu vollständig behoben werden.

Im Gegensatz dazu beeinträchtigt die L221P-Mutation die strukturelle Integrität des SNARE-Motivs. Die Prolin-Substitution beeinflusst die Helizität von Stx1B, was die Stabilität des SNARE-Komplexes verringert und die Effizienz und Geschwindigkeit der *in vitro*-Liposomenfusion signifikant reduziert. Die unterschiedlichen molekularen Auswirkungen dieser beiden Mutationen zeigen, wie spezifische Veränderungen innerhalb desselben SNARE-Motivs zu vielfältigen pathophysiologischen Ergebnissen führen können.

*In vivo*-Experimente mit Zebrafischen, die humane Stx1B-Wildtyp- und Mutantenkonstrukte exprimierten, durchgeführt in Zusammenarbeit mit der Universität Oslo, zeigen bei den Mutanten eine erhöhte Krampfaktivität und -dauer, gemessen anhand der lokalen Feldpotenziale. Zudem weist die E210K-Mutante eine beeinträchtigte Berührungsreaktion auf. Diese Effekte werden durch die Rettungsmutante Stx1B<sup>E210K,K82E</sup> abgeschwächt, wodurch normale Feldpotenziale und Verhaltensreaktionen teilweise wiederhergestellt werden konnten.

Des Weiteren untersuchen wir die Interaktion von Syb2 mit Munc18-1 und der MUN-Domäne von Munc13-1, die für die Ausrichtung und Stabilisierung der SNARE-Motive entscheidend sind. Unsere Ergebnisse zeigen, dass die juxtamembrane Domäne (JMD) von Syb2 an die C-terminale Region der MUN-Domäne bindet, wobei die beiden Tryptophanreste als Ankerpunkte fungieren. Zudem zeigen Crosslinking-Massenspektrometrie-Experimente, dass sich das SNARE-Motiv von Syb2 an der konkaven Seite der MUN-Domäne ausrichtet, und wir identifizierten eine zusätzliche Bindungsstelle für Syb2 in Domäne 1 von Munc18-1.



## 1. Introduction

### 1.1. Mechanisms of fast and reliable neurotransmission

Fast and reliable neurotransmission is a key process for every human being. It is the crucial mechanism that underpins communication within the nervous system, enabling us to think, feel and experience the world around us. Involving the transmission of signals between neurons or non-neural cells like muscle or sensory cells, it is a dynamic and highly orchestrated process. Neuronal networks are one of the most intricately organized structures to have ever evolved in organisms. The human nervous system contains  $10^{10} - 10^{11}$  neurons, each forming 10000 or more functional connections, forming a network of extreme complexity [1].

Despite the great complexity of the nervous system, much is already understood about its molecular modes of operation. The function of the nervous system depends largely on the electrical activity of excitable neurons and the complexity of the nervous system is not based on a large number of fundamentally different signals, but in the number and complexity of connections formed between neurons [1].

Neurons, often referred to as the basic building blocks of the nervous system, play a fundamental role in transmitting and processing information within the intricate neuronal network. These specialized cells are responsible for the electrochemical communication that underlies all cognitive functions, sensory perceptions, and motor actions [2]. Structurally, neurons exhibit a distinct morphology comprising three main components: the cell body (soma), dendrites, and an axon with its axon terminals (**Fig. 1.1 A**). The soma, housing the nucleus and vital organelles, serves as the metabolic hub of the neuron. Dendrites, extending in branching patterns from the cell body, receive signals from neighboring neurons or sensory receptors. The axon, a lengthy projection stemming from the cell body, carries nerve impulses away from the soma, facilitating signal transmission to other neurons or effector cells [3]. Axon terminals, situated at the extremities of the axon, play a crucial role in establishing functional connections with the dendrites of subsequent neurons [2].

These functional connections between neurons are called synapses (**Fig. 1.1 A**). They represent the meeting points of neurons, where the exchange of messages takes place. Based on the transmission mechanism, two types of synapses are distinguished: Chemical synapses and electrical synapses [4].

At electrical synapses, nerve impulses are transmitted directly as electrical impulses from the presynaptic to the postsynaptic neuron and the transmission practically takes place without delay (**Fig. 1.1 B**) [4, 5]. The continuous transmission of action potentials is made possible by the fact that the synaptic cleft at the electrical synapse is very narrow. The connection between the two neurons is established by current-conducting channels, gap junctions, formed by protein clusters, through which the action potentials are propagated directly into the neighboring neuron [6]. This allows for a bidirectional signal transmission which is essential for synchronizing neuronal activity in neural circuits responsible for rhythmic activities such as cardiac muscle contractions, breathing and motor coordination [7, 8]. Therefore, electrical synapses are found in regions like the central

nervous system, peripheral nervous system and sensory organs where synchronous spreading of activity within a cell cluster is needed [9].

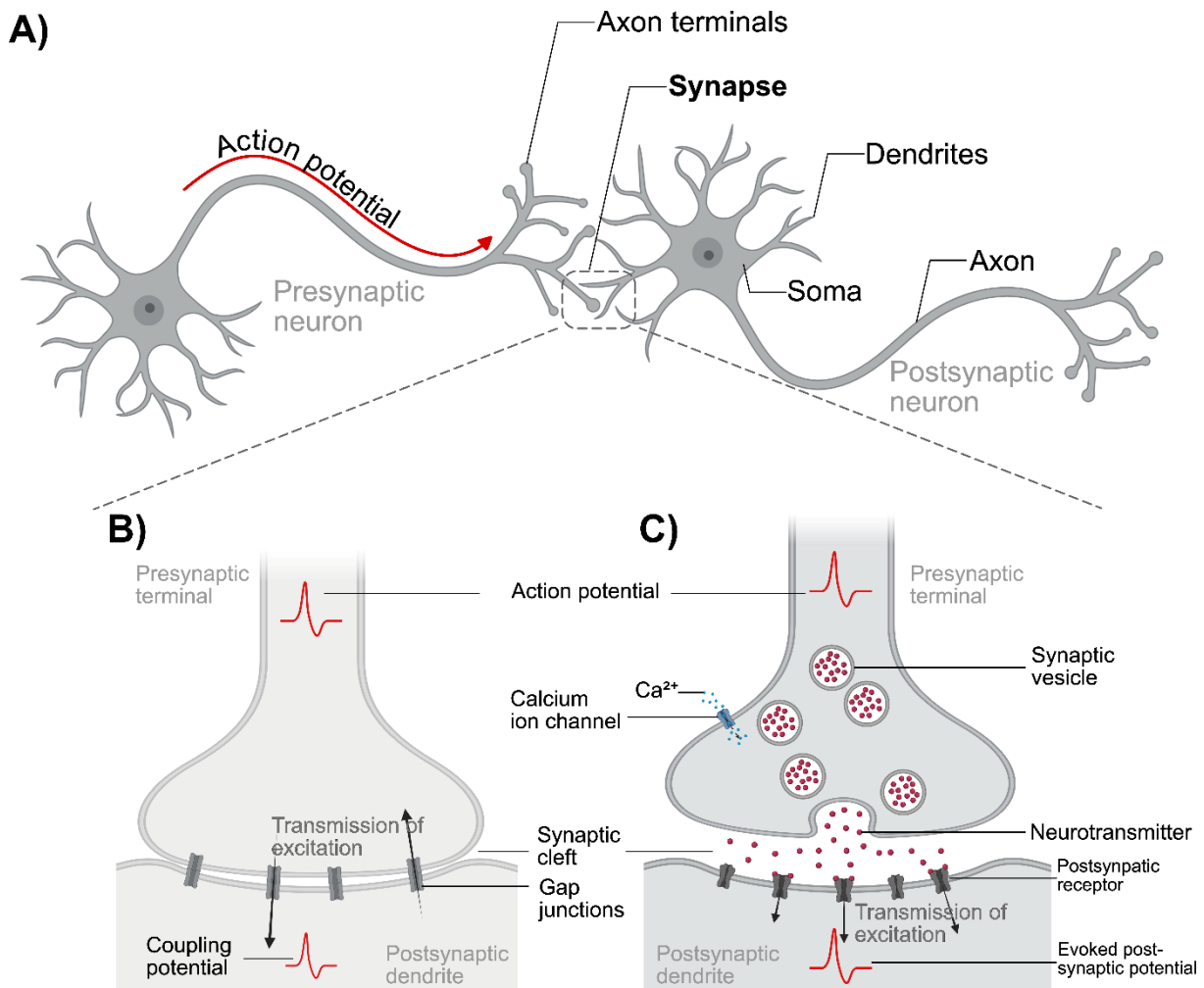


**Figure 1.1:** Neurotransmission describes the process of the transfer of an action potential **A)** from a presynaptic neuron to a postsynaptic neuron through functional connections called synapses. **B)** Electrical synapses transmit the action potential *via* gap junctions, that connect the interior of two neighboring cells and thereby enable bidirectional signal transmission. **C)** Chemical synapses transmit the action potential by synaptic vesicle exocytosis and release of neurotransmitters into the synaptic cleft, which bind to postsynaptic receptors, triggering a new neuronal signal (created using elements from BioRender.com [10]).

Chemical synapses on the other hand are the more common form in in the nervous system [4, 9]. There, the transmission of excitation information from one cell to the next takes place by means of a chemical messenger, the neurotransmitter (**Fig. 1.1 C**). When an action potential reaches the axon terminal, the presynaptic membrane gets depolarized which leads to an opening of voltage-gated ion channels followed by an influx of calcium ions. This process triggers synaptic vesicles (SV) to be transported to and fuse with the presynaptic membrane at distinct active zones in an exocytotic way, releasing neurotransmitters into the synaptic cleft. The amount of transmitter released (or the number of SVs emptied) depends on the excitation strength in the axon of the neuron. The released neurotransmitters then diffuse through the synaptic cleft and bind to receptors on the postsynaptic side. This opens or closes ion channels depending on the neuron type, leading

to conductance changes in the postsynaptic membrane. The altered ionic currents through the channels of the postsynaptic membrane cause the membrane potential of the postsynaptic cell to change – a postsynaptic potential is created [11].

The postsynaptic potential is graduated, its level depends on the strength of the excitation in the synapse and thus on the amount of released transmitters [4]. It can be depolarizing or hyperpolarizing. Depending on whether the membrane is depolarized or hyperpolarized, it is described as an excitatory postsynaptic potential (EPSP) or an inhibitory postsynaptic potential (IPSP) [12]. Thus, this leads to the fact that synapses can either promote or inhibit the generation of an action potential in the postsynaptic cell. Whether the postsynaptic membrane responds with depolarization or hyperpolarization depends on the receptor molecules and the ion channels they bind to. Acetylcholine, for example, is an excitatory transmitter found primarily in neuromuscular synapses. GABA is often found in inhibitory synapses. Glutamate, in turn, is the most important excitatory transmitter in the brain.

After the neurotransmitters have fulfilled their signaling role, they are typically removed from the synaptic cleft. This can occur through reuptake by the presynaptic neuron or enzymatic degradation [11]. Thereby a termination of signal is achieved which ensures that the synaptic communication is transient, allowing for precise regulation of neuronal activity.

The quantal release of neurotransmitters was postulated by Sir Bernhard Katz and for his observations he was awarded with the Nobel Prize for Physiology or Medicine in 1970 [13, 14].

Compared to other cellular signaling processes, synaptic transmission operates with remarkable speed, with only 50-100  $\mu$ s between the depolarization of the membrane and the fusion of SVs [15]. This rapid coordination is achieved through precise spatial and temporal alignment of these events within a specialized area of the synapses known as the active zone. Within this zone, there is a concentration of proteins, termed the cytomatrix of the active zone (CAZ) [16]. Protein scaffolds of the CAZ are characterized by their multi-domain nature, which links various functionalities, and their direct or indirect connection to membranes. This combination creates neat interaction surfaces that facilitate the spatial and temporal organization of protein-protein interactions as well as enzymatic activities. Examples of components in the CAZ include large proteins like Bassoon and Piccolo, Rab3 interacting molecules (RIMs), and the soluble *N*-ethylmaleimide-sensitive-factor (NSF) attachment receptor (SNARE) regulator Munc13-1 (**Fig. 1.2 A**) [17]. These proteins facilitate a close-knit physical and functional connection between the calcium channels in the presynaptic neuron and the machinery responsible for vesicle fusion [18].

### **1.2. Molecular mechanisms of synaptic vesicle docking, priming and fusion**

To ensure rapid and synchronized coupling of action potentials to neurotransmitter exocytosis, a number of SVs are directly docked at the active zone, poised to respond to calcium influx. These docked vesicles can be referred to as the readily-releasable pool (RRP), the size of which may vary between synapses. In cerebellar, cortical, and hippocampal typically around ten SVs can be found docked to each active zone [17, 19]. The docking of SVs relies on interactions between vesicle

proteins and components of the CAZ. A central figure in this process is the vesicular GTPase Rab3, which forms a complex with CAZ proteins RIM and Munc13, guiding vesicles to the active zone and initiating docking (**Fig. 1.2 A**) [20-22]. Interestingly, in Rab3 knockout mice, complete abolition of SV docking does not occur, suggesting compensatory mechanisms involving other vesicle proteins [23]. RIM, in conjunction with the RIM-binding protein (RIM-BP), also forms a complex that tethers calcium channels, ensuring their concentration at the active zone. Docked vesicles exhibit significantly reduced mobility compared to cytoplasmic vesicles. However, they can still be easily differentiated from the almost stationary primed vesicles [24].

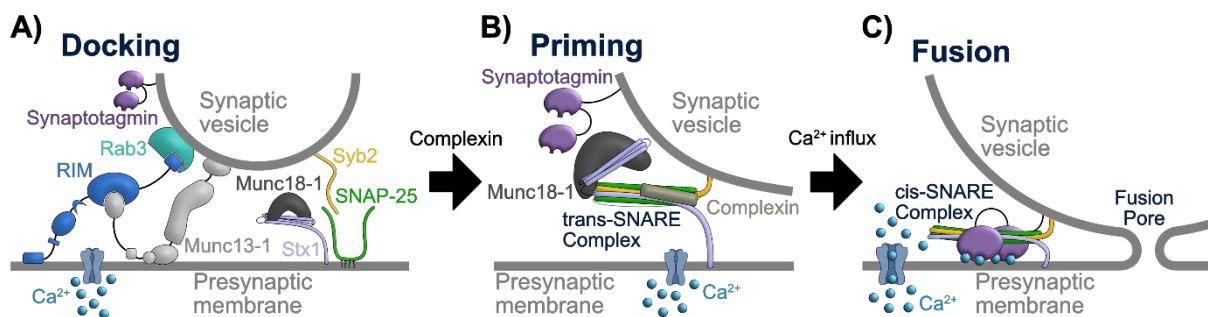


**Figure 1.2:** Molecular mechanism of synaptic vesicle docking, priming and fusion **A)** Synaptic vesicle docking is conducted through the interaction between Rab3 and RIM, and Munc13-1's vesicle tethering. **B)** Partially assembled SNARE complex enables synaptic vesicle priming. Complexin disables complete SNARE complex formation. **C)** Ca<sup>2+</sup>-influx triggers conformational change of Synaptotagmin, displacing Complexin and enabling complete SNARE complex formation, thereby exerting force on the membrane and culminating in vesicle fusion with the presynaptic membrane.

Vesicle priming is essential for enabling rapid fusion in response to elevated calcium levels and relies heavily on SNARE proteins and Sec1/Munc18-like family (SM) proteins [25]. The formation of a partially assembled SNARE complex between these proteins brings the vesicle into close proximity to the plasma membrane. In the final priming step, Complexin inhibits the completion of complex formation, leaving the vesicle fusion machinery in a primed, metastable state (**Fig. 1.2 B**) [26]. With the SV now primed for Ca<sup>2+</sup>-triggered fusion, Synaptotagmin undergoes a conformational change upon Ca<sup>2+</sup> influx, displacing Complexin. This enables the completion of trans-SNARE complex assembly, generating force transferred onto the membrane, leading to vesicle fusion with the plasma membrane in microseconds [27]. Recent research also suggests a more intricate role of Synaptotagmin in membrane fusion through dynamic interactions with both the SNARE complex and the plasma membrane [28]. Fusion of the SV with the plasma membrane opens a fusion pore, allowing neurotransmitters to diffuse into the synaptic cleft. This leads to complete merging of the vesicle and plasma membrane, converting the trans-SNARE complex into a stable cis-SNARE complex (**Fig. 1.2 C**).

Active dissociation of this complex into its monomers is facilitated by the AAA+ ATPase *N*-ethylmaleimide sensitive factor (NSF) and its cofactor soluble NSF-attachment protein ( $\alpha$ -SNAP), with recent structural insights suggesting an ATP hydrolysis-induced shearing motion in NSF as the underlying mechanism of SNARE complex disassembly [29].



### 1.3. The SNARE complex: driving force of synaptic vesicle fusion

The key driving force of vesicle fusion is the formation of the SNARE complex. This allows the opposing vesicular and plasma membrane to be pulled towards each other until a fusion pore is formed which, in most cases, expands until a complete fusion of the vesicle membrane and the plasma membrane is fully achieved eventually. Earlier studies indicate that it may take as few as one to three SNARE complexes to surpass the activation energy required for the fusion of lipid bilayers [30, 31]. The unraveling of the function of the SNARE complex was awarded with a shared Nobel Prize for Physiology or Medicine to James E. Rothman. Together with Randy W. Schekman and Thomas C. Südhof they were honored “(...) *for their discoveries of machinery regulating vesicle traffic, a major transport system in our cells.*” [32].

The core component of the SNARE complex consists of SNARE proteins which were originally identified as membrane attached receptors for soluble NSF attachment proteins (SNAPs) and from where their name originates: SNAP-receptors, in short: SNAREs [33]. There exist more than 60 mammalian SNARE proteins characterized by a shared homologous sequence known as the SNARE motif [34, 35]. Overall, they can be categorized into two distinct groups: vesicle-associated SNAREs (v-SNAREs) anchored at vesicle membranes, and target membrane-associated SNAREs (t-SNAREs) positioned on the target membrane. Both v-SNAREs and t-SNAREs encompass the SNARE motif, which comprises a conserved stretch of roughly 60-70 amino acids. Individually largely unstructured, together they form a stable four helical bundle through coiled-coil interactions involving heptad repeats which is referred as the SNARE complex (**Fig. 1.3 A**) [36].

SNARE complexes occur in various cellular contexts, including intracellular trafficking within cells and the Golgi Apparatus. However, the most extensively studied is the synaptic SNARE complex, composed of Synaptobrevin-2 (Syb2) and Syntaxin-1 (Stx1), each providing one SNARE motif and Synaptosome-associated protein 25 kDa (SNAP-25) contributing two helices to the four helical bundle [34].

The formation of the SNARE complex undergoes two distinct stages. When the vesicle membrane and the plasma membrane approach, t-SNAREs and v-SNAREs from separate membranes form the *trans*-SNARE complex. Following the fusion, the SNARE proteins that participated in the complex formation are now termed as *cis*-SNARE complex as they now inhabit a single resulting membrane (**Fig. 1.2 B, C**) [37].

The advancing formation of the SNARE complex is also known as SNARE zippering. Imagining a zipper of a jacket that would be zippered up from one end to the other, the zippering starts initially at the N-termini of the SNARE proteins and proceeds in C-terminal direction during which the tightly bound helical bundle formed by the SNARE proteins draws the vesicle and target membranes together, leading to the creation of a fusion pore, allowing the release of cargo into the synaptic cleft [38, 39]. It is hypothesized that SNARE zippering provides the necessary energy to overcome the energy barriers, including the hydrophobic core resistance of lipid bilayers, electrostatic repulsion between the negatively charged membranes, and the tension and curvature of the membranes, which would otherwise prevent them from fusing [40-42].

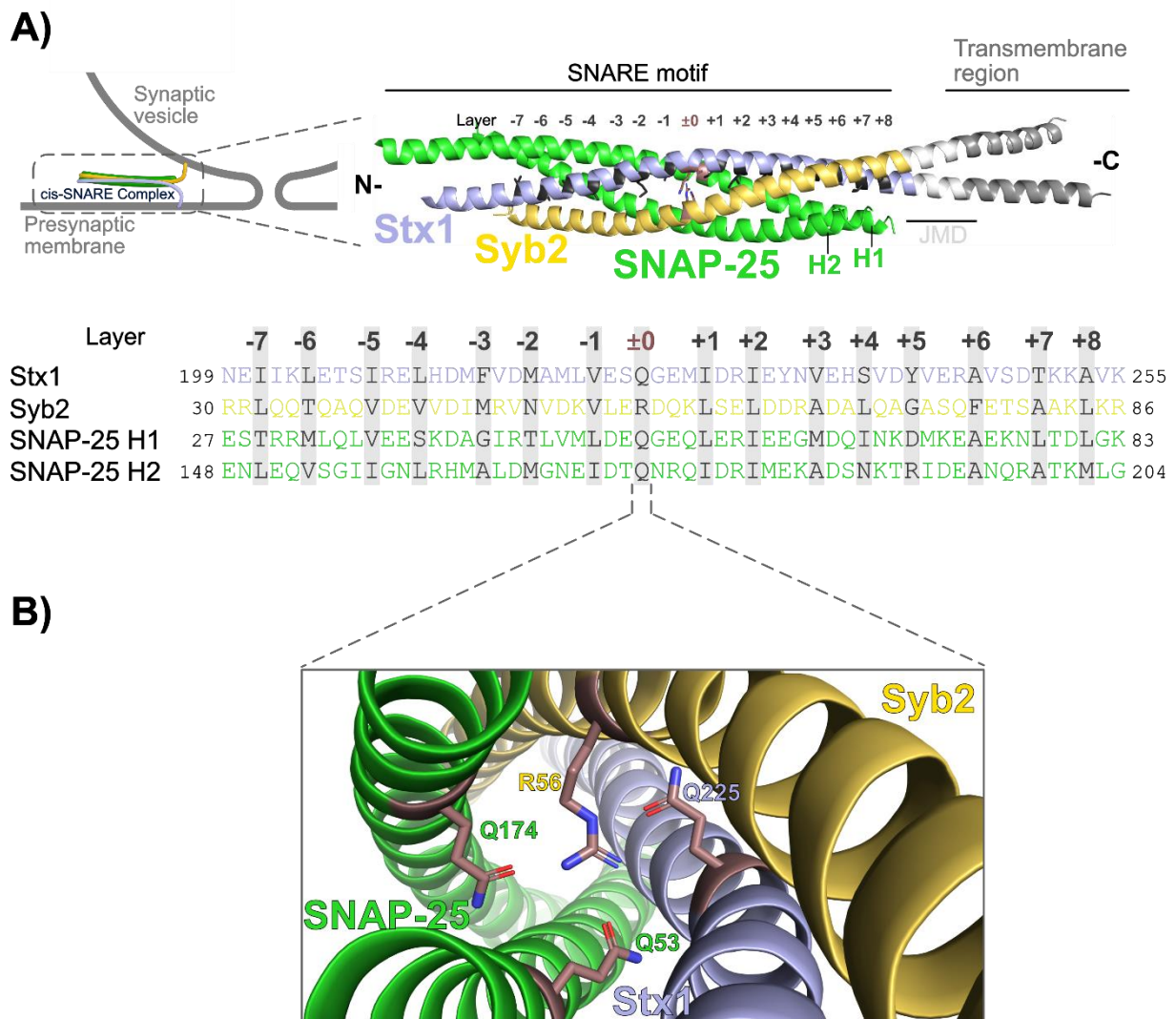


**Figure 1.3: A)** The SNARE complex is assembled by the SNARE motifs of Stx1 and Syb2, both contributing one helix, and SNAP25, contributing two helices, and comprises 15 hydrophobic layers and one zero layer in the center (PDB: 3HD7). **B)** The zero layer is the primary ionic interaction site and is formed by three glutamines (Q) of Stx1 and SNAP-25 and one arginine (R) of Syb2.

Fully formed, the SNARE complex comprises 15 hydrophobic binding layers (-7 to -1 and +1 to +8) and an ionic binding layer (zero-layer) at the center. In each layer, there are four amino acid residues, with one residue corresponding to each of the four  $\alpha$ -helices (**Fig. 1.3 A**). The zero ionic layer serves as the primary site of interaction within the core of the SNARE complex, probably serving as a proofreading site for correct assembly [43]. It achieves stability through the ionic bonds between three partially negatively charged carbonyl groups found in glutamine residues (Q) and a positively charged arginine (R). The Qs are provided from the t-SNAREs, Stx1 donating one and two from SNAP-25 (one from each corresponding SNARE helix) while the R is brought in by the v-SNARE Syb2 (**Fig. 1.3 B**) [44, 45]. The flanking layers are maintained by hydrophobic interactions and act as leucine zippers, which allow for a water-tight sealing to keep the ionic interactions of the zero-layer isolated from the surrounding solvent. [46]

The *cis*-SNARE complex exhibits extraordinary stability, characterized by *in vitro* melting temperatures above 80 °C. This makes an active, ATP-dependent process for its disassembly into its individual monomers necessary, which is believed to be done by a mechanism through which  $\alpha$ -SNAP and NSF facilitate the recycling of SNARE proteins following the conclusion of synaptic vesicle fusion. Here a disruption of the seal, often achieved by breaking the leucine zipper, exposes the zero-layer to the surrounding water solvent. This exposure leads to a loss of stability in the SNARE complex. [44]

It shall be mentioned here that terminology of v-SNAREs and t-SNAREs is discussed as it is not comprehensive enough, e.g., when describing a homotypic fusion. Additionally, numerous SNARE proteins are found on both vesicular and target membranes. Hence, a more contemporary classification system considers the structural attributes of SNAREs, distinguishing them into R-SNAREs and Q-SNAREs. In many cases, R-SNAREs function as v-SNAREs, while Q-SNAREs take on the role of t-SNAREs. As the name already implies, R-SNAREs furnish an arginine residue (R) and Q-SNAREs conversely contribute a glutamine residue (Q) to form the zero-layer. Furthermore, Q-SNAREs are categorized as Qa-, Qb-, or Qc-SNAREs based on their position within the four-helix bundle [38].

However, for the remainder of this work, we will stick to the nomenclature of v-SNARE and t-SNARE since it is all-encompassing for the context of SNARE complex formation at the presynaptic membrane.

### **1.4. Syntaxin-1: central hub of the SNARE complex**

As mentioned, one of the two t-SNARE proteins for synaptic SNARE complex formation is Syntaxin-1. In fact, however, the term must be split between two proteins: Syntaxin-1A (Stx1A) and Syntaxin-1B (Stx1B), two isoforms of the Syntaxin-1 protein that coexist in neurons. While they share a high degree of sequence and structural similarity, studies have identified distinct functional and regulatory differences. It has been shown that Stx1A is the predominant isoform in many neuronal tissues, particularly in the neocortex, hippocampus and cerebellum, while Stx1B tends to be less abundant [47, 48]. Nevertheless, in situations where Stx1A is compromised (i.e., by genetic alterations) Stx1B can compensate for its loss of function or absence to keep up neurological activities [49, 50]. Some studies suggest, that Stx1B may be more prevalent in specific neuronal subpopulations or brain regions, reflecting specialized roles for Stx1B on specific neural circuits or functions [51, 52]. Fundamentally, however, both isoforms play the same crucial role in mediating synaptic vesicle exocytosis at neuronal synapses and perform the same mechanistic pathway by interacting with a similar set of regulatory proteins. These interactions include Munc18-1 and Munc13-1, which play important roles in modulating the process of SNARE complex formation.

**Stx1**

(288 aa, 33.2 kDa)

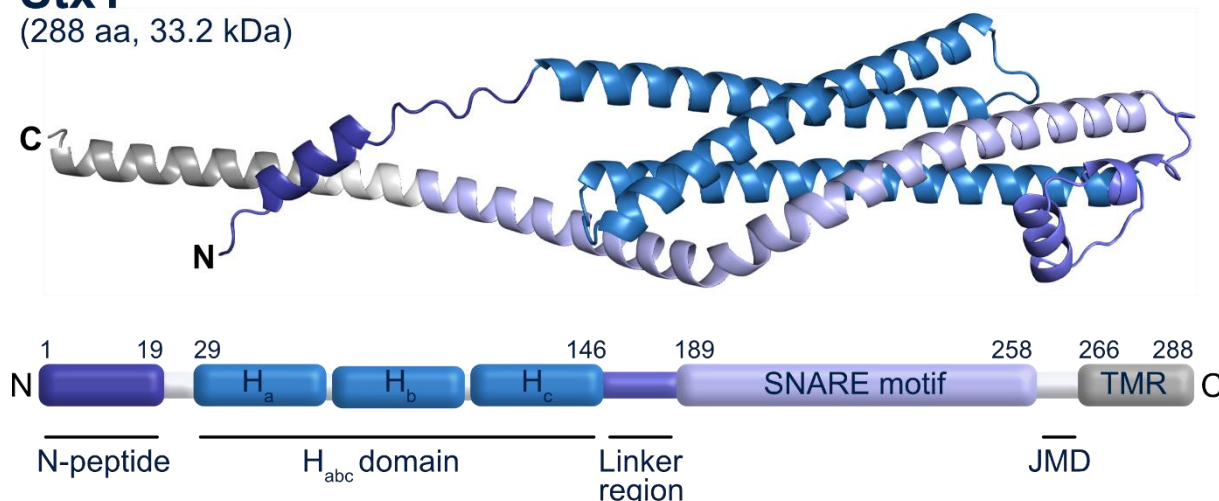


**Figure 1.4:** AlphaFold 2 structure of Syntaxin-1 (Stx1) (AF-P61266-F1, [53]) with domain organization diagram. Stx1 is a helical, multidomain protein, consisting of a short N-peptide, the  $H_{abc}$ -domain formed by three helices ( $H_a$ ,  $H_b$  and  $H_c$ ), the linker region, followed by the SNARE motif, a JMD and the C-terminal TMR. The  $H_{abc}$ -domain serves as regulatory domain, folding onto the SNARE motif, forming a ‘closed’ conformation, prohibiting premature SNARE complex formation. The TMR anchors Stx1 into the presynaptic membrane.

Stx1 (Stx1 collectively refers to Stx1A and Stx1B throughout this work) are two of 16 syntaxin protein homologues, each of which encoded by specific genes and has distinct tissue distribution and subcellular localization, reflecting their specialized roles in various cellular processes; i.e., while Syntaxin-4 is found in a wide range of cells and is involved in glucose transport, Stx1 is tied to neurons. This whole syntaxin family is also seen as a subset of the larger SNARE family, making them essential for membrane fusion events, particularly in the regulation of vesicle trafficking and exocytosis [38]. For that, Stx1 is primarily located on the plasma membrane at synapses of neurons. There it is anchored by a C-terminal transmembrane region (TMR) which is preceded by a short polybasic juxtamembrane domain (JMD, **Fig. 1.4**). The JMD is composed of a basic residue stretch that exhibits properties resembling the phosphatidylinositol 4,5-bisphosphate ( $PIP_2$ ) binding motif [54].

Indeed, research has demonstrated that the JMD promotes the  $PIP_2$ - or phosphatidylinositol 3,4,5-triphosphate ( $PIP_3$ )-dependent clustering of Stx1 [54, 55]. Additionally, disrupting its interaction with  $PIP_2/PIP_3$  results in impairments in neurotransmitter release [55]. Notably, and this is unusual for the majority of transmembrane proteins, Stx1 is palmitoylated in its TMR [56, 57]. This proposes an mechanism for the tilting and flexibility of TMR within the membrane [58, 59]. Regardless of the specific mechanism responsible for a slanted orientation of Stx1’s in the membrane, it is established that their tilted structure results in the immersion of their polybasic JMDs into the membrane. This immersion potentially counteracts the repulsive forces between the opposing vesicular and plasma membranes. Consequently, it is plausible that the JMD and TMD of Stx1 actively modulate vesicle fusion by reducing the energy barrier for membrane merging [60-62]. In line with these findings, studies indicate that the JMD of Stx1 controls the palmitoylation of its TMD. Disruption of Stx1 palmitoylation, either due to mutational charge reversion or loss of TMD cysteines hinders spontaneous vesicle fusion [63].

Precedent to the JMD is the SNARE motif which is the important structural element for Stx1's function (**Fig. 1.4**). When examined individually, outside the context of a complex, the SNARE motif consists of two well-organized helices with the zero-layer residue Q225 (Stx1B) / Q226 (Stx1A) positioned between them (**Fig. 1.4**, see the kink in the middle of the SNARE domain, separating it in almost two individual helices) [43]. The structured arrangement of both the N- and C-terminal halves of the unbound SNARE motif supports the findings of partially zippered SNARE complex intermediates, where the zero-layer acts as a site for double checking accurate assembly of the SNARE complex [64, 65]. Furthermore, it has been shown that the SNARE motif appears to have a tendency to associate itself with the membrane surface. However, when assembled into a complex with an interaction partner, the SNARE motif is lifted from the membrane, which is crucial for the assembly of the SNARE complex and subsequent membrane fusion [43].

A structural characteristic that makes Stx1 outstanding from the other two SNARE proteins involved in synaptic SNARE complex formation is the autoinhibitory  $H_{abc}$  domain (**Fig. 1.4**). It is a N-terminal regulatory domain of Stx1, characterized by a three-helix bundle structure, composed of the helices  $H_a$ ,  $H_b$  and  $H_c$  [39]. Functionally, the  $H_{abc}$  domain plays a pivotal role in inhibiting premature SNARE complex formation by folding onto the SNARE motif, creating a 'closed' conformation, making it inaccessible for the other SNARE proteins to induce SNARE complex formation. This 'closed' conformation is further stabilized by the binding to Munc18-1, one of the modulating proteins critical for membrane fusion regulation (**Fig. 1.5**) [49, 66].

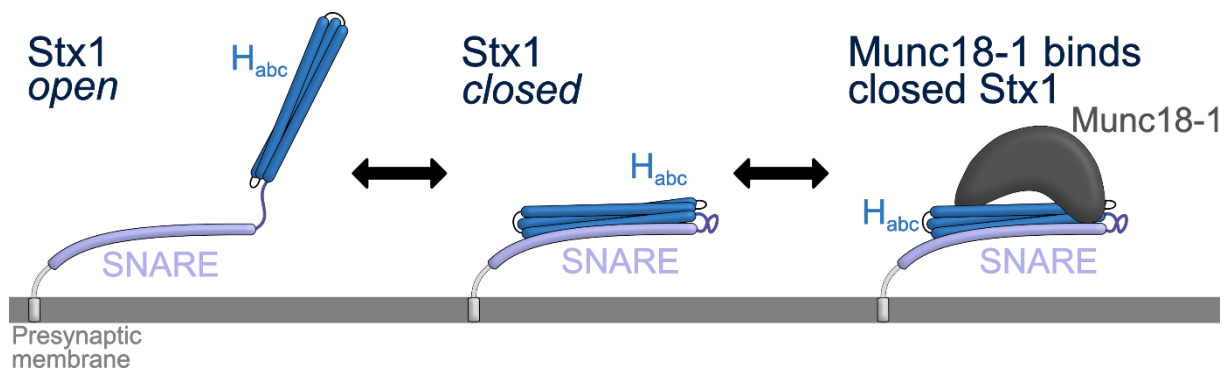


**Figure 1.5:** Schematic representation of the structural conformations of Stx1. Stx1 can either adopt an open conformation, in which the SNARE motif is free, or a closed conformation where the  $H_{abc}$  domain folds onto the SNARE motif. Munc18-1 binds to the closed conformation of Stx1 and clamps it into this conformation.

Phosphorylation sites within the  $H_{abc}$  domain enable dynamic regulation of Stx1, and also other post-translational modifications at this site can modulate interactions with other proteins, exerting influence over the synaptic vesicle fusion process. This underscores the indispensable role of the  $H_{abc}$  domain in synaptic transmission [39, 67].

The  $H_{abc}$  domain is N-terminally attached to the SNARE motif through a linker region, which reveals a high level of conformational adaptability (**Fig. 1.4**). It has been shown that the structure of the linker alternates between random coil state and well-defined secondary structure, depending on the conformation of Stx1 and its interaction partners [68, 69]. Previous works also indicate that the linker region plays a crucial role in the conformational structure of Stx1 itself, being 'opened' or

'closed' (**Fig. 1.5**), but also for the binding and complex formation to other proteins like Munc13-1. The mutation of two distinct amino acid within the linker region, the LE/AA mutation (L164A E165A for Stx1B and L165A E166A for Stx1A) forces Stx1 into its open conformation, while two other conserved residues, R150, I154 (Stx1B) / R151, I155 (Stx1A) seem to be key sites for the interaction with the MUN domain of Munc13-1. [68, 70]

The N-terminus of Stx1 is characterized by the N-terminal peptide region, a short structured amino acid stretch also known as N-peptide, which precedes the H<sub>abc</sub> domain (**Fig. 1.4**). The N-peptide serves, additionally to the H<sub>abc</sub> domain as binding site for Munc18-1 and by that contributes to the regulation of Stx1's conformation, as the binding to Munc18-1 favors the 'closed' conformation [71, 72]. Dysregulations or loss of the N-peptide have been implicated in morphological aberration of the RRP in the synapse and various neurological disorders [73, 74]. Additionally, there is an ongoing debate to which degree the N-peptide is important for synaptic transmission, however, data indicate that it is pivotal in regulating factors such as the Ca<sup>2+</sup>-sensitivity and short-term plasticity of vesicular release [67, 74].

With all its regulating domains and modulating binding partners, Stx1 can really be seen as a central hub within the SNARE complex formation machinery and as a versatile player within the SNARE protein family.

### **1.5. Molecular mechanisms and functions of Synaptosome-associated protein 25 kDa**

The other t-SNARE protein for synaptic SNARE complex formation is SNAP-25. Similar to Stx1, there are two isoforms of SNAP-25, labeled SNAP-25a and SNAP-25b in human, which arise from the alternative splicing of exon 5 of the SNAP-25 gene. These isoforms exhibit distinct expression patterns throughout development. Specifically, SNAP-25a is prevalent during the embryonic stage, whereas SNAP-25b emerges as the dominant isoform in postnatal life [75, 76]. Unlike Stx1, SNAP-25 does not contain a TMR but is anchored to the cytosolic side of the synaptic membrane through palmitoyl side chains that are covalently attached to cysteine residues located in the central linker region of the molecule. The linker region is situated between two SNARE motifs, which are both contributed to the SNARE complex by providing one glutamine on each helix for the zero layer — Q53 on the first helix and Q226 on the second (**Fig. 1.6**) [33, 77].

Earlier studies have shown that in absence of SNAP-25, vesicle docking at the presynaptic active zones remains intact. However, the pool of vesicles prepared for release is depleted, and the rapid calcium-triggered exocytosis is no longer functional [78]. Additionally, through calcium-dependent interaction with Synaptotagmin, SNAP-25 is important in both vesicle docking and priming as well as in initiating rapid exocytosis [30]. Its role has been affirmed as the proteolytic cleavage of SNAP-25 by botulinum toxins, a neurotoxin produced by the bacterium *Clostridium botulinum*, impeding exocytosis and preventing neurotransmitter release, which can lead to the characteristic neuroparalysis seen in cases of botulism [79, 80]. The commercially used form of this neurotoxin



is named Botox, which is applied for muscle disorder treatments and cosmetic purposes using adjusted doses.

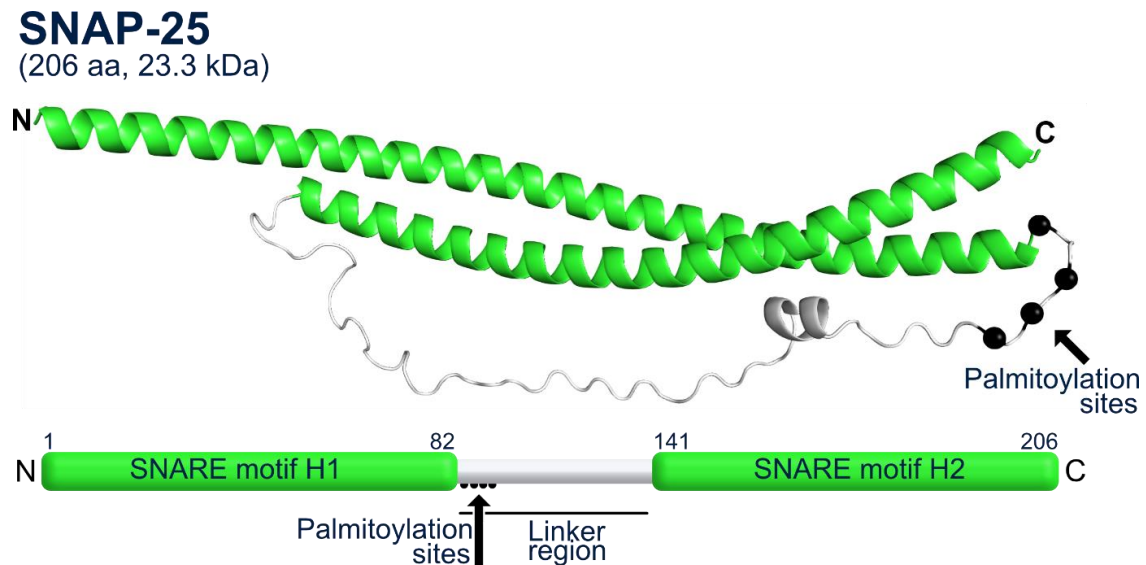


**Figure 1.6:** AlphaFold structure of SNAP-25 (AF-P60880-F1, [53]) with domain organization diagram. SNAP-25 comprises two  $\alpha$ -helical SNARE motifs (H1 and H2), connected by a linker region. Both SNARE motifs are contributing to the formation of one SNARE complex. SNAP-25 is anchored through palmitoylation modifications into the presynaptic membrane through palmitoylation site within the early linker region.

It has been found that both t-SNARE proteins, Stx1 and SNAP-25 can form a t-SNARE complex in a 1:1 or 2:1 ratio [81]. The 2:1 ratio complex, however, is branded as a 'dead-end' complex as a direct incorporation of the v-SNARE Syb2 is not feasible [82]. This ineligible complex is especially favored when adverse membrane conditions prevail and therefore has to be regulated. Experiments using electron paramagnetic resonance (EPR) spectroscopy have shown that Munc18-1 can separate the 2:1 complex resulting in a 1:1:1 complex (Stx1:SNAP-25:Munc18-1), where the equilibrium of the 'open'-'closed' conformation of Stx1 is shifted towards the open conformation [81]. Yet the 'dead-end' complex might have its use, as interferometric fluorescence measurements in lipid bilayers have shown that the SNARE motif of unbound Stx1 interacts with lipid bilayers. The interaction with SNAP-25 lifts the SNARE motif off the membrane making Stx1 accessible for interaction partners and might be critical for SNARE complex formation and membrane fusion further down the road [43].

There is an ongoing debate on how much SNAP-25 is directly involved in the interactions with the regulatory protein Munc13-1 for SNARE complex formation. While it can be said with reasonable certainty that SNAP-25 interacts with Munc18-1 only indirectly through Stx1, studies showed opposite conclusions regarding the interaction with Munc13-1. Investigations *via* microscale thermophoresis (MST) analysis and fluorescence resonance energy transfer (FRET) using different function impairment mutation on both sides showed that Munc13-1 recruits SNAP-25 by direct binding through specific binding sites between the MUN domain of Munc13-1 and the linker region of SNAP-25 [83]. Contradictory to that, studies with nuclear magnetic resonance (NMR)

spectroscopy using  $^{15}\text{N}$ -labeled SNAP-25 showed no clear sign of binding under the addition on Munc13-MUN [84].

In addition to its established function in exocytosis, SNAP-25 also influences a range of voltage-gated calcium channels through interactions with different channel types [85]. Studies have demonstrated that SNAP-25 exerts a negative regulatory effect on neuronal calcium responsiveness to depolarization by inhibiting voltage-gated calcium channels. Consequently, the silencing of native SNAP-25 in glutamatergic neurons leads to heightened activity in these channels [86-88].

SNAP-25 is also involved in the slower, clathrin-dependent endocytosis process at synapses, potentially playing a role in the coupling of exocytosis and endocytosis [89]. Since SNARE proteins are responsible for mediating exocytosis at all nerve terminals, their dual function in both exo- and endocytosis is likely a widespread principle. However, the precise mechanisms by which SNARE proteins participate in endocytosis are still not fully understood [85]. While Stx1 i.e. binds to Dynamin, SNAP-25 has been found to interact with the endocytic protein Intersectin [90, 91].

With its many interactions, SNAP-25 represents a multifunctional protein important for a smooth activity at the synaptical site. This is further supported by the clinical significance of reduced levels of functional protein. SNAP-25 has been found to share biological pathways among different neurological, neurodevelopmental and mental disorders [85]. Many studies have demonstrated the existence of multiple polymorphisms within the SNAP-25 gene and low expression levels which have been linked among others to ADHD, schizophrenia, and early-onset bipolar disorders [92-94].

### **1.6. Synaptobrevin-2: essential v-SNARE in synaptic transmission**

Opposing the two t-SNARE proteins SNAP-25 and Stx1 is the v-SNARE protein Synaptobrevin-2 (Syb2), also known as Vesicle-Associated Membrane Protein 2 (VAMP-2). It is part of the VAMP family including the other homolog isoforms VAMP-1, VAMP-3, VAMP-4, VAMP-7 and VAMP-8. In human, these six VAMPs are found in various post-Golgi vesicular compartments and facilitate vesicle fusion with the plasma membrane, the trans-Golgi network and endosomes [95-100]. I.e., Vamp-7 is crucial for mediating membrane fusion events involved in late endosome-lysosome fusion and autophagosome-lysosome fusion and is important for docking of vesicular Linker of activated T-cells (LAT) during T-cell receptor (TCR) signaling, while VAMP-1 is essential for sustaining nerve impulse transmission at neuromuscular synapses [46, 101-104].

Syb2 resides on the SV membrane and is composed of a soluble extravesicular region and a C-terminal TMR which anchors it into the vesicle membrane (**Fig. 1.7**). There, it constitutes the predominant protein component, with as many as 70 copies per vesicle. Other highly abundant vesicle constituents include Synaptophysin (~31 copies), Synaptotagmin-1 (~15 copies), and Synapsin-1 (~7 copies) [105, 106].

The soluble region is intrinsically disordered and consists of an N-terminal proline-rich domain, the SNARE motif and a JMD with an increasing structural rigidity from the N- to the C-terminus, which aligns with an observed increased affinity for lipid binding, along with a documented accelerated



rate of C-terminal SNARE zippering compared to the N-terminal counterpart (**Fig. 1.7 B**) [107]. Studies have indicated that the soluble part of Syb2 remains almost completely disordered both in solution and when associated with lipid nanodiscs [108, 109]. However, a high resolution NMR analysis of the full-length Syb2 in dodecylphosphocholine micelles revealed that besides the TMR certain segments of the SNARE motif and the JMD also adopt a helical structure while associated to the membrane (**Fig. 1.7 A**) [110]. This helix-interfacial association diminishes when Syb2 is transitioned from micelle to bicelle and to bilayer environments eventually, suggesting that the inclination towards interfacial binding is influenced by membrane curvature [111].

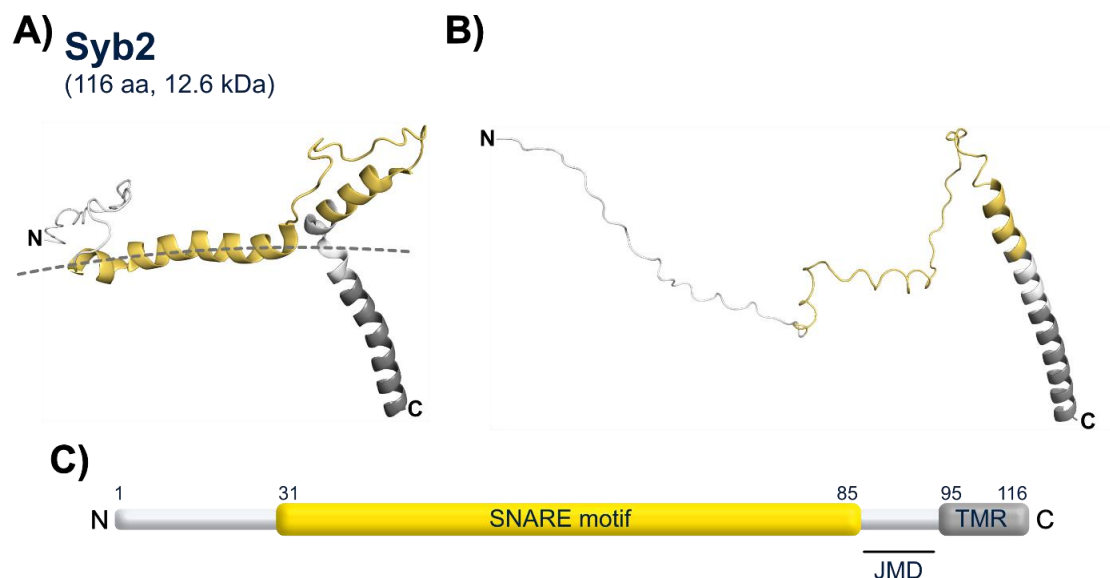


**Figure 1.7:** Synaptobrevin-2 (Syb2) is characterized by a 94 residue-long cytosolic part which includes a highly conserved SNARE motif and a dynamic JMD. The TMR anchors Syb2 into the presynaptic membrane. Generally, the N-terminal part is intrinsically disordered but can adapt a helical conformation when associated to other interaction partners. **A)** NMR structure of Syb2 on DPC micelles (PDB: 2KOG, state 1/20). A part of the N-terminal region associates with the membrane surface indicated by a grey dashed line. **B)** AlphaFold 2 structure of Syb2 showing a majorly disordered N-terminal part and a helical C-terminal region (PDB: AF-F8WCA0-F1). **C)** Domain organization diagram of Syb2.

Interestingly, similar to the JMD and TMR of Stx1, the transient interaction of Syb2 with the membrane might counteract the repulsive forces between the two membranes and the SNARE motifs. This assistance in disrupting the hydrophilic-hydrophobic boundary within the bilayer in turn aids the membrane fusion between the vesicle and presynaptic membrane driven by the formation of the SNARE complex [112-114]. Furthermore, it has been shown in multiple studies, that the JMD and TMR of Syb2 are crucial for the fusion process [112, 113, 115]. This provides a mechanistic understanding of how interactions between an intrinsically disordered protein (IDP) and lipids can lower the energy required for membrane fusion [107, 116].

Upon SNARE complex formation, the unstructured parts of the SNARE motifs form a continuous  $\alpha$ -helix, contributing the arginine (R) to the zero layer of the SNARE complex. It is discussed that the shift from a disordered to an ordered state could potentially unleash free energy to facilitate the transformation of the SNARE complex [116, 117]. Additionally, studies have shown that the electrostatic interaction between Syb2 and Stx1 trigger membrane bending forces, leading to the

convergence of SVs and presynaptic membranes, ultimately promoting membrane fusion and exocytotic events [62, 117, 118]. Furthermore, cross-linking mass spectrometry (XL-MS) experiments applied on purified and unstimulated SVs revealed a strikingly large interaction network, showing that Syb2 was cross-linked with 32 out of 56 proteins assayed, supporting a key role in SV fusion [106].

Besides from the interactions with proteins on SVs, Syb2 also engages interactions with the proteins Munc13-1 and Munc18-1, important for the orchestration of SNARE complex formation. In early studies, Vps45p, a homolog of Munc18-1, has been found to bind the v-SNARE Snc1p and t-SNARE Stx1 equivalent in yeast, indicating that Munc18-1 and homologs interact not only with t-SNARE proteins but also with v-SNAREs, setting a precedent for a potential interaction between Munc18-1 and Syb2 [119, 120]. This was further supported with the finding that Munc18-1 directly binds Syb2, albeit sub-stoichiometric, suggesting an active recruitment and positioning of Syb2 by Munc18-1 for subsequent SNARE complex formation [121]. A first concrete model for this interaction has been found for *Chaetomium thermophilum* homologs. A seminal crystal structure of the Munc18-1 homolog Vps33 with the v-SNARE homolog Nyv1 show a binding of the SNARE motif of Nyv1 to a region of Vps33, proposing that the furled loop of Munc18-1 needs to be extended for Syb2 binding [122, 123]. Based on this idea, it was reported that the helices 11 and 12 of the mentioned furled loop of Munc18-1 in fact do bind Syb2's central region which is crucial for SNARE complex formation and synaptic transmission [124]. Taken the findings together, they imply that Munc18-1 has the potential to act as a template, bringing Stx1 and Syb2 into close proximity and forming a template complex to facilitate the accurate assembly of the SNARE complex [125, 126]. Recently indeed, two cryo-electron microscopy (EM) structures have been reported, showing cross-linked Syb2 and Stx1 binding to Munc18-1. The linking was facilitated at the N-terminals of both SNARE motifs respectively, allowing a glimpse on the nucleation of the SNARE complex through the SNARE motifs and the linker region of Stx1, facilitated on Munc18-1, which provides the platform for proper alignment [69].

Munc13-1 on the other side has been demonstrated to enhance the stability of template complex by engaging with the C-terminal membrane-proximal linker region of Syb2 [123, 127]. Moreover, it was noted that Munc13-1 orchestrates the recruitment of synaptic vesicles containing Syb2 to the target plasma membrane, bringing the SNARE motifs of Syb2 into closer proximity with the Stx1:Munc18-1 complex [115, 123]. This suggests that the interaction between Syb2 and Munc13-1 is synchronized with that of Munc18-1 and Stx1, enabling the formation of the complete SNARE complex [128-130].

### **1.7. Mammalian uncoordinated 18-1: templating the SNARE complex for synaptic vesicle fusion**

The rapid and robust SNARE complex formation, which is important for fast and reliable neurotransmission, goes hand in hand with a strong binding of the SNARE motifs of the individual SNARE proteins to each other. This high affinity towards each other, however, could lead to random

synaptic vesicle fusion and uncontrolled release of neurotransmitters, making a regulation of the SNARE complex formation inevitable. This also ensures the maintenance of neurotransmitter and SV stores, which would deplete by uncontrolled fusion events leading to an impairment of effective communication between neurons. Furthermore, in a cellular environment where NSF and SNAPs favor complex disassembly, additional factors are required to overcome this disassembly activity and facilitate proper SNARE assembly [131]. Additionally, neuronal circuits rely on precise timing and synchronization of action potential. Orchestration of SNARE complex formation ensures that neurotransmitter release is tightly coupled with the action potential arrival, enabling synchronized activity [132].

## Munc18-1

(594 aa, 67.5 kDa)

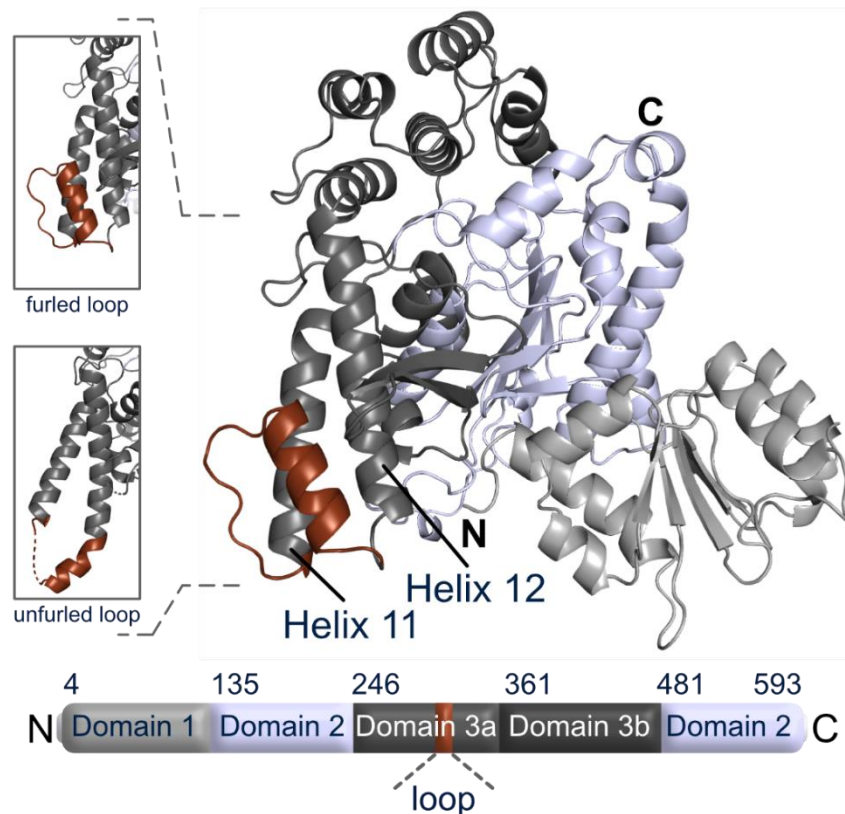


**Figure 1.8:** AlphaFold 2 structure of Munc18-1 (AF-P61764-F1, [53]) with domain organization diagram. Munc18-1, a multidomain protein, comprises three domains, with domain 3 further divided into 3a and 3b. It showcases an arch-shaped configuration where domains 1 and 3 serve as the legs that accommodate the binding of Stx1 in between. Within domain 3a, situated between helix 11 and helix 12, lies the furlled loop, which unfurls to elongate both helices, rendering the formation of the SNARE complex (insets show the furlled and unfurled conformation of the loop. Unfurled loop conformation derived from Stepien *et al.* (2022) (7UDB) [69]).

One of these orchestrating proteins is Mammalian uncoordinated 18-1 (Munc18-1), also known as Syntaxin-binding protein 1 (Stxbp1), which plays a pivotal role in the process of neurotransmission. Munc18-1 is part of the Sec1/Munc18 (SM) proteins, a conserved protein family crucial for membrane trafficking events and indispensable for the regulation of membrane fusion [133]. Within the human genome, there are seven homologues SM proteins. Among these, Munc18-1, Munc18-

2 and Munc18-3 play roles in secretion. While Munc18-2 is primarily found in platelets and is involved in platelet exocytosis, Munc18-3 is ubiquitously expressed but found mainly in the pancreas and is involved in the regulated secretion of insulin from pancreatic beta cells [134, 135]. Munc18-1 exhibits high expression levels in neurons and neuroendocrine cells [136]. It is a multidomain protein, containing domains 1-3 with domain 3 being further divided into the sub-domains 3a and 3b. The tertiary structure exhibits an arched structure where domains 1 and 3a render the characteristic central cavity (**Fig. 1.8**) [40, 137]. The structural most interesting region is the furled loop at helix 11 and 12 in domain 3a, which, when extended, works as a template for the precise pairing of cognate SNARE proteins and is important for SNARE complex formation and vesicle priming (**Fig. 1.8 inset**) [126, 138].

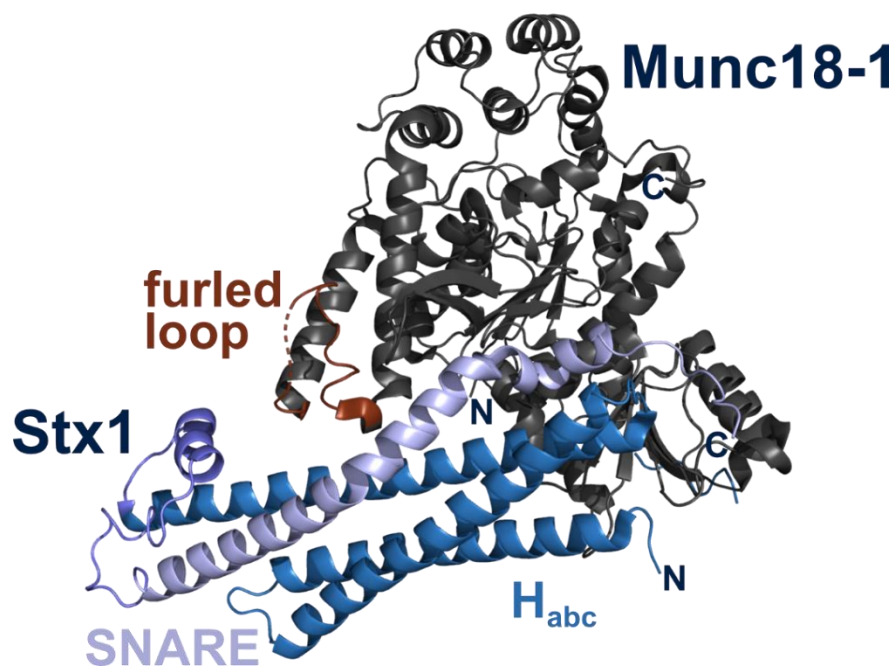


**Figure 1.9:** Crystal structure of the Stx1:Munc18-1 complex shows Munc18-1 (black) binding Stx1 in its closed conformation, with the H<sub>abc</sub> domain (blue) is bound onto the SNARE motif (light-purple) of Stx1 (PDB: 3C98). The loop within Munc18-1's domain 3a (brown) is furled.

Much has been already said about the interactions of Munc18-1 with the SNARE proteins in the previous chapters. Munc18-1's closest binding partner is Stx1, which is bound in its 'closed' conformation in the central cavity formed by domain 1 and 3a. There, Stx1's H<sub>abc</sub> domain folds back onto the SNARE motif to adopt the closed conformation through intramolecular interactions and Munc18-1 locks it into this conformation (**Fig. 1.9 A**). This precludes the clamped Stx1 from SNARE complex assembly. Remarkably, this inhibitory binding mode enables Munc18-1 to precisely chaperone Stx1 to the presynaptic membrane, facilitating the accumulation of vesicles around the plasma membrane [139]. Alongside its central cavity, domain 1 also harbors an additional site dedicated to binding the N-peptide of Stx1 [140].

To release Stx1 from Munc18-1's tight clamp and making it accessible for SNARE complex formation, a conformational change is required. This happens at the furled loop of domain 3a. There,

the furled linker between the helices 11 and 12 unfurls, allowing for a subsequential realignment of the SNARE motif of Stx1 along the outside of the extended helix 12 of Munc18-1 [69]. This concept was originally established through the pivotal crystal structure of the yeast vacuolar SM homolog Vps33 in association with the SNARE motif of the Stx1 homolog Vam3, where the SNARE motif was found binding next to an extended helix region and has recently been confirmed [69, 122].

A second structure of the same study (and mentioned in the previous **Chapter 1.6**) showed the binding of Syb2 homolog Nyv1 into the helical hairpin region of Vps33, a conserved region similar to the unfurled loop of Munc18-1 and right next to the SNARE motif binding region. This indicated that Syb2 can bind into the binding groove between helix 11 and 12, formed by the extension of the furled loop region. Furthermore, this and others studies suggested that Vps33 and probably other SM proteins like Munc18-1 bind two SNAREs simultaneously close to each other and by that act as template to render the initiation of SNARE complex formation and generate partially zippered SNARE assembly intermediates [122-124, 127, 141]. This idea was confirmed by two cryo-EM structures, showing Munc18-1 bound to covalently cross-linked Stx1 and Syb2 as the direct binding of Syb2 to Munc18-1 is aggravated by low affinity [69, 142].

The exact mechanism of the unfurling of the loop in domain 3a remained elusive and the sequence of conformational changes were unclear. Is it the linker region of Stx1 that undergoes a rearrangement allowing for an opening of the furled loop, or is it the opening of the furled loop, which induces a structural rearrangement of the linker region and a subsequent alignment of the SNARE motif to the extended helix 12 [84, 143, 144]? Recent studies indicate that the opening of the linker region of Stx1 allows for the opening of the furled loop [69, 84]. Either way, it is a fact that this conformational restructuring does not happen by itself, but is catalyzed by another orchestrating protein, Munc13-1. However, the binding of Munc13-1 to the template complex is extremely transient, making it very difficult to study the exact binding mechanisms and sites. [84, 129]. Studies have shown that the MUN domain of Munc13-1 does weakly interact with the linker region of Stx1 but a direct, yet transient interaction between Munc18-1 and Munc13-1 has also been reported [84, 141, 145]. Perhaps these interactions might trigger the unfurling of the loop to facilitate the alignments of the SNARE motifs.

Multiple loss-of-function mutations within the furled loop region were identified including i.e., Q301A, K332E/K333E and L348R as well as gain-of-function mutations like P335A and D326K, which allow for SNARE complex formation even in the absence of Munc13-1 [141].

Generally, the regulatory mechanism of Munc18-1 is intricate, encompassing both the facilitation and inhibition of SNARE assembly. Nonetheless, the promotion process takes precedence over the two [146].

With its templating role, Munc18-1 plays an important role in modulating synaptic plasticity, neurodevelopment and the function of neuroendocrine cells. Additionally, it has the capacity to regulate brain-derived neurotrophic factors, influence synaptic development and impact cognitive functions. Studies with genetic knockout of Munc18-1 in mice have shown an impaired synaptic plasticity, associated with diminished neurotransmitter release and reduced size of vesicle pool,

resulting in impaired learning and memory [71, 147]. Hence, irregular Munc18-1 expression plays a role in the development of several neurological disorders and is closely linked to conditions like epileptic encephalopathy, autism, schizophrenia, Parkinson disease, Alzheimer disease and multiple sclerosis [148, 149]. This makes Munc18-1 an interesting target for therapeutic interventions in neurological disorders. Research in this area aims to develop drugs that modulate Munc18-1 function to restore normal synaptic transmission [150].

### 1.7. Mammalian uncoordinated 13-1: catalyzing synaptic vesicle Fusion

The other orchestrating protein of the SNARE complex formation machinery is Mammalian uncoordinated-13 (Munc13-1). Like Munc18-1, Munc13-1<sup>(1)</sup> has a central role in the process of synaptic vesicle fusion at the presynaptic active zone, but does not (or at least not fully) act in a templating way, but rather as an exchange factor that assists in the reshuffling of helices towards the formation of the SNARE complex helical bundle.

Munc13-1, also known as Unc-13 homolog A (Unc13A), is the most abundant isoform in the mammalian brain, mainly found in the presynaptic terminal [151, 152]. It is part of the complexes associated with tethering containing helical rods (CATCHR) family, a group of proteins involved in membrane trafficking within cells and which play a crucial role in the tethering step, a process that ensures accurate and specific targeting of vesicles to their correct destination membrane [153, 154]. Munc13-1 can fulfill this task due to its architecture. It is a large multidomain protein, including a variable N-terminal region and a conserved C-terminal region throughout all Munc13 isoforms [155]. The N-terminal section encompasses a C<sub>2</sub>A domain that forms both homodimers and heterodimers with  $\alpha$ RIMs, connecting RIM-dependent forms of plasticity with the priming machinery [21, 156-159]. It also features a calmodulin-binding region (CaMb) that plays a role in Ca<sup>2+</sup>-dependent short-term plasticity (**Fig. 1.10**) [16, 160].

The conserved C-terminal region of Munc13-1 comprises several crucial domains. This includes the C<sub>1</sub> domain, which mediates diacylglycerol (DAG)/phorbol ester-dependent potentiation of release [161]. The subsequent C<sub>2</sub>B domain binds both Ca<sup>2+</sup> and PIP<sub>2</sub> and plays a role in Ca<sup>2+</sup>-dependent short-term plasticity [162]. Additionally the MUN domain, an elongated, arch-shaped architecture formed by  $\alpha$ -helical bundles, facilitates the opening of Stx1 [84, 145]. And finally, the C<sub>2</sub>C domain binds weakly to membranes in a Ca<sup>2+</sup>-independent manner [163]. In the crystal structure of a Munc13-1 fragment comprising the C<sub>1</sub>, C<sub>2</sub>B, and MUN domain, it was observed that the C<sub>1</sub> and C<sub>2</sub>B domains are situated at the N-terminal end of the extensively elongated MUN domain (**Fig. 1.10**).

Notably, their DAG- and Ca<sup>2+</sup>/PIP<sub>2</sub>-binding sites are oriented in the same direction [164]. It is anticipated that the C<sub>2</sub>C domain protrudes from the opposite end of the MUN domain.

(1) Did you know that the 'Munc' prefix of Munc18-1 and Munc13-1 stands for 'mammalian uncoordinated'? These names were chosen based on the fact that the genes encoding these proteins were identified as mammalian homologs of proteins first discovered in *C. elegans*, known as Uncoordinated-13 (Unc-13) and Uncoordinated-18 (Unc18). In *C. elegans*, Unc-13 and Unc-18 play crucial roles in synaptic vesicle exocytosis, and mutations in their encoding genes lead to uncoordinated movements and locomotion defects, hence the name 'uncoordinated' [16, 151].

This structural arrangement facilitates Munc13-1's ability to bridge membranes, giving rise to a proposed model where the C<sub>2</sub>C domain attaches to the vesicle membrane, while the C<sub>1</sub>-C<sub>2</sub>B region binds to the plasma membrane [163, 165].

Mutations within the membrane-binding residues of the C<sub>2</sub>C domain reduced the ability for liposome clustering *in vitro* and showed impaired vesicle docking and release of neurotransmitters in neurons, which supported the idea of this membrane bridging model [163]. While the peripheral C<sub>1</sub>, C<sub>2</sub>B and C<sub>2</sub>C domains promote the tethering of the vesicle membrane to the presynaptic membrane, the MUN domain plays a crucial role in facilitating the transition from the closed conformation of the Stx1:Munc18-1 complex to an open, fusion competent state [84, 129, 141, 145]. However, the exact mechanism through which Munc13-MUN facilitates the activation of Stx1 has been a subject of debate, partly due to the varied nature of interactions observed between Munc13-1 and Stx1 and due to its apparent transient interaction with components of the SNARE complex and with Munc18-1.

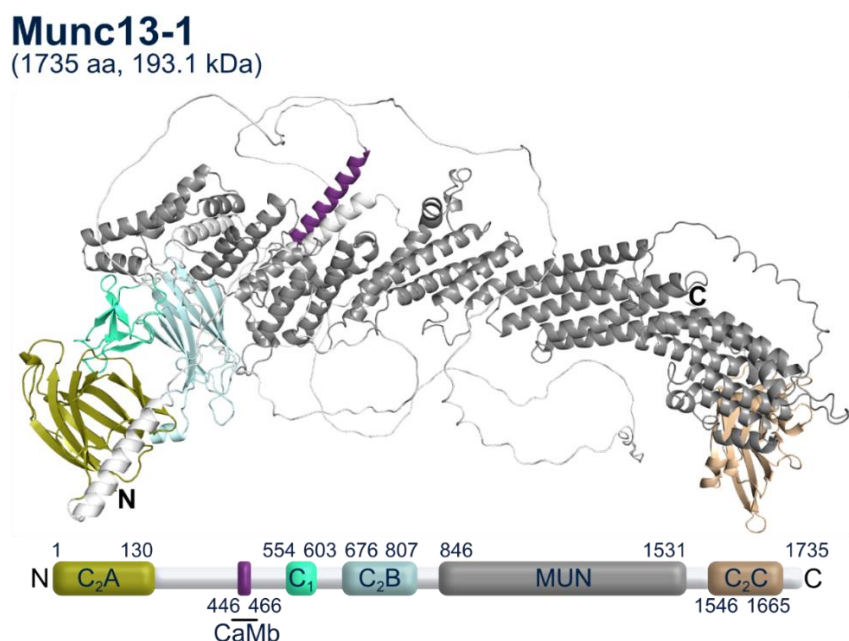


**Figure 1.10:** AlphaFold 2 structure of Munc13-1 (AF-Q9UPW8-F1, [53]) with domain organization diagram. Munc13-1 is a large multidomain protein consisting of six distinct domains, with the MUN domain being the largest one. This allows Munc13-1 to be a platform for multiple interaction sites and partners to prime (C<sub>2</sub>A) and to tether synaptic vesicles to the presynaptic membrane (C<sub>1</sub>, C<sub>2</sub>B and C<sub>2</sub>C) and to catalyze the SNARE complex formation (MUN).

Early studies with yeast-two-hybrid assays discovered that a segment encompassing a portion of the H<sub>abc</sub> domain of Stx1 binds to a C-terminal fragment containing the Munc13-1 C<sub>2</sub>C domain. Yet, pulldown assays suggested involvement of the MUN domain [166]. Further examinations using NMR spectroscopy demonstrated that the MUN domain accelerates the transition from the Stx1:Munc18-1 complex to the SNARE complex. Additionally, it was found that the MUN domain exhibits a relatively weak binding affinity to Stx1's N-terminal portion of the SNARE motif. The N-terminal region, encompassing the H<sub>abc</sub> domain, and the Munc13-1 C<sub>2</sub>C domain did not seem to play a substantial role in this binding interaction [145, 163]. These findings proposed a model in



which the MUN domain acts to disengage the SNARE motif from the tight clamping Munc18-1, thereby initiating the opening of syntaxin-1 and promoting the assembly of the SNARE complex.

Conversely, an alternative study put forth the idea that the MUN domain's role in stimulating SNARE complex formation hinges on interactions with the linker region connecting the H<sub>abc</sub> domain and the SNARE motif of Stx1, rather than with the SNARE motif itself. This model suggests that the MUN domain, albeit through very transient and hardly detectable binding, destabilizes the closed conformation and provides a scaffold for SNARE complex assembly [84]. The validity of this model was reinforced by the discovery that mutations within the linker region (R150A, I154A (Stx1B) / R151A, I155A (Stx1A)) hinder MUN domain-facilitated SNARE complex formation. This impairment was further evident in liposome fusion during reconstitution assays and in neurotransmitter release within neurons [70].

With perspective from the other side, a crystal structure and sequence alignment revealed a highly conserved hydrophobic pocket in the middle of the MUN domain which seems to be crucial for the interaction with the linker region of Stx1 [167]. There, two residues, N1128 and Phe1131 (referred to as NF), have been identified to play a vital role in facilitating the transition from the Stx1:Munc18-1 complex to the SNARE complex and an introduction of a double mutation to alanine (NFAA) completely abolished the functionality of the MUN domain [70, 129, 167].

These observations suggest that a series of conformational changes, involving the release of existing interactions and the establishment of new ones, is necessary for the shift from the Stx1:Munc18-1 complex to the SNARE complex. Additionally, there exist a subtle equilibrium between interactions that impede or facilitate this transition. Consequently, it might explain that even extremely transient interactions, which may be challenging or even impossible to discern through conventional biochemical techniques, can exert a crucial influence in tipping this equilibrium [84].

Besides this interaction with the Stx1:Munc18-1 complex, the MUN domain has been found to interact with Syb2 and by that, renders the Syb2 SNARE motif more accessible to the Stx1:Munc18-1 complex. Early studies have suggested a possible interaction of the C-terminus of Syb2 with the MUN domain, which was later confirmed by a crystal structure showing the MUN domain binding a short synthesized Syb2 peptide of its C-terminal JMD [123, 127, 168]. There, the residues W89 and W90 were found to bind into a small hydrophobic pocket at the C-terminal region of the MUN domain. Additionally, it is indicated that the residues R86 and K87 of Syb2 likely bind to a negatively charged patch further up the sequence of the MUN domain. In contrast to the  $\alpha$ -helical structure of the Syb2 JMD when it is bound within the cis-SNARE complex, the JMD adopts a folded, albeit non- $\alpha$ -helical conformation when it is bound to the MUN domain. Pull-down experiments have revealed that the preassembled SNARE complex exhibited a diminished interaction with the MUN domain compared to isolated Syb2. This suggests that, upon the final zippering of the SNARE complex into the membranes, the MUN domain might detach from the JMD of Syb2 [123].

Mutations within the MUN domain disrupting the binding to the C-terminal region of Syb2 have been found to strongly impair both the mini-inhibitory postsynaptic currents (mIPSCs) frequency



and the action potential-evoked IPSCs in cultured mouse cortex neurons. Furthermore, the size of the RRP has been found to be majorly reduced, leading to the assumption that the interaction between Syb2 and the MUN domain of Munc13-1 is essential for docking and priming of synaptic vesicles [123]. Moreover, general dysfunctions of Munc13-1 can lead to neurodevelopmental disorders characterized by cognitive and behavioral impairments like Autism or Schizophrenia but also to more severe physiological malformations like microcephaly, cortical hyperexcitability leading to amyotrophic lateral sclerosis (ALS) and fatal myasthenia [169, 170]. These discoveries indicate that the energy barriers introduced by the Munc18-1 furled loop and the closed conformation of Stx1 play a crucial role in making neurotransmitter release reliant on Munc13-1 [84].

### 1.8. Integrating the mechanisms of SNARE-mediated vesicle fusion

Based on the gathered information from the various studies on the key components introduced thus far, it is valuable to present a theoretical model of the step-by-step process underlying the mechanism of vesicle fusion.

Initially, SVs are guided and docked to the target membrane's CAZ by Rab3 which interacts with its interaction partner, the Rab-effector RIM at the presynaptic site [21]. This docking process is additionally aided by Munc13-1, which tethers the SV membrane to the target membrane through its bordering C<sub>1</sub>, C<sub>2B</sub> and C<sub>2C</sub> domains (**Fig. 1.2 A**) [163].

At the presynaptic membrane, Munc18-1 forms a tight complex with the t-SNARE Stx1 (and possibly with SNAP-25), binding Stx1 in its closed conformation, with the H<sub>abc</sub> domain coordinated onto the SNARE domain, inhibited for unwanted SNARE complex formation (**Fig. 1.11 A**) [145]. The MUN domain of Munc13-1 binds the v-SNARE Syb2 *via* a small hydrophobic pocket and negatively charged patch at the C-terminal end and renders the coordination to the initiation site for the SNARE complex formation [123, 127]. Additionally, the MUN domain catalyzes the opening of the furled loop of Munc18-1. This may occur through a transient interaction between the highly conserved hydrophobic pocket situated at the center of the MUN domain and the linker region of Stx1 (**Fig. 1.11 B**) [167].

A potential structural rearrangement of the linker region permits the extension of the loop, creating a binding site for the SNARE domain of Syb2 between helices 11 and 12 of Munc18-1's domain 3a. Furthermore, these conformational changes enable the SNARE domain of Stx1 to escape inhibition by the H<sub>abc</sub> domain and coordinate alongside the extended loop [69]. This resultant complex of Stx1, Munc18-1, and Syb2 acts as a template for SNARE complex formation, initiating the nucleation of a four-helix bundle that leads to the establishment of the trans SNARE complex upon incorporation of SNAP-25 (**Fig. 1.11 B, C**) [69, 129]. As the SNARE complex partially zippers, the SV becomes primed to the presynaptic membrane with Complexin maintaining this state by impeding full zippering (**Fig. 1.2 B**) [143]. The ensuing influx and increased concentration of Ca<sup>2+</sup> prompts the release of Complexin through the displacement by Synaptotagmin-1 at the SNARE complex, enabling complete zippering (**Fig. 1.2 C**) [143]. This draws the opposing membranes together until a fusion pore forms, expanding until complete fusion of the vesicle membrane and plasma

membrane is achieved, ultimately leaving behind a cis-SNARE complex and releasing neurotransmitters into the synaptic cleft (**Fig. 1.11 D**) [30]. These neurotransmitters traverse through the synaptic cleft and bind to receptors on the postsynaptic side, culminating in neurotransmission (**Fig. 1.1 C**).

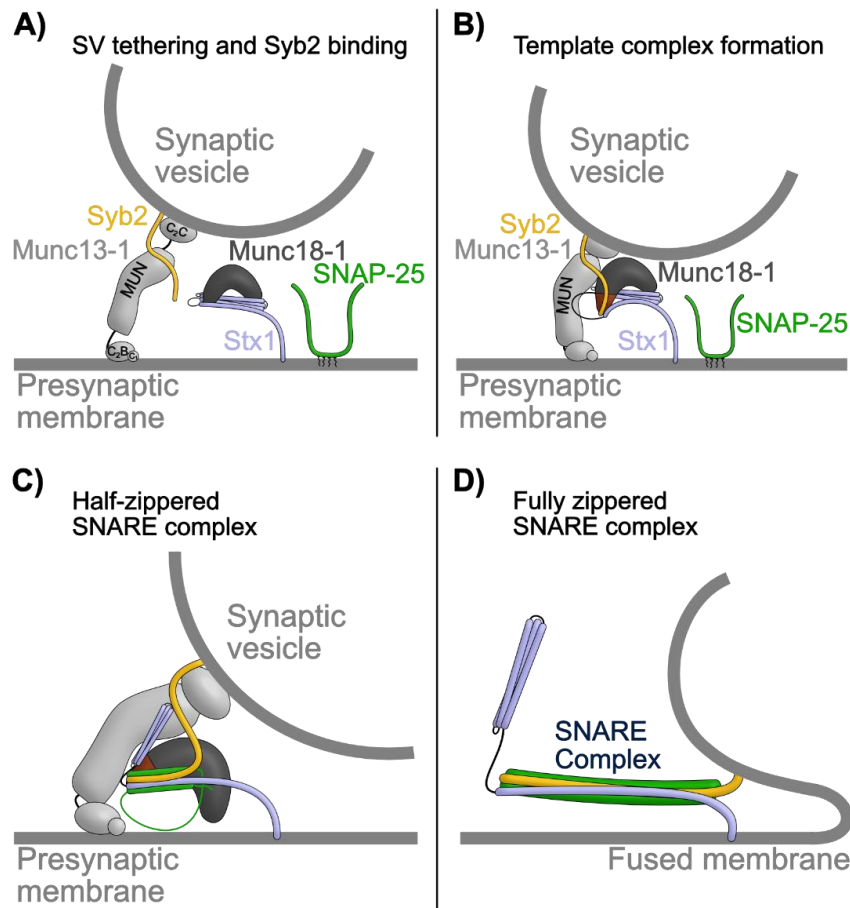


**Figure 1.11:** Working model of the orchestrated SNARE complex formation by Munc18-1 and Munc13-1 (figure adapted from Wang *et al.* (2019) [123]). **A)** SV is tethered to the presynaptic membrane through the C1, C2B and C2C domains of Munc13-1. Furthermore, Munc13-1 binds and coordinates Syb2. Munc18-1 clamps Stx1 in its autoinhibited conformation. **B)** The MUN domain of Munc13-1 catalyzes the opening of this closed conformation by a possibly transient interaction with the linker of Stx1. Additionally, helix 11 and 12 in domain 3a of Munc18-1 get extended by the unfurling of the furled loop (schematically indicated in brown) and Syb2 gets rendered into the newly formed binding groove forming a template complex of Munc18-1, Stx1 and Syb2. **C)** Formation of a half-zipped SNARE complex with the entry of SNAP-25 and release of Munc18-1 clamping. **D)** Full-zipping of the SNARE complex leads to fusion of SV membrane and presynaptic membrane.

## 1.9. SNAREopathies: disorders of the synaptic vesicle fusion machinery

Accurate neurotransmission is highly dependent on the proper function of the vesicle fusion machinery with its core components including the t-SNARE proteins Stx1 and SNAP-25, the v-SNARE protein Syb2 as well as the orchestrating proteins Munc18-1 and Munc13-1. Given its various interactions with each other, conformational changes and mechanisms, this intricate and crucial apparatus plays an essential role in ensuring the correct function of neurons at the synaptic site. It is therefore not surprising that disruptions within the vesicle fusion machinery can lead to a range of neurological and neurodevelopmental disorders (**Fig. 1.12**) [71, 148, 149, 169, 170].

Being that indispensable, it is striking that there is no contingency plan in place for these fusion reactions. Due to this absence of backup, mutations in the human genes responsible for these proteins are anticipated to have significant clinical implications on brain function. The majority of documented mutations consist of heterozygous *de-novo* missense or loss-of-function mutations [171]. Interestingly, while it could be anticipated that mutations in any part of this interconnected system would result in comparable symptoms, recent studies indicate that alterations of the proteins can manifest in a remarkably wide range of symptoms (**Fig. 1.12**). Foremost among these are neurodevelopmental delays in speech, language, motor function, and intellectual capacity. Additionally, individuals with severe developmental delays may exhibit neurological characteristics, including seizures, epileptiform abnormalities, and motor difficulties like spasms and ataxia [171]. Thus, while these proteins collaborate within a tightly integrated molecular system, mutations in individual components result in a surprisingly wide range of symptoms and diagnoses. Much like channelopathies refer to a group of disorders characterized by abnormal functioning of voltage gated ion channels, regulating the flow of  $K^+$ ,  $Na^+$ ,  $Ca^{2+}$  ions in and out of the cell, leading to various symptoms, Verhage *et al.* (2020) proposed to unify disorders emerging from mutations in the functionally related SNARE machinery in the term of SNAREopathy [171, 172]. It can be seen as a subgroup of the previous defined synaptopathy, which, in contrast, comprises a much more diverse group of encoded proteins localized at different neuronal cell compartments and various molecular functions, while SNAREopathies narrows the scope down to the diseases caused by mutations affecting the SNARE machinery [171, 173].

Remarkably, in the clinical cases of SNAREopathies, the *stxbp1* gene, encoding for Munc18-1, emerges as the most frequent reported one by far (**Fig. 1.12**). This suggests that the *stxbp1* gene is particularly susceptible to mutations, with many resulting in functional abnormalities of the protein. Roughly 60% of the documented mutations to date involve truncations or partial or complete gene deletions, which are anticipated to halve protein levels [169]. This strongly indicates that inadequate expression is a central factor in this disorder. Missense mutation, dispersed across the gene without a clear pattern may compromise protein stability, resulting in a reduction of protein levels below hemizygoty [174]. Reports have shown that certain mutants, in addition to their reduced stability, form protein aggregations that could also ensnare wild-type proteins, leading to their degradation [175].

Mutations in the three SNAREs, Syb2, Stx1B, and SNAP-25, that lead to diseases frequently manifest as point mutations concentrated in the SNARE domains or the crucial  $H_{abc}$  domain of Stx1B. This pattern strongly suggests that the symptoms are likely attributable to a disruption in the canonical SNARE function of these proteins [176-178]. Compared to Munc18-1, however, there are significantly fewer reported cases for the SNARE proteins as well as for Munc13-1, with Stx1B appearing to be the most likely one of the three SNAREs to be affected (**Fig. 1.12**). Interestingly, when comparing the paralogs Stx1A and Stx1B, almost no mutations are described in relation to SNAREopathies for Stx1A, however, many more for Stx1B. Yet, these mutations translate into comparably mild symptoms showing a redundancy depending on the presence of the other paralog

[171]. The reason why Stx1B seemingly masks or compensates for the loss of Stx1A better than *vice versa* remains somewhat unclear. Answers might be found in the subtle functional distinctions and expression patterns between Stx1A and Stx1B, as well as their specific roles within synaptic transmission, which could influence their capacity for mutual compensation [52, 179, 180].

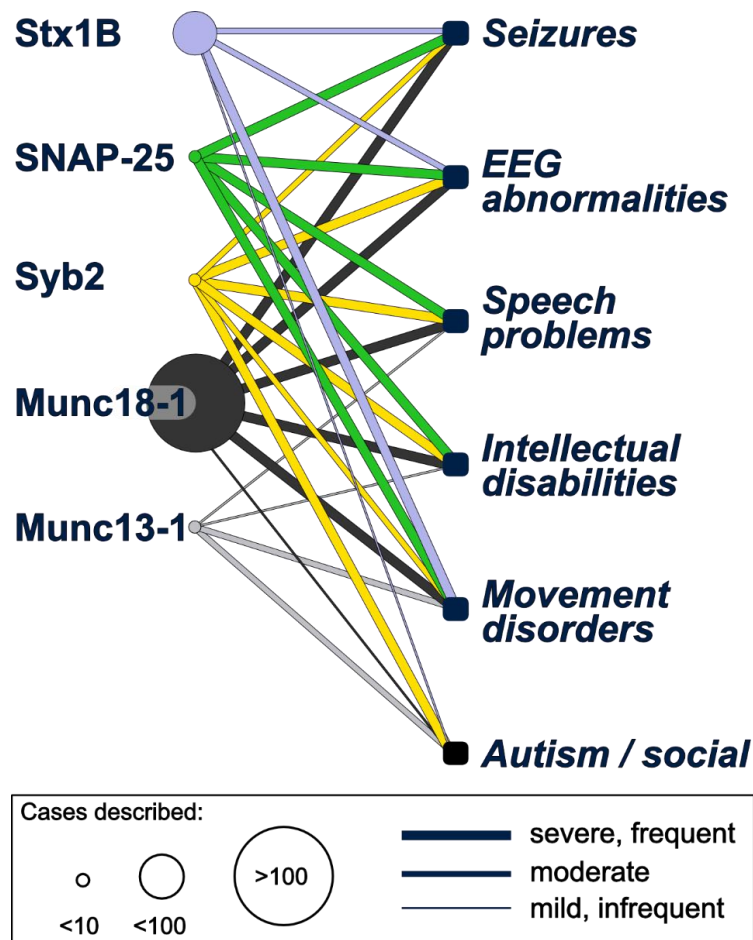


**Figure 1.12:** Incidence of symptoms associated with mutations in SNARE complex formation proteins linked to SNAREopathies. The width of the lines signifies the frequency of documented symptoms, while the dimensions of the circles denote the total reported cases per gene (June, 2020, figure adapted from Verhage *et al.* (2020) [171]).

Many SNAREopathic mutations found within Stx1B are linked to various types of epilepsy, one of the most common neurological symptoms with a prevalence of > 0.5% [171, 181-183]. Epilepsy comprises a diverse range of syndromes with numerous underlying causes, defined by recurrent, unprovoked seizures and altered neuronal excitability. Epileptic seizures result from abnormal and excessively hypersynchronous neuronal activity. They typically endure for seconds or minutes and can be categorized as generalized, focal, or epileptic spasms. Clinically, they are characterized by a sudden, brief period of altered or lost consciousness, along with involuntary movements or convulsions [184]. The pathophysiology of epilepsy is multifaceted, with genetic factors often playing a significant role, while it can also emerge in an otherwise unaffected and healthy brain following events such as stroke, injury, trauma, or infection. Additionally, processes related to neuronal plasticity, development, and degenerative disorders may contribute significantly to the development of epilepsy [185, 186].

Approximately 60% of cases have an unidentified origin. The highest incidence of epilepsy occurs in young children and the elderly. Developmental and epileptic encephalopathies (DEE), resulting from genetic defects, are more prevalent in younger individuals [187]. In most instances, these are thought to arise from the interplay of various genetic and environmental factors. A smaller proportion of cases can be attributed to monogenic defects, involving over 140 genes identified to date [188].

A commonly accepted theoretical framework for understanding seizures proposes a disruption in the delicate balance between brain excitation and inhibition [186, 189]. It is theorized that the seizure events may induce self-reinforcement, generating activity levels capable of either suppressing or promoting inhibition or excitation, thereby offering the essential positive feedback to perpetuate the seizure. The primary mechanism believed to trigger seizures is activity-dependent disinhibition, which arises from the dysregulation of ionic concentrations within intra- and extracellular spaces. Disruption in ionic balance can be influenced by mutations in transmembrane channels and transporters (channelopathies) [185]. A second mechanism is the already mentioned altered neuronal plasticity, which, among others, falls back onto SNAREopathies. Disruptions within the synaptic vesicle fusion and neurotransmitter release machinery lead to a dysfunctional neurotransmission, affecting the excitation or inhibition of the postsynaptic neurons and can result in epileptic triggers [186].

Prolonged imbalances in excitation and inhibition can lead to a process called epileptogenesis, where the brain undergoes long-lasting changes that increase its susceptibility to future seizures. This can involve alterations in the structure and function of neurons, as well as changes in synaptic connectivity. Understanding the intricacies of the excitation-inhibition balance in epilepsy is a focal point of ongoing research. Advances in this field may lead to the development of more targeted and effective treatments for epilepsy [190].

### **1.9.1. Stx1B mutations translate into SNAREopathic neurological disorders**

In the intricate orchestration of events governing neurotransmission, Stx1 emerges as a key conductor at the presynaptic membrane. Its interaction with other SNARE proteins, Syb2 and SNAP-25, forms the core of the SNARE complex, crucial for membrane fusion during exocytosis. The significance of Stx1 in synaptic vesicle fusion is manifold; not only does it serve as a binding partner in SNARE complex formation, but it also undergoes dynamic conformational changes, including those in the linker region and the H<sub>abc</sub> domain. This autoinhibitory domain acts as a molecular switch, finely tuning the transition between closed and open conformations of Stx1. Strictly regulated, this mechanism ensures the precise timing and execution of neurotransmitter release. Furthermore, Stx1's association with the coordinating proteins Munc18-1 and Munc13-1 further underscores its intricate involvement in the finely tuned process of vesicle priming and fusion. The importance of Stx1's function, particularly that of Stx1B, is evident in the considerable number of reported clinical cases within the realm of SNAREopathies. Genetic mutations within Stx1B exhibit significantly more reported cases compared to the other SNARE proteins Syb2 and

SNAP-25, ranking second only to Munc18-1 in the synaptic vesicle fusion machinery (**Fig. 1.12**) [171]. Additionally, numerous epileptogenic mutations have been identified in both the regulatory  $H_{abc}$  domain and the effector SNARE motif of Stx1B [181, 182]. Interestingly, these mutations lead to epilepsy with a diverse range of phenotypes, prompting the question of whether they impact the function of Stx1B in various ways. In an earlier study, we investigated three paradigmatic Stx1B mutations, an insertion/deletion (InDel) mutation (K45/RMCIE, L46M) within the  $H_{abc}$  domain, a G226R mutation and a V216E mutation within the SNARE motif, which have been described to exert distinct epileptic phenotypes [178, 181, 182]. While the Stx1B<sup>InDel</sup> mutation, associated with mild epilepsy, results in an unfolded protein unable to bind to Munc18-1 and incapable of sustaining neurotransmission, the Stx1B<sup>G226R</sup> mutation, linked to epileptic encephalopathies, significantly impairs interaction with Munc18-1, reduces the expression of both proteins, diminishes the size of the readily releasable pool (RRP), and hampers  $Ca^{2+}$ -triggered neurotransmitter release when expressed in Stx1-null neurons [178]. In contrast, the Stx1B<sup>V216E</sup> mutation, also associated with epileptic encephalopathies, has a less pronounced impact on interactions with Munc18-1 and Munc13-1. Yet, it enhances fusiogenicity and increases vesicular release probability, even in Stx1-null neurons [178].

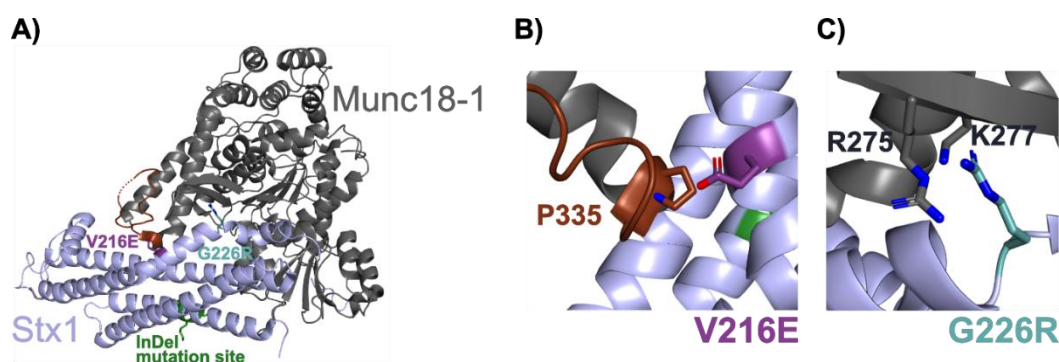
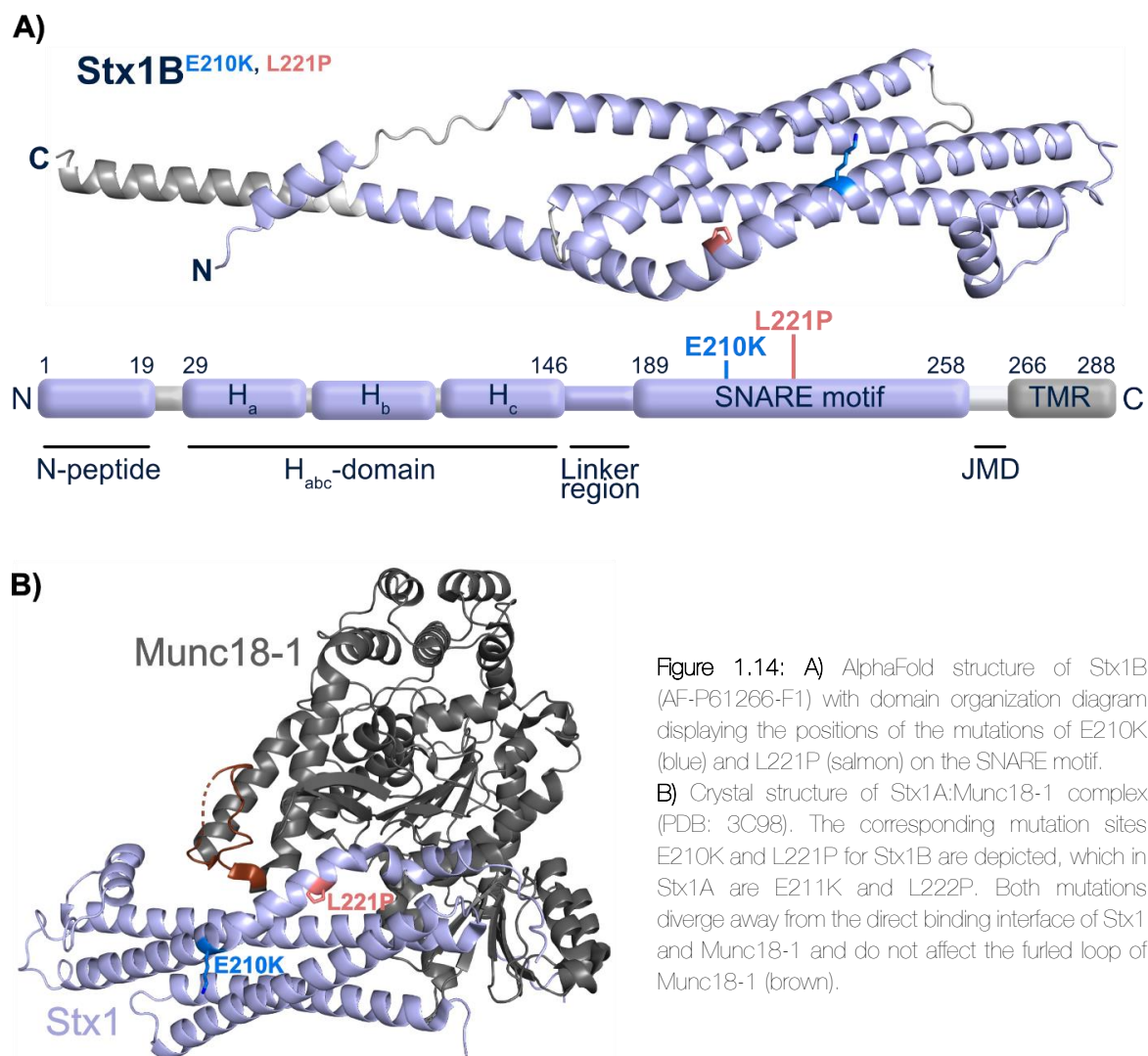


**Figure 1.13:** **A)** Crystal Structure of the Stx1A:Munc18-1 complex from *R. norvegicus* (PDB: 4JEU). The highlighted sections indicate the specific corresponding positions of the Stx1B mutations InDel, V216E and G226R. Note that M217 and G227 in Stx1A correspond to V216 and G226, respectively, in Stx1B **B)** Detailed image of the location of the Stx1B V216E mutation. The proximity of the charged residue to the hinge proline 335 might alter the structural composition of the ‘furred loop’ of Munc18-1. **C)** Detailed image of the location of the Stx1B G226R mutation. The large side chain of the introduced arginine residue is directed toward a positively charged pocket, encompassing residues R275 and K276 in Munc18-1 (figure adapted from Vardar, Gerth, **Schmitt**, *et al.* (2020) [178]).

When examining the structure of the Stx1:Munc18-1 complex, it becomes evident that these mutations exert a direct influence on the interaction with the close binding partner and regulatory protein Munc18-1 (**Fig. 1.11**). With the exception of the Stx1B<sup>InDel</sup> mutation, both Stx1B<sup>G226R</sup> and Stx1B<sup>V216E</sup> mutations are positioned directly at the interface of the interaction site between the two proteins. Specifically, the introduction of the bulky and positively charged arginine side chain in the Stx1B<sup>G226R</sup> mutant potentially impedes the interaction with Munc18-1 by charge repulsion through a positively charged cavity within the Munc18-1–Stx1B interface (**Fig. 1.13 C**). Furthermore, the Stx1B<sup>V216E</sup> mutation, situated in close proximity to the hinge proline at position 335 of Munc18-1, has the potential to alter the conformation of the furred loop (**Fig. 1.13 B**). Concerning the Stx1B<sup>InDel</sup>

mutation, it is perceptible that the incorporation of new and additional residues can induce structural alterations, consequently altering the conformation and stability of the protein itself, which in turn affect interactions between the binding partners.

Recognizing this, we deemed it crucial to explore two additional mutations that, instead of directly facing the interaction interface, deviate from it. While examining the reported mutations of Stx1B, two mutations particularly caught our attention; the E210K and the L221P mutations [182]. Both mutations are situated at the core of the functionally crucial SNARE motif but diverge away from the interaction interface with Munc18-1 (**Fig. 1.14 B**).



Stx1B<sup>E210K</sup> is associated with genetic generalized epilepsy (GGE), an umbrella term for various epilepsy syndromes that commence during childhood or adolescence. Four of these syndromes (childhood absence seizure/epilepsy (Abs), juvenile Abs, juvenile myoclonic epilepsy (Myo) and epilepsy with generalized tonic-clonic seizures (GTCS)) commonly endure into adulthood, collectively constituting 15-20% of all adult epilepsy cases. Functional imbalances in frontothalamocortical brain networks give rise to seizures and cognitive impairment in GGE [182, 191]. Consistent with this, the patient reported by Wolking *et al.* (2019) with Stx1B<sup>E210K</sup> mutation



presented impaired executive functions and revealed seizure types of GTCS, Myo and Abs [182]. Although the neurological examination did not identify any abnormalities, the electroencephalogram (EEG) revealed generalized sharp waves (GSW) and photosensitivity (**Table 1.1**) [182].

On the contrary, Stx1B<sup>L221P</sup> is associated with developmental and epileptic encephalopathies, a condition marked by epileptiform abnormalities leading to a progressive decline in cerebral functions. This term encompasses eight syndromes, including Ohtahara syndrome, West syndrome, and myoclonic encephalopathies [192]. The patient documented by Wolking *et al.* (2019) carrying the Stx1B<sup>L221P</sup> mutation showed developmental stagnation and exhibited various seizure types, including GTCS, Abs and Myo, similar to the patient carrying the Stx1B<sup>E210K</sup> mutation, but additionally showed atonic seizures (AS) and complex partial seizures (CPS) [182]. The neurologic examination revealed a mild ataxia and the EEG displayed GSW and generalized polyspikes (GPS, **Table 1.1**) [182].

**Table 1.1:** Condensed phenotypes of patients with Stx1B mutations

<b>Mutation</b>	<b>Intellectual disability</b>	<b>Neurologic examination</b>	<b>Seizure types</b>	<b>EEG</b>
<b>Stx1B<sup>E210K</sup> (g628a)</b>	Dysfunctional executive abilities	No abnormalities	<ul style="list-style-type: none"> <li>- Generalized tonic-clonic seizure</li> <li>- Generalized myoclonic seizure</li> <li>- Absence seizure</li> </ul>	<ul style="list-style-type: none"> <li>- Generalized sharp waves</li> <li>- Photosensitive</li> </ul>
<b>Stx1B<sup>L221P</sup> (t662c)</b>	Developmental stagnation	Mild ataxia	<ul style="list-style-type: none"> <li>- Generalized tonic-clonic seizure</li> <li>- Generalized myoclonic seizure</li> <li>- Absence seizure</li> <li>- Atonic seizure</li> <li>- Complex partial seizure</li> </ul>	<ul style="list-style-type: none"> <li>- Generalized polyspikes and sharpwaves</li> <li>- Generalized polyspikes</li> </ul>

Table adapted from Wolking *et al.* [182]

Despite their close proximity, both mutations lead to a diverse range of phenotypes, underscoring how even subtle changes can produce various effects, even when situated in similar positions. This aspect increases the interest in exploring the molecular and mechanistic effects of these mutations. Additionally, the significance is further emphasized by their distinct biochemical impacts: the E210K mutation causes a local charge reversal, while the L221P mutation likely affects the protein's secondary structure.



## 2. Aim

The SNARE complex formation machinery is essential for mediating the fusion of synaptic vesicles with the presynaptic membrane, enabling neurotransmitter release, which is crucial for fast and precise communication between neurons. This process involves an intricate, multi-step mechanism, including the rearrangement of the helical domains of Stx1, Syb2, and SNAP-25, leading to the formation of the SNARE complex helical bundle. The process is regulated and facilitated by key orchestrating proteins, Munc18-1 and Munc13-1.

In recent years, substantial effort has been invested in advancing our understanding of the molecular mechanisms underlying neurotransmitter release. Many interactions among the key participants in this process are now well understood. However, despite these advancements, which have resulted in increasingly refined and detailed models of the molecular mechanism, several interactions remain incompletely characterized. Among these is the role of Syb2 and its interactions with the MUN domain of Munc13-1 and Munc18-1.

Despite the complexity and critical nature of this mechanism, there seems to be no backup system for membrane fusion reactions. Mutations in individual SNARE proteins or their orchestrating partners can disrupt synaptic transmission, leading to neurological diseases and encephalopathies, collectively referred to as SNAREopathies [171].

Recent studies by Schubert *et al.* and Wolking *et al.* have identified mutations within the gene encoding Stx1B, providing valuable insights into the clinical spectrum of epileptic disorders associated with these mutations [181, 182]. These studies have expanded the understanding of Stx1B-related epilepsies, revealing that Stx1B mutation variants display significant diversity and are implicated in various epilepsy phenotypes.

In this thesis, we focus on two specific mutations, E210K and L221P, both within the SNARE motif of Stx1B. These mutations result in distinct phenotypes in patients but do not directly affect the known binding interfaces of the SNARE complex, rendering their mode of action elusive. Additionally, we aim to explore the interaction and binding behavior of Syb2 with the orchestrating proteins Munc18-1 and the MUN domain of Munc13-1. Therefore, the objectives of this work are to:

- Investigate the molecular impacts of the Stx1B<sup>E210K</sup> and Stx1B<sup>L221P</sup> mutations on the SNARE complex formation machinery.
- Characterize the binding interactions of Syb2 with the orchestrating proteins Munc18-1 and the MUN domain of Munc13-1.
- Establish and utilize cross-linking mass spectrometry to structurally investigate the interactions within the SNARE complex formation machinery and uncover binding sites and potential conformational changes induced by Stx1B mutations.

### 3. Materials and Methods

#### 3.1. Materials

##### 3.1.1. Devices and consumables

All devices and consumables used in this work are listed in **Table 3.1**.

**Table 3.1:** Devices and consumables used in this work

<b>Devices / Consumables</b>	<b>Company</b>
<i>AccuBlock Digital DryBath D1302</i>	Labnet International, Inc. (Edison, USA)
<i>Amersham Protran West. Blot. Membr. (0.2 µm)</i>	Cytiva (Amersham, UK)
<i>Asys UVM-340 Microplate reader</i>	Biochrom Ltd. (Cambridge, UK)
<i>AVANCE III 700 MHz spectrometer</i>	Bruker (Billerica, USA)
<i>Avanti J-26 XP</i>	Beckman Coulter (Brea, USA)
<i>BioFrac Fraction Collector</i>	Bio-Rad Laboratories, Inc. (Hercules, USA)
<i>Ultrospec 2100 pro spectrophotometer</i>	Amersham Biosciences (Amersham, UK)
<i>Dual LED Blue/White Light Transillumination</i>	Serva (Heidelberg, Germany)
<i>Centrifuge 5415 D</i>	Eppendorf (Hamburg, Germany)
<i>Centrifuge 5415 R</i>	Eppendorf (Hamburg, Germany)
<i>Centrifuge 5804 R</i>	Eppendorf
<i>ChemoCam HR16-3200 Imager</i>	Intas Sci. Imaging Instruments GmbH (Göttingen, Germany)
<i>Drying Oven ED 53</i>	Binder (Tuttlingen, Germany)
<i>Duran Borosilicate Glassware (var. size/volume)</i>	DWK Life Sciences (Wertheim, Germany)
<i>Empore SPE Disks C18</i>	CDS (Oxford, USA)
<i>ENrich 10x100 column</i>	Bio-Rad Laboratories, Inc.
<i>Enrich SEC 650 10 x 300 column</i>	Bio-Rad Laboratories, Inc.
<i>French Press Emulsifex-C5</i>	Avestin (Mannheim, Germany)
<i>HiLoad 16/600 Superdex 75 pg column</i>	GE Healthcare (Boston, USA)
<i>Inject Lyer Solo Syringe (var. volume)</i>	B.Braun (Melsngen, Germany)
<i>L60 Ultracentrifuge</i>	Beckman Coulter
<i>Multitron Incubator Shaker</i>	Infors HT (Bottmingen, Switzerland)
<i>Mastercycler X50 – PCR Thermocycler</i>	Eppendorf
<i>MicroCal iTC200 Calorimeter</i>	Malvern Panalytical GmbH (Malvern, UK)
<i>MIKRO 185 Micro Centrifuge</i>	Hettich (Tuttlingen, Germany)
<i>B30 UF Ultrapure Water</i>	Adrona (Riga, Latvia)
<i>Measuring Cylinders and Beakers (var. size/vol.)</i>	Vitlab (Grossostheim, Germany)
<i>Micro-Pipette Tips (var. size/vol.)</i>	Corning (Corning, USA)
<i>Mini-PROTEAN TGX 4-20% Gradient Gel</i>	Bio-Rad Laboratories, Inc.
<i>Minisart NML Syringe Filter (sterile, 0.22 µm)</i>	Sartorius AG (Göttingen, Germany)
<i>Minisart NMR Syringe Filter (sterile, 0.45 µm)</i>	Sartorius AG
<i>Nanodrop 2000</i>	Thermo Fisher Scientific (Waltham, USA)
<i>NGC Discover 10 Plus Chromatography System</i>	Bio-Rad Laboratories, Inc.
<i>NGC Quest 10 Plus Chromatography System</i>	Bio-Rad Laboratories, Inc.
<i>NMR Tubes</i>	Deutero GmbH (Kastellaun, Germany)

<i>NucleoSpin Gel and PCR Clean-up Kit</i>	Machery-Nagel GmbH & Co. KG (Düren, Germany)
<i>NucleoSpin Plasmid Kit</i>	Machery-Nagel GmbH & Co. KG
<i>Peristaltic Pump P-1</i>	Pharmacia Biotech (Uppsala, Sweden)
<i>PES Membrane Filter (0.22 µm)</i>	Merck Millipore KGaA (Darmstadt, Germany)
<i>Pipetus PipettePump</i>	Hirschmann Laborgeräte GmbH (Eberstadt, Germany)
<i>PowerPac Basic Power Supply</i>	Bio-Rad Laboratories, Inc.
<i>Protino Glutathione Agarose 4B</i>	Machery-Nagel GmbH & Co. KG
<i>Protino GST/4B 5 ml column</i>	Machery-Nagel GmbH & Co. KG
<i>Protino Nickel-NTA 5 ml column</i>	Machery-Nagel GmbH & Co. KG
<i>Q Exactive HF-Mass Spectrometer</i>	Thermo Fisher Scientific
<i>RCT Basic Magnetic Stirrer</i>	IKA (Staufe, Germany)
<i>Research Plus Pipettes (various volumes)</i>	Eppendorf
<i>S20 SevenEasy pH meter</i>	Mettler Toledo (Columbus, USA)
<i>SafeLock Tubes 1.5 ml / 2ml</i>	Eppendorf
<i>SafeSeal MicroTubes 1.5 ml</i>	Sarstedt (Nümbrecht, Germany)
<i>Scale ACJ 120-4M</i>	Kern & Sohn GmbH (Balingen, Germany)
<i>Scale EW 1500-2M</i>	Kern & Sohn GmbH
<i>Slide-A-Lyzer Mini Dialysis Device (var. MWCO)</i>	Thermo Fisher Scientific
<i>Slide-A-Lyzer G2 Dialysis Cassette (var. MWCO)</i>	Thermo Fisher Scientific
<i>Superdex 200 Increase 10/300 GL column</i>	GE Healthcare
<i>Thermomixer comfort</i>	Eppendorf
<i>UltiMate 3000 nano HPLC system</i>	Thermo Fisher Scientific
<i>Ultrasonics Sonifier SFX250/SFX550</i>	Branson (Brookfield Connecticut)
<i>Univapo 150H</i>	UniEquip (Planegg, Germany)
<i>UV Cuvettes (semi-micro, single use, 1.5 ml)</i>	BRAND GmbH & Co. KG (Wertheim, Germany)
<i>Vivaspin 6 Centrifugal Concentrator (10K MWCO)</i>	Sartorius AG
<i>Vivaspin 20 Centrifugal Concentrator (var. MWCO)</i>	Sartorius AG
<i>Vortex Genie 2</i>	Scientific Industries, Inc. (Bohemia, USA)
<i>ZelluTrans Mini Dialyzer</i>	Carl Roth GmbH + Co. KG (Karlsruhe, Germany)

### 3.1.2. Standard Chemicals

All standard chemicals used for buffer and sample preparations, unless otherwise specified, were purchased from Carl Roth GmbH & Co. KG (Karlsruhe, Germany) or Sigma-Aldrich (St. Louis, USA). DNA-Ladders (100 bp and 1 kb) as well as Gel Loading Dye (6x, purple) were bought from New England BioLabs GmbH (Frankfurt am Main, Germany). Protein Ladders (Mark12™ Unstained Standard and PageRuler™ Prestained) and crosslinkers (disuccinimidyl sulfoxide (DSSO) and disuccinimidyl dibutyric urea (DSBU)) were bought from Thermo Fisher Scientific. cOmplete™ EDTA-free Protease Inhibitor Cocktail Tablets were purchased from Roche (Basel, Switzerland). In-house made StageTips were prepared with Empore™ Octadecyl C18 Disks from CDS Analytical, Inc. (Oxford, USA).

### 3.1.3. Isotopes

<sup>15</sup>N-labeled ammonium chloride for isotope-labeling of proteins for NMR experiments was purchased from Cambridge Isotope Laboratories, Inc. (Tewksbury, USA), CAMPRO Scientific GmbH (Berlin, Germany) or Sigma-Aldrich. Deuterium oxide for 10% supplementation of NMR samples was purchased from Sigma-Aldrich.

### 3.1.4. Enzymes

All enzymes were utilized for various tasks such as molecular cloning, modifications, protein purification and analysis. **Table 3.2** provides a list of enzymes employed.

**Table 3.2:** Enzymes used in this work

<i>Enzymes</i>	<i>Company</i>
<i>Restriction Enzymes (DpnI, EcoRI, NdeI, XhoI)</i>	New England Biolabs
<i>T4 DNA Ligase</i>	New England Biolabs
<i>Antarctic Phosphatase</i>	New England Biolabs
<i>KOD Hot-Start DNA Polymerase</i>	Novagen/Merck Millipore KGaA
<i>Pfu DNA Polymerase</i>	EURx (Gdansk, Poland)
<i>Pfu Plus! DNA Polymerase</i>	EURx
<i>Benzonase (Nuclease)</i>	Sigma-Aldrich
<i>DNase</i>	AppliChem GmbH (Darmstadt, Germany)
<i>RNAse</i>	Sigma-Aldrich
<i>Thrombin</i>	Merck Millipore KGaA
<i>Trypsin</i>	Promega Corp. (Madison, USA)

(All commercially acquired enzymes were utilized with buffers either provided or recommended by the manufacturers.)

### 3.1.5. Oligonucleotides

All oligonucleotides used as primers for site-directed mutagenesis (SDM), cloning or sequencing *via* PCR were synthesized by Integrated DNA Technologies (Coralville, USA). Sequencing services were provided by Mircosynth Seqlab GmbH (Göttingen, Germany). The oligonucleotides utilized in this study are shown in **Table 3.3**.

**Table 3.3:** Oligonucleotides used as primers for SDM, cloning or sequencing

<i>Primer</i>	<i>Sequence (5'-3')</i>	<i>Usage</i>
<i>Stx1B-QC-E210K-for</i>	gagaccagcatccgcaagctgcacgatatgt	SDM forward Stx1B E210K
<i>Stx1B-QC-E210K-rev</i>	acatatcgtgcagcttgcggatgctgtctc	SDM reverse Stx1B E210K
<i>Stx1B-QC-L221P-for</i>	ggacatggccatgccgtagagaccagg	SDM forward Stx1B L221P
<i>Stx1B-QC-L221P-rev</i>	cctggctctctacgggcatggccatgtcc	SDM reverse Stx1B L221P
<i>Stx1B-QC-K82E-for</i>	atctcactgcagacatcgagaagacggccaacaag	SDM forward Stx1B K82E

## Materials and Methods

<i>Stx1B-QC-K82E-rev</i>	ctgttgccgtctctcgcgatgtctgcagtgagat	SDM reverse Stx1B K82E
<i>Stx1B-QC-K83E-for</i>	cactgcagacatcaaggagacggccaacaagg	SDM forward Stx1B K83E
<i>Stx1B-QC-K83E-rev</i>	cctgttgccgtctccttgatgtctgcagtg	SDM reverse Stx1B K83E
<i>Stx1B-QC-KK82-83EE-for</i>	gatctcactgcagacatcgaggagacggccaacaaggttc	SDM forward Stx1B K82E, K83E
<i>Stx1B-QC-KK82-83EE-rev</i>	gaacctgttgccgtctcctcgcgatgtctgcagtgagatc	SDM reverse Stx1B K82E, K83E
<i>Stx1B-CL-25-EcorI-for</i>	atagaattccgggaccacttcatggatgag	Cloning Stx1B 25 N→C restriction site EcoRI
<i>Stx1B-CL-252-XhoI-rev</i>	ataactcgcagtcatttctgtgtgcagacacagctcgc	Cloning Stx1B 252 C→N restriction site XhoI, incl. Stop
<i>Stx1B-CL-179-NdeI-for</i>	atacatatggacatcaaaatggactcacagatgacg	Cloning Stx1B 179 N→C restriction site NdeI
<i>Stx1B-CL-262-XhoI-rev</i>	tatctcgcagtcacctccgggccttgct	Cloning Stx1B 262 C→N restriction site XhoI, incl. Stop
<i>Stx1B-SQ-for</i>	gggctgaaccgttctcctccgcg	Sequencing forward Stx1B N→C
<i>Stx1B-SQ-rev</i>	ccagttctcgttggtgggtg	Sequencing reverse Stx1B C→N
<i>Syb2-QC-A3K-for</i>	ccccggaattcatgtcgaagaccgctgccaccgtcc	SDM forward Syb2 A3K
<i>Syb2-QC-A3K-rev</i>	ggacggtggcagcgtctctgcacatgaattccgggg	SDM reverse Syb2 A3K
<i>Syb2-R30K-QC-for</i>	aaatcttaccagtaacaagagactgcagcagaccc	SDM forward Syb2 R30K
<i>Syb2-R30K-QC-rev</i>	gggtctgctgcagtcctgttactggtgaagattt	SDM reverse Syb2 R30K
<i>Syb2-R47K-QC-for</i>	gagggtgggacatcatgaaggtgaatgtggac	SDM forward Syb2 R47K
<i>Syb2-R47K-QC-rev</i>	gtccacattcaccttcatgatgtccaccacctc	SDM reverse Syb2 R47K
<i>Syb2-QC-W89A-for</i>	caagctcaagcgcaaatcgcggtgaaaaacctcaagatg	SDM forward Syb2 W89A
<i>Syb2-QC-W89A-rev</i>	catcttgaggttttccacgcgtatttgcgcttgagcttg	SDM reverse Syb2 W89A
<i>Syb2-QC-W90A-for</i>	gctcaagcgcaaatcgtggcgaaaaacctcaagatgatg	SDM forward Syb2 W90A
<i>Syb2-QC-W90A-rev</i>	catcatctgaggttttcgcccagatttgcgcttgagc	SDM reverse Syb2 W90A
<i>Syb2-QC-WWAA-for</i>	cagccaagctcaagcgcaaatcgcggcgaaaaacctcaagatgatgtaac	SDM forward Syb2 W89A, W90A
<i>Syb2-QC-WWAA-rev</i>	gttacatcatcttgaggttttccgcccgtatttgcgcttgagcttggctg	SDM reverse Syb2 W89A, W90A
<i>Munc18-QC-D326K-for</i>	aagaccaccatgcggaagctgtcccagatgctg	SDM forward Munc18-1, D326K
<i>Munc18-QC-D326K-rev</i>	cagcatctgggacagctccgcgatgtgtgtctt	SDM reverse Munc18-1, D326K
<i>Munc18-QC-P335A-for</i>	tcccagatgctgaagaaaatggcccagtagcagaag	SDM forward Munc18-1, P335A
<i>Munc18-QC-P335A-rev</i>	cttctgtactgggccatttctcagcatctggga	SDM reverse Munc18-1, P335A
<i>Munc18-CL-1-EcoRI-for</i>	atagaattcgccccattggcctca	Cloning Munc18-1 1 N→C restriction site EcoRI
<i>Munc18-CL-594-XhoI-rev</i>	tatctcgcagtcactgctatttctcgtctgtttattcagct	Cloning Munc18-1 594 C→N restriction site XhoI, incl. Stop

<i>Munc18-SQ-for</i>	atagaattcgccccattggcctca	Sequencing forward Munc18-1 N→C
<i>Munc18-SQ-rev</i>	tatctcgagcaactgcttattctctgctgttttattcagct	Sequencing reverse Munc18-1 C→N
<i>His-SQ-for</i>	atacatatgcgggaccacttcatggatgag	Sequencing forward His-Tag N→C
<i>GST-SQ-for</i>	atagaattccgggaccacttcatggatgag	Sequencing forward GST- Tag N→C
<i>Gex3-rev</i>	gcttacagacaagctgtgac	Sequencing reverse pGEX-4T1 plasmid C→N
<i>pET-down</i>	gattatgcggccgtgtac	Sequencing reverse pET28-a(+) plasmid
<i>T7term</i>	tgctagtattgctcagcgg	Sequencing reverse pTol2 plasmid

### 3.1.6. Constructs

DNA encoding the desired protein constructs were incorporated into different plasmid vectors, depending on which tag or properties were needed for expression and purification of the protein.

**Table 3.4** provides a list of all protein constructs used for this thesis.

**Table 3.4:** Protein constructs with the corresponding plasmid vector

<b>Protein Construct Name</b>	<b>Plasmid</b>	<b>Description</b>
<i>Stx1B Full-length<sup>P</sup></i>	hrtTA-VP16	Stx1B (1-288), <i>Homo sapiens</i>
<i>Stx1B<sup>WT</sup></i>	pGEX-4T1	Stx1B (25-252), <i>Homo sapiens</i>
<i>Stx1B<sup>WT-ZF</sup> ±</i>	pTol2	Stx1B (1-288), <i>Homo sapiens</i>
<i>Stx1B<sup>WT</sup> SNARE-long *</i>	pGEX-4T1	Stx1B (179-262), <i>Homo sapiens</i>
<i>Stx1B<sup>WT</sup> SNARE-long</i>	pET28-a(+)	Stx1B (179-262), <i>Homo sapiens</i>
<i>Stx1B<sup>WT</sup> SNARE-TMR</i>	pET28-a(+)	Stx1B (189-288), <i>Homo sapiens</i>
<i>Stx1B<sup>E210K</sup></i>	pGEX-4T1	Stx1B (25-252), E210K, <i>Homo sapiens</i>
<i>Stx1B<sup>E210K-ZF</sup></i>	pTol2	Stx1B (1-288), E210K, <i>Homo sapiens</i>
<i>Stx1B<sup>E210K</sup> SNARE-long</i>	pET28-a(+)	Stx1B (179-262), E210K, <i>Homo sapiens</i>
<i>Stx1B<sup>E210K</sup> SNARE-TMR</i>	pET28-a(+)	Stx1B (189-288), E210K <i>Homo sapiens</i>
<i>Stx1B<sup>E210K,K82E</sup></i>	pGEX-4T1	Stx1B (25-252), K82E, E210K, <i>Homo sapiens</i>
<i>Stx1B<sup>E210K,K82E-ZF</sup></i>	pTol2	Stx1B (1-288), K82E, E210K, <i>Homo sapiens</i>
<i>Stx1B<sup>E210K,K83E</sup></i>	pGEX-4T1	Stx1B (25-252), K83E, E210K, <i>Homo sapiens</i>
<i>Stx1B<sup>E210K,KKEE</sup></i>	pGEX-4T1	Stx1B (25-252), K82E, K83E, E210K, <i>Homo sapiens</i>
<i>Stx1B<sup>V216E</sup> *</i>	pGEX-4T1	Stx1B (25-252), V216E, <i>Homo sapiens</i>
<i>Stx1B<sup>L221P</sup></i>	pGEX-4T1	Stx1B (25-252), L221P, <i>Homo sapiens</i>
<i>Stx1B<sup>L221P-ZF</sup></i>	pTol2	Stx1B (1-288), L221P, <i>Homo sapiens</i>
<i>Stx1B<sup>L221P</sup> SNARE-long</i>	pET28-a(+)	Stx1B (179-262), L221P, <i>Homo sapiens</i>
<i>Stx1B<sup>L221P</sup> SNARE-TMR</i>	pET28-a(+)	Stx1B (189-288), L221P, <i>Homo sapiens</i>
<i>SNAP-25 †</i>	pET28-a(+)	SNAP-25 (1-206), <i>Homo sapiens</i>
<i>Syb2</i>	pGEX-4T1	Syb2 (1-96), <i>Homo sapiens</i>
<i>Syb2 †</i>	pET28-a(+)	Syb2 (1-96), <i>Homo sapiens</i>
<i>Syb2<sup>A3K</sup></i>	pGEX-4T1	Syb2 (1-96), A3K, <i>Homo sapiens</i>
<i>Syb2<sup>R30K</sup></i>	pGEX-4T1	Syb2 (1-96), R30K, <i>Homo sapiens</i>
<i>Syb2<sup>R47K</sup></i>	pGEX-4T1	Syb2 (1-96), R47K, <i>Homo sapiens</i>

<i>Syb2</i> <sup>W89A</sup>	pGEX-4T1	<i>Syb2</i> (1-96), W89A, <i>Homo sapiens</i>
<i>Syb2</i> <sup>W90A</sup>	pGEX-4T1	<i>Syb2</i> (1-96), W90A, <i>Homo sapiens</i>
<i>Syb2</i> <sup>WWAA</sup>	pGEX-4T1	<i>Syb2</i> (1-96), W89A, W90A, <i>Homo sapiens</i>
<i>Munc18-1</i> <sup>P</sup>	pM18-IRES2-EGFP-lenti	<i>Munc18-1</i> (1-594), <i>Rattus norvegicus</i>
<i>Munc18-1</i> <sup>WT</sup> •	pGEX-4T1	<i>Munc18-1</i> (2-594), <i>Rattus norvegicus</i>
<i>Munc18-1</i> <sup>D326K</sup>	pGEX-4T1	<i>Munc18-1</i> (2-594), D326K, <i>Rattus norvegicus</i>
<i>Munc18-1</i> <sup>P335A</sup>	pGEX-4T1	<i>Munc18-1</i> (2-594), P335A, <i>Rattus norvegicus</i>
<i>Munc13-MUN</i> <sup>‡</sup>	pMA-T	<i>Munc13-1</i> (859-1531, Δ1408-1452), <i>Rattus norvegicus</i>
<i>Munc13-MUN</i> •	pGEX-4T1	<i>Munc13-1</i> (859-1531, Δ1408-1452), <i>Rattus norvegicus</i>

(Constructs labeled with P were kindly gifted by the Lerche Lab (Universitätsklinikum Tübingen). Constructs labeled with • were cloned by Dr. Fabian Gerth in the Freund Lab (Freie Universität Berlin). Constructs labeled with ‡ were cloned by Dr. Wietske van der Ent in the Esguerra Lab (University of Oslo). Constructs labeled with † were kindly gifted by the Wahl Lab (Freie Universität Berlin). Constructs labeled with ‡ were synthesized by and purchased from Twist BioScience (San Francisco, USA).)

### 3.1.7. Bacterial strains

Various heat-shock-competent *E. coli* strains were utilized for DNA amplification and heterologous protein expression. A comprehensive list of these bacterial strains can be found in **Table 3.5**.

**Table 3.5:** Bacterial strains used for cloning or protein expression

<i>E. coli</i> strain (Distributor)	Application	Description
<i>DH5α</i> (New England Biolab)	Subcloning and plasmid amplification	<i>endA1 recA1 φ80d lacZΔM15 Δ(lacZYA-argF) U169 deoR hsdR17(r<sub>K</sub> m<sub>K</sub><sup>+</sup>)</i>
<i>XL1-Blue</i> (In-house)	Subcloning and plasmid amplification	<i>endA1 gyrA96(nalR) thi-1 recA1 relA1 lac glnV44 F'::Tn10 proAB+ lacIq Δ(lacZ)M15] hsdR17(r<sub>K</sub> m<sub>K</sub><sup>+</sup>)</i>
<i>Top10</i> (In-house)	Subcloning and plasmid amplification	<i>F- mcrA Δ(mrr-hsdRMS-mcrBC) φ80lacZΔM15 ΔlacX74 nupG recA1 araD139 Δ(ara-leu)7697 galE15 galK16 rpsL(Str<sup>R</sup>) endA1 λ</i>
<i>BL21(DE3)</i> (New England Biolab)	Protein expression	<i>B F<sup>-</sup> ompT gal dcm lon hsdS<sub>B</sub>(r<sub>B</sub><sup>-</sup> m<sub>B</sub><sup>-</sup>) λ(DE3 [lacI lacUV5-T7 gene 1 ind1 sam7 nin5]) [malB<sup>+</sup>]<sub>K-12</sub>(λ<sup>S</sup>)</i>
<i>Rosetta(DE3)</i> (Novagen/Merck Millipore KGaA)	Protein expression	<i>B F<sup>-</sup> ompT gal dcm lon hsdR<sub>B</sub>(r<sub>B</sub><sup>-</sup> m<sub>B</sub><sup>-</sup>) λ(DE3 [lacIq lacUV5-T7 gene 1 ind1 sam7 nin5]) [malB<sup>+</sup>]<sub>K-12</sub>(λ<sup>S</sup>)</i>

### 3.1.8. Growth media

Different growth media were utilized for cell cultivation and protein expression. **Table 3.6** shows a list of the media used.

**Table 3.6:** Media used to cultivate cells and express proteins

Medium	Composition
<i>Lysogeny Broth (LB) Medium</i>	10 g/l tryptone, 5 g/l yeast extract, 10 g/l NaCl, pH 7.0
<i>Double Yeast Tryptone (2YT) Medium</i>	16 g/l tryptone, 10 g/l yeast extract, 5 g/l NaCl, pH 7.0
<sup>15</sup> N-enriched M9 Minimal Medium	8 g/l Na <sub>2</sub> PO <sub>4</sub> , 2 g/l KH <sub>2</sub> PO <sub>4</sub> , 0.5 g/l NaCl, 1 mM MgSO <sub>4</sub> , 0.3 mM CaCl <sub>2</sub> , 7.5 μM ZnCl <sub>2</sub> , 0.8 μM CuSO <sub>4</sub> , 36 μM FeSO <sub>4</sub> , 1.5 mg/l thiamine, 1.5 mg/l biotin, 0.75 g/l <sup>15</sup> N- NH <sub>4</sub> Cl, 2 g/l, 4 g/l D-glucose, pH 7.0

### 3.1.9. Standard buffers, dyes and other solutions

Standardized buffers, dyes, and solutions were routinely employed in the laboratory for specific experiments. These can be found in **Table 3.7**. Any additional buffers or modifications to the listed ones are detailed in the methods section.

**Table 3.7:** Standard Buffers, dyes and other solutions

<b>Solution</b>	<b>Composition</b>
<i>TAE (50x)</i>	2 M Tris acetat, 50 mM EDTA, pH 8.3
<i>GST Lysis/Wash Buffer (2x)</i>	300 mM NaCl, 20 mM Na <sub>2</sub> HPO <sub>4</sub> , 10 mM EDTA, pH 7.4
<i>GST Elution Buffer (2x)</i>	40 mM Glutathione (reduced), 200 mM Tris, 10 mM EDTA, pH 8.0
<i>Native IMAC Lysis/Wash-1 Buffer (2x)</i>	600 mM KCl, 100 mM KH <sub>2</sub> PO <sub>4</sub> , 10 mM Imidazole, pH 8.0
<i>Native IMAC Wash-2 Buffer (2x)</i>	600 mM KCl, 100 mM KH <sub>2</sub> PO <sub>4</sub> , 20 mM Imidazole, pH 8.0
<i>Native IMAC Elution Buffer (2x)</i>	600 mM KCl, 100 mM KH <sub>2</sub> PO <sub>4</sub> , 500 mM Imidazole, pH 8.0
<i>Munc18-1 Lysis Buffer</i>	PBS, 2 mM EDTA, 1 mM EGTA, 2 mM DTT
<i>Munc13-MUN Lysis Buffer</i>	50 mM Tris, 250 mM NaCl, 1 mM TCEP, pH 8.0
<i>PBS</i>	137 mM NaCl, 2.7 mM KCl, 4.3 mM Na <sub>2</sub> HPO <sub>4</sub> , 1.4 mM NaH <sub>2</sub> PO <sub>4</sub> , pH 7.4
<i>SDS Sample Loading Buffer (5x)</i>	1,5 M Tris, 50 vol% Glycerol, 10% SDS, 0.25% Bromphenol Blue, 25 vol% β-Mercaptoethanol, pH 6.8
<i>SDS Running Buffer</i>	25 mM Tris, 192 mM Glycine, 0.1% SDS, pH 8.3
<i>Coomassie Dye</i>	2.5 g/l Coomassie Brilliant Blue, 50 vol% Methanol, 10 vol% Acetic Acid
<i>Coomassie Destainer</i>	39 vol% Methanol, 10 vol% Acetic Acid
<i>Transfer Buffer</i>	48 mM Tris, 39 mM Glycine, 0.075% SDS, 20 vol% Methanol, pH 8.3
<i>TBS</i>	20 mM Tris, 150 mM NaCl, pH 7.4
<i>TBS-T</i>	20 mM Tris, 150 mM NaCl, 0.5 vol% Tween-20, pH 7.4
<i>M9 Salt solution (10x)</i>	80 g Na <sub>2</sub> HPO <sub>4</sub> x H <sub>2</sub> O, 20 g KH <sub>2</sub> PO <sub>4</sub> , 5 g NaCl, (H <sub>2</sub> O ad 1 L)
<i>Trace Element solution</i>	2.5 g EDTA, 250 mg FeSO <sub>4</sub> , 25 mg ZnCl <sub>2</sub> , 5 mg CuSO <sub>4</sub> (H <sub>2</sub> O ad 500 ml)

## 3.2. Molecular biology methods

### 3.2.1. Molecular cloning

The desired bacterial expression constructs were generated using appropriate templates of the respective genes and specific oligonucleotides (**Table 3.3**) through polymerase chain reaction (PCR). See **Table 3.8** for the composition of reactants and **Table 3.9** for detailed PCR settings. After amplification, the DNA fragments were analyzed on an agarose gel (0.5%, 120 V, 30 min) and purified using the NucleoSpin™ Gel and PCR Clean-up Kit from Macherey-Nagel (Düren, Germany).

Subsequently, these fragments and the desired plasmid were treated with an appropriate set of restriction enzymes with the 10x Cut Smart buffer (New England Biolab) at 37°C for 2 h to generate compatible overhangs for subsequent ligation with a linearized plasmid. For constructs tagged with



GST, cloning was performed into the pGEX-4T1 vector using EcoRI and XhoI restriction sites, while His-tagged constructs were integrated into the pET28-a(+) vector at the N-terminus using NdeI and XhoI restriction sites. To ensure vector restriction stability, the linearized plasmids underwent a 5'-dephosphorylation step at 37°C for 1 hour, preventing self-ligation. The treated vector was then run on (120 V, 40 min) and extracted from an agarose gel (0.5%) using the NucleoSpin™ Gel and PCR Clean-up Kit again.

The ligation process involved combining the insert and vector in a 3:1 molar ratio and incubating them with 200 U of T4 DNA ligase and 1x T4 DNA ligation buffer in a total reaction volume of 20 µl at 16 °C overnight. Following this, 6-8 µl of the ligation mixture was introduced into 50 µl of competent *E. coli* strains (XL1-Blue, Top10, or DH5α) using heat shock transformation at 42°C. After transformation, the bacterial cultures were plated and incubated at 37 °C overnight. The resulting colonies were picked for glycerol stock preparation and the inserts were validated through sequencing by Microsynth Seqlab. Positively confirmed constructs were introduced into the BL21(DE3) *E. coli* strain for protein expression, following heat shock transformation procedures similar to those described for the DH5α *E. coli* cells.

**Table 3.8:** Reactant composition for cloning using PCR

<b>Component</b>	<b>C<sub>stock</sub></b>	<b>V (µl)</b>	<b>C<sub>final</sub></b>
<i>Template</i>	-	1.0	0.5–1.0 ng/µl
<i>KOD Hot-Start DNA Polymerase</i>	20 U/µl	0.5	0.2 U/µl
<i>Primer forward</i>	10 µM	1.5	0.3 µM
<i>Primer reverse</i>	10 µM	1.5	0.3 µM
<i>dNTP mix</i>	2 mM	5	0.2 µM
<i>KOD PCR Buffer</i>	10x	5	1x
<i>H<sub>2</sub>O (sterile)</i>	-	35.5	-

**Table 3.9:** Detailed listing of the PCR settings for DNA construct amplification

<b>Step</b>	<b>Time</b>	<b>Temperature (°C)</b>	<b>Number of Cycles</b>	<b>Process</b>
1	5 min	95	1x	initial denaturation
2	30 s	95	30 x	denaturation
3	30 s	56 – 64		annealing
4	30 s – 2 min	68 – 74		elongation
5	5 min	56 – 64	1x	final elongation
6	∞	4	1x	hold

### 3.2.2. Site-directed mutagenesis

Site-directed mutagenesis (SDM) was conducted to introduce distinct point mutations into a DNA construct. This allowed for the alteration of one or more amino acids, resulting in the desired protein mutation. For this purpose, the required DNA construct served as a template in PCR using the specific oligonucleotides listed in **Table 3.3**. The reactant mixture composition is shown in

**Table 3.10.** PCR reactions were conducted at three distinct annealing temperatures for each primer pair, with the specific conditions detailed in **Table 3.11**. Gel electrophoresis on a 1% agarose gel at 120 V for 30 min was used for quality assessment, using 5  $\mu$ l of each PCR product. Plasmids that showed successful amplification were purified using the NucleoSpin™ Gel and PCR Clean-up Kit. The purified DNA was eluted with 15  $\mu$ l of H<sub>2</sub>O.

To process methylated DNA templates, a mixture of 1  $\mu$ l DpnI (20 U/  $\mu$ l), 2.5  $\mu$ l sterile water, and 1.5  $\mu$ l of the 10x Cut Smart buffer was combined with 10  $\mu$ l of the PCR product. This was followed by incubation at 37 °C for 1 h and subsequent inactivation at 80 °C for 20 min. DH5 $\alpha$  competent *E. coli* cells were transformed by adding 2.5  $\mu$ l of the digested mixture to 20  $\mu$ l of cells, chilling on ice for 10 min, then subjecting to a heat shock at 42 °C for 1 min, and finally cooling on ice for 3 min. 1 ml of LB medium was added to the transformed DH5 $\alpha$  *E. coli* cells and incubated for 1 h at 37 °C. After incubation, 200  $\mu$ l were plated and incubated at 37 °C overnight. The resulting colonies were picked for glycerol stock preparation and the mutated DNA constructs were validated through sequencing by Microsynth Seqlab. Positively confirmed constructs were introduced into the BL21(DE3) *E. coli* strain for protein expression, following heat shock transformation procedures similar to those described for the DH5 $\alpha$  *E. coli* cells.

**Table 3.10:** Reactant composition for SDM using PCR

<b>Component</b>	<b>C<sub>stock</sub></b>	<b>V (<math>\mu</math>l)</b>	<b>C<sub>final</sub></b>
<i>Template</i>	-	1.0	0.5–1.0 ng/ $\mu$ l
<i>Pfu (Plus!) DNA Polymerase</i>	5 U/ $\mu$ l	0.5	0.05 U/ $\mu$ l
<i>Primer forward</i>	10 $\mu$ M	1.5	0.3 $\mu$ M
<i>Primer reverse</i>	10 $\mu$ M	1.5	0.3 $\mu$ M
<i>dNTP mix</i>	2 mM	5	0.2 $\mu$ M
<i>Pfu Buffer</i>	10x	5	1x
<i>H<sub>2</sub>O (sterile)</i>	-	35.5	-

**Table 3.11:** Detailed listing of the PCR settings for SDM

<b>Step</b>	<b>Time</b>	<b>Temperature (°C)</b>	<b>Number of Cycles</b>	<b>Process</b>
1	5 min	95	1x	initial denaturation
2	30 s	95	18 x	denaturation
3	30 s	58, 60, 62		annealing
4	6-8 min	68		elongation
5	7 min	68	1x	final elongation
6	$\infty$	4	1x	hold

### 3.3. Protein biochemistry methods

#### 3.3.1. Protein expression

For protein expression, precultures were first prepared by inoculating a small sample of glycerol stock into 10 ml of LB medium with the appropriate antibiotic (ampicillin for constructs in pGEX-4T1, kanamycin for constructs in pET28-a(+)) and incubated overnight at 37 °C, 180 rpm. On the next

day, the precultures were upscaled by transfer into 1 L of 2xYT medium supplemented with the appropriate antibiotic.

Protein constructs intended to be measured *via* NMR needed to be <sup>15</sup>N isotope labeled and therefore were expressed in 2 L of M9 minimal medium containing 750 mg/L of <sup>15</sup>N-enriched (99%) ammonium chloride (**Table 3.6**) and the appropriate antibiotic. A 10 ml portion of this <sup>15</sup>N-enriched M9 medium was first inoculated with a small sample from the glycerol stock to serve as a preculture, which was incubated at 37°C overnight with shaking at 180 rpm. The next day, the preculture was upscaled by transfer into the initial <sup>15</sup>N-enriched M9 minimal medium.

The cultures were incubated at 37 °C at 180 rpm and frequently checked for their density. When the absorption at 595 nm reached an OD<sub>595</sub> value of 0.6-0.8, the cultures were cooled down on ice for 5-10 min. Then, the protein expression was induced by the addition of isopropyl-β-D-1-thiogalactopyranoside (IPTG). For Stx1B SNARE and Stx1B SNARE-TMR constructs, Syb2 constructs and SNAP-25 constructs 1 mM of IPTG was added. For Stx1B<sup>25-252</sup> constructs 0.5 mM of IPTG was added. For Munc18-1 constructs 0.35 mM of IPTG and for Munc13-1 MUN constructs 0.3 mM of IPTG was added. The induced cultures were incubated overnight at 25 °C, 20 °C, 18 °C and 16 °C respectively.

On the following day, the cells were harvested by centrifugation at 6000 xg at 4 °C for 15 min. The resulting cell pellets were transferred into 50 ml falcons containing 15 ml of appropriate lysis buffer (GST-tagged Stx1B constructs and Syb2 constructs in GST Lysis Buffer; HIS-tagged Stx1B constructs, Syb2 constructs and the SNAP-25 construct in Native IMAC Lysis Buffer; GST-tagged Munc18-1 constructs in Munc18-1 Lysis Buffer; GST-tagged Munc13-MUN constructs in Munc13-MUN Lysis Buffer (detailed buffer compositions in **Table 3.7**)) supplemented with one tablet of cComplete™ EDTA-free Protease Inhibitor Cocktail. After resuspension, the cells were snap frozen in liquid nitrogen and stored at -20 °C until purification.

### 3.3.2. Protein purification

#### 3.3.2.1. Purification of GST-Stx1B and GST-Syb2 wild-type and mutant constructs

*E. coli* cells expressing GST-tagged Syb2 or Stx1B wild-type and mutants were lysed by sonication. For that, the suspension was first thawed at room temperature in a water bath. Subsequently, a spatula tip of RNaseA, along with 5 µl of Benzonase and 100 µl of 1 M MgCl<sub>2</sub>, was added. Sonication was carried out continuously and the maximum temperature was set to 15 °C with a total sonication time of 20 min. Following sonication, the lysate was centrifuged at 15000 xg for 30 min at 4 °C. The clarified supernatant was then sequentially filtered through 0.45 µm and 0.2 µm pore-size filters.

The proteins were initially purified *via* affinity chromatography using a Protino GST / 4B FPLC 5 ml column (Macherey-Nagel). The column was first equilibrated with 50 ml of GST Lysis/Wash Buffer (**Table 3.7**). Subsequently, the lysate was applied to the column with a flow rate of 1 ml/min. Unbound proteins were then washed off using 50 ml of GST Lysis/Wash Buffer (**Table 3.7**). Finally,

the GST-tagged proteins were eluted from the column using 20 ml of GST Elution Buffer (**Table 3.7**, **Appendix Fig. 1 A**) and **Appendix Fig. 2 A**)).

To cleave-off the GST-tag, the eluted proteins were treated with 50  $\mu$ l of thrombin (1U/ $\mu$ l) and left overnight at 4 °C rotating. Subsequently, the treated proteins were concentrated to a volume of ~5 ml and then further purified *via* size exclusion chromatography using a HiLoad 16/600 Superdex 75 pg column (GE Healthcare). Prior to this, the size exclusion column had been equilibrated with the appropriate buffer. Fractions were assessed using SDS-PAGE according to the size-exclusion chromatogram, and those containing the desired protein were collected (**Appendix Fig. 1 B**), **D**) and **Appendix Fig. 2 B**), **D**)).

Following this, two Protino GST / 4B FPLC 5 ml columns, connected in series, were primed with the appropriate buffer. The pooled fractions were subsequently passed through these columns to separate the detached GST-tag from the purified protein. The resulting flowthrough, containing the purified protein, was collected. The retained GST was then eluted using the GST Elution Buffer. The purified proteins were then concentrated, with concentration measured *via* NanoDrop™ (Thermo Fisher Scientific), aliquoted, snap frozen using liquid nitrogen and stored at -80°C until subsequent experiments (**Appendix Fig. 1 C**) and **Appendix Fig. 2 C**)).

After each purification step, a small sample was taken for SDS-PAGE to assess the quality and correct size of the desired proteins (**Appendix Fig. 1** and **Appendix Fig. 2**)).

### 3.3.2.2. Purification of His-SNAP-25, His-Syb2 and His-Stx1BSNARE wild-type and mutant constructs

*E. coli* cells expressing His-tagged SNAP-25, Syb2 or Stx1B<sup>SNARE</sup> wild-type and mutants were lysed by sonication. For that, the suspension was first thawed at room temperature in a water bath. Subsequently, a small spatula tip of RNaseA, along with 5  $\mu$ l of Benzonase and 100  $\mu$ l of 1 M MgCl<sub>2</sub>, was added. Sonication was carried out continuously, ensuring the temperature did not exceed 15 °C, with a total sonication time of 20 min. After sonication, 6 M urea was added to the lysate to linearize the proteins, thereby preventing nonspecific aggregation. The lysate was then centrifuged at 45000 xg for 30 min at 4 °C. The clarified supernatant was then sequentially filtered through 0.45  $\mu$ m and 0.2  $\mu$ m pore-size filters.

The proteins were then purified *via* affinity chromatography using a Protino Ni-NTA FPLC 5 ml column (Macherey-Nagel). The column was first equilibrated with 50 ml of Native IMAC Lysis/Wash-1 Buffer (**Table 3.7**), supplemented with 6 M urea. Subsequently, the lysate was applied to the column with a flow rate of 1 ml/min. The bound protein on the column underwent two wash cycles with Native IMAC Lysis/Wash-1 Buffer and Native IMAC Wash-2 Buffer (**Table 3.7**), each consisting of 50 ml and both supplemented with 6 M urea. Finally, the His-tagged proteins were eluted from the column using 20 ml of Native IMAC Elution Buffer (**Table 3.7**), supplemented with 6 M urea. The eluates were then concentrated until the desired concentration was achieved, as confirmed by Nanodrop™ (Thermo Fisher Scientific) measurements or BCA assay. Subsequently,

the proteins were divided into aliquots, snap frozen in liquid nitrogen and stored at -80 °C for later applications.

After each purification step, a small sample was taken for SDS-PAGE to assess the quality and correct size of the desired proteins (**Appendix Fig. 3**).

### 3.3.2.3. Purification of His-Stx1B<sup>SNARE-TMR</sup> wild-type and mutant constructs

*E. coli* cells expressing His-tagged Stx1B<sup>SNARE-TMR</sup> wild-type and mutants were lysed by sonication. For that, the suspension was first thawed at room temperature in a water bath. Subsequently, a small spatula tip of RNaseA, along with 5 µl of Benzonase and 100 µl of 1 M MgCl<sub>2</sub>, was added. Sonication was carried out continuously, ensuring the temperature did not exceed 15 °C, with a total sonication time of 20 min. After sonication, 6 M urea and 5% sodium cholate were added to the lysate and incubated for 30 min, slowly rotating at 4 °C. Afterwards, the lysate was centrifuged at 45000 xg for 45 min at 4 °C. The clarified supernatant was then sequentially filtered through 0.45 µm and 0.2 µm pore-size filters. The proteins were then purified *via* affinity chromatography using a Protino Ni-NTA FPLC 5 ml column (Machery-Nagel GmbH & Co. KG). The column was first equilibrated with 50 ml of Native IMAC Lysis/Wash-1 Buffer (Table 3.6), supplemented with 6 M urea and 3% sodium cholate. Subsequently, the lysate was applied to the column with a flow rate of 1 ml/min. The bound protein on the column underwent two wash cycles with Native IMAC Lysis/Wash-1 Buffer and Native IMAC Wash-2 Buffer, each consisting of 50 ml and both supplemented with 6 M urea and 3% sodium cholate. Finally, the His-tagged proteins were eluted from the column using 20 ml of Native IMAC Elution Buffer, supplemented with 6 M urea and 3% sodium cholate (refer to Table 3.6 for detailed Native IMAC lysis, wash and elution buffer composition, **Appendix Fig. 4 A**).

The eluate was then transferred into Slide-A-Lyzer<sup>TM</sup> dialysis cassettes (2.0 MWCO, 30 ml, Thermo Fisher Scientific), to remove the urea and introduce 1% CHAPS through a stepwise dialysis against a HEPES-buffer with decreasing urea concentrations (Buffer-A: 20 mM HEPES, 0.5 M NaCl, 1 mM EDTA, 1 mM DTT, 1% CHAPS, 3 M Urea, pH 7.4; Buffer-B: 20 mM HEPES, 50 mM NaCl, 1 mM EDTA, 1 mM DTT, 1% CHAPS, 1.5 M Urea, pH 7.4; Buffer-C: 20 mM HEPES, 50 mM NaCl, 1 mM EDTA, 1 mM DTT, 1% CHAPS, 0 M Urea, pH 7.4). The Buffer was changed every 6 h and during the last dialysis step, the His-tag was cleaved by the addition of 50 U of thrombin at 4 °C overnight (**Appendix Fig. 4 B**).

The dialyzed and digested samples were then further purified by ion-exchange, loading the samples onto an ENrich<sup>TM</sup> 10x100 column (Bio-Rad Laboratories, Inc.) for anion-exchange chromatography. For that, an increasing gradient of NaCl was used to purify and elute the sample from the column (Buffer-1: 20 mM HEPES, 50 mM NaCl, 1 mM EDTA, 1 mM DTT, 1% CHAPS, pH 7.4; Buffer-2: 20 mM HEPES, 1 M NaCl, 1 mM EDTA, 1 mM DTT, 1% CHAPS, pH 7.4). The gradual gradient increase was set from 0% Buffer-2 to 80% Buffer-2 within 20 ml, followed by an increase to 100% Buffer-2 for 30 ml to remove leftover impurities (**Appendix Fig. 4 C, D**).

The eluted fractions were validated by SDS-PAGE according to the chromatogram, and those containing the desired protein were collected and their concentration was measured via NanoDrop™. The purified proteins were then aliquoted, snap frozen using liquid nitrogen and stored at -80 °C until subsequent experiments (**Appendix Fig. 4 C**).

After each purification step, a small sample was taken for SDS-PAGE to assess the quality and correct size of the desired proteins (**Appendix Fig. 4**).

### **3.3.2.4. Purification of GST-Munc18-1 and GST-Munc13-MUN wild-type and mutant constructs**

*E. coli* cells expressing GST-tagged Munc18-1 as well as Munc13-MUN wild-type and mutants were lysed by French pressure cell press. For that, the suspension was first thawed at room temperature in a water bath and topped up to 50 ml with the respective lysis buffer. Subsequently, a small spatula tip of RNaseA, along with 15 µl of Benzonase and 250 µl of 1 M MgCl<sub>2</sub>, was added. Additionally, 50 µl of 2 M DTT was added for Munc18-1. The French press was washed with water and equilibrated with lysis buffer. Then, the cell suspension was passed through three times and the resulting lysate underwent centrifugation at 15000 xg for 30 min at 4 °C. The clarified supernatant was then sequentially filtered through 0.45 µm and 0.2 µm pore-size filters.

To extract the GST-fused Munc proteins, 1 ml of Protino Glutathione Agarose 4B beads (Macherey-Nagel) were added to the lysate, and rotated at 4 °C either for 2 hours (for Munc13-MUN) or overnight (for Munc18-1). Once incubation was complete, the beads were settled in a falcon and spun down at 500 xg for 5 minutes at 4 °C. The supernatant was removed and the beads, now bound with GST-tagged Munc18-1 or Munc13-MUN proteins, were resuspended in the first washing buffer (PBS, 1% Triton X-100) and transferred to a 2 ml Eppendorf tube. The beads were then washed once with the second washing buffer (PBS, 1 M NaCl, 5% Glycerol) and five times with the third washing buffer (PBS, 5% Glycerol). Finally, the beads were washed two times with the thrombin cleavage buffer (50 mM Tris, 200 mM NaCl, 2.5 mM CaCl<sub>2</sub>, pH 8.0). All centrifugations between the washing steps to sediment the beads were carried out at 1.6 xg for 1 min at 4 °C. For on-bead digestion and removal of the GST-tag, 25 µl of Thrombin (1 U/µl) was introduced to the beads in the thrombin cleavage buffer, after which the tubes were rotated at 4 °C overnight (**Appendix Fig. 5 A**) and **Appendix Fig. 6 A**).

After digestion, the beads were sedimented again and the supernatants were transferred to a fresh Eppendorf tube and pooled with respective remaining protein that was subsequently washed off the beads in a stepwise manner. Protein concentrations of the supernatants after each wash were determined by NanoDrop™ and the beads were washed until the protein concentration of the supernatants dropped below an absorption ratio  $\frac{260\text{ nm}}{280\text{ nm}}$  of 0.05. The pooled GST-free proteins were then filtered (0.2 µm) and concentrated to a final volume of 1 ml. Subsequent gel-filtration was performed on a Superdex 200 Increase 10/300 GL column (GE Healthcare) equilibrated with the required buffer. The eluted fractions were validated by SDS-PAGE according to the chromatogram, and those containing the desired protein were collected (**Appendix Fig. 5 B**), **C**) and

**Appendix Fig. 6 B), C)**). The purified proteins were then concentrated, with concentration measured using NanoDrop™ (Thermo Fisher Scientific), aliquoted, snap frozen using liquid nitrogen and stored at -80°C until subsequent experiments

After each purification step, a small sample was taken for SDS-PAGE to assess the quality and correct size of the desired proteins (**Appendix Fig. 5** and **Appendix Fig. 6**).

### 3.3.3. SDS-PAGE

Protein size and purity in solution were assessed using sodium dodecyl sulfate-polyacrylamide gel electrophoresis (SDS-PAGE). A minimum of 1 µg of the protein was combined with SDS loading buffer (5x) (**Table 3.7**) and diluted to achieve a final 1x concentration. The samples were then usually boiled for 5 min at 95 °C and loaded and electrophoresed on either a discontinuous homemade 15% polyacrylamide gel following Laemmli's method having a stacking and a resolving gel part (see **Table 3.12** for in house made gel composition) or a commercial 4-20% Mini-PROTEAN TGX Gradient Gel from Bio-Rad (Bio-Rad Laboratories, Inc.) with a voltage range of 190-210 V for 45-55 min. After electrophoresis, the gels were stained with Coomassie dye and destained using Coomassie destainer (**Table 3.7**). Protein sizes were approximated by comparing their bands to those of a Mark12™ Unstained Standard or PageRuler™ Prestained that were run alongside on the same gel.

**Table 3.12:** Composition of the in house made 15% polyacrylamide gels

<i>Component</i>	<i>Stacking Gel</i>	<i>Separation Gel</i>
<i>H<sub>2</sub>O</i>	13.8 ml	27.2 ml
<i>1.5 M Tris, pH 8.8</i>	15 ml	-
<i>1.5 M Tris, pH 6.8</i>	-	5 ml
<i>10% SDS</i>	0.6 ml	0.4 ml
<i>10% APS</i>	0.6 ml	0.4 ml
<i>30% Acrylamide</i>	30 ml	6.8 ml
<i>TEMED</i>	24 µl	25 µl

### 3.3.4. Bicinchoninic acid (BCA) assay

The BCA assay was performed in order to determine concentration of proteins that cannot be measured *via* NanoDrop™ or for organelle lysates. For this purpose, the Pierce™ BCA Protein Assay Kit (Thermo Fisher Scientific) was employed. Bovine serum albumin served as a standard and was prepared in 9 varying concentrations: 2000 µg/ml, 1500 µg/ml, 1000 µg/ml, 750 µg/ml, 500 µg/ml, 250 µg/ml, 125 µg/ml, 25 µg/ml, and 0 µg/ml. The test sample was diluted twice, using dilution factors of 10 and 100. Additionally, the sample buffer was assessed in the BCA assay.

In each instance, 25 µl of the sample was dispensed into a well of a 96-well plate, repeated three times for consistency. Subsequently, 200 µl of the prepared reagent mixture was introduced into every well, followed by a 30-second shaking period. The plate was then placed in an incubator for

30 min at 37°C. After incubation, the absorbance was read at 562 nm using a plate reader at room temperature.

The protein concentration was extrapolated based on the absorbance values of the known protein concentrations, and an average value across the various dilutions was derived.

### 3.3.5. SNARE complex formation assay

His-tagged Syb2 (1-96), SNAP-25 (1-206) and Stx1B<sup>SNARE</sup> (179-262) wild-type, E210K or L221P mutant in Native IMAC Elution Buffer, supplemented with 6 M urea, were combined in an equimolar 1:1:1 ratio (150 µM) and transferred into Slide-A-Lyzer<sup>TM</sup> dialysis cassettes (3.5 MWCO, 3 ml, Thermo Fisher Scientific). Urea was removed stepwise through dialysis against a Tris-buffer with decreasing urea concentrations (Buffer-A: 20 mM Tris-HCl, 0.5 M NaCl, 3 M Urea, pH 7.4; Buffer-B: 20 mM Tris-HCl, 0.5 M NaCl, 1.5 M Urea, pH 7.4; Buffer-C: 20 mM Tris-HCl, 0.5 M NaCl, 0 M Urea, pH 7.4). The buffer was changed every 6 h and after the last dialysis step, the NaCl concentration was lowered to 200 mM (Digestion-Buffer: 20 mM Tris-HCl, 0.2 M NaCl, pH 7.4) and the His-tags were cleaved by the addition of 50 U of thrombin at 4 °C overnight. The dialyzed and digested SNARE assembly assays were then centrifuged at 15000 xg and filtered through 0.2 µm pore-size filters to remove debris and aggregation. Unassembled components were removed by size exclusion chromatography using a Superdex 200 Increase 10/300 GL column. The eluted fractions were validated by SDS-PAGE according to the chromatogram, and those containing the desired SNARE complex were collected. 4 µg of each SNARE complex were loaded with and without boiling onto an SDS-PAGE together with 2 µg the individual proteins as size control, likewise with and without boiling. Protein bands were identified and validated *via* liquid chromatography-mass spectrometry (LC-MS) through tryptic in-gel digestion.

### 3.3.6. Tryptic in-gel digestion

Protein bands of interest from the SDS-PAGE gel were cut out and sliced into small fragments (~1 mm in size) using a sterilized blade and then transferred to a 0.5 ml low binding Eppendorf tube. To these gel fragments, 200 µl of destaining buffer (50 mM NH<sub>4</sub>HCO<sub>3</sub> / acetonitrile (1:1, v/v)) was added and incubated for 15 min at 45°C with continuous agitation. After discarding the buffer, the fragments were treated with 200 µl of trypsin buffer (50 mM NH<sub>4</sub>HCO<sub>3</sub>, pH 7.8) and incubated similarly. If remnants of blue staining persisted on the gel fragments, the previous steps were reiterated. Subsequent to this, the fragments were treated with 100 µl of acetonitrile (ACN) for 10 min at 45°C, after which the ACN was carefully removed.

The gel fragments, having reduced in size post-ACN treatment, were then treated with 1 µg of trypsin enzyme in 30 µl of 50 mM NH<sub>4</sub>HCO<sub>3</sub>-buffer to ensure comprehensive coverage. This mixture was incubated at 37°C overnight.

Upon completion, the digestion process was halted using 30 µl of a stop-solution (0.5% TFA in ACN). The resulting supernatant was transferred to a sterilized glass vial or Eppendorf tube. The gel remnants were then treated with 10 µl of ACN, incubated at room temperature for 10 min, and



centrifuged briefly. The resulting supernatant was combined with the previously collected one in the glass vial.

The combined supernatant underwent drying in a vacuum centrifuge (speed vac.) for a duration of 1-2 h, until the solution completely evaporated. Once dried, the peptides were either stored at -20 °C for future use or reconstituted in 10 µl of a solution containing 5% ACN and 0.1% TFA for subsequent measurements *via* LC-MS.

### 3.3.7. SNARE lipid vesicle preparation

#### 3.3.7.1. ΔN-SNARE complex formation <sup>(1)</sup>

The ΔN-SNARE complex, comprising Stx1B<sup>SNARE-TMR</sup> (189-288), SNAP-25 (1-206), and ΔN-Syb2 (49-96), was formed by combining purified monomers (SNAP-25, ΔN-Syb2 (49-96) and full-length Syb2 (1-116) were kindly provided by Dr. Agata Witkowska). The monomers were mixed in a 1:1:1.5 molar ratio, respectively, with the addition of 1% CHAPS, and left to incubate overnight. Following this, the complex was purified using ion exchange chromatography with a Mono Q 4.6/10 PE (GE Healthcare) anion exchanger in the presence of 1% CHAPS, employing a 2-step linear NaCl gradient. Fractions eluted from the chromatography were verified *via* SDS-PAGE analysis of unboiled samples according to the chromatogram, and those containing the desired complex were collected. The purified complex was then aliquoted, rapidly frozen using liquid nitrogen, and stored at -80°C until further use [193].

#### 3.3.7.2. Small unilamellar vesicle (SUV) preparation <sup>(2)</sup>

Two lipid mixtures were prepared for liposome formation. The mixture of the liposomes carrying the ΔN-SNARE complex composed of L-α-phosphatidylcholine (PC), L-α-phosphatidylethanolamine (PE), L-α-phosphatidylserine (PS), cholesterol and Phosphatidylinositol 4,5-bisphosphate (PIP<sub>2</sub>) in a ratio of 48:20:20:10:2 respectively. For the liposomes carrying only the full-length Syb2, the mixture composed of PC, PE, PS, cholesterol, NBD-PE and LissRhod-PE in a ratio of 50:17:20:10:1.5:1.5, respectively. The lipid mixture was dried under a stream of nitrogen and subsequently reconstituted in a liposome buffer (20 mM HEPES, 150 mM KCl, 1 mM EDTA, 1 mM DTT, pH 7.4) supplemented with 5% sodium cholate at a total lipid concentration of 13.5 mM. Full-length Syb2 as well as the ΔN-SNARE complex was incorporated at a protein-to-lipid ratio of 1:500.

Following the addition of the SNARE proteins, the mixture underwent size-exclusion chromatography using Sephadex G-50 Superfine (Sigma-Aldrich) resin, which has been pre-equilibrated with liposome buffer. Liposome-rich fractions were identified by light scattering upon illumination with a laser pointer. Fractions containing SUVs were collected and stored at 4 °C until further use [193].

(1) Conducted together with Dr. Agata Witkowska (Haucke Lab, FMP Berlin).

(2) Conducted by Dr. Agata Witkowska (Haucke Lab, FMP Berlin).

### 3.3.8. GST pull-down assay of Munc18-1 via Stx1B wild-type and mutants

The pull-down assay was conducted to quantify the *in vitro* binding of both Stx1B wild-type and mutant to endogenous Munc18-1. GST-Stx1B wild-type and mutant fusion proteins were purified following the protocol outlined in **Chapter 3.3.2.1** with the only alteration being the exclusion of the trypsin digestion step to keep the GST-tag covalently linked to the Stx1B proteins (**Appendix Fig. 7**). In order to couple the GST-tagged STX1B<sup>WT</sup>, Stx1B<sup>L221P</sup>, Stx1B<sup>E210K</sup> or Stx1B<sup>E210K,K82E</sup> to the beads, 50 µg of the GST fusion protein was incubated with 20 µl of Protino Glutathione Agarose-4B beads in a low-binding Eppendorf tube. As a negative control, only GST was used and coupled. Then, the tubes were topped up to 1 ml with PBS and rotated for 1 h at room temperature.

Meanwhile, the mouse brain lysate was prepared by adding 4 ml of ice-cold Mouse Brain Lysis Buffer (20 mM HEPES, 50 mM KCl, 2 mM MgCl<sub>2</sub>, pH 7.4) supplemented with 0.5 mM EDTA to a frozen mouse brain. Then, the mouse brain was homogenized with a glass-homogenizer. Afterwards the lysate was further blended by pressing it through a G27 syringe needle 15 times. Thereafter, the lysate was centrifuged at 15000 xg for 30 min at 4 °C and the protein concentration was determined *via* BCA assay.

After that, the beads coupled to the GST-fused Stx1B proteins were washed three times with 500 µl of PBS and then incubated with 2 mg of mouse brain lysate proteins in 1 ml of PBS and rotated for 1 h at room temperature. Afterwards, the beads were washed two times with 1 ml of Mouse Brain Lysis Buffer including 1% Triton X-100 and lastly washed with 1 ml PBS. To elute the proteins from the beads, SDS-Loading Buffer (3x) was added and the samples boiled for 5 min at 95 °C. The SDS-samples were then run on two SDS-PAGEs, one for staining with Coomassie dye and one for western blotting.

### 3.3.9. Western blot

To transfer proteins from an SDS-PAGE gel to a nitrocellulose membrane, the wet blotting technique was employed. Initially, a commercial 4-20% Mini-PROTEAN TGX Gradient Gel was run as previously outlined, using the PageRuler™ Prestained marker. The gel was not stained but was briefly immersed in transfer buffer. For the western blot procedure, four filter papers and two 0.2 µm nitrocellulose membranes were trimmed to match the SDS-PAGE gel dimensions and pre-soaked in transfer buffer supplemented with 20% methanol. The nitrocellulose membrane and the SDS-PAGE gel were layered between the filter papers, and the SDS-PAGE gel was positioned towards the negative pole (cathode). The chamber was subsequently filled with transfer buffer and chilled using an ice pack during the electroblotting process. As an electric current is initiated, the negatively charged proteins from the gel migrate towards the positively charged anode, embedding themselves in the nitrocellulose membrane. The blotting proceeded for 1 h at 100 V and ~200 mA. The membrane was then treated with a 5% non-fat milk powder solution in TBS-T for an hour to block nonspecific binding sites. Subsequently, it was exposed to the primary antibody, STXBP1 Rabbit (1:5000, proteintech® (Rosemont, USA)), in TBS-T for another hour. The membrane

underwent three consecutive 5-minute washes with TBS-T. Following this, the secondary antibody, goat anti-Rabbit IgG (H+L) linked with HRP (1:10000, Thermo Fisher Scientific), was applied and allowed to incubate for 1 h. The membrane was then rinsed thrice with TBS-T for 5 min each time. Finally, the western blot was developed using equal parts of HRP juice components A and B. The resulting chemiluminescence was captured using the ChemoCam HR16 - 3200 Imager from INTAS Science Imaging Instruments GmbH (Göttingen, Germany). The western blot image was analyzed using ImageJ. A rectangular area, matching the size and shape of the largest band, was defined for analysis. The mean grey value (indicative of intensity) for each band within this rectangle was calculated. Additionally, the average intensity of the background was determined and subtracted from each band's intensity value. The sample with the highest intensity was normalized to a value of 1.0 and the resulting ratios for the other samples were plotted on a bar graph.

### 3.4. Biophysical methods

#### 3.4.1. Circular dichroism (CD) spectroscopy

CD spectroscopy exploits the differential absorption of left circularly polarized light (L-CPL) and right circularly polarized light (R-CPL) by chiral molecules (**Fig. 3.1 A**) [194]. The inherent chirality of biomolecules, arising from their asymmetric molecular structures, results in distinct interactions with these circularly polarized light forms (**Fig. 3.1 B**) [195]. The CD spectrum, generated by measuring the difference in absorbance between L-CPL and R-CPL over a range of wavelengths, offers a unique fingerprint revealing information about the secondary structure of proteins [196].

Each secondary structure element in proteins exhibits characteristic features in the CD spectrum, allowing for their differentiation (**Fig. 3.1 C**):  $\alpha$ -Helices, prevalent secondary structures in many proteins, contribute negative peaks around 208 nm and 222 nm in the CD spectrum [197]. These features arise from the unique dipole moments associated with the helical structure.  $\beta$ -Sheets on the other hand manifest as a negative peak near 218 nm in the CD spectrum. The distinct CD signature of beta sheets allows for their identification and quantification [197]. Lastly, turns and random coils, representing more flexible regions in protein structures, contribute to the overall spectrum shape without well-defined peaks. Their presence is often inferred from the smoother background of the CD spectrum [198].

CD spectra can be used to approximate the proportion of a molecule adopting specific conformations, such as the  $\alpha$ -helix,  $\beta$ -sheet or other configurations like random coil. These fractional assignments impose significant constraints on the potential secondary conformations assumed by the protein [199]. However, it's important to note that, in general, CD cannot precisely pinpoint the location of detected alpha helices within the molecule or predict their exact quantity. Nevertheless, CD proves to be a valuable tool to characterize structural conformations of proteins and in highlighting conformational changes. For example, it can be employed to investigate alterations in the secondary structure concerning variables like temperature or the concentration of denaturing agents [197].

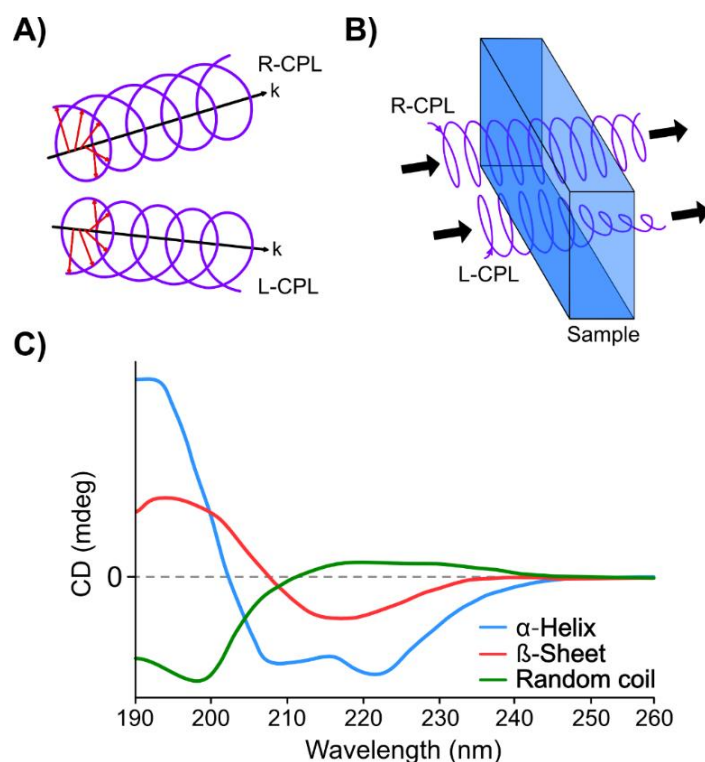


**Figure 3.1:** **A)** Circularly polarized light is generated when the electric field vector undergoes rotational movement around its direction of propagation ( $k$ ) while maintaining a constant magnitude. The trajectory of the electric vector in circularly polarized light traces a helical path along the direction of propagation ( $k$ ). In the case of left circularly polarized light (L-CPL) the electric vector rotates counterclockwise. Conversely, for right circularly polarized light (R-CPL), the electric vector rotates clockwise (figure adapted from Snyder (2010) [200]). **B)** R-CPL and L-CPL are influenced differently in a layer containing an enantiomer of an optically active chiral substance (figure adapted from Commons wiki (2006) [201]). **C)** The exemplary standard CD spectra illustrate that each of the three fundamental secondary structures in a polypeptide chain ( $\alpha$ -helix,  $\beta$ -sheet, and random coil) exhibits a uniquely distinctive CD spectrum (figure adapted from Wei *et al.* (2014) [202]).

### 3.4.1.1. CD Spectroscopy of Stx1B Wild-Type and Mutant Constructs, and Wild-Type and Mutant SNARE Complexes

For CD spectroscopy measurements, the Stx1B constructs (25-252) and formed SNARE complexes were dialyzed into a 10 mM sodium phosphate buffer, pH 7.4 and set to a final concentration of 10-20  $\mu$ M. The Jasco J-810 spectropolarimeter (Jasco Products Company (Oklahoma City, USA)) was employed to record the spectra, utilizing quartz cuvettes with a path length of 1 mm. Far-UV CD spectra were obtained within the 190-260 nm wavelength range at 25  $^{\circ}$ C. Melting curves were documented at 222 nm, spanning temperatures from 25-90  $^{\circ}$ C.

Recorded data were analyzed and plotted in OriginPro-2023 (OriginLab Corporation, (Northampton, USA)). The measured CD spectra were converted into molar ellipticity ( $CD_{mdeg}$ ) according to equation (1).

$$CD_{mdeg} = \frac{\theta_{obs}}{10000 * l * c * n} \quad (1)$$

$\theta$  = Wavelength

$l$  = pathlength (cuvette)

$c$  = sample concentration

$n$  = number of residues

Melting curves were normalized and fitted to the sigmoidal Boltzmann function according to equation (2).

$$y = \widehat{CD}_{mdeg} = \frac{A_1 - A_2}{1 + e^{(x - x_0)/d_x}} + A_2 \quad (2)$$

$A_1$  = CD signal at the start of the transition (baseline at the low end of  $x$ )

$A_2$  = CD signal at the end of the transition (baseline at the high end of  $x$ )

$x$  = Temperature

$x_0$  = Inflection point

$d_x$  = slope factor (smaller  $d_x$  equals steeper transition, larger  $d_x$  equals more gradual transition)

### 3.4.2. Vesicle fusion assay – lipid mixing fluorescence detection <sup>(1)</sup>

A widely used technique for detecting membrane fusion events involves observing lipid mixing, which arises when two vesicles merge. Lipid mixing assays, commonly employed to study vesicle fusion *in vitro*, rely on fluorescence resonance energy transfer (FRET) between fluorophores embedded within the vesicle membranes [193, 203, 204].

The FRET signal measurement varies depending on the approach employed. The fluorescence of the fluorophores can either increase or decrease upon fusion, contingent upon whether the FRET donor and acceptor are situated on the membrane of the same initial set of vesicles or not [203-205]. When the fluorophores are initially located on separate vesicles, energy transfer from the donor to the acceptor occurs only upon fusion-mediated lipid mixing. This results in a decrease in the donor fluorescence intensity and in an increase in the acceptor fluorescence intensity [205].

When the fluorophores are initially situated on the same membrane, vesicle fusion triggers a dilution of the fluorophores due to the addition of more unlabeled lipids. Consequently, the average distance between the donor and acceptor fluorophores increases, leading to a decrease in FRET. This manifests as an increase in the donor fluorescence intensity and simultaneously a decrease in the acceptor fluorescence intensity [204].

In this study, both the donor and acceptor fluorophores were located on the same membrane of the vesicles, which also integrated the full-length Syb2 at the beginning of the reaction. Specifically, NBD-PE (Avanti Polar Lipids (Alabaster, USA)) served as donor fluorophore, while LissRhod-PE (Avanti Polar Lipids (Alabaster, USA)) was utilized as acceptor.

Vesicle fusion reactions were conducted and monitored at 37 °C using an FP-6500 spectrofluorometer (Jasco Products Company), equipped with a magnetic stirrer and temperature control. The excitation and emission wavelengths were set to 488 nm and 520 nm, respectively to record the fluorescence emission of the donor fluorophore.

To initiate the assay, 10  $\mu$ l of the eluted full-length Syb2-SUVs were added to a measurement quartz cuvette with a magnetic stirrer containing 500  $\mu$ l of assay buffer (20 mM HEPES, 150 mM KCl, pH 7.4) and stirred for 60 s. Subsequently, 10  $\mu$ l of the eluted  $\Delta$ N-SNARE complex-SUVs were added to the cuvette, and the increase in fluorescence was recorded under continuous stirring. At the end of the measurement, 5  $\mu$ l of 10% Triton X-100 were introduced to terminate the reaction and asses

(1) Conducted together with Dr. Agata Witkowska (Haucke Lab, FMP Berlin).

the maximum de-FRET signal of NBD-PE and LissRhod-PE. After each run, the measurement cuvette undergoes two washes with isopropanol followed by two washes with buffer solution before proceeding with a new sample.

### 3.4.3. Isothermal titration calorimetry (ITC)

Isothermal Titration Calorimetry (ITC) stands as a gold standard in providing a direct and quantitative measure of the heat changes associated with molecular interactions in solution [206, 207]. This method plays a pivotal role in unraveling the thermodynamics governing binding events between various biomolecules, such as proteins, nucleic acids, and small molecules. The fundamental principle underlying ITC lies in its ability to monitor the heat produced or absorbed during a controlled titration process, offering unique insights into the nature of molecular associations [208].

At its core, ITC operates on the principle that when molecules interact, a temperature change occurs due to binding events or chemical reactions, which is precisely recorded by the calorimeter. The method is isothermal, meaning the temperature of the system is kept constant throughout the experiment [209].

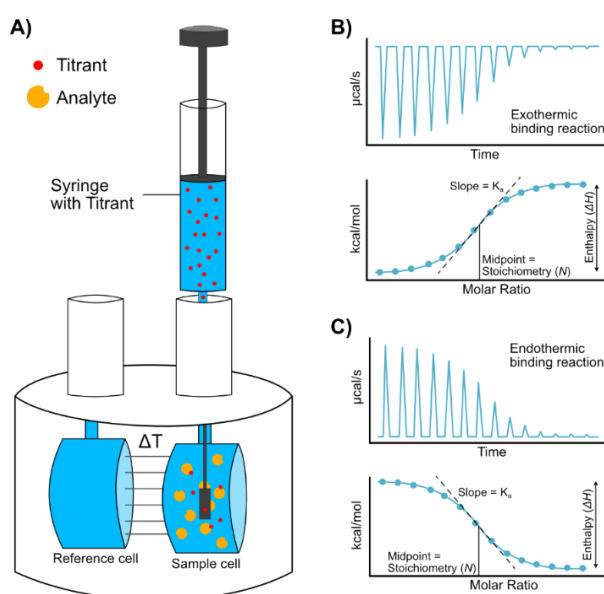


**Figure 3.2:** **A)** Schematic representation of an ITC instrument with coin-shaped cells. The sample and reference cells are enclosed within an adiabatic jacket, effectively isolating them from the external environment and maintaining a consistent temperature. A step motor, situated in the syringe holder, regulates the plunger of a hermetically sealed syringe, administering the titrant solution into the sample cell. Stirring mechanisms ensure rapid homogenization following each titrant addition. Simultaneously, the temperature difference between the cells is continuously converted into a voltage signal through the Seebeck effect using the thermopile. This signal is subsequently transformed into a thermal power signal. Upon the addition of the titrant from the syringe to the reaction vessel, it binds to the analyte within the cell, with any excess remaining in solution within the cell (figure adapted from Srivastava *et al.* (2019) [210]). **B)** Schematic recording of a typical ITC experiment displaying an exothermic binding reaction. Integrating the area under the injection peaks leads to a sigmoidal curve which can be fitted and used to determine molar ratio enthalpy and the  $K_D$ -value (figure adapted from S. Caulton (2019) [211]). **C)** Schematic recording of a typical ITC experiment displaying an endothermic binding reaction. Integrating the area under the injection peaks leads to a sigmoidal curve which can be fitted and used to determine molar ratio enthalpy and the  $K_D$ -value (figure adapted from S. Caulton (2019) [211]).

The ITC instrument consists of two chambers – a sample cell containing one of the interacting components (analyte) and a reference cell containing the solvent or buffer. The analyte is titrated with the other component (titrant), which is added in small, controlled increments using a syringe (**Fig. 3.2 A**).

As the titrant is injected into the analyte, any heat changes associated with the binding or chemical reaction are directly measured by the calorimeter. If the reaction is exothermic (heat-releasing), the temperature in the sample cell will increase. If it is endothermic (heat-absorbing), the temperature will decrease. The heat produced or absorbed during each injection is directly measured by the calorimeter (**Fig. 3.2 B**, **C**). The resulting data is a plot of heat change against the molar ratio of titrant to analyte. This is accomplished by integrating the area under the injection peaks and graphing the individual values based on the molar ratio of the binding event against  $\Delta H$  [209, 212]. The resulting sigmoidal curve allows for determination of the stoichiometry ( $N$ ), enthalpy ( $\Delta H$ ). The  $K_D$ -value can be calculated according to equation (3).

$$K_D = 1/K_a \quad (3)$$

These data also allow the calculation of Gibb's free energy changes ( $\Delta G$ ) and entropy changes ( $\Delta S$ ) according to equation (4) and (5).

$$\Delta G = -RT \ln K_a \quad (4)$$

$$R = 8.314 \frac{J}{mol \cdot K}$$

T = Temperature

$$\Delta G = \Delta H - T\Delta S \quad (5)$$

In addition to validating direct interactions with the target molecule, thermodynamic measurements offer valuable insights into the underlying noncovalent forces driving binding. Polar interactions typically make favorable contributions to the enthalpic component, while entropically favored interactions tend to be more hydrophobic in nature [213].

### 3.4.3.1. ITC measurements of Stx1B WT and Mutant constructs with Munc18-1

For ITC experiments, Stx1B constructs (25-252) and Munc18-1 (2-594) were purified and brought into a HEPES buffer (20 mM HEPES, 125 mM NaCl, 3 mM TCEP, pH 7.4) through gel filtration. The concentrations of different Stx1B constructs were measured subsequently adjusted to a concentration of 80  $\mu$ M for the ITC measurement. Furthermore, the concentration of Munc18-1 was assessed, and the sample was diluted to 8  $\mu$ M.

Measurements were performed using a MicroCal iTC-200 (Malvern Panalytcs). The cell-chambers underwent a Decon90 wash under stirring at 50 °C. Subsequently, the cells were thoroughly rinsed with distilled water and finally washed with ITC buffer. The entire system was set to 25 °C. The reference cell was then loaded with 300  $\mu$ l of the HEPES buffer, and the sample cell was filled with

300  $\mu\text{l}$  of 8  $\mu\text{M}$  Munc18-1<sup>WT</sup>. Subsequently, the syringe underwent washing and was loaded with 60  $\mu\text{l}$  of 80  $\mu\text{M}$  Stx1B protein. The measurement commenced at 25 °C, involving 16 injections with an initial delay of 120 s, a spacing time of 180 s, a stirring speed of 750 rpm, and a reference power set to 5  $\mu\text{Cal/s}$ .

The data were processed using MicroCal PEAQ-ITC Analysis Software (Malvern Panalytcs). Baseline correction was performed as needed and subsequently subtracted. The recording plots and  $K_D$ -values were also extracted using the same software.

### 3.4.4. Nuclear magnetic resonance (NMR) spectroscopy

Nuclear magnetic resonance (NMR) spectroscopy is a versatile technique utilized for the detailed investigation of molecular structures and interactions at the atomic level. The principle of NMR is grounded in the behavior of atomic nuclei within a homogeneous magnetic field interacting with radiofrequency electromagnetic radiation. Most atomic nuclei possess an intrinsic angular momentum  $\vec{L}$ , known as nuclear spin which depends on the spin quantum number  $I$  with  $|\vec{L}| = \hbar\sqrt{I(I+1)}$ . The angular momentum is associated with a magnetic moment  $\vec{\mu}$  through the gyromagnetic ratio  $\gamma$  ( $\vec{\mu} = \gamma * \vec{L}$ ). The gyromagnetic ratio varies for different isotopes. Nuclei with an odd mass number typically exhibit a half-integer spin quantum number, while those with an even mass number display an integer spin quantum number [214].

Nuclei with a spin quantum number  $I$  of  $\frac{1}{2}$ , such as  $^1\text{H}$ ,  $^{15}\text{N}$ , and  $^{13}\text{C}$ , are particularly relevant for NMR experiments due to their single transition properties, which facilitate the study of macromolecules like proteins. In the presence of an external magnetic field  $B_0$ , spins can occupy  $2I + 1$  energy levels. In case of  $I = \frac{1}{2}$ , only two possible energy levels are available. Due to the slightly higher population of the lower energy level, this results in a net magnetization along the magnetic field direction, known as the Zeeman Effect. When subjected to a radiofrequency pulse aligned perpendicular to  $B_0$ , the nuclei undergo a transition between energy levels, inducing phase coherence among spins and leading to a tilting of the net magnetization into the xy-plane (**Fig. 3.3**) [214].

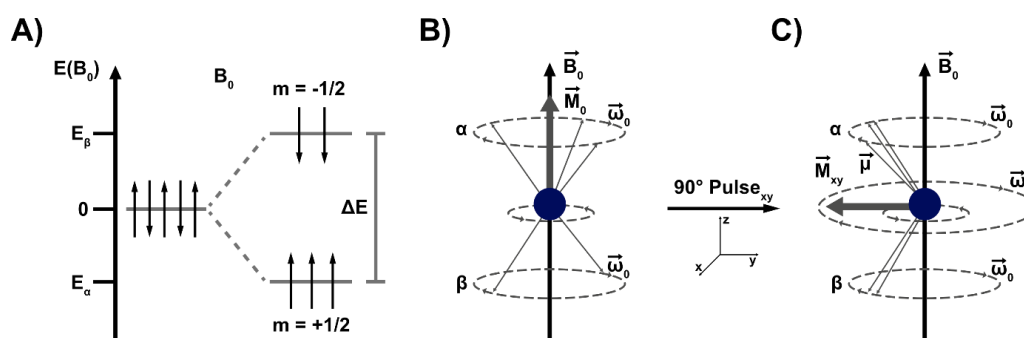


**Figure 3.3:** (Figure adapted from F. Gerth [215]) **A)** Illustration of the energy levels of nuclei with  $I=\frac{1}{2}$  before and after the application of an external magnetic field, demonstrating the Zeeman Effect. **B)** Depiction of the orientation and precession of magnetic moments, resulting in the generation of net magnetization  $\vec{M}_0$ . **C)** Projection of the macroscopic magnetization vector  $\vec{M}$  into the xy-plane following the application of a  $90^\circ$  pulse.



Subsequent relaxation processes cause the net magnetization to return to its equilibrium state along the z-axis, resulting in the generation of a time-dependent signal known as the free induction decay (FID). Fourier transformation of the FID yields the resonance frequencies of the nuclei, which can be plotted relative to a reference substance to determine chemical shifts in parts per million (ppm) [216].

The chemical environment surrounding a nucleus influences its Larmor frequency and chemical shift, providing valuable information about molecular structure and dynamics. Shielding effects from electron shells and spin-spin coupling interactions contribute to distinct signals in the NMR spectrum, aiding in the elucidation of molecular interactions and structural determination.

To overcome limitations posed by molecular size and complexity, multidimensional NMR experiments are employed to correlate NMR-sensitive isotopes within molecules. By incorporating variable evolution times before FID detection, these experiments enable the direct correlation of nuclei within a molecule, expanding the scope of structural analysis and interaction studies (**Fig. 3.4**) [214].

In protein-NMR analysis, the coupling of protons with heteronuclei such as  $^{15}\text{N}$  or  $^{13}\text{C}$  is of significant interest as it allows for correlation between these nuclei while taking advantage of the higher sensitivity of  $^1\text{H}$ . However, due to the low natural abundance of  $^{15}\text{N}$  and  $^{13}\text{C}$  isotopes, proteins intended for these types of NMR experiments must be artificially enriched during recombinant expression. To leverage proton sensitivity, NMR experiments employ methods where magnetization is transferred between protons and heteronuclei, known as 'insensitive nuclei enhanced by polarization transfer' (INEPT) (**Fig. 3.4**). Among these techniques, the  $^1\text{H}$ - $^{15}\text{N}$ -heteronuclear single-quantum correlation (HSQC) experiment is the most commonly used in protein-NMR.

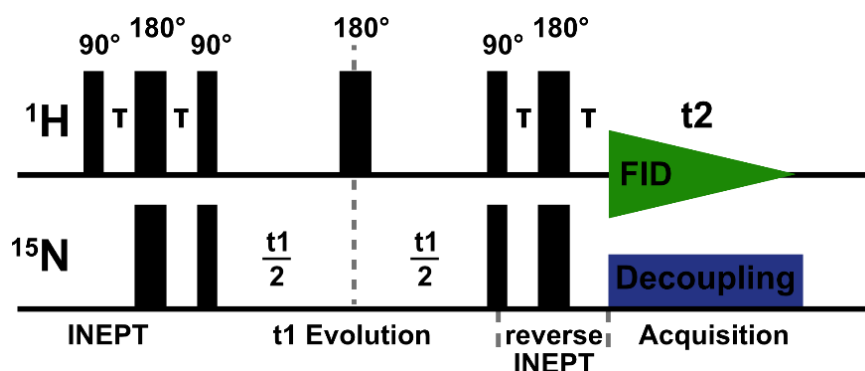


**Figure 3.4:** Decoupled INEPT  $^1\text{H}$ - $^{15}\text{N}$ -pulse sequence for acquiring a two-dimensional  $^1\text{H}$ - $^{15}\text{N}$ -HSQC experiment (figure adapted from M. Pascal [214]).

The  $^1\text{H}$ - $^{15}\text{N}$ -HSQC experiment is widely utilized to correlate nitrogen and proton resonances, providing valuable insights into protein backbone structure and dynamics. Each peak corresponds to an NH-group in the proteins, acting as a unique fingerprint and providing structural information (**Fig. 3.5**). Peak intensity, shape, and width convey details about the molecular weight and dynamics [217].

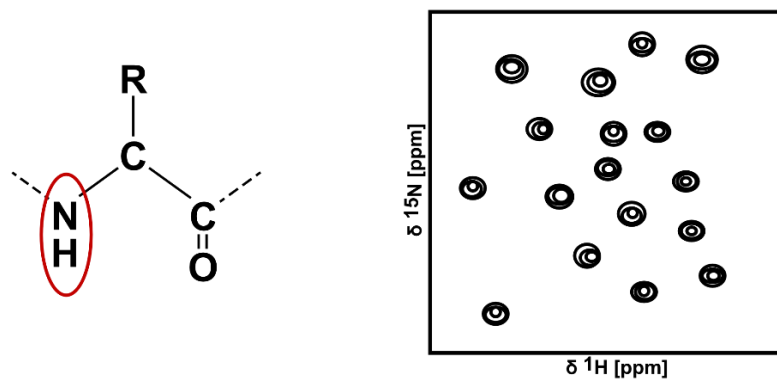


**Figure 3.5:** Schematic illustration of a 2D  $^1\text{H}$ - $^{15}\text{N}$ -HSQC spectrum (right), where proton and nitrogen atoms are correlated (left), resulting in each NH-group of the protein backbone producing a resonance signal within the spectrum (figure adapted from J. Sticht [218]).

Signals from the nitrogen-bound protons of specific amino acid side chains, including asparagine, glutamine, and tryptophan, also contribute to the spectrum. NH signals from histidine, lysine, and arginine are typically observed outside the measured spectral range, with lysine occasionally folding in as negative peaks. Proline residues lack an amide proton, thus do not contribute signals to a  $^1\text{H}$ - $^{15}\text{N}$ -HSQC spectrum [217].

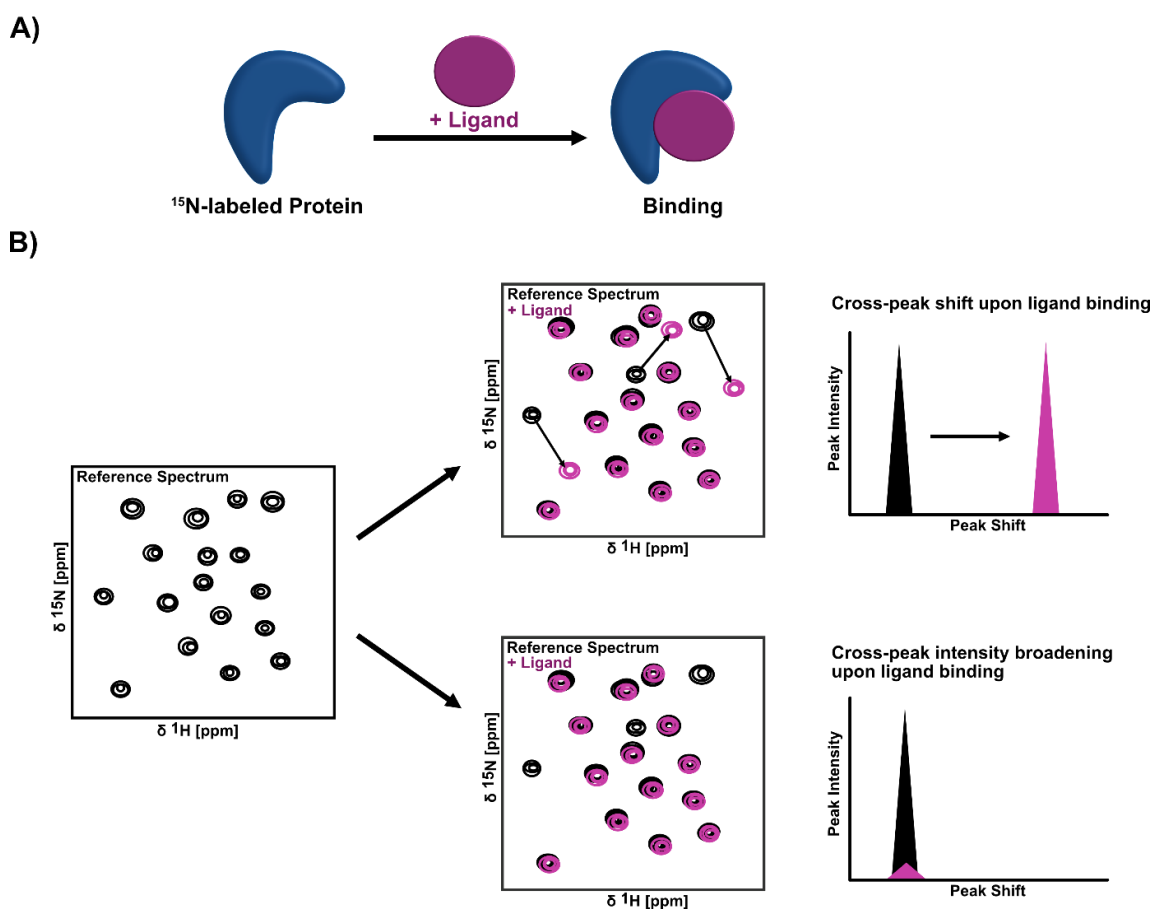


**Figure 3.6:** **A)** Schematic illustration depicting the binding of a ligand molecule to a  $^{15}\text{N}$ -labeled protein. **B)** Following the addition and binding of the ligand, changes occur in the  $^1\text{H}$ - $^{15}\text{N}$ -HSQC spectrum compared to the reference spectrum, manifesting as either cross-peak shifts or cross-peak broadening, resulting in the disappearance of certain peaks (figure adapted from J. Sticht [218]).

By analyzing changes in resonance patterns following the addition of ligands or other binding partners, HSQC titrations offer valuable insights into molecular interactions and their strengths, crucial for drug discovery and molecular biology research. Initially, a reference spectrum is obtained, typically featuring the  $^{15}\text{N}$ -labeled protein alone. Subsequently, an unlabeled binding partner is added to the protein. If interaction occurs between the molecules, observable differences in the resonances compared to the reference spectrum emerge (**Fig. 3.6**). Furthermore, HSQC titrations involve incrementally increasing concentrations of the ligand added to the protein sample. This approach allows for the assessment of interaction strength, characterized by either fast or slow exchange compared to the NMR timescale. This is discerned by peaks shifting linearly with binding partner concentration or a decrease in peak intensity (**Fig. 3.6**). Specifically, peaks shifting linearly with the concentration of the binding partner suggest fast exchange relative to the NMR timescale. Conversely, peaks that decrease in intensity and increase in intensity at a shifted position suggest slow exchange. Additionally, if peaks disappear without reappearing elsewhere, this usually indicates intermediate exchange or the formation of a complex that is significantly large in size [218].

### **3.4.4.1. NMR spectroscopy measurements of Syb2 wild-type and mutant constructs with Munc13-MUN and Munc18-1**

For NMR spectroscopy experiments,  $^{15}\text{N}$ -labeled Syb2 constructs (1-96) were expressed in M9 minimal medium containing 750 mg/L of  $^{15}\text{N}$ -enriched (99%) ammonium chloride, purified and brought into a HEPES buffer (20 mM HEPES, 150 mM NaCl, 1 mM TCEP, pH 6.0 or 7.1) through gel filtration (see section 3.3.). Stx1B constructs (25-252), the Munc13-MUN construct (859-1531,  $\Delta$ 1408-1453) and Munc18-1 (2-594) constructs were expressed in 2YT medium, purified and brought into the same HEPES buffer through gel filtration. The samples were prepared according to the required concentration and supplemented with 10%  $\text{D}_2\text{O}$ . 2D  $^1\text{H}$ - $^{15}\text{N}$ -HSCQ measurements were acquired on a AVANCE III 700 MHz spectrometer (Bruker), equipped with a 5 mm triple-resonance cryoprobe. Measurement settings were set to 300 K with 64 scans and 160 scans or 280 K with 40 scans and 160 scans. Spectral data were processed with TopSpin 3.2 (Bruker) and plotted as well as analyzed using CcpNMR Analysis v.2.4.2 and v.3.1.2 [219, 220]. Cross-peak intensities were analyzed and plotted using Microsoft Excel (Microsoft, Redmond, USA) and binding curves were analyzed, fitted and plotted using OriginPro 2023 (OriginLab).

### **3.4.5. Cross-linking mass spectrometry (XL-MS)**

#### **3.4.5.1. Mass spectrometry (MS)**

Mass spectrometry (MS) is a powerful analytical method used to determine the mass-to-charge ( $m/z$ ) ratio and intensity of ions in the gas phase. Initially employed in various research domains to analyze small molecules, MS has evolved into a well-established technique for investigating the structural and biophysical properties of bioorganic molecules such as peptides and proteins. As

such, MS has emerged as a valuable tool for experimental protein structure analysis, detecting structural alterations induced in solution and subsequently observed in the gas phase [221].

Fundamentally, a mass spectrometer comprises three key components: an ion source for generating a stream of gaseous ions from the sample, a mass analyzer to separate these ions based on their  $m/z$  ratio, and a detector to measure the ion masses and intensities. The signals are then presented in a mass spectrum, displaying the ion intensities over their  $m/z$  ratio.

In this work, we employed an UltiMate 3000 nano HPLC system coupled online to a Q Exactive HF-mass spectrometer (both by Thermo Fisher Scientific) to perform nanoscale liquid chromatography-mass spectrometry (LC-MS, **Fig. 3.7. A**).

Liquid chromatography (LC) plays a pivotal role in the analysis of complex mixtures by separating their constituent molecules before they undergo mass spectrometry. This step is indispensable because biological samples, like protein or peptides mixtures, or metabolites can harbor a multitude of components with diverse molecular weights and chemical characteristics. Without separation, these components would inundate the mass spectrometer simultaneously, causing overlapping signals and hindering accurate identification and quantification of individual analytes. By pre-separating the components, the LC-system enables the mass spectrometer to analyze compounds consecutively, thereby enhancing sensitivity, resolution, and reliability. This process improves the detection and characterization of specific molecules within the sample, leading to more precise and comprehensive results [222].

Achieving separation involves passing the sample through a chromatographic column, where different components interact with the stationary phase, causing them to elute at distinct times. The LC-system precisely controls the flow rate of the mobile phase and the solvent composition gradient, facilitating the separation of analytes based on their chemical properties. Subsequently, the separated components are introduced into the mass spectrometer, amplifying sensitivity, specificity, and overall performance of the analysis [223].

For the transfer into the mass spectrometer, the separated sample molecules are ionized through an ion source, which in the case of the Q Exactive HF-mass spectrometer was an electrospray ionization (ESI) source (**Fig. 3.7. C**). There, the sample solution is introduced into a metal capillary tube and the application of a high voltage to the capillary, often ranging from 1 to 5 kilovolts, induces the formation of a Taylor cone at its tip. This cone arises from the interplay between the solvent's surface tension and the electrostatic forces. As the voltage intensifies, the solvent at the tip of the Taylor cone becomes charged, leading to the ejection of charged droplets. During their airborne journey, solvent molecules evaporate from the droplet surface due to the strong electric field, gradually reducing droplet size and yielding charged aerosol droplets. Continued evaporation causes the charged droplets to reach a critical point where repulsive forces between same charges overwhelm surface tension, resulting in a Coulombic explosion. This explosion breaks the droplets into smaller entities, each potentially containing one or more charged molecules. With further solvent evaporation, the remaining charged molecules become increasingly concentrated until all solvent is evaporated, leaving behind gas-phase ions of the original molecules. ESI is highly

valuable for analyzing large biomolecules such as proteins, peptides, and nucleic acids due to its gentle ionization process, which minimizes fragmentation. These gas-phase ions can then be introduced into the mass spectrometer for detailed analysis [222, 224, 225].

After entering the mass spectrometer through the sample cone, the gas phase ions are then focused by a stacked-ring ion guide (S-lens), and guided by active beam guides further through the bent flatapole towards the quadrupole. The bent flatapole, equipped with a wide bore at the bend, serves to expel solvent droplets and other neutral species, preventing them from advancing deeper into the instrument (**Fig. 3.7. B), C)** [226].

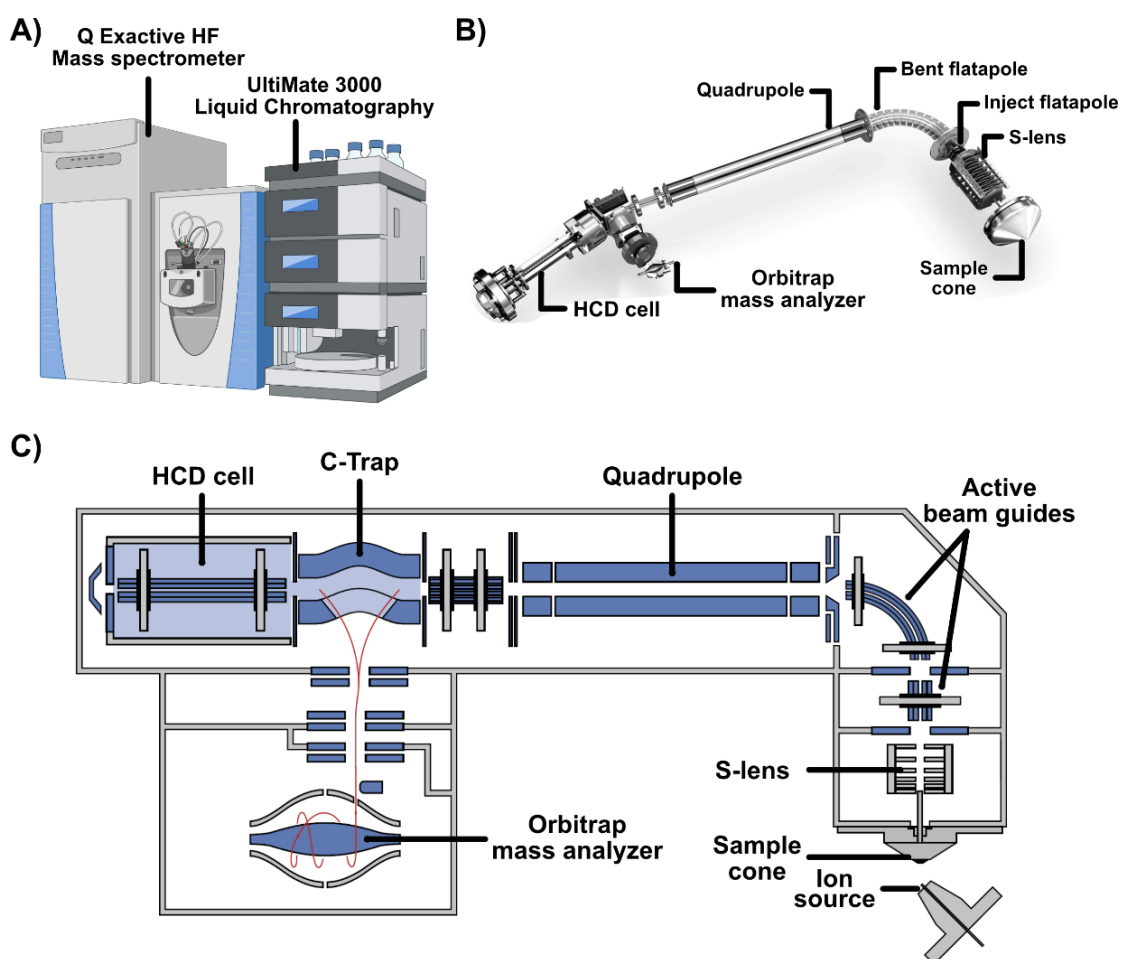


**Figure 3.7:** **A)** Schematic representation of the Q Exactive HF mass spectrometer (left) alongside the UltiMate 3000 LC-system (right) (created by using elements from BioRender.com [10]). **B)** Detailed construction layout of the Q Exactive HF, comprising a sample cone, followed by a stacked-ring ion guide (S-lens), a mass selection pre-filter integrated at the injection flatapole, an actively guiding bent flatapole, a segmented quadrupole, a high-energy collisional dissociation (HCD) cell, and ultimately an Orbitrap mass analyzer. (Image adapted from Scheltema *et al.* (2014) [226]). **C)** Schematic blueprint of the Q Exactive HF's construction. Ions generated at the ion source are introduced into the mass spectrometer *via* the sample cone. The ion beam is subsequently focused *via* the S-lens and directed through the bent flatapole by active beam guides, proceeding into the quadrupole. In MS mode, all ions are transferred through the quadrupole into the curved linear trap (C-trap) before being directed into the Orbitrap mass analyzer for the measurement of peptide ion masses (MS<sub>1</sub> spectrum). In tandem MS (MS/MS) mode, precursor ions are selected by the quadrupole mass filter and then guided into the HCD cell for collision-induced dissociation (CID). Fragment ions are then directed *via* the C-trap into the orbitrap mass analyzer for the measurement of fragment masses (MS/MS spectrum, schematic adapted from Thermo Fisher Scientific (2014) [227]).

The quadrupole comprises four cylindrical bars aligned in parallel and polarized crosswise (**Fig. 3.7. B**). Through the application of a high-frequency field to this rod system, ions can be selectively filtered based on their  $m/z$  ratio. This is achieved by employing both radio frequency and direct current voltages on the quadrupole rods, creating a stable trajectory for ions with specific  $m/z$  ratio. Ions with different  $m/z$  ratio collide with the quadrupole's rods, while those within the desired range pass through. Acting as a mass filter, the quadrupole permits the passage of ions of interest while excluding undesired ones. By adjusting radio frequency and direct current voltages, the quadrupole can selectively transmit ions of varying  $m/z$  ratio, facilitating the isolation and analysis of specific ions within complex mixtures [228].

A notable technique within this context is tandem MS (MS/MS), where several analyzers are coupled in tandem. MS/MS allows more comprehensive studies about the analyte, such as its fragmentation behavior or selectivity behavior. Typically, behind the quadrupole, a collision cell is integrated, such as the high collisional dissociation (HCD) cell found in the Q Exactive HF-mass spectrometer (**Fig. 3.7. B, C**). Following ion selection by the quadrupole, a defined number of ions are trapped in the C-trap before being directed as a package either to the Orbitrap mass analyzer (MS1 spectrum) or into the HCD cell for fragmentation and then to the Orbitrap mass analyzer (MS/MS spectrum). Within the HCD cell, inert gases like helium or nitrogen serve as collision agents, while electrodes generate an electric field to accelerate the ions. As ions collide with these gases, they absorb kinetic energy which is converted into internal energy within the ions. The internal energy raises the vibrational energy levels of the molecular bonds within the ions. Once the vibrational energy exceeds the bond dissociation energy, the bond breaks, resulting in fragmentation. This fragmentation process is called collision-induced dissociation (CID) or higher-energy collisional dissociation (HCD) [229]. The fragmented ions are then returned to the C-trap before injection into the Orbitrap for detection of fragment ion masses in form of a MS/MS spectrum (**Fig. 3.7. B, C**).

The Orbitrap mass analyzer stands as a pivotal element within mass spectrometers, renowned for its exceptional resolution and accuracy in determining ion masses [226]. Its functionality hinges on the principle of trapping and detecting ions within a high-frequency oscillating electric field. When ions enter the Orbitrap, they are subjected to an electrostatic field created by the central spindle electrode and the outer barrel electrode. This field forces the ions to spiral around the central electrode in a stable, elliptical trajectory, as they are electrostatically attracted to the inner electrode while their inertia balances this attraction [230].

The primary motion of the ions is radial, which helps determine their  $m/z$  ratio. In addition to this radial motion, the ions also exhibit an axial ( $z$ ) component in their movement, oscillating back and forth along the axis of the Orbitrap, creating a frequency in the  $z$ -direction (**Fig. 3.7. C**). This axial oscillation is a key feature of the Orbitrap's operation, with the frequency of this motion directly related to the ions'  $m/z$  ratio [231].

Both radial and axial motions contribute to the overall trajectory of the ions within the Orbitrap. However, it is the frequency of the axial ( $z$ ) oscillations that is primarily used to determine the  $m/z$

ratio of the ions. As the ions oscillate, they induce an image current in the outer electrode. This current is a time-dependent signal that contains information about the frequency of ion oscillations. The induced current is collected over a period, generating a time-domain signal. This signal represents changes in the current over time and is a sum of all the frequencies corresponding to different  $m/z$  ratios of the trapped ions [230].

Fourier transformation is applied to convert the time-domain signals into a frequency-domain signal. The process involves breaking down the time-domain signal into its constituent sine and cosine waves of varying frequencies. The frequency-domain signal consists of peaks at specific frequencies corresponding to the oscillation frequencies of the ions. Each peak's position is proportional to the  $m/z$  ratio of the ions. The frequencies obtained from the Fourier transform are converted into  $m/z$  ratios using calibration equations that account for the specific characteristics of the Orbitrap. The angular frequency is given by  $\omega = \sqrt{\frac{k}{m/z}}$ , where  $k$  is the force constant of the potential. The  $m/z$  ratios and their corresponding intensities (derived from the magnitude of the frequency peaks) are plotted to produce a mass spectrum. This spectrum shows the distribution of ions based on their  $m/z$  ratios, with peaks indicating the presence of specific ion species [230].

### 3.4.5.2. Protein cross-linking

Cross-linking covalently links protein sites that are in close proximity. Since these covalent bonds withstand denaturing conditions, they enable the analysis of protein complexes that would typically dissociate. The advent of peptide mass spectrometry propelled the development of cross-linking methods by promising efficient identification of cross-linked proteins and precise determination of the involved residues [232]. Knowledge of the actual cross-linking sites can help to improve structure determination, from entire proteins to smaller sections, known as 'peptide-level resolution' [233]. Cross-linked amino acids serve as distance constraints, aiding in determining the fold of proteins or domains. Advances in mass spectrometers, protocols, and algorithms have enabled cross-linking mass spectrometry (XL-MS) for analyzing multi-protein complexes, even those challenging to analyze by other methods [232]. XL-MS offers several strengths. It operates in solution, focusing on large structures like proteins and domains in their native and quaternary structures. Although sample heterogeneity may prolong analysis time and challenge data interpretation, the method remains versatile. Cross-linking has been successful in various environments, including bacterial lysates, living cell membranes, cell compartments, and isolated recombinant proteins. It is applicable to diverse structural motifs and enables the study of conformational changes, such as those induced by other molecules. As proteins undergo conformational changes, certain sites may come into closer proximity, allowing cross-linkers to capture these proximities that were not previously in range [234-237].

Proteins are typically cross-linked using a chemical reaction involving a cross-linker and amino acid side chains. Amino groups, thiols, and carboxylic acids are prime targets for cross-linking. Cross-linkers usually have two reactive groups separated by a spacer, targeting those primary

functional groups. Due to the high frequency of lysine in proteins, cross-linkers exclusively targeting amino groups are commonly used in XL-MS studies of multi-protein complexes, enhancing the chance of identifying cross-links [232].

In this study, we utilized two cross-linkers: disuccinimidyl sulfoxide (DSSO) and disuccinimidyl dibutric urea (DSBU), with DSBU being the primary cross-linker employed. Both DSSO and DSBU are MS-cleavable cross-linkers that feature an amine-reactive N-hydroxysuccinimide (NHS) ester at each end, connected by a 7-atom and 11-atom carbon spacer arm, respectively (**Fig. 3.8 A**) [238, 239]. NHS esters efficiently react with primary amine groups (-NH<sub>2</sub>), found in lysine residues and at the protein N-terminus, forming stable amide bonds. In this reaction, the lone pair of electrons on the nitrogen atom of the lysine amine group attacks the electrophilic carbon atom of the NHS ester, resulting in the formation of a stable amide bond (**Fig. 3.8 B**) [240].

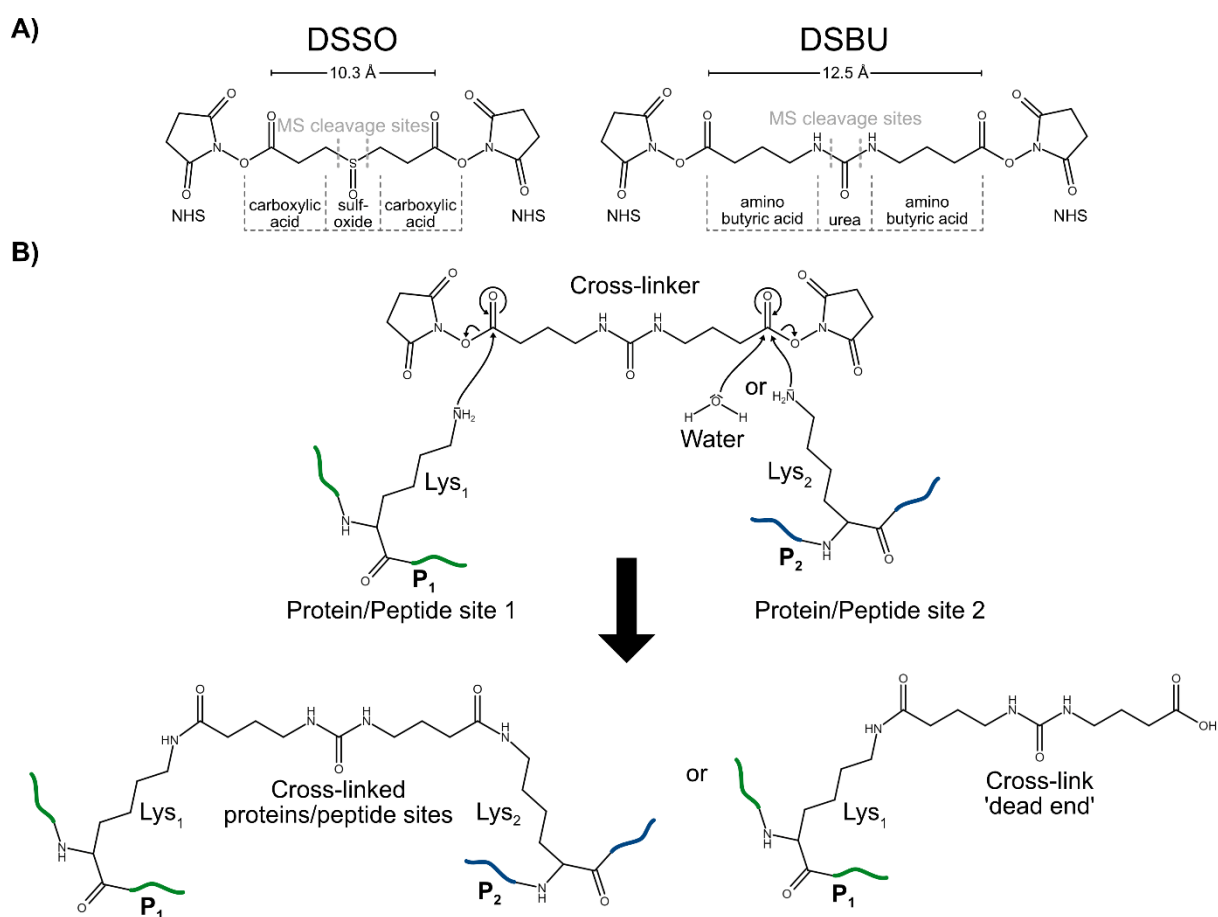


**Figure 3.8:** **A)** Chemical structures of disuccinimidyl sulfoxide (DSSO) and disuccinimidyl dibutric urea (DSBU). DSSO features a 10.3 Å spacer length, while DSBU possesses a 12.5 Å spacer length. Both cross-linkers contain N-hydroxysuccinimide (NHS) ester at each end, linked by a 7-atom (DSSO) and 11-atom (DSBU) carbon spacer arm. The central moieties, sulfoxide in DSSO and urea in DSBU, are susceptible to cleavage in the gas phase during MS/MS. **B)** Illustration of the amine-reactive NHS ester reaction, exemplified with DSBU. The reaction involves a nucleophilic attack by the lysine residue's amino group on the electrophilic center of the cross-linker. This yields various reaction products, including intermolecular cross-links or intramolecular cross-links, depending on whether the cross-linked sites originate from the same protein or different proteins. Additionally, 'dead-end' cross-links may occur, where only one side is connected to a lysine residue and the other is hydrolyzed. A particular instance of intramolecular cross-links is the intrapeptide cross-link, wherein both lysine residues are located on the same peptide.



Both cross-linkers incorporate linkers containing either a sulfoxide in DSSO or urea in DSBU, which can be cleaved in the gas phase during MS/MS using CID. The ability to selectively cleave cross-linked peptides during MS/MS facilitates targeted acquisition methods, aiding in peptide sequencing *via* traditional database search engines. Additionally, the cleavage of DSSO and DSBU during MS/MS produces distinctive ion doublets, allowing for searchability using database search engines like XlinkX v2.0, which we used in this work (**Appendix Fig. 24** and **Appendix Fig. 25**) [241, 242].

### **3.4.5.3. Chemical cross-linking and peptide purification**

For cross-linking, Stx1B constructs (25-252), Syb2 constructs (1-96), Munc18-1 constructs (2-594) and Munc13-MUN (859-1531,  $\Delta$ 1408-1453) were purified and brought into a HEPES buffer (20 mM HEPES, 125 mM NaCl, 2 mM DTT, pH 7.8) through gel filtration. The constructs were then concentrated to 5-40  $\mu$ M in 70  $\mu$ l (5-40  $\mu$ M for cross-linker experiments, 10  $\mu$ M for protein complex investigations). Freshly resuspended DSSO or DSBU (50 mM stock solution in anhydrous DMSO, Thermo Fisher Scientific) were added to a final concentration of 0.5 mM and incubated at room temperature for 20 minutes. This step was repeated, and after another 20 minutes, the reaction was quenched by the addition of Tris buffer (1 M, pH 8.0) to a final concentration of 20 mM and incubated at room temperature for 30 minutes. The reaction volume was then doubled by adding 100 mM ammonium bicarbonate (ABC) buffer, and both crystalline urea and DTT were added to final concentrations of 8 M and 5 mM, respectively, to denature and reduce the cross-linked proteins at 56°C for 30 minutes. The samples were then alkylated with 8 mM iodoacetamide for 30 minutes in the dark at room temperature. To initiate digestion of the cross-linked proteins, Lys-C (0.25  $\mu$ g/ $\mu$ l, 2  $\mu$ l) was added and samples were incubated for 4 hours at 37°C. Subsequently, the reaction solution was diluted to a final concentration of less than 2 M urea by adding 100 mM ABC, and the samples were further digested with trypsin (1  $\mu$ g/ $\mu$ l, 2  $\mu$ l) at 37°C overnight. The next day, the digestion reaction was stopped by adding formic acid to a final concentration of 1%, and the resulting peptide mixtures were desalted and purified using in-house-made C18-StageTips (Rappsilber *et al.*, 2007 [243]). The StageTip C18-membranes were activated with methanol, washed with Peptide Elution Buffer (50% acetonitrile, 1% formic acid), and twice with Peptide Washing Buffer (Milli-Q water, 1% formic acid). The samples were then loaded onto the StageTips, washed with Peptide Washing Buffer, eluted with Peptide Elution Buffer, collected in a glass vial, and dried under vacuum.

### **3.4.5.4. LC-MS data acquisition and XL-MS data analysis**

Dried peptides were reconstituted in 10  $\mu$ l of 0.05% trifluoroacetic acid (TFA) and 4% acetonitrile in water. Sample volumes of 1  $\mu$ g were loaded and analyzed using an Ultimate 3000 reversed-phase capillary nano liquid chromatography (LC) system connected to a Q Exactive HF mass spectrometer (Thermo Fisher Scientific). Samples were injected and concentrated on a trap column (PepMap100 C18, 3  $\mu$ m, 100 Å, 75  $\mu$ m i.d.  $\times$  2 cm, Thermo Fisher Scientific) equilibrated with

0.05% TFA in water. After switching the trap column inline, LC separations were performed on a capillary column (Acclaim PepMap100 C18, 2  $\mu\text{m}$ , 100  $\text{\AA}$ , 75  $\mu\text{m}$  i.d.  $\times$  50 cm, Thermo Fisher Scientific) at a flow rate of 300 nl/min. Mobile phase A contained 0.1% formic acid in water, and mobile phase B contained 0.1% formic acid in 80% acetonitrile / 20% water. The column was pre-equilibrated with 5% mobile phase B, followed by a gradient increase from 5% to 44% mobile phase B over 130 minutes. Mass spectra were acquired in data-dependent mode with a single MS survey scan (375-1575 m/z) at a resolution of 120000, and MS/MS scans of the 10 most intense precursor ions at a resolution of 60000. The dynamic exclusion time was set to 30 seconds. Automatic gain control was set to  $3 \times 10^6$  for MS scans and  $1 \times 10^5$  for MS/MS scans. Fragmentation was induced by higher-energy collisional dissociation (HCD) with stepped collision energies of 21 eV, 27 eV, and 33 eV. MS/MS spectra were recorded using a fixed first mass of 150 m/z. MS/MS spectra acquisition was triggered only for peptides with charge states of 4+ to 7+.

The acquired RAW files were converted into peak lists (.mgf format) using Proteome Discoverer (Thermo, version 2.1). The CID-MS2 spectra were deconvoluted with the add-on node MS2-Spectrum Processor using default settings. For the main search of the cross-linked peptides, the in-house developed algorithm XlinkX v2.0 was used (Liu *et al.*, 2017 [242]). The following search parameters were used: DSBU cross-linker mass: 196.0848 Da (short arm: 85.0528 Da, long arm: 111.0320 Da) or DSSO cross-linker mass: 158.00376 Da (short arm: 54.01056 Da, long arm: 85.98264 Da); MS1 precursor ion mass tolerance: 10 ppm; MS2 fragment ion mass tolerance: 20 ppm; fixed modifications: Cys carbamidomethylation; variable modification: Met oxidation; enzymatic digestion: Trypsin; allowed number of missed cleavages: 3. All MS2 spectra were searched against a concatenated target-decoy database generated based on the WT and mutant sequences of the proteins employed in the respective cross-linking experiment. Cross-links were reported at a 2% false discovery rate (FDR) based on a target decoy calculation strategy (Liu *et al.*, 2017 [242]). The detected cross-links were mapped on available PyMol structures.

### 3.5. Biological Methods

#### 3.5.1. Zebrafish maintenance and breeding <sup>(1)</sup>

Adult AB strain and *stx1b*<sup>WT/mut</sup> (sa17797) zebrafish (*Danio rerio*, Zebrafish International Resource Center) were housed in standard aquaculture conditions at 28.5 °C with a 14-hour light/10-hour dark cycle. Fertilized eggs were obtained through natural spawning, and embryos were cultured in embryo medium (1.5 mM HEPES, 17.4 mM NaCl, 0.21 mM KCl, 0.12 mM MgSO<sub>4</sub>, and 0.18 mM Ca(NO<sub>3</sub>)<sub>2</sub>, pH 7.6). The incubation was performed in a 28.5 °C incubator under a 14-hour light/10-hour dark cycle. All experiments utilized larvae aged 1–6 days post-fertilization (dpf). Ethical approval for zebrafish experiments was granted by the Norwegian Food Safety Authority (FOTS permit ID 15469 and 23935). All experiments were performed in compliance with the European Community Council Directive of November 2010 for Case and Use of Laboratory Animals (Directive 2010/63/EU) and ARRIVE guidelines.

(1) Conducted by Dr. Wietske van der Ent (Esguerra Lab, University of Oslo).

### 3.5.2. Generating transient transgenic zebrafish <sup>(1)</sup>

A minimal *Tol2* vector (*pTol2*) containing the human *stx1b* gene linked to mCherry *via* a self-cleaving p2a peptide, under control of the zebrafish Her4.1 promoter, was co-injected with transposase mRNA into fertilized eggs through microinjection at the single cell stage. The transposase protein, translated from the injected mRNA, catalyzes the excision of the transposon construct from the vector, facilitating its stable integration into the genome. Both the injected mRNA and transposase protein gradually degrade, and once transposase activity concludes, the *Tol2* insertions attain stability. Integration events take place during the early stages of embryonic development. Zebrafish larvae expressing the transferred human Stx1B construct were identified through fluorescence resulting from the co-expressed mCherry [244].

### 3.5.3. Tectal field recordings <sup>(2)</sup>

For local field potential (LFP) recordings, a glass electrode, connected to a high-impedance amplifier, was filled with artificial cerebrospinal fluid (124 mM NaCl, 2 mM KCl, 2 mM MgSO<sub>4</sub>, 2 mM CaCl<sub>2</sub>, 1.25 mM KH<sub>2</sub>PO<sub>4</sub>, 26 mM NaHCO<sub>3</sub>, 4 mM sucrose and 10 mM glucose). Subsequently, a larva was embedded in 2% low-melting-point agarose (Invitrogen (Waltham, USA)), and the glass electrode was carefully positioned in the optic tectum of the larva. Recordings were conducted in current clamp mode with low-pass filtering set below 1 kHz, high-pass filtering above 0.1 Hz, a digital gain of 10, and a sampling interval of 500  $\mu$ s. This was achieved using a MultiClamp 700B amplifier and Digidata 1550 digitizer, both obtained from Molecular Devices (San Jose, USA). Single recordings were conducted over a 20-minute duration, with spontaneous events considered when the amplitude surpassed three times the background noise. Spike analysis was performed using Clampfit 10.7 software (Molecular Devices).

Zebrafish selected for expression of human Stx1B originated from the same parental family each experiment, of which the uninjected offspring displays on average <1 event per 20-minute recording (data not shown). It is important to note that zebrafish studies and subsequent data analysis were not conducted in a blinded manner. The number of zebrafish for experimental conditions ranged from 15 to 27 individuals. It is essential to highlight that sample sizes were not predetermined in this study.

### 3.5.4. Touch response recording <sup>(2)</sup>

Touch response of the offspring of *stx1b*<sup>WT/mut</sup> zebrafish was tested in open-field recording of zebrafish larvae 3 days past fertilization (dpf) at room temperature. The larvae were individually placed into an embryo medium-filled 5 cm diameter petri dish and were gently touched on the tail using a blunt needle. Recordings were taken from three to five populations, each containing a minimum of 35 individual zebrafish larvae.

(1) Cloning was done by me, generation of transient zebrafish line was conducted by Dr. Wietske van der Ent (Esguerra Lab, University of Oslo).

(2) Conducted by Dr. Wietske van der Ent (Esguerra Lab, University of Oslo).

## 4. Results

### 4.1. E210K and L221P mutations affect helicity but not thermal stability of Stx1B

To investigate the impact of the point mutations in Stx1B<sup>E210K</sup> and Stx1B<sup>L221P</sup> on the overall protein structure and stability, circular dichroism (CD) spectroscopy experiments were conducted to examine the secondary structure and thermostability of the Stx1B constructs. The obtained spectrum of Stx1B wild-type (WT) displayed a characteristic pattern indicative of an  $\alpha$ -helical protein, with minima at wavelengths 208 nm and 222 nm (**Fig. 4.1 A**). This aligns with crystal and predicted structures, confirming Stx1B as primarily an  $\alpha$ -helical protein. Stx1B<sup>E210K</sup> and Stx1B<sup>L221P</sup> exhibited typical spectra for  $\alpha$ -helical proteins as well, indicating that the overall secondary structure is unaffected by either point mutation. Interestingly, the spectrum of Stx1B<sup>E210K</sup> showed a slightly enhanced helicity, while Stx1B<sup>L221P</sup> exhibited a slightly reduced helicity compared to Stx1B<sup>WT</sup>, indicated by increased minima for Stx1B<sup>E210K</sup> and reduced minima for Stx1B<sup>L221P</sup> (**Fig. 4.1 A**).

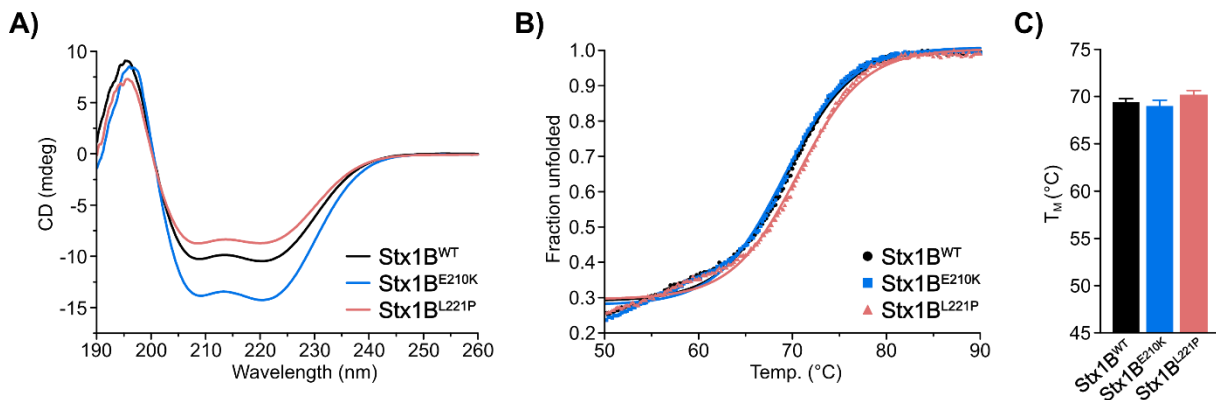


**Figure 4.1:** CD-spectroscopy investigation of Stx1B<sup>WT</sup> (black), Stx1B<sup>E210K</sup> (blue) and Stx1B<sup>L221P</sup> (salmon). 20  $\mu$ M of each protein was used. **A)** Far-UV CD spectra depict dominantly helical content in Stx1B<sup>WT</sup>, Stx1B<sup>E210K</sup>, and Stx1B<sup>L221P</sup>. Stx1B<sup>L221P</sup> exhibits reduced helicity, while Stx1B<sup>E210K</sup> shows increased helicity compared to Stx1B<sup>WT</sup>. **B)** CD melting curves of Stx1B<sup>WT</sup>, Stx1B<sup>E210K</sup> and Stx1B<sup>L221P</sup> recorded at 222 nm, normalized to the maximum value and fitted according to the sigmoidal Boltzmann function:  $f(x) = \frac{A_1 - A_2}{1 + e^{(x-x_0)/d_x}} + A_2$ . Turning point of the function represents the melting temperatures of the examined proteins. WT and mutants display a similar unfolding pattern (full fraction unfold spectra in **Appendix Fig. 8 A**). **C)** Bar diagram of melting temperatures from Stx1B<sup>WT</sup> and mutants ( $\pm$  SEM,  $n = 3$ ). All three proteins exhibit similar melting temperatures with no significant differences.

The cause for this might be attributed to the characteristics of the substituted side chains. Lysine, recognized for its high helix-forming propensity, has the potential to act as a helix enhancer, increasing the stability of  $\alpha$ -helical structures [245]. This is attributed to its amino head group's capability to form hydrogen bonds with the carbonyl oxygen of the protein backbone, thus contributing to the stabilization of the helical conformation. Furthermore, in accordance with the side-chain interactions observed in the helical wheel pattern, where residues at positions [i+3] and [i+4] align on the same side of the helix as the residue at position [i], promoting helix stability, we observe that three positions behind the introduced positively charged lysine in Stx1B<sup>E210K</sup> ([i+3]), a negatively charged aspartic acid is present (**Appendix Fig. 9**) [246]. Together, they can form an additional stabilizing interaction, not present in the wild-type protein.

Conversely, proline is known for its feature to disrupt helical structures and is commonly referred to as a helix breaker [245]. Proline disrupts a helix by either causing a break or introducing a kink. This is attributed to its inability to donate an amide hydrogen bond (due to the absence of the amide hydrogen achieved by the loop back of its propyl side chain back to the amide nitrogen). Furthermore, its sidechain causes steric interference with the backbone of the preceding turn. Within a helix, this interference results in a bend of approximately 30° in the backbone, disrupting the helical configuration (**Appendix Fig. 10**) [247, 248]. As a consequence, Stx1B<sup>L221P</sup> exhibits reduced helicity in CD spectroscopy.

Regarding protein stability, no significant differences in the thermostability were observed among the individual constructs. All mutants and the WT exhibited similar melting curves in the fraction unfold spectrum, revealing only minor differences in the melting temperatures ( $T_M$ ) with Stx1B<sup>WT</sup>:  $69.42 \pm 0.31$  °C, Stx1B<sup>E210K</sup>:  $69.08 \pm 0.54$  °C and Stx1B<sup>L221P</sup>:  $70.56 \pm 0.49$  °C (**Fig. 4.1 B, C**). This shows that the introduction of the different mutations does affect the helical content of Stx1B, but has no impact on the overall protein stability.

#### 4.2. Stx1B<sup>L221P</sup> diminishes stability and helicity of the SNARE complex

Given that both point mutations are situated in the SNARE motif, we aimed to assess whether their introduction has any impact on SNARE complex formation. The residues E210 and L221 are positioned between the layers -5 and -4 and the layers -2 and -1 respectively, and do not directly contribute to the formation of the hydrophobic core of the SNARE complex (**Fig. 1.3 A** and **Fig. 4.4 A**). However, introducing a residue with a different charge (Glu (-) → Lys (+)), and particularly a structurally influential residue like proline, could potentially disrupt the proper assembly of a stable SNARE complex. To examine the stability and folding of the mutant SNARE complexes, we analyzed the Stx1B<sup>SNARE-WT</sup>, Stx1B<sup>SNARE-E210K</sup> and Stx1B<sup>SNARE-L221P</sup> constructs (179-262) *in vitro* using a SNARE complex reconstitution assay (detailed in **Chapter 3.3.5**).

While both Stx1B<sup>SNARE-WT</sup> and Stx1B<sup>SNARE-E210K</sup> formed SDS-stable SNARE complexes with Syb2 and SNAP-25, displaying comparable band intensities, the SDS-stable SNARE complex formation ability of Stx1B<sup>SNARE-L221P</sup> was significantly reduced, as evidenced by a substantial decrease in band intensity on SDS-PAGE (**Fig. 4.2 A**). Notably, only Stx1B<sup>SNARE-WT</sup> exhibited a strong band indicating the formation of the t-SNARE complex with SNAP-25 (band at ~37 kDa). In contrast, both mutants, Stx1B<sup>SNARE-E210K</sup> and Stx1B<sup>SNARE-L221P</sup>, showed significantly weaker bands. Furthermore, boiling led to the breakdown of all complexes into their individual components (**Fig. 4.2 B**).

To further investigate the reduced SNARE complex formation ability of the L221P mutant, we conducted CD-spectroscopy experiments comparing the wild-type and mutant SNARE complexes. Consistently, the inability of Stx1B<sup>SNARE-L221P</sup> to form a stable SNARE complex was evident in the CD spectra. All three SNARE complexes predominantly displayed an  $\alpha$ -helical structure, with the helicity of the SNARE complex formed with Stx1B<sup>SNARE-E210K</sup> being more pronounced and that of

## Results

the SNARE complex formed with Stx1B<sup>SNARE-L221P</sup> being less pronounced compared to the wild-type SNARE complex, likely due to the reasons mentioned earlier (**Fig. 4.3 A**).

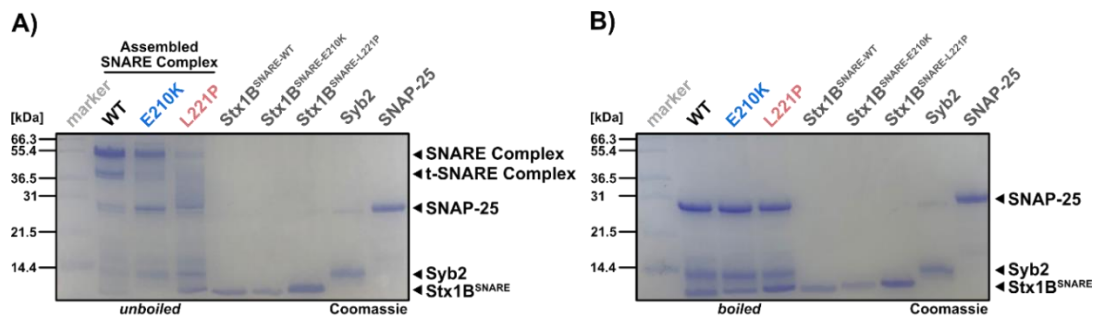


**Figure 4.2:** **A)** Coomassie-stained SDS-PAGEs of assembled SNARE complexes using Stx1B<sup>SNARE-WT</sup>, Stx1B<sup>SNARE-E210K</sup> and Stx1B<sup>SNARE-L221P</sup> along with Syb2 and SNAP-25. Both Stx1B<sup>SNARE-WT</sup> and Stx1B<sup>SNARE-E210K</sup> formed SDS-stable SNARE complexes, while the SNARE complex formation with Stx1B<sup>SNARE-L221P</sup> was diminished. Furthermore, only the wild-type displayed a strong band for the t-SNARE complex, while the band intensity was significantly reduced for both mutants. All samples were not boiled prior to loading on the gel. (Unmodified full-size Coomassie-stained SDS-PAGE in **Appendix Fig. 11**). **B)** For control, all samples were boiled before gel loading. Boiling caused the SDS-stable SNARE complex to dissociate, revealing bands corresponding to the individual components.

The thermal stability of the E210K SNARE complex showed a slight but not significant increase ( $T_M = 83.81 \pm 0.46$  °C) while it was drastically reduced for the L221P SNARE complex ( $T_M = 75.72 \pm 0.86$  °C) compared to the WT SNARE complex ( $T_M = 83.54 \pm 0.56$  °C, **Fig. 4.3 B**, **C**). Collectively, these results indicate that the E210K mutation within Stx1B's SNARE motif does not impede proper SNARE complex formation. In contrast, the Stx1B L221P mutation significantly impacts both the formation and stability of the complex.

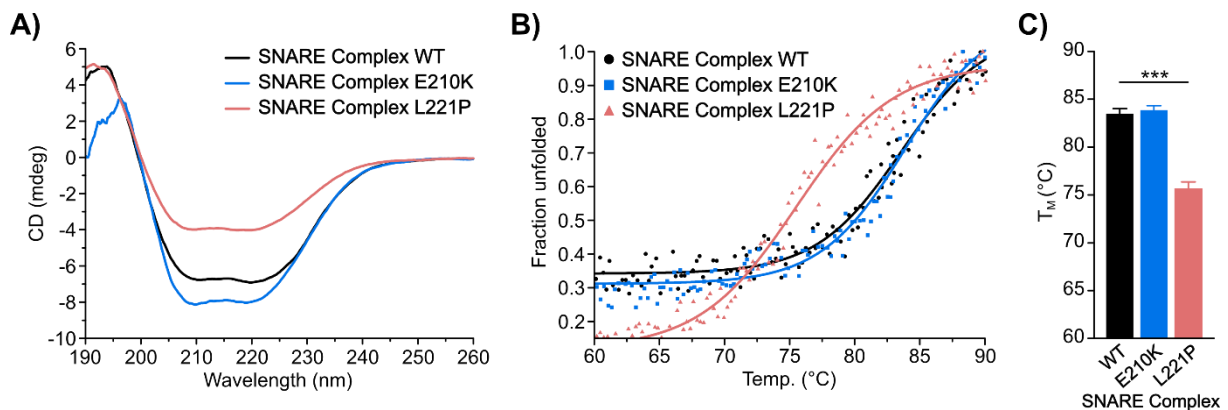


**Figure 4.3:** CD-spectroscopy investigation of SNARE complexes formed with SNAP-25, Syb2 and Stx1B<sup>SNARE-WT</sup>, Stx1B<sup>SNARE-E210K</sup> or Stx1B<sup>SNARE-L221P</sup>. 10  $\mu$ M of each SNARE complex was used for the measurements. **A)** Far-UV CD spectra depict dominantly helical content in SNARE complex WT (black), SNARE complex E210K (blue), and SNARE complex L221P (salmon). SNARE complex L221P shows a reduced helical content, while SNARE complex E210K reveals an increased helicity compared to SNARE complex WT. **B)** CD melting curves of SNARE complex WT, SNARE complex E210K and SNARE complex L221P recorded at 222 nm, normalized to the maximum value and fitted according to the sigmoidal Boltzmann function:  $f(x) = \frac{A_1 - A_2}{1 + e^{(x-x_0)/dx}} + A_2$ . Turning point of the function represents the melting temperatures of the examined proteins (full fraction unfold spectra in **Appendix Fig. 8 B**). **C)** Bar diagram of melting temperatures from SNARE complex WT and mutants ( $\pm$  SEM,  $n = 3$ ). While SNARE complex WT and SNARE complex E210K display similar melting temperatures, the thermal stability of SNARE complex L221P is drastically reduced (t-test, \*\*\* $p < 0.001$ , two-tailed).

The reason might lie in the layer composition of the SNARE complex and the helix-breaking characteristics of the proline residue (**Fig. 1.3 A**), **Fig. 4.4 A**) and **Appendix Fig. 10 A**, **B**)). While the zero layer achieves stability through ionic interactions between charged glutamine and arginine residues, the adjacent layers are upheld by hydrophobic interactions, enabling a water-tight seal to isolate the ionic interaction of the zero layer from the surrounding solvent (**Fig. 1.3 B**)) [44, 45]. The introduction of proline directly next to the -1 layer may disrupt the proper formation of this layer, as the  $\alpha$ -helical configuration is disturbed (**Fig. 4.4 B**) and **Appendix Fig. 10 B**)). This could compromise both the water-tight seal, exposing the zero layer to the solvent and diminishing its interaction, and the complete zipping of the SNARE complex through the zero layer. As a result, it could ultimately impede the successful formation of a stable complex.

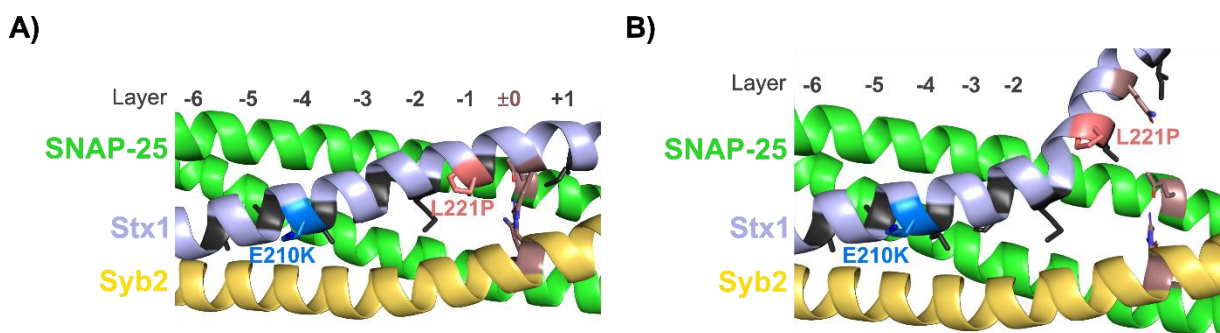


**Figure 4.4:** **A)** Section of the SNARE complex comprising of Syb2, SNAP-25 and Stx1A, showing the layers -6 to +1 and the corresponding locations of the mutations E210K and L221P on the Stx1B SNARE motif, which in Stx1A are E211K and L222P (PDB: 3HD7). Neither of the mutated residues is part of the of the hydrophobic core; instead, they point outwards. **B)** A potential model suggests how the L221P mutation could hinder the formation of a functional SNARE complex due to the properties of the introduced proline. Proline can disrupt hydrogen bonding along an  $\alpha$ -helix, potentially creating a bend in the helical structure or even completely disrupting it just after layer -2. This could prevent proper continuation of the zipping process, thereby preventing the formation of subsequent layers.

### 4.3. FRET-based Vesicle fusion assay using $\Delta$ N-SNARE complexes to study the effects of Stx1B E210K and L221P mutations <sup>(1)</sup>

#### 4.3.1. Stx1B L221P mutation significantly impairs vesicle membrane fusion

To assess the potential impact of the diminished SNARE complex formation ability caused by Stx1B<sup>L221P</sup> on membrane fusion and neurotransmitter release, we conducted a liposome fusion assay. This assay aimed to mimic the mechanism and environment of synaptic vesicle fusion, including factors like membrane curvature and charge repulsion between opposing membranes. For that, we purified the whole C-terminal part of Stx1B, encompassing the SNARE motif, the JMD and TMR (Stx1B<sup>SNARE-TMR</sup>, 189-288), allowing the Stx1B constructs to anchor into the vesicle membrane. Due to the involvement of the JMD and especially the TMR, the purification of these Stx1B membrane protein constructs posed challenges. A detailed description of the purification can be found in **Chapter 3.3.2.3**.

<sup>(1)</sup> Protein expression and purification was done by me. Vesicle fusion assay experiments were carried out together with Dr. Agata Witkowska (Haucke Lab, FMP Berlin).

In short, Stx1B<sup>SNARE-TMR</sup> wild-type and mutant constructs were expressed in *E. coli* cells and subsequently lysed by sonication under the addition of urea and sodium cholate as detergent to linearize the proteins and prevent aggregation while maintaining solubility. The resulting lysate was then ultra-centrifuged and the filtered supernatant was purified via Ni-NTA affinity chromatography (**Appendix Fig. 4 A**). All buffers used in this purification process were supplemented with urea and sodium cholate. The eluted proteins underwent stepwise dialysis against a HEPES buffer containing 1% CHAPS and with decreasing urea concentrations and were treated with thrombin to cleave the His-tag (**Appendix Fig. 4 B**). The digested proteins were then further purified by ion-exchange chromatography with a steep NaCl gradient to ensure efficient elution of the whole desired protein sample (**Appendix Fig. 4 C, D**). This approach allowed for a highly concentrated elution sample, eliminating the need for additional concentration processes that could potentially compromise the integrity of the membrane proteins, which are not conducive to concentration in conventional concentrators.

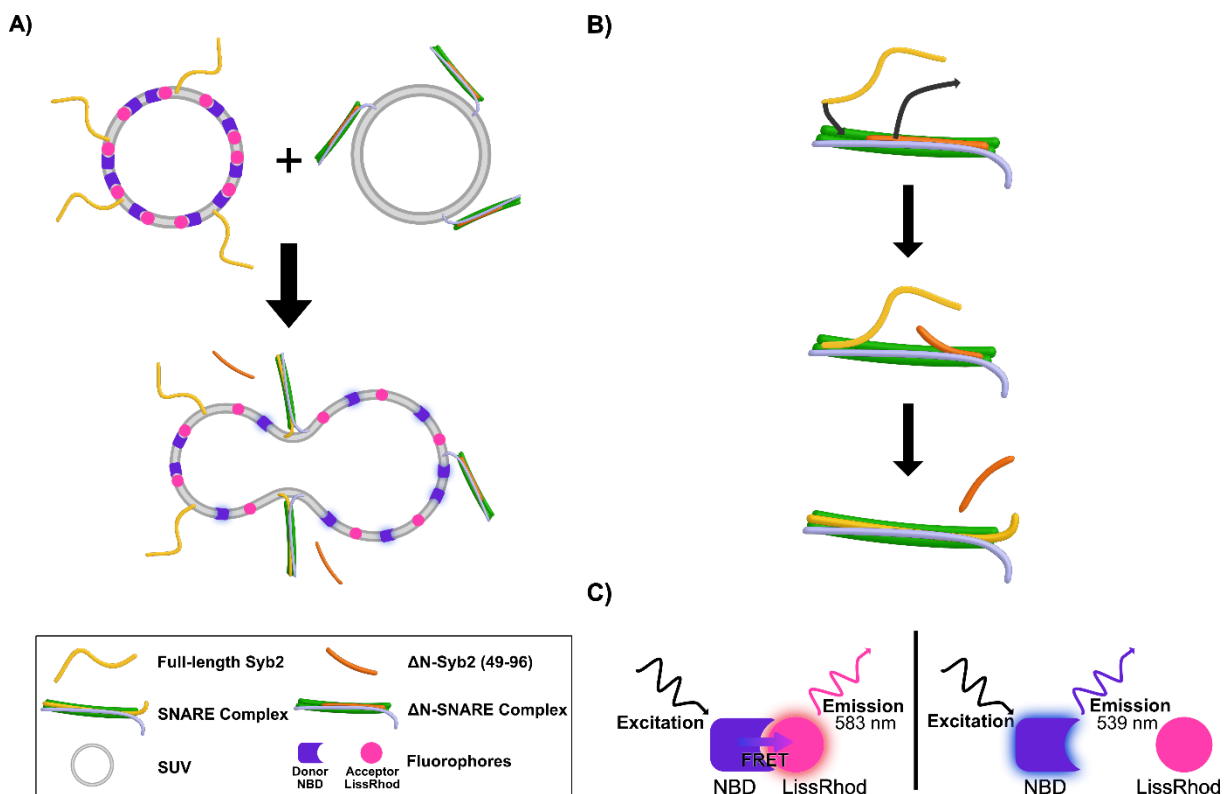


**Figure 4.5:** **A)** Schematic representation of the vesicle fusion assay.  $\Delta$ N-SNARE complexes are anchored into the membrane of small unilamellar vesicles (SUVs). Upon conflation with SUVs covered with membrane anchored full-length Syb2 as well FRET labels, the SNARE complex is formed, driving vesicle fusion. As membrane fusion occurs, the fluorophores get diluted, causing an increase in distance between the FRET labels. This results in an increase in the fluorescence emission of the donor, which is detected. **B)** Schematic overview of the transition from a  $\Delta$ N-SNARE complex to a fully formed SNARE complex. Full-length Syb2 zippers into the  $\Delta$ N-SNARE complex in the N- to C-terminal direction, replacing the  $\Delta$ N-Syb2 and thereby forming the complete SNARE complex. **C)** Upon excitation of the donor fluorophore, FRET occurs when the donor and acceptor fluorophores are in close proximity. This leads to the quenching of the emission fluorescence of the donor, while the acceptor emits fluorescence. However, with membrane fusion and subsequent dilution, the distance between the FRET labels widens, hindering FRET. Consequently, only the donor emits fluorescence upon excitation.



Together with SNAP-25 and a  $\Delta N$ -Syb2 construct (Syb2, 49-96), a pre-formed  $\Delta N$ -SNARE complex (Stx1B<sup>SNARE-TMR</sup>:SNAP-25: $\Delta N$ -Syb2) was generated and anchored into the vesicle membrane of small unilamellar vesicles (SUVs) through Stx1B's TMR (**Fig. 4.5 A**). Full-length Syb2 was anchored through its TMR into the membrane of other SUVs (**Fig. 4.5 A**). As the opposing SUVs come into close vicinity, a complete SNARE complex is formed, facilitated by the replacement of the  $\Delta N$ -Syb2 construct with its full-length counterpart, through N- to C-terminal zippering, driving the membrane fusion (**Fig. 4.5 B**) [193, 249].

To monitor vesicle fusion, we utilized a negative FRET lipid mixing assay. Both the donor fluorophore, NBD-PE, and the acceptor fluorophore, LissRhod-PE, were situated on the same initial vesicle membrane, incorporating the full-length Syb2 [193, 249]. At excitation wavelength for NBD and close proximity to the acceptor, FRET occurs between the two labels, resulting in the quenching of NBD's fluorescence emission (**Fig. 4.5 C**) [193]. However, upon membrane fusion, the fluorophores are diluted as a result of the net addition of unlabeled lipids. This causes an increase in the average distance between the donor and acceptor fluorophores, resulting in a decrease in FRET. Consequently, there is an increase in the emission fluorescence intensity of NBD (**Fig. 4.5 A, C**). Monitoring this fluorescence enables the tracking and quantification of fusion events between vesicles, providing valuable insights into the membrane fusion process.

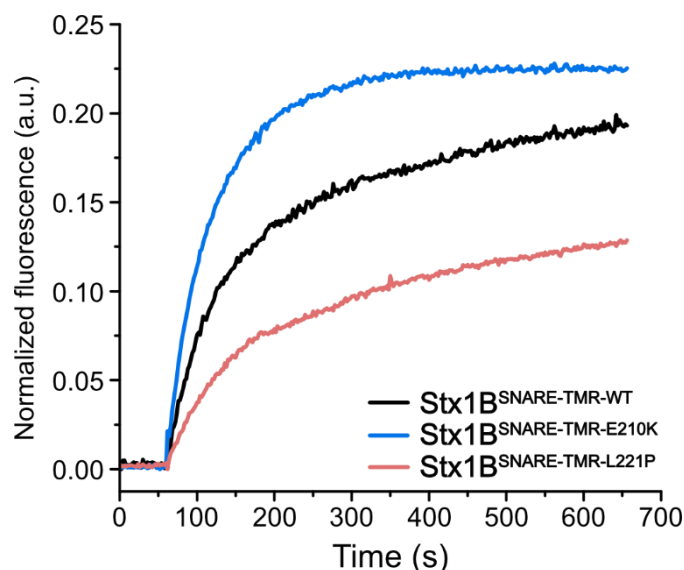


**Figure 4.6:** Representative fluorescence diagram, monitoring vesicle fusion with Stx1B<sup>SNARE-TMR-WT</sup>, Stx1B<sup>SNARE-TMR-E210K</sup> and Stx1B<sup>SNARE-TMR-L221P</sup> through lipid mixing using FRET, normalized to individual maximum values after addition of Triton X-100 (**Appendix Fig. 12**). The E210K mutant generally exhibited a rapid increase in fluorescence, often reaching the plateau faster than the wild-type construct. The L221P mutant showed the slowest fluorescence increase.

For the first 60 s, only SUVs with full-length Syb2 and fluorophores were held in the measurement cuvette under constant stirring to assess baseline fluorescence. After 60 s, SUVs with the pre-formed  $\Delta N$ -SNARE complex including Stx1B<sup>SNARE-TMR-WT</sup>, Stx1B<sup>SNARE-TMR-E210K</sup> or Stx1B<sup>SNARE-TMR-L221P</sup> were added into the measurement cuvette, starting the vesicle fusion (**Appendix Fig. 12**). The increase of the donor fluorescence emission was monitored and at the end of the measurements,

Triton X-100 was added to dissolve all vesicles and ultimately terminating the vesicle fusion assay. The dissolution and release of the components resulted in a sudden increase of the measured fluorescence, indicating profound dequenching (**Appendix Fig. 12**).

In our analysis, we focused on the 600-second time frame immediately following the addition of SUVs with the pre-formed  $\Delta$ N-SNARE complex. For comparison of the data, we normalized the fluorescence intensity of each run to its maximum value after Triton X-100 addition. As suspected, the fluorescence intensity increase was significantly reduced for the measurements with vesicles incorporating Stx1B<sup>SNARE-TMR-L221P</sup>, strongly suggesting a reduced vesicle fusion rate due to the impaired SNARE complex formation capability caused by the L221P mutation within the SNARE motif (**Fig. 4.6**). Surprisingly, the fluorescence intensity increase was significantly higher in the measurements with vesicles incorporating Stx1B<sup>SNARE-TMR-E210K</sup>, even surpassing those with Stx1B<sup>SNARE-TMR-WT</sup> vesicles. This suggests that the vesicle fusion rate was accelerated by the E210K mutation.

The reason for this acceleration might lie in an increased clustering of the pre-formed  $\Delta$ N-SNARE complexes due to the additional positive charge introduced by the E210K mutation in Stx1B. This additional positive charge might enhance binding to the PIP<sub>2</sub> microdomains on the vesicle membrane surface, bringing it closer to  $\Delta$ N SNARE complex clusters. Along with Stx1B's JMD, it may also mask the negative charge of the membrane. This masking effect could reduce repulsive forces between the two membranes, making it easier for them to come together and fuse [114, 250, 251].

### 4.3.2. Differential effects Stx1B E210K and L221P mutations on vesicle membrane fusion kinetics

To gain quantitative insights into vesicle fusion kinetics, we analyzed data from 600 seconds after adding SUVs with the pre-formed  $\Delta$ N SNARE complex. This allowed us to compare the time needed to reach half-maximal fluorescence intensity and the initial fusion speed when all vesicles are unfused and have maximum binding potential (**Fig. 4.7**). Since fluorescence intensity corresponds to vesicle fusion, reaching half-maximal fluorescence means half-maximal vesicle fusion within the reaction time. We compared the average time taken by wild-type and mutant SNARE complexes to reach half-maximal fluorescence to determine the fusion rate (**Fig. 4.7 A, B**)).

Our measurements showed that vesicle fusion with the E210K mutation occurred the fastest, with an average half-maximal fusion time of 49 seconds. Vesicle fusion with the L221P mutation was the slowest, taking 85 seconds, almost twice as long (**Fig. 4.7 B**)). The wild-type construct had an average half-maximal fusion time of 61 seconds, not much slower than E210K but significantly faster than L221P (**Fig. 4.7 B**)). While wild-type data were somewhat similar to E210K, there was less overlap with L221P data. The wild-type showed greater variation in the upper quartile, while E210K showed large variations in both quartiles. This suggests different  $\Delta$ N SNARE complex forms in the wild-type, some causing significantly faster or slower fusion rates, with a lower limit of 37

seconds. E210K surpassed this limit. L221P had less variation and longer fusion times compared to wild-type and E210K.

These findings suggest that the L221P mutation hinders vesicle fusion, while E210K might enhance it, as it required less time to reach half-maximal fusion compared to wild-type, though the difference was not statistically significant.

To determine the fusion velocity at the initiation of the reaction, we conducted a data fit and calculated the derivative to obtain the slope within the starting point (**Fig. 4.7 C), D)**). The starting point was set at the 62-second mark to mitigate human error, as the reaction was manually initiated by adding SUVs with full-length Syb2. While this addition was intended to occur at the 60-second mark after the initial content leakage control, there might be a slight variation in the actual starting time, given the manual initiation of the reactions.

As fit function we used:

$$f(x) = \frac{a*(x-t)}{b+x-t} \quad (4)$$

Since it is a fractional rational function, the quotient rule must be applied:

$$f(x) = \frac{u(x)}{v(x)} \quad (5)$$

$$f'(x) = \frac{u'(x)*v(x)-u(x)*v'(x)}{(v(x))^2} \quad (6)$$

Therefore:

$$f'(x) = \frac{a*(b+x-t)-a*(x-t)*1}{(b+x-t)^2} = \frac{a*b+a*(x-t)-a*(x-t)}{(b+x-t)^2} \quad (7)$$

$$f'(x) = \frac{a*b}{(b+x-t)^2} \quad (8)$$

Since  $t = 62$  s (set starting point of the reaction) and we want to calculate the slope for each reaction at the point of  $x = 62$  s the equation simplifies to:

$$f'(x) = \frac{a*b}{b^2} = \frac{a}{b} \quad (9)$$

Consistent with the half-maximal fusion rate data, the L221P mutant showed a significantly lower average slope of 0.0102 a.u./s compared to both the wild-type and the E210K mutant. Notably, the data exhibited minimal variation, indicating precise measurements around the median. The E210K mutant had the highest average slope of 0.0241 a.u./s but also displayed the greatest dispersion, particularly in the upper quartile, suggesting the potential for very high vesicle fusion velocity. The wild-type showed an average slope of 0.0178 a.u./s with moderate dispersion of the data points, overlapping substantially with the E210K values and only slightly with the L221P mutant

## Results

(**Fig. 4.7 D**)). This suggests that the initial fusion velocity may be influenced by the mutations within the Stx1B SNARE motif. The L221P mutation appears to decrease the velocity, while the E210K mutation seems to increase it.

Taken together, the vesicle fusion assay confirmed the initial observations, strongly indicating that the L221P mutation within the SNARE motif of Stx1B significantly impedes vesicle fusion, likely due to its reduced capacity for SNARE complex formation. This consistent trend was evident across repeated runs, with minimal variation in the data.

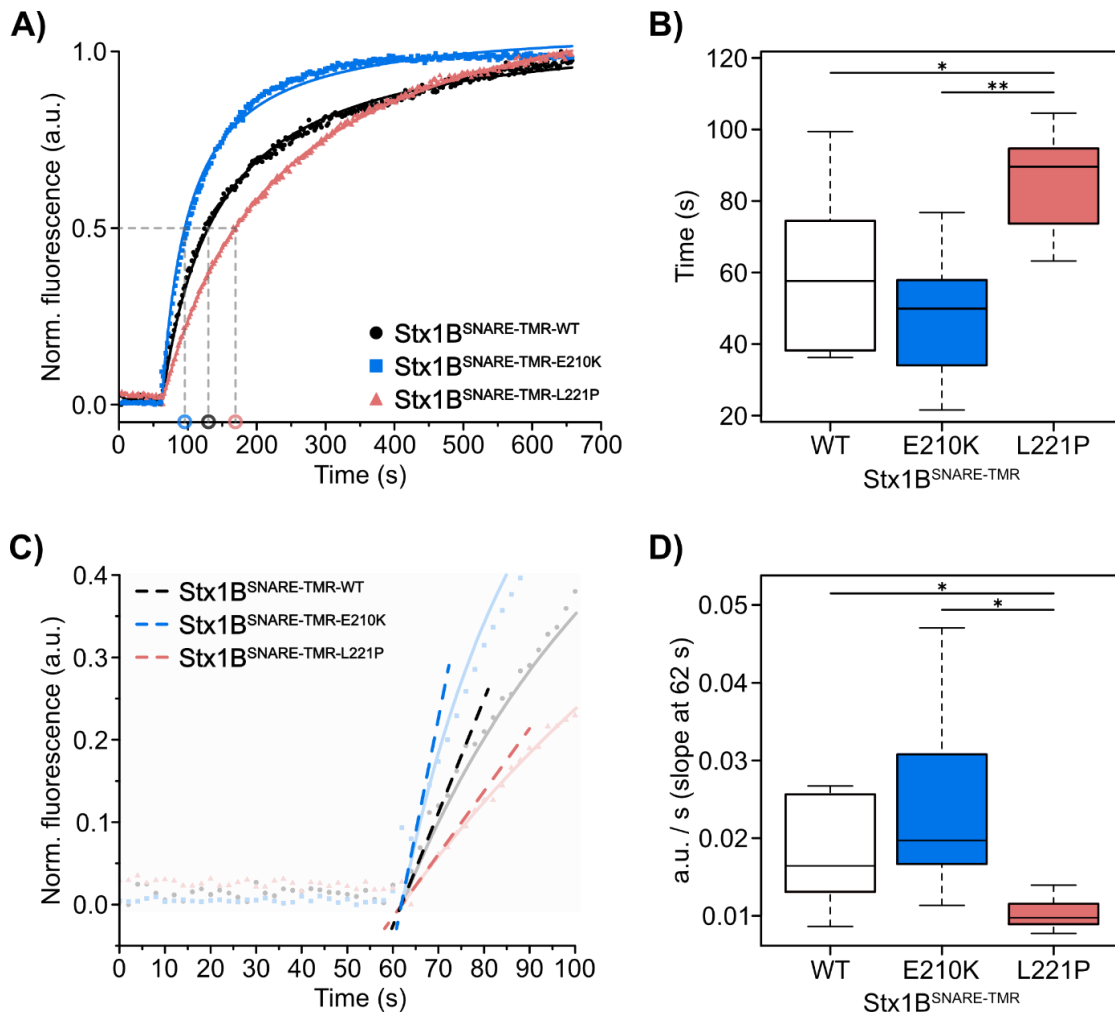


**Figure 4.7:** Quantification of vesicle fusion assay. **A)** Representative normalized fluorescence diagram of Stx1B<sup>SNARE-TMR-WT</sup>, Stx1B<sup>SNARE-TMR-E210K</sup> and Stx1B<sup>SNARE-TMR-L221P</sup>. Normalized fluorescence diagrams were fitted using the function:  $y = \frac{a*(x-t)}{b+(x-t)}$ ,  $t = 62$ , and the time required to reach half-maximum fluorescence ( $y = 0.5$ , half-maximum fusion) was calculated. **B)** Box plot of half-maximum fusion time shows that Stx1B<sup>SNARE-TMR-L221P</sup> ( $n = 7$ ) reaches half-maximum fusion significantly slower but exhibits lower data dispersion compared to Stx1B<sup>SNARE-TMR-WT</sup> ( $n = 6$ , t-test, \* $p < 0.05$ , two-tailed, statistical normal distribution was verified by Shapiro-Wilk-test) and Stx1B<sup>SNARE-TMR-E210K</sup> ( $n = 9$ , t-test, \*\* $p < 0.01$ , two-tailed, statistical normal distribution was verified by Shapiro-Wilk-test). **C)** To calculate the initial fusion velocity, the fitted curves were differentiated at the 62-second point ( $f'(x) = \frac{a}{b}$ ). **D)** Box plot of the initial fusion velocity reveals a significantly lower initial fusion velocity and small data dispersion for Stx1B<sup>SNARE-TMR-L221P</sup> (compared to Stx1B<sup>SNARE-TMR-WT</sup> (Welch-test, \* $p < 0.05$ ) and Stx1B<sup>SNARE-TMR-E210K</sup> (Welch-test, \* $p < 0.05$ )).

Interestingly, the E210K mutation increased both the half-maximum vesicle fusion and fusion velocity, suggesting a potential gain-of-function effect. This might be due to the mutation's additional

negative charge, which could enhance coordination and clustering on the vesicle membrane. Furthermore, both mutants amplify certain effects observed in the wild-type, either accelerating (E210K) or decelerating (L221P) vesicle fusion. This is indicated by the wide variation in data points for the wild-type construct, suggesting the presence of multiple species capable of either fast or slow vesicle fusion.

#### 4.4. Characterizing the interaction of Stx1B<sup>E210K</sup> and Stx1B<sup>L221P</sup> with Munc18-1

##### 4.4.1. Stx1B<sup>E210K</sup> and Stx1B<sup>L221P</sup> show reduced affinity to Munc18-1, rescued by Stx1B<sup>E210K,K82E</sup>

While Stx1B<sup>L221P</sup> clearly reduces the formation and the stability of the SNARE complex, as well as vesicle fusion, Stx1B<sup>E210K</sup> does not appear to significantly affect these characteristics. Only a subtle increase in the vesicle fusion capacity in our assay was observed, which could suggest a potential gain-of-function effect, influencing the delicate balance of the neurotransmitter release mechanism within the synapse. Yet, this effect was moderate compared to the wild-type and may not have a significant physiological influence. Therefore, the physiological effects of Stx1B<sup>E210K</sup> probably arise from another molecular mechanism.

Given that Munc18-1 is the primary binding partner of Stx1B, we decided to examine their interaction. However, we anticipated minimal impact by the mutants since both mutations are located away from the direct binding interface of these proteins (based on the crystal structure of the Stx1A:Munc18-1 complex (PDB: 3C98) [140].

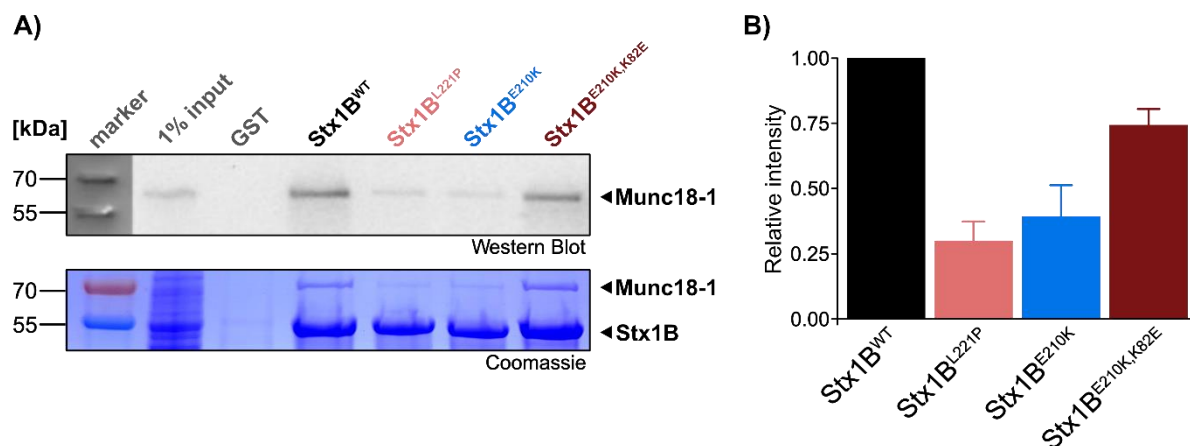


**Figure 4.8:** **A)** Pull-down assay using Stx1B wild-type and mutant constructs coupled to a GST-tag as a bait for Munc18-1 within mouse brain lysate. The pull-down bait and prey proteins were run on SDS-PAGE (lower section) and Munc18-1 was detected by western blotting using Munc18-1 antibody (upper section, full-size Coomassie-stained SDS-PAGE and western blot in **Appendix Fig. 13**). **B)** Quantification of western blots from pull-down experiments using ImageJ. Intensities were normalized to the band intensities of Stx1B<sup>WT</sup> ( $\pm$  SEM, n = 3). While Stx1B<sup>E210K</sup> and Stx1B<sup>L221P</sup> show clearly reduced binding towards Munc18-1, the rescue mutations Stx1B<sup>E210K,K82E</sup> displayed a band intensity almost at wild-type level.

First, we conducted GST-pull down experiments, expressing and purifying the Stx1B constructs fused with a GST-tag and coupled to beads as bait, and incubated them in a mouse brain lysate to assess their interaction with Munc18-1 as the prey (detailed in **Chapter 3.3.8**). As a negative control,

only GST was coupled to the beads. The results were identified through SDS-PAGE and confirmed by western blotting with an antibody for Munc18-1 detection, comparing the binding affinities of different STX1B mutants based on band intensity and calculating the ratio to the wildtype (**Fig. 4.8 A, B**). While the pull down-assay with Stx1B<sup>WT</sup> showed a strong band for Munc18-1 in the SDS-PAGE and on the western blot, surprisingly the Munc18-1 band intensities for both mutants were substantially reduced compared to the Stx1B<sup>WT</sup>. This strongly suggests a reduced capability of Munc18-1 binding for both Stx1B mutants which is notable considering that both mutations diverge from the interaction interface with Munc18-1 (**Fig. 1.14 B**).

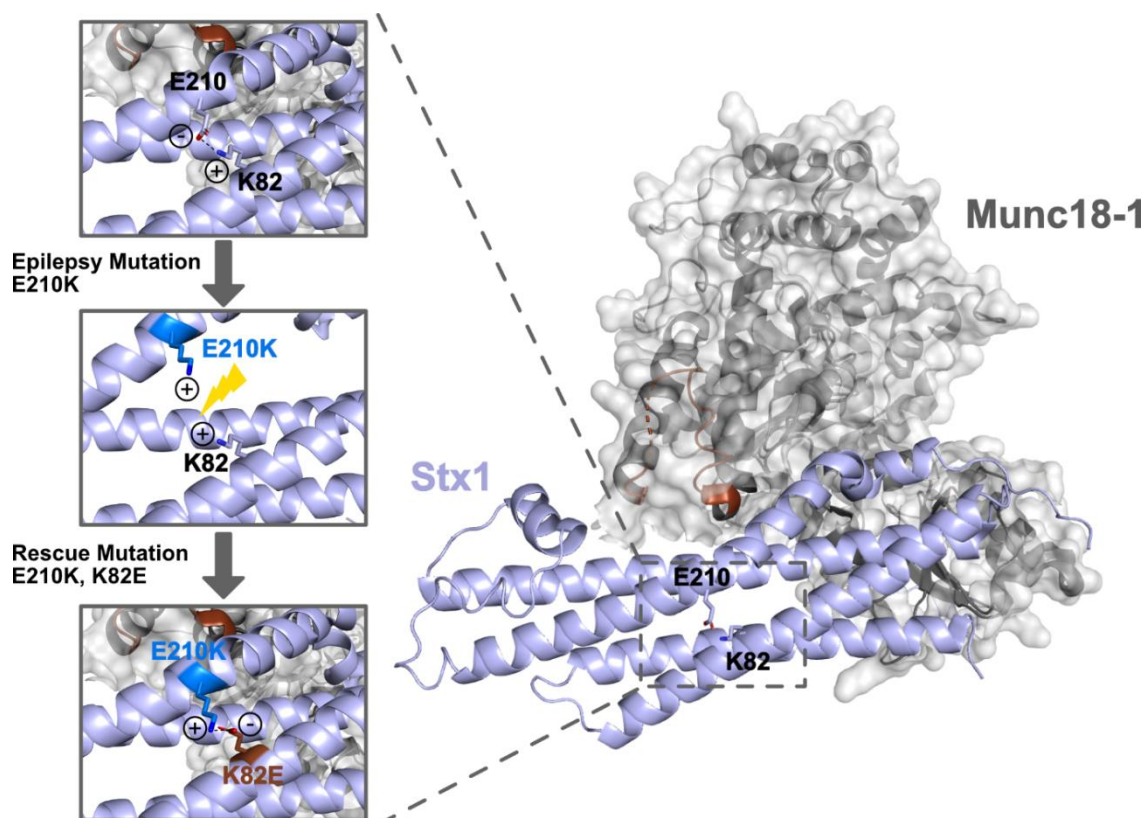


**Figure 4.9:** Crystal structure of Stx1A:Munc18-1 complex (PDB: 3C98). The corresponding mutation sites of E210(K) and K82(E) for Stx1B are depicted, which in Stx1A are E211(K) and K83(E). The panels illustrate a proposed model detailing how the E210K mutation influences Stx1B's conformation and its binding affinity to Munc18-1. In the Stx1B<sup>WT</sup>, E210, located on the SNARE motif, forms a salt bridge with K82 from the H<sub>b</sub> helix of the H<sub>abc</sub> domain, maintaining a closed conformation where the SNARE motif folds onto the H<sub>abc</sub> domain in which Stx1B<sup>WT</sup> binds to Munc18-1. The E210K mutation introduces a charge repulsion with K82, potentially preventing the SNARE motif from aligning with the H<sub>abc</sub> domain and by that diminish binding towards Munc18-1. However, adding the rescue mutation K82E counteracts this effect. This adjustment allows the SNARE motif to fold onto the H<sub>abc</sub> domain again, establishing a salt bridge with E210K and maintaining the closed conformation, allowing to bind to Munc18-1 again.

Nevertheless, the structural impact of proline could potentially influence the overall binding interface between Stx1B and Munc18-1, given the disruption of the  $\alpha$ -helical composition. Particularly intriguing is the case of the Stx1B<sup>E210K</sup> mutant as the introduction of the additional lysine rather has a secondary structure gaining effect than a disturbing effect. However, upon examining the structure of Stx1B, it becomes apparent that opposite from the negatively charged E210, at position 82 (on helix H<sub>b</sub> of Stx1B's H<sub>abc</sub> domain), there is a positively charged lysine (K82), which forms a salt bridge

with E210 in the closed conformation (**Fig. 4.9**). A charge reversion by the introduction of a positively charged lysine at position 210 could potentially disrupt the original salt bridge, leading to charge repulsion. We hypothesized that this may prevent the folding of the SNARE motif onto the  $H_{abc}$  domain, hindering the formation of the closed conformation in which Munc18-1 typically binds Stx1, thus disrupting the binding mode between Munc18-1 and Stx1B (**Fig. 4.9**).

Following this reasoning, we generated a rescue mutation by introducing a negatively charged side chain at position 82. This approach aimed to restore the salt bridge, promoting a stable folding of the SNARE motif onto the  $H_{abc}$  domain. Moreover, this strategy seeks to confirm our hypothesis as it should allow for an increased binding affinity towards Munc18-1. To achieve this, we created the rescue mutant Stx1B<sup>E210K,K82E</sup>, implementing a double charge reversion to mimic wild-type status (**Fig. 4.9**). And indeed, the pull-down assay with the rescue mutant displayed a band intensity similar to that of the wild-type, validating our approach (**Fig. 4.8 A, B**).

To more precisely quantify the influence of the Stx1B mutations on the interaction towards Munc18-1, we conducted isothermal titration calorimetry (ITC) experiments to determine the individual dissociation constants ( $K_D$ ). The binding of both proteins displayed an exothermic reaction in a 1:1 stoichiometry for all measurements (**Fig. 4.11**). As expected, Stx1B<sup>WT</sup> demonstrated a low  $K_D$ -value of  $9.9 \pm 1.6$  nM, indicative of a high affinity towards Munc18-1 and aligning with values reported in the literature for the interaction between Stx1A/B and Munc18-1. Stx1B<sup>L221P</sup> on the other hand exhibited a  $K_D$ -value of  $216 \pm 7.2$  nM, representing a ~20-fold reduction in affinity towards Munc18-1 compared to Stx1B<sup>WT</sup>. Remarkably, this affinity decrease was even more pronounced for Stx1B<sup>E210K</sup>, revealing a  $K_D$ -value of  $2.3 \pm 0.4$   $\mu$ M, marking an affinity decrease of approximately 100-fold compared to the wild-type.

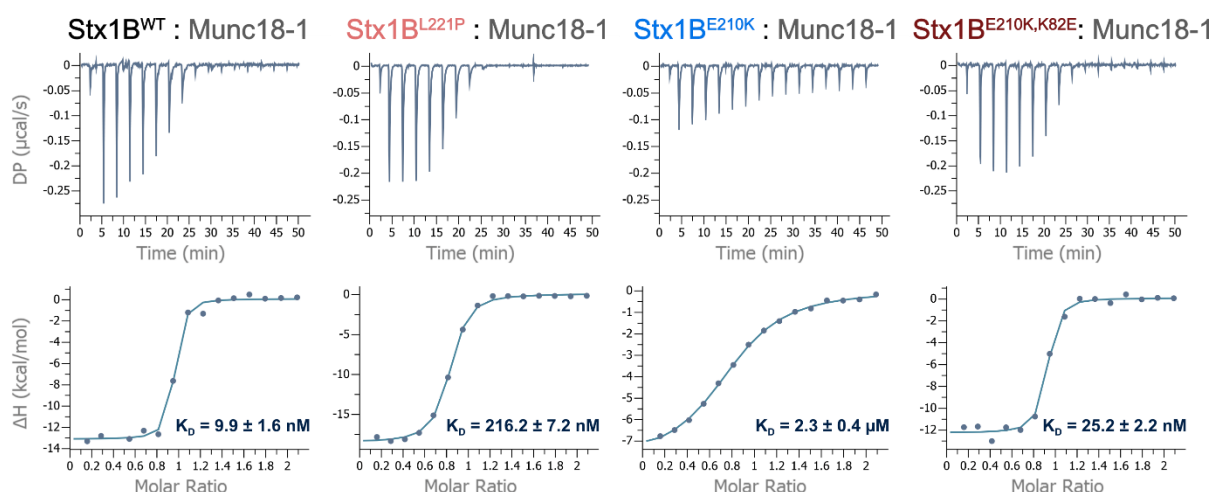


**Figure 4.10:** Representative isothermal titration calorimetry (ITC) profiles of Stx1B<sup>WT</sup>, Stx1B<sup>L221P</sup>, Stx1B<sup>E210K</sup> and the rescue mutant Stx1B<sup>E210K,K82E</sup> titrated against Munc18-1. *Top:* Heat changes upon ligand injection. *Bottom:* The integrated power peaks fitted with a 1:1 model. The derived dissociation constants ( $K_D$ ) are shown in the bottom right corner of each panel ( $\pm$  SEM,  $n = 3$ ). The data were processed and analyzed using MicroCal PEAQ-ITC Analysis Software (Malvern Panalytcs).



To explore the suggested rescue effect, we also examined the mutant Stx1B<sup>E210K,K82E</sup> using ITC. And indeed, the binding affinity towards Munc18-1 was partially restored, closely mirroring that of Stx1B<sup>WT</sup>, with a  $K_D$ -value of  $25.2 \pm 2.2$  nM.

In addition to confirming direct interactions, ITC measurements offer valuable insights into the mechanisms of noncovalent forces driving binding. Typically, polar interactions contribute favorably to the enthalpic component, while those favored entropically tend to involve more hydrophobic interactions [213]. Analysis of the binding signature plots for each reaction reveals that the binding of Stx1B<sup>WT</sup>, Stx1B<sup>L221P</sup>, and Stx1B<sup>E210K,K82E</sup> to Munc18-1 is primarily driven by hydrogen bonding and van der Waals interactions, accompanied by significant conformational changes indicated by the negative binding enthalpy ( $\Delta H$ ) and unfavorable positive temperature-entropy-product ( $-T\Delta S$ ) (**Appendix Fig. 14**). Notably, only the interaction with Stx1B<sup>E210K</sup> appears to be more entropy-driven, suggesting a greater involvement of hydrogen bonding and hydrophobic interactions, supported by the favorable binding enthalpy ( $\Delta H$ ) and entropy factor ( $-T\Delta S$ , **Appendix Fig. 14**).

Taken together, the findings underscore the critical role of Stx1B's conformational and structural state in its binding to Munc18-1. Specifically, when Stx1B adopts an open conformation due to charge repulsion from the E210K mutation, instead of its stabilized closed conformation, the binding to Munc18-1 is significantly impaired. Additionally, the results imply that the impact of the E210K mutation in Stx1B significantly manifests in the interaction with Munc18-1. Stx1B<sup>L221P</sup> is also affected, albeit to a lesser extent.

#### 4.4.2. Only K82E mutation compensates for Stx1B<sup>E210K</sup>-induced Munc18-1 interaction deficits, but not a neighboring K83E mutation

Guided by the Stx1B sequence, we pinpointed an additional lysine at position 83 on the H<sub>b</sub> helix of the H<sub>abc</sub> domain, adjacent to the discussed K82 (**Fig. 4.11 A**). Based on the solved structures of Syntaxin-1 existent, K83 was not expected to influence any interactions, either with the SNARE domain of Stx1B or with Munc18-1, as it adopts a different orientation (**Fig. 4.11 B**). However, given that only the structures of the Stx1A isoform are solved *via* protein structure determination techniques, while those of the Stx1B isoform remain elusive, we also examined the neighboring side chain. Subtle structural rearrangements in the solvent environment or sequence deviations might affect the local structural arrangement. Based on this, we generated two additional mutants, Stx1B<sup>E210K,K83E</sup> and Stx1B<sup>E210K,KK82-83EE</sup> (KKEE), to explore any potential compensatory effects using ITC (**Fig. 4.12**).

Interestingly, while Stx1B<sup>E210K,KKEE</sup> exhibited a rescue effect akin to Stx1B<sup>E210K,K82E</sup> with a  $K_D$ -value of  $17.5 \pm 2.4$  nM, Stx1B<sup>E210K,K83E</sup> abolished binding to Munc18-1 completely. This was surprising since, based on existing structures, the lysine at position 83 (or position 84 in Stx1A respectively) does not seem to interfere with the interactions interface between Stx1 and Munc18-1 or with any intramolecular interaction of Stx1. Hence, this K to E mutation was not expected to have such a significant impact.



A)

Stx1B 71 KQELEDLTADIKKTANKVRSKSLKAIEQSIE 100

Stx1A 71 TKEELEELMSDIKKTANKVRSKSLKSIEQSI 100

B)

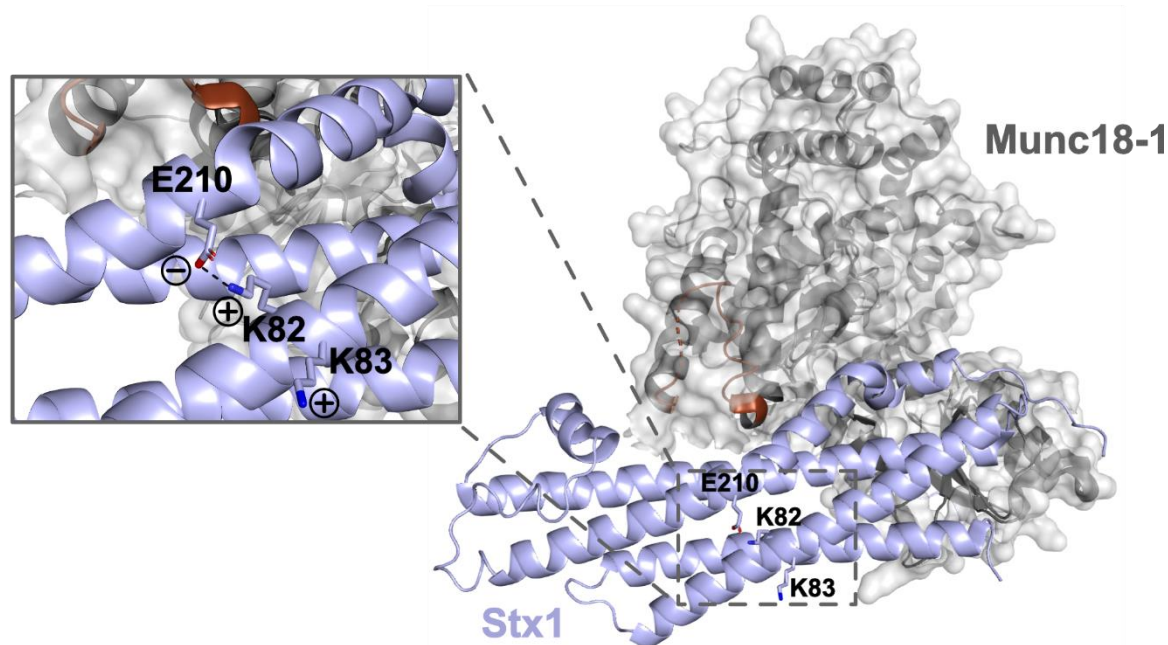


**Figure 4.11: A)** Sequence alignment of the helix H<sub>b</sub> in the H<sub>abc</sub> domain for the Stx1B and Stx1A isoforms. The C-terminal half is conserved between both isoforms, but the sequences are shifted by one residue. **B)** Crystal structure of Stx1A:Munc18-1 complex (PDB: 3C98). The labeled residues correspond to the sequence of Stx1B, which in Stx1A are K83, K84 and E211. The labeled K83 takes on a distinct orientation compared to the labeled K82, which forms a salt-bridge with E210. Because of the sequence shift and possible subtle changes may be due to the chemical environment, a local structural difference between Stx1A and Stx1B might be plausible, where Stx1B's K83 would be involved in intramolecular interactions towards E210.

To determine if the additional K83E modification altered the structural conformation, possibly leading to unfolding of Stx1B<sup>E210K,K83E</sup> and impacting the protein stability and the interaction towards Munc18-1, we conducted a detailed analysis using CD spectroscopy. The rescue mutant, Stx1B<sup>E210K,K82E</sup>, demonstrated an increased thermal stability with a  $T_M = 72.96 \pm 0.18$  °C compared to the epilepsy-relevant Stx1B<sup>E210K</sup> mutant. This suggests that the additional introduction of the K82E mutation contributes to enhanced thermal stability (**Fig. 4.13 B, C**). Similar to Stx1B<sup>E210K</sup>, albeit to a lesser degree, its CD spectrum exhibited a well-defined pattern with distinct minima at 208 nm and 222 nm, characteristic of a predominantly  $\alpha$ -helical protein (**Fig. 4.13 A**). Conversely, Stx1B<sup>E210K,K83E</sup> showed a notable shift in the CD spectrum, with both minima at 208 nm and 222 nm displaying an increased ellipticity (**Fig. 4.13 A**). This nearly flat trace, almost lacking well defined peaks suggests a significant reduction in helical content, hinting at potential partial unfolding and increased fraction of random coils and turns or even aggregation [198, 252, 253]. This reduced structural consistency was corroborated by a significantly lower thermal stability, with a  $T_M = 66.65 \pm 0.35$  °C (**Fig. 4.13 B, C**).

## Results

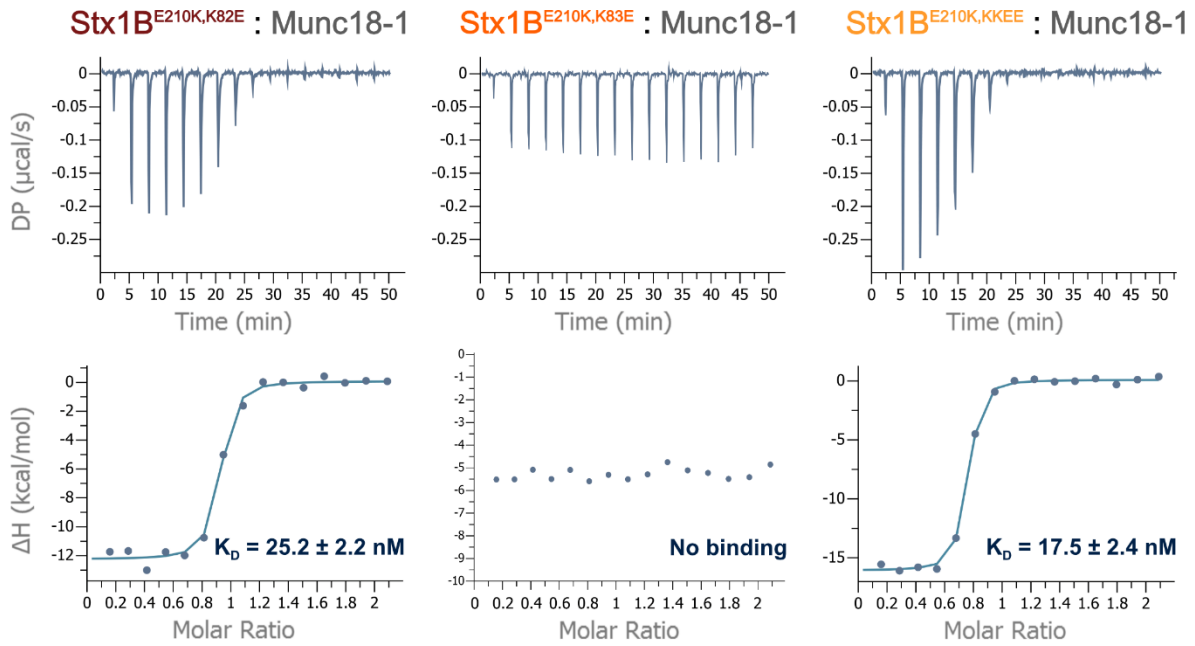


**Figure 4.12:** Representative isothermal titration calorimetry (ITC) profiles of Stx1B<sup>E210K,K82E</sup>, Stx1B<sup>E210K,K83E</sup> and Stx1B<sup>E210K,KKEE</sup> titrated against Munc18-1. *Top:* Heat changes upon ligand injection. *Bottom:* The integrated power peaks fitted with a 1:1 model. The derived dissociation constants ( $K_D$ ) are shown in the bottom right corner of each panel ( $\pm$  SEM,  $n = 3$ ). The data were processed and analyzed using MicroCal PEAQ-ITC Analysis Software (Malvern Panalytcs).

In summary, the Stx1B E210K mutation doesn't affect Stx1B's thermostability or its ability to form SNARE complexes, but it notably diminishes its binding to Munc18-1. Both the pull-down assay and ITC experiments indicated a reduced Munc18-1 binding for the Stx1B<sup>E210K</sup> and Stx1B<sup>L221P</sup> mutants.

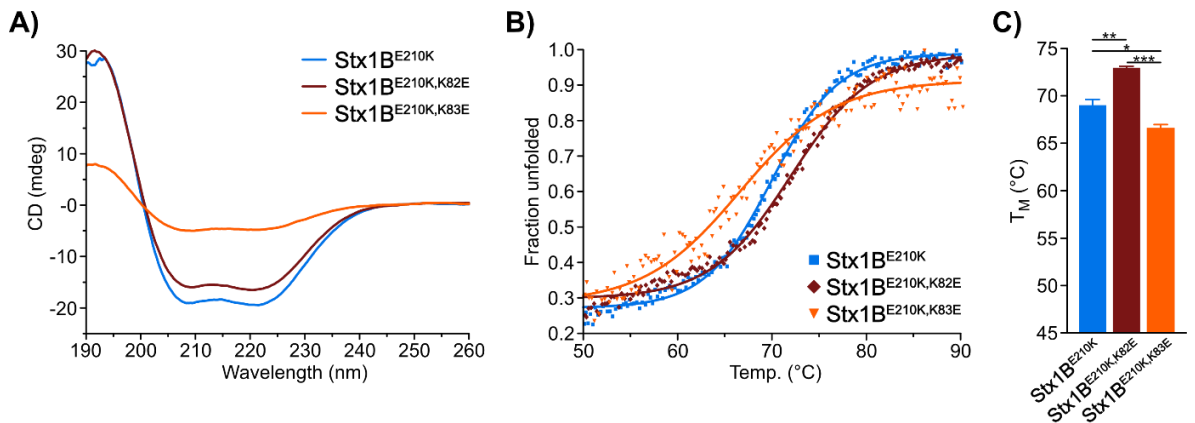


**Figure 4.13:** CD-spectroscopy investigation of Stx1B<sup>E210K</sup> (blue), Stx1B<sup>E210K,K82E</sup> (brown) and Stx1B<sup>E210K,K83E</sup> (orange). 10  $\mu$ M of each protein was used. **A)** Far-UV CD spectra depict dominantly helical content in Stx1B<sup>E210K</sup> and Stx1B<sup>E210K,K82E</sup>. Stx1B<sup>E210K,K83E</sup> exhibits a majorly reduced helicity **B)** CD melting curves of Stx1B<sup>E210K</sup>, Stx1B<sup>E210K,K82E</sup> and Stx1B<sup>E210K,K83E</sup> recorded at 222 nm, normalized to the maximum value and fitted according to the sigmoidal Boltzmann function:  $y = \frac{A_1 - A_2}{1 + e^{(x - x_0) / dx}} + A_2$ . Turning point of the function represents the melting temperatures of the examined proteins. All three mutants display distinct unfolding pattern leading to different melting temperatures (full fraction unfold spectra in **Appendix Fig. 15**). Bar diagram of melting temperatures from Stx1B<sup>E210K</sup>, Stx1B<sup>E210K,K82E</sup> and Stx1B<sup>E210K,K83E</sup> ( $\pm$  SEM,  $n = 3$ ). Stx1B<sup>E210K,K82E</sup> revealed a significantly higher melting temperature compared to both Stx1B<sup>E210K</sup> (t-test,  $**p < 0,01$ , two-tailed) and St1x1B<sup>E210K,K83E</sup> (t-test,  $***p < 0,001$ , two-tailed). Stx1B<sup>E210K,K83E</sup> exhibited the lowest melting temperature, even significantly lower than Stx1B<sup>E210K</sup> (t-test,  $*p < 0,05$ , two-tailed).

However, the reduction was particularly pronounced for Stx1B<sup>E210K</sup>, highlighting a significant decrease in affinity for the Stx1B<sup>E210K</sup> mutant. Introducing the rescue mutation, Stx1B<sup>E210K,K82E</sup>, reinstated the binding affinity to that of wild-type level, emphasizing the crucial role of the ionic bond between the SNARE motif and the H<sub>abc</sub> domain for Stx1B's high-affinity binding to Munc18-1. Interestingly, exploring the adjacent residue, K83, yielded unexpected results: while Stx1B<sup>E210K,K83E</sup> showed a rescue effect similar to Stx1B<sup>E210K,K82E</sup>, Stx1B<sup>E210K,K83E</sup> completely abolished the binding. This underscores a potential pivotal role of K83 in Stx1B, which may not be fully apparent from existing Stx1A crystal structures. CD spectroscopy provided insights into the structural and stability changes that might account for these altered binding behaviors.

### 4.5. *In vivo* expression of human Stx1B patient variants in zebrafish <sup>(1)</sup>

#### 4.5.1. Expression of human Stx1B patient variants leads to epileptiform activity in wild-type zebrafish larvae

To investigate the impact of the defective Stx1B mutants *in vivo*, we utilized zebrafish models to record and analyze behavioral deviations and developmental abnormalities. Zebrafish (*Danio rerio*) stand out as a valuable model in neurobiology, owing to several advantages. Notably, its ease of breeding and maintenance, high fertility, swift external development, larval-stage transparency, and the availability of efficient methods for generating genetically modified strains contribute to its appeal in research [254]. Moreover, zebrafish demonstrate significant physiological and genetic homology with humans, boasting over 82% of disease-associated genes in humans having identifiable orthologs in zebrafish [255].

In the realm of epilepsy research, zebrafish offer crucial advantages, including the ability to conduct: 1) high-throughput behavioral analysis through automated video tracking systems, 2) local field potential (LFP) recordings in both larval and adult stages, 3) *in vivo* brain imaging utilizing activity-dependent bioluminescent/fluorescent reporters. Collectively, these characteristics position zebrafish as a valuable model for investigating epileptogenesis and conducting high-throughput screenings of compounds with potential antiepileptic or antiseizure properties [254, 256-260].

The Stx1B protein in humans and zebrafish, as well as the Munc18-1 protein, exhibit a remarkable 97% and 87% identity, respectively (**Appendix Fig. 16**). This high level of similarity positions them as ideal genetic models for our investigation, utilizing the mutants explored in this study and as it has been shown before in other studies from Schubert *et al.* (2014) and Grone *et al.* (2016) [148, 181].

Using an active *ToI2* transposon system, we introduced human Stx1B<sup>WT</sup>, Stx1B<sup>L221P</sup>, Stx1B<sup>E210K</sup>, and Stx1B<sup>E210K,K82E</sup> mutants into the zebrafish genome, thereby generating transgenic zebrafish. In this process, a minimal *ToI2* transposon vector was employed, featuring a *Her4.1* promoter and two open reading frames. The first open reading frame encoded human Stx1B, while the latter contained mCherry, facilitating the monitoring of successful genetic transfer.

(1) The cloning and site-directed mutagenesis to introduce the E210K and L221P point mutations into the *stx1b* DNA construct within the minimal *ToI2* transposon vector were performed by me. The constructs were then sent to Dr. Wietske van der Ent (Esguerra Lab, University of Oslo) where the zebrafish experiments and data acquisition were conducted.

A *p2a*-self cleavage site was strategically positioned between both proteins, ensuring that, once expressed, the bulky fluorescence proteins does not interfere with Stx1B. Terminal inverted repeats at both ends, recognized by the *Tol2* transposase, facilitated the integration into the genomic DNA of the zebrafish (**Fig. 4.14 A**). The minimal *Tol2* vector, along with synthetic mRNA encoding the transposase, was introduced into fertilized eggs through microinjection [244].

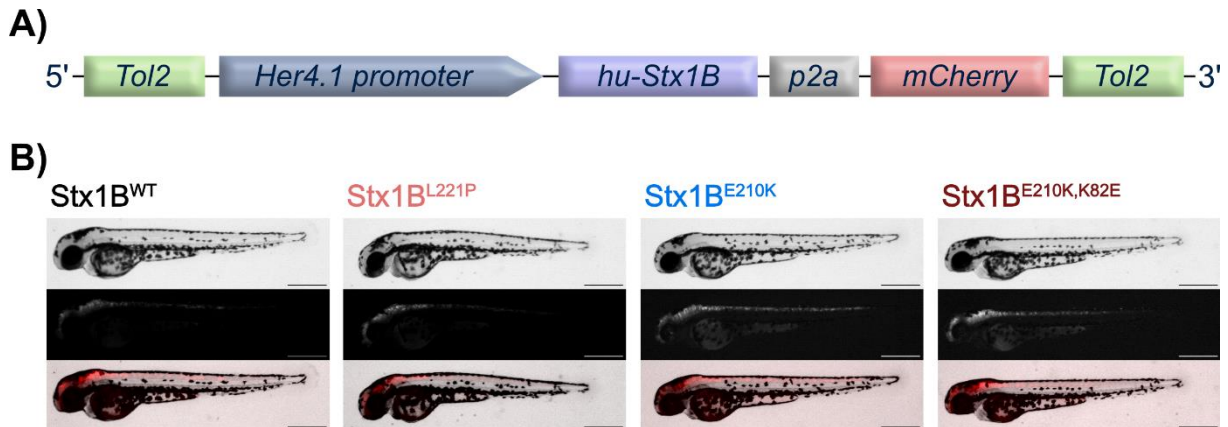


**Figure 4.14: A)** Structure of the minimal *Tol2* vector designed for integrating human Stx1B constructs into the zebrafish genome. The vector includes terminal inverted repeats, a *Her4.1* promoter, and two expression cassettes for the human Stx1B construct and mCherry fluorescence protein, separated by a *p2a*-self cleavage site. **B)** Representative images of larvae injected with human Stx1B<sup>WT</sup>, Stx1B<sup>L221P</sup>, Stx1B<sup>E210K</sup> and Stx1B<sup>E210K,K82E</sup> 3 dpf. The red fluorescence confirms successful DNA incorporation and protein expression, specifically in the brain and spinal cord (scale bars: 0.5 mm)

At 3 days post-fertilization (dpf), the zebrafish larvae expressing human Stx1B were examined. They were identified by the red fluorescence caused by co-expressed mCherry, predominantly in the brain and along the spinal cord (**Fig. 4.14 B**). Based on the observed fluorescence, an approximately equal expression rate can be estimated in all transgenic zebrafish. Furthermore, it can be stated that all zebrafish appear healthy and exhibit no morphological abnormalities. Especially the development of the heart and the swim bladder, which are typical criteria, showed no irregularities.

To explore irregular brain activity, we conducted 20-minute LFP recordings to identify epileptiform activities and examine the morphology of seizures 5 dpf (**Fig. 4.15**). Most zebrafish larvae injected with Stx1B<sup>WT</sup> exhibited no discharge events and displayed baseline activity almost constantly. Only a few larvae occasionally displayed ictal or inter-ictal activity in the LFP recordings with relatively modest amplitudes and short durations (**Fig. 4.15**). However, these ictal events do not necessarily have to be attributed to the injected Stx1B<sup>WT</sup>. Presumably, they are rather an artifact of the measurement method, as uninjected larvae occasionally also exhibit ictal or interictal events. This may be more likely due to the trauma caused by electrodes in the brain. All together this indicates that the insertion and expression of human Stx1B<sup>WT</sup> have no adverse impact on the zebrafish and do not affect its neurological and vital functions.

In contrast to the other transgenic zebrafish, larvae expressing Stx1B<sup>L221P</sup> displayed the highest number of ictal discharges within the recorded time frame (**Fig. 4.15**). The measured epileptiform

## Results

spikes displayed a modest amplitude, approximately three times higher than the baseline and comparable to  $Stx1B^{WT}$ . However, they demonstrated a significantly longer duration, noteworthy for its distinctive characteristic. These findings imply that  $Stx1B^{L221P}$  induces mild seizure events but with a high and regular frequency in zebrafish.

$Stx1B^{E210K}$ , on the other hand, exhibited markedly fewer discharge events in the zebrafish larvae within the recorded time frame. Nevertheless, the ictal events were much more pronounced than in all other mutants and the wild-type, exceeding five times the baseline level (**Fig. 4.15**). The captured seizures were so intense that partial overshoots were observed in the LFP recordings when relaxing back onto baseline level, which also influenced the duration of the seizure events, making them considerably longer. In some cases, the strong ictal event even led to an aftershock event, secondary electrical discharges describing an ongoing epileptic activity.

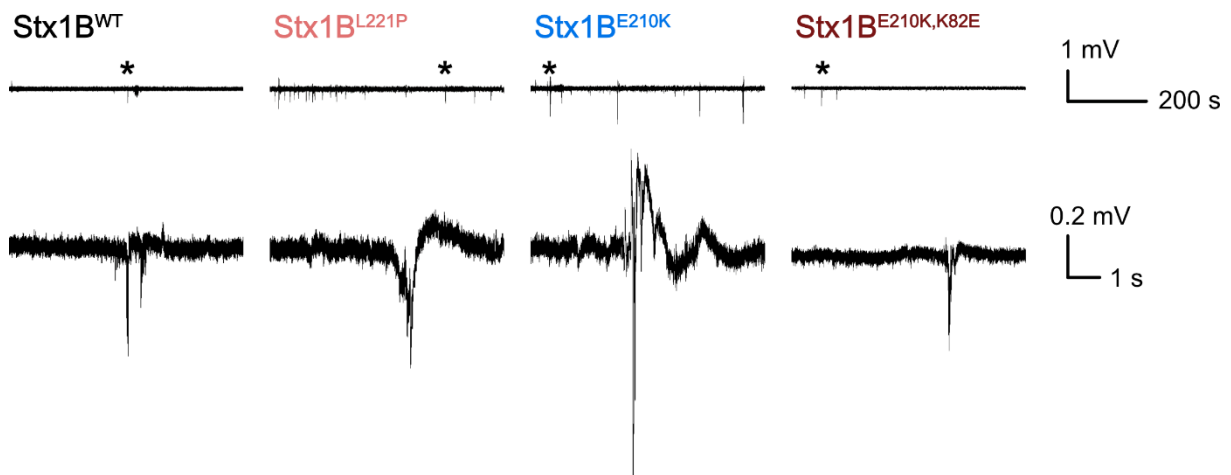


**Figure 4.15:** Representative 600-second LFP recordings of zebrafish larvae injected with  $Stx1B^{WT}$ ,  $Stx1B^{L221P}$ ,  $Stx1B^{E210K}$ , and  $Stx1B^{E210K,K82E}$  at 5 dpf, illustrating epileptiform activities of varying severity and durations. The upper portion displays the entire 600-second LFP recording, while the lower portion provides zoomed-in views labeled with an asterisk. Larvae injected with  $Stx1B^{WT}$  exhibit almost no discharge events, whereas transgenic larvae expressing  $Stx1B^{L221P}$  and  $Stx1B^{E210K}$  show frequent ictal occurrences, with  $Stx1B^{E210K}$  evoking stronger discharges but  $Stx1B^{L221P}$  exhibiting them more frequently. The expression of  $Stx1B^{E210K,K82E}$  brings the LFP appearance almost back to wild-type levels.

The mutant  $Stx1B^{E210K,K82E}$ , which exhibited rescue effects in the *in vitro* experiments, also demonstrated a remarkable recovery effect *in vivo* within transgenic zebrafish larvae. Similar to  $Stx1B^{WT}$ , only a limited number of epileptiform discharges were observed in the LFP recordings, with the majority of the recording displaying baseline activity (**Fig. 4.15**). Furthermore, the recorded ictal events exhibited a low amplitude and short duration, implying that  $Stx1B^{E210K,K82E}$  demonstrates a rescuing effect for the zebrafish in terms of neurological function compared to  $Stx1B^{E210K}$ , nearly restoring it to wild-type levels.

Quantification of the recorded LFP recordings provides a clear overview that supports the stated findings. When comparing the frequency of seizure events, it is apparent that zebrafish injected with  $Stx1B^{L221P}$  exhibit, on average, the highest number of seizures within the 20-minute recording, albeit with a high variance (**Fig. 4.16 A**). Larvae with  $Stx1B^{E210K}$  display a slightly lower average number of seizure events compared to  $Stx1B^{L221P}$ , but notably more than  $Stx1B^{WT}$  and

Stx1B<sup>E210K,K82E</sup>. Interestingly, it seems that these larvae can be roughly divided into two subsets, with some showing a high number of epileptiform activities and others showing only a few.

Larvae expressing the claimed rescue mutant Stx1B<sup>E210K,K82E</sup> indeed rescue the average number of seizure events back to wild-type levels, mostly showing only one seizure event within the recorded 20-minute time frame.

It is important to note that in this representation with only seizure positive zebrafish, a statistical comparison with Stx1B<sup>WT</sup> is not feasible. (This also applies to all plots in **Fig. 4.16 A) - C)**). This is because the vast majority of Stx1B<sup>WT</sup> zebrafish larvae showed no seizure events within the 20-minute recording period and, therefore, were not included in these graphs. Only one comparison specimen could be plotted, as it exhibited two epileptiform discharges. The data plots with the representation of all measured specimens, including those that did not exhibit seizures, can be found in the appendix (**Appendix Fig. 17**). There, significant differences between Stx1B<sup>WT</sup> and the L221P and E210K mutants are evident; however, no significant difference between the wild-type and the rescue mutant, as anticipated. Intriguingly, no statistically significant differences in the average number of seizure events between the L221P and E210K mutants were observed, likely due to the uneven variance in both data sets.

When examining the average durations of recorded seizure events in zebrafish larvae, all three mutants, Stx1B<sup>L221P</sup>, Stx1B<sup>E210K</sup>, and Stx1B<sup>E210K,K82E</sup>, exhibit no significant differences to each other but show a descending trend (**Fig. 4.16 B)**). Surprisingly, larvae expressing Stx1B<sup>L221P</sup> have, on average, slightly longer seizures than those expressing Stx1B<sup>E210K</sup>. This finding was unexpected, considering the recorded high amplitudes of the ictal events, suggesting strong seizures that would imply a longer duration.

However, this observation appears to be somewhat nuanced when incorporating all measured zebrafish larvae into the statistics, including those without seizures (**Appendix Fig. 17**). As more specimens with Stx1B<sup>L221P</sup> show no seizure events compared to those with Stx1B<sup>E210K</sup>, a trend becomes apparent: While many larvae with Stx1B<sup>L221P</sup> were recorded not having any seizure events, when seizures did occur, they happened more frequently within the 20-minute recording period and lasted longer than in larvae with Stx1B<sup>E210K</sup>. Furthermore, both mutants exhibit a substantial increase in average durations compared to larvae with Stx1B<sup>WT</sup>, whereas the rescue mutant Stx1B<sup>E210K,K82E</sup> demonstrated an increase as well, but not significantly and also showing a compensation of the effect of the single E210K mutation.

The average cumulative durations of discharge events within the measured 20 min align with the previous findings (**Fig. 4.16 C)**). While larvae with Stx1B<sup>WT</sup> exhibited the lowest average cumulative duration, as only one specimen was recorded seizing at all, and only twice, the average cumulative durations for larvae expressing Stx1B<sup>L221P</sup> and Stx1B<sup>E210K</sup> were much higher, with L221P seizing for the longest average total duration.



## Results

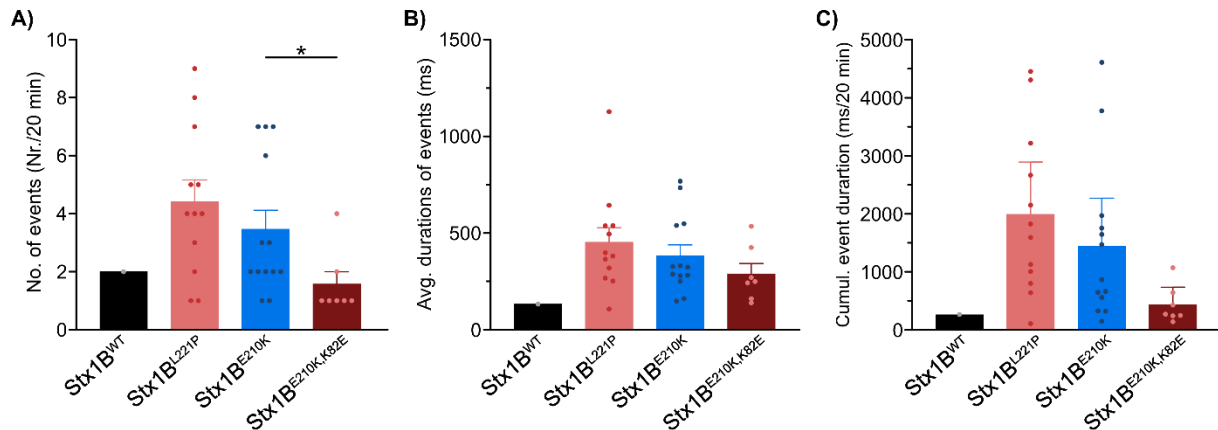


**Figure 4.16:** Quantification of seizure-positive events within 20-minute LFP recordings. **A)** Incidence of epileptiform discharge events in larvae expressing different human Stx1B wild-type and mutants. Sample size: Stx1B<sup>WT</sup>, n = 1; Stx1B<sup>L221P</sup>, n = 12; Stx1B<sup>E210K</sup>, n = 13; Stx1B<sup>E210K,K82E</sup>, n = 7. Statistical analysis between WT and mutants is not feasible due to the natural occurrence of a low sample size of WT. A significant difference between Stx1B<sup>E210K</sup> and Stx1B<sup>E210K,K82E</sup> was observed (Mann Whitney-test, U = 18.5, \*p < 0.05, two-tailed). **B)** Mean duration of discharge events in the measured zebrafish larvae (sample size similar to A)). **C)** Cumulative duration of epileptiform events in the measured zebrafish larvae. Stx1B<sup>E210K,K82E</sup> exhibited a substantial reduction in the overall seizing time compared to the other mutants (sample size similar to A)).

As hinted earlier, the expression of Stx1B<sup>E210K,K82E</sup> in the larvae led to a pronounced rescue by significantly reducing the average cumulative duration of epileptiform discharges. The same trend is evident when including all measured larvae, even those that did not exhibit seizure events. In this case, a significant difference between the wild-type and the mutants L221P and E210K was observed, while Stx1B<sup>E210K,K82E</sup> showed no significant difference and was rather similar to the wild-type, as anticipated.

### 4.5.2. Human Stx1B<sup>WT</sup>, Stx1B<sup>L221P</sup> and Stx1B<sup>E210K,K82E</sup> partially rescue zebrafish Stx1B-null larvae

To evaluate the ability if human Stx1B (wild-type and mutants) could rescue the loss of zebrafish Stx1B, a zebrafish line was used where endogenous Stx1B was mutated to contain an early stop codon, leading to nonsense-mediated decay (nmd). In offspring from this line, given the heterozygous background, approximately 25% of the larvae were homozygous with nmd of *stx1b*, resulting in dysfunctional Stx1B. Phenotypically, this resulted in hyperpigmented larvae with absent muscle activity. About 50% had a heterozygous background, possessing only half the amount of functioning endogenous Stx1B compared to normal. These larvae were indistinguishable from the remaining 25% of larvae with a wild-type background with the normal amount of functioning endogenous Stx1B. To evaluate sensory processing and motor responses, touch response experiments were conducted at 3 dpf using zebrafish larvae from a heterozygous line, transiently expressing human Stx1B wild-type or mutant (**Fig. 4.17**).

Each experiment involved three to five populations, and each population comprised at least 35 individual larvae. The averages of touch responses within each population were plotted, further averaged, and subsequently compared.

For wild-type zebrafish larvae without genetic modification, all exhibited touch responses (**Fig. 4.17**).

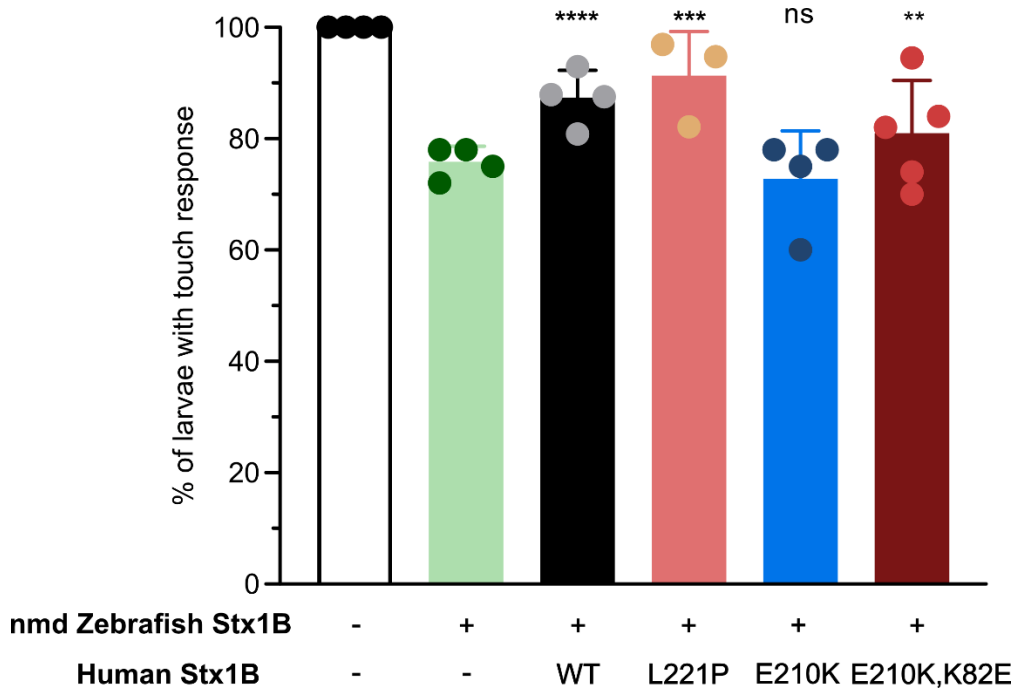


**Figure 4.17:** Proportion of touch response within three to five zebrafish larvae populations, each comprising of at least 35 individuals (3 dpf). These populations were derived from a heterozygous zebrafish line with endogenous Stx1B, resulting in a mixed genetic background concerning the homology and heterology of Stx1B. Approximately 25% of the larvae had a homologous background with Stx1B nonsense-mediated decay (nmd), 50% had a heterologous background of endogenous Stx1B, and another 25% had a homologous background with a normal amount of endogenous Stx1B. The average proportion of touch response was calculated for each population, and the averages were further combined across populations before being plotted. In wild-type zebrafish larvae populations without endogenous Stx1B nmd or injected human Stx1B, all displayed touch responses. In line with the crossbreeding scheme, only about 75% of zebrafish showed touch response. This proportion was significantly increased when human Stx1B<sup>WT</sup>, Stx1B<sup>L221P</sup> or Stx1B<sup>E210K,K82E</sup> was additionally injected (significances were calculated against the expected observation of 75% with touch response, binomial exact test, \*\*\*\*p < 0.0001, \*\*\*p < 0.001, \*\*p > 0.01). Injection of Stx1B<sup>E210K</sup> showed no significant difference.

Zebrafish larvae from the described heterozygous line exhibited a touch response in approximately 75% of cases, which was expected since around 25% of the larvae were homozygous for nonsense-mediated decay of Stx1B, leading to the loss of touch response in that group. When injected with human Stx1B<sup>WT</sup>, this loss of motor sensory function was partially compensated, resulting in 87.3% showing touch response, suggesting a significant increase in touch response. This indicates that the injected human Stx1B<sup>WT</sup> replaces the function of the endogenous Stx1B (**Fig. 4.17**).

Interestingly, the expression of Stx1B<sup>L221P</sup> resulted in 91.2% of the larvae displaying a touch response, indicating that this mutant retains enough activity to partially compensate for the lack of endogenous Stx1B protein, performing even slightly better than Stx1B<sup>WT</sup>. Yet, the difference is minor and not statistically significant.

Injection with Stx1B<sup>E210K</sup>, on the other hand, showed no compensational effect; instead, it decreased the average number of larvae per population exhibiting touch response. This effect of Stx1B<sup>E210K</sup> was partially rescued by Stx1B<sup>E210K,K82E</sup>, to about 80.9% showing touch response, albeit with a broad dispersion (**Fig. 4.17**).



In summary, the investigation into the impact of defective Stx1B mutants *in vivo*, utilizing zebrafish models, revealed diverse behavioral and developmental outcomes. Through an active *ToI2* transposon system, successful introduction of human Stx1B<sup>WT</sup>, Stx1B<sup>L221P</sup>, Stx1B<sup>E210K</sup>, and Stx1B<sup>E210K,K82E</sup> mutants into zebrafish genomes was achieved, confirmed by the observed fluorescence from the coupled mCherry expression. At 3 dpf, transgenic zebrafish larvae exhibited normal development with no morphological abnormalities.

Zebrafish wild-type larvae injected with Stx1B<sup>WT</sup> displayed no adverse effects, maintaining normal LFP recording patterns and behavior. Moreover, there was a reduction in the average number of larvae showing no touch response in an Stx1B-null background, suggesting that the expressed human Stx1B<sup>WT</sup> counteracts nonsense-mediated decay.

Stx1B<sup>L221P</sup> induced the highest number of ictal discharges within the recorded time frame, with epileptiform spikes displaying modest amplitudes and longer durations, indicating mild seizures occurring at a high and regular frequency. Counterintuitively, Stx1B<sup>L221P</sup> increased the number of larvae with a touch response in the zebrafish *stx1b* mutant line. This suggests that this mutant retains enough functional activity to partially compensate for the loss of functional endogenous Stx1B protein, performing at a level comparable to Stx1B<sup>WT</sup>.

The discrepancy between Stx1B<sup>L221P</sup> inducing high numbers of ictal discharges but improving the touch response can be explained by the different neuronal circuits involved. The touch response is a simple reflex driven by sensory and motor neurons (Rohon-Beard neurons and trigeminal sensory neurons), which may be less affected by synaptic dysregulation compared to the more complex circuits responsible for ictal discharges. Stx1B<sup>L221P</sup> likely impairs neurotransmitter release in higher-order neurons, leading to seizures, but still allows sufficient function in basic motor circuits to maintain the touch response. Additionally, different neuron types may have varying sensitivities to the mutation, with motor neurons being more resilient. Thus, while Stx1B<sup>L221P</sup> disrupts complex brain functions, it can still support basic sensorimotor activity.

Larvae expressing Stx1B<sup>E210K</sup> exhibited fewer discharge events but with significantly stronger and intense seizures, even triggering aftershock events. Furthermore, Stx1B<sup>E210K</sup> mildly increased the proportion of larvae with no touch response, indicating motor sensory dysfunctions.

Rescue effects were evident with the expression of Stx1B<sup>E210K,K82E</sup>. Transgenic larvae displayed limited epileptiform discharges similar to Stx1B<sup>WT</sup>, with low amplitude and short duration, indicating a rescuing effect on neurological functions. Additionally, cumulative durations of seizures were significantly reduced, nearly restoring to wild-type levels. Stx1B<sup>E210K,K82E</sup> partially rescued the worsened touch response of Stx1B<sup>E210K</sup> but did not fully restore wild-type levels.

## 4.6. NMR characterization of the Syb2 binding to the Munc13-MUN domain

### 4.6.1. C-terminal JMD of Syb2 responsible for binding to Munc13-MUN

Having closely examined the formation and interaction of the SNARE complex, particularly focusing on the influence of mutations of Stx1B, also towards Munc18-1, and the physiological implications, we only covered one part of the synaptic vesicle fusion machinery. While Munc18-1 and the SNARE proteins are crucial for the eventual SNARE complex formation and the affiliated vesicle fusion, Munc13-1 and, notably, its MUN domain, is equally essential for the catalyzation of this reaction overcoming autoinhibitory modes, and coordinating the reaction.

While the peripheral C<sub>1</sub>, C<sub>2</sub>B and C<sub>2</sub>C domains are primarily responsible for tethering the vesicle membrane to the presynaptic membrane, it is the MUN domain, that is thought to catalyze the opening of the autoinhibitory binding mode of the closed conformation of Stx1B and Munc18-1, facilitating subsequent SNARE complex formation.

Recently, studies have demonstrated that the MUN-domain can bind a C-terminal region of Syb2, making the interaction between Syb2 and Munc13-MUN a vital bridge between participants in SNARE complex formation from the vesicle membrane side and those from the presynaptic side [123, 127].

To delve deeper into the Syb2 and Munc13-MUN interaction, we utilized nuclear magnetic resonance (NMR) spectroscopy. This technique offers the ability to analyze peptides or proteins, providing detailed information about individual residues down to atomic resolution. NMR spectroscopy unveils the structural flexibility and dynamics of proteins, allowing the exploration of side-chain motions, backbone dynamics, and consequential conformational changes pivotal for comprehending protein function and interactions. As such, NMR spectroscopy yields invaluable insights into protein structure, ligand binding, and potential interactions with other molecules.

A compelling instance of structural changes uncovered through NMR spectroscopy is the unfolding of Stx1B's H<sub>abc</sub> domain triggered by alterations in the amino acid sequence resulting from the InDel mutation, as demonstrated in our previous study (**Appendix Fig. 18**). In the two-dimensional <sup>1</sup>H-<sup>15</sup>N-HSQC spectrum of the <sup>15</sup>N-labeled Stx1B-H<sub>abc</sub><sup>WT</sup> domain, we observed a well-resolved cross-peak dispersion with uniform cross-peak intensities, suggesting a well-folded protein conformation. However, in the spectrum of the <sup>15</sup>N-labeled Stx1B-H<sub>abc</sub><sup>InDel</sup> variant, the corresponding cross-peaks shifted towards the center of the spectrum and we noted a narrower cross-peak dispersion, leading to considerable overlap in the middle of the spectrum, characteristic of an unfolded or intrinsically disordered protein (IDP) state (**Appendix Fig. 18 A**) [178, 261]. This was corroborated by CD spectroscopy, which revealed a significantly reduced helicity and thermal stability of Stx1B-H<sub>abc</sub><sup>InDel</sup> variant compared to the wild-type counterpart (**Appendix Fig. 18 B, C**) [178].

The <sup>1</sup>H-<sup>15</sup>N-HSQC spectrum of a <sup>15</sup>N-Syb2 construct (1-96), spanning the cytosolic region, shows the characteristics of an intrinsically disordered protein. Notably, the spectrum displays a narrow cross-peak dispersion with numerous overlaps in the center. Furthermore, the cross-peak

## Results

intensities vary considerably, indicative of a disordered protein state, as anticipated for Syb2 and shown in studies before [108, 110, 262]. Only a few cross-peaks, assigned to the C-terminal JMD, displayed a wider distribution, suggesting that this region possesses some level of structure (**Fig. 4.18**). The overall intrinsically disordered structure can be attributed partially to the numerous prolines within the amino acid sequence, especially in the N-terminal region.

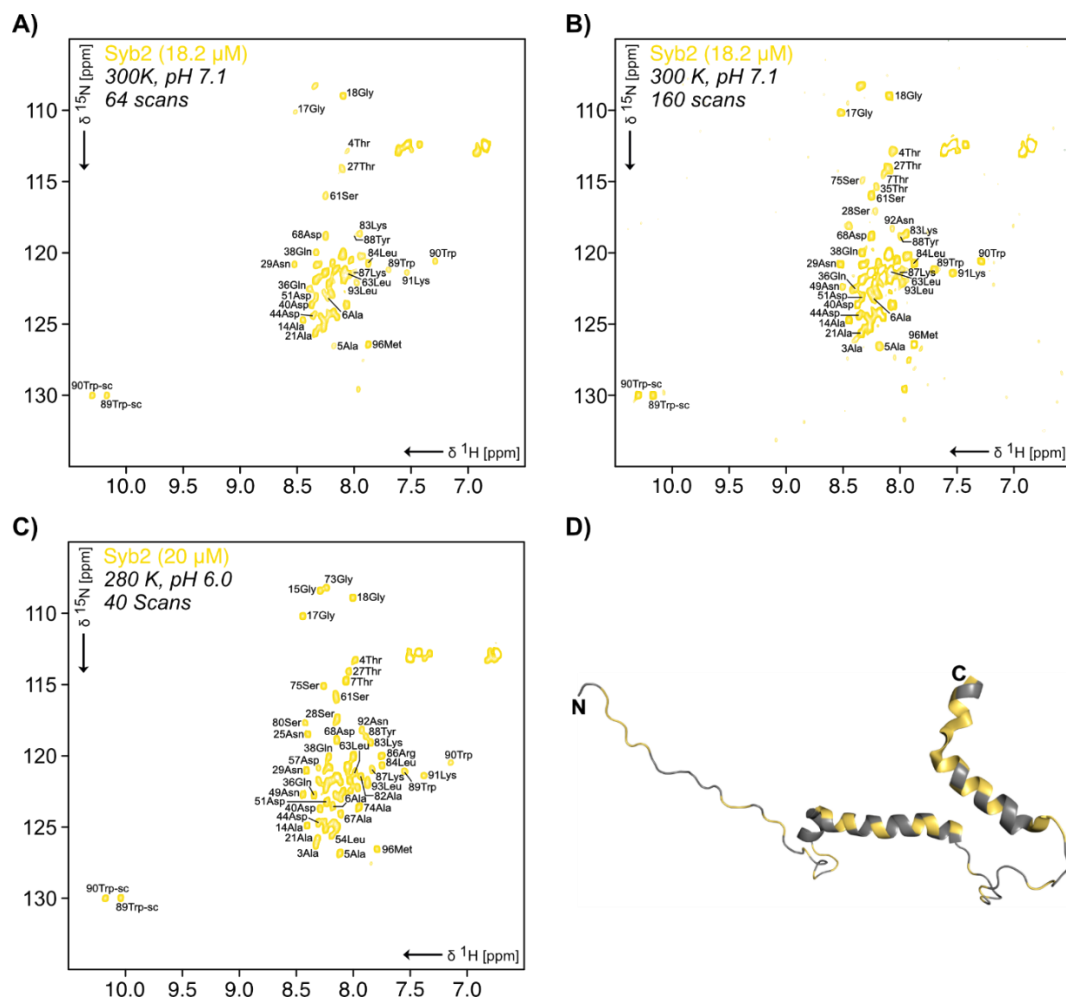


**Figure 4.18: A)**  $^1\text{H}$ - $^{15}\text{N}$ -HSQC spectrum of  $^{15}\text{N}$ -labeled Syb2<sup>WT</sup> (1-96), measured at 300 K, pH 7.1 with 64 scans, revealing limited cross-peak dispersion, characteristic of an IDP. Out of 88 cross-peaks, only 26 could be unequivocally assigned. Assignments were taken from BMRB entry 16514 [110]. **B)**  $^1\text{H}$ - $^{15}\text{N}$ -HSQC spectrum of  $^{15}\text{N}$ -labeled Syb2 (1-96), measured at 300 K, pH 7.1 with 160 scans, resulting in more and clearer cross-peaks and enabling the assignment of additional peaks, specifically 33 out of 88. **C)**  $^1\text{H}$ - $^{15}\text{N}$ -HSQC spectrum of  $^{15}\text{N}$ -labeled Syb2 (1-96), measured at 280 K, pH 6.0 with 40 scans, significantly improved the spectrum's quality while also reducing the measurement time, allowing for the unambiguous assignment of 42 out of 88 cross-peaks. **D)** NMR structure of Syb2 (PDB: 2KOG, residues 1-96). Assigned regions highlighted in yellow, while unassigned regions appear in grey.

To identify the recorded cross-peaks, we transferred the assignments from Koo *et al.* (2011) [262]. It is worth noting that the eight prolines of Syb2 do not appear as cross-peaks in a  $^1\text{H}$ - $^{15}\text{N}$ -HSQC spectrum but both tryptophan appear as two distinct peaks due to the additional NH-group in tryptophan's indole side chain. However, we were able to unambiguously transfer the assignments for only 26 out of 88 assignable cross-peaks due to peak overlap or low signal intensity (**Fig. 4.18 A**). To enhance the spectrum's quality and achieve higher resolution to detect more

distinct cross-peaks, we increased the number of scans from 64 to 160. Consequently, both cross-peak intensities and resolution improved, enabling us to assign more peaks through assignment transfer, specifically 33 out of 88 (**Fig. 4.18 B**).

To ensure that the measurement time remained within a reasonable timeframe, particularly when multiple runs were necessary for a comprehensive analysis, we pursued an alternative approach to optimize spectrum quality. This involved lowering the temperature from 300 K to 280 K and adjusting the buffer pH from 7.1 to 6.0. These adjustments aimed to minimize exchange broadening with solvent protons and reduce structural dynamics, thus enhancing spectrum quality [261]. Strikingly, despite a lower number of scans, the spectrum exhibited significantly enhanced resolution, with sharper and more distinct cross-peaks. This improvement facilitated a more precise assignment transfer, enabling us to assign 42 out of 88 cross-peaks (**Fig. 4.18 C**).

Although the assigned cross-peak count is modest with 47.7%, the coverage spans the entire amino acid sequence adequately, as we've obtained assignments from all regions of the protein (**Fig. 4.18 D**). Furthermore, in light of our expectation of interactions, particularly towards the MUN domain of Munc13-1, primarily involving the C-terminus, a region well-represented in our assignments, we have progressed to undertake further analysis. Specifically, our focus has shifted towards a more intricate examination of the interaction with Munc13-MUN through the implementation of a titration experiment. Upon the addition of Munc13-MUN, we observed gradual cross-peak broadening of the C-terminal region of  $^{15}\text{Syb2}$ . This decrease in peak intensity persists until the peaks are entirely obscured at a 1:2 molar ratio, strongly implying an interaction between JMD of Syb2 and Munc13-MUN (**Fig. 4.19**).

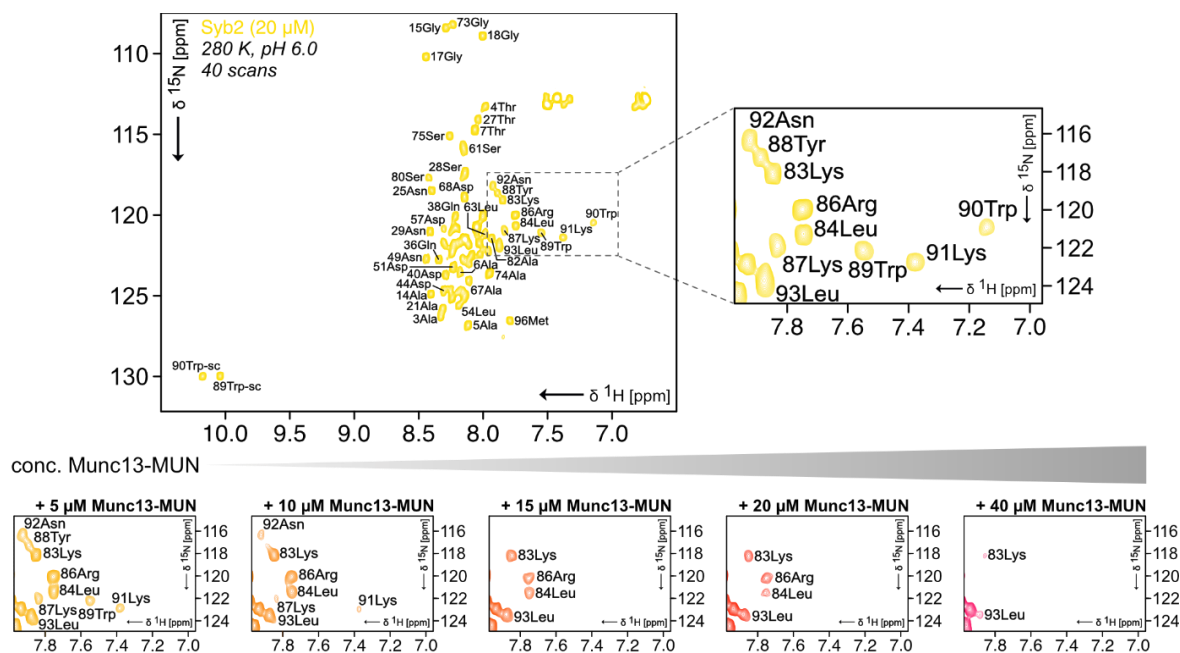


**Figure 4.19:**  $^1\text{H}$ - $^{15}\text{N}$ -HSQC spectra of  $^{15}\text{N}$ -labeled Syb2<sup>WT</sup> (1-96), acquired at 280 K and pH 6.0 with 40 scans, reveals primarily dispersed cross-peaks corresponding to Syb2's JMD, indicative of its structured nature (see inset). Notably, under the addition of increasing concentrations of Munc13-MUN, these cross-peaks experience significant line broadening, a phenomenon that amplifies with higher Munc13-MUN concentrations (full-scale spectra can be found in **Appendix Fig. 19**).

## Results

Observing cross-peak broadening, rather than distinct shifts, hints at a slow to intermediate exchange rate, possibly reflecting similar kinetics between binding and dissociation and the associated chemical shift alterations. Consequently, instead of clear cross-peak shifts, we observed cross-peak broadening. This broadening occurs because the NMR signal averages over both bound and unbound states, making differentiation challenging [263]. Moreover, the binding of the relatively small  $^{15}\text{N}$ -labeled Syb2 to the considerably larger MUN domain of Munc13-1 can further magnify the broadening effect. As the size of the complex increases compared to the isolated  $^{15}\text{N}$ -labeled protein, structural flexibility and dynamics decrease within the complex, consequently altering signal intensity for the labeled protein. In some instances, binding can induce overall broadening of NMR signals for stably folded proteins exhibiting a rigid conformation. However, cross-peaks originating from flexible regions may largely remain unaffected if they are not involved in binding, as internal motions generate very sharp resonances for flexible regions regardless of molecular size [263].

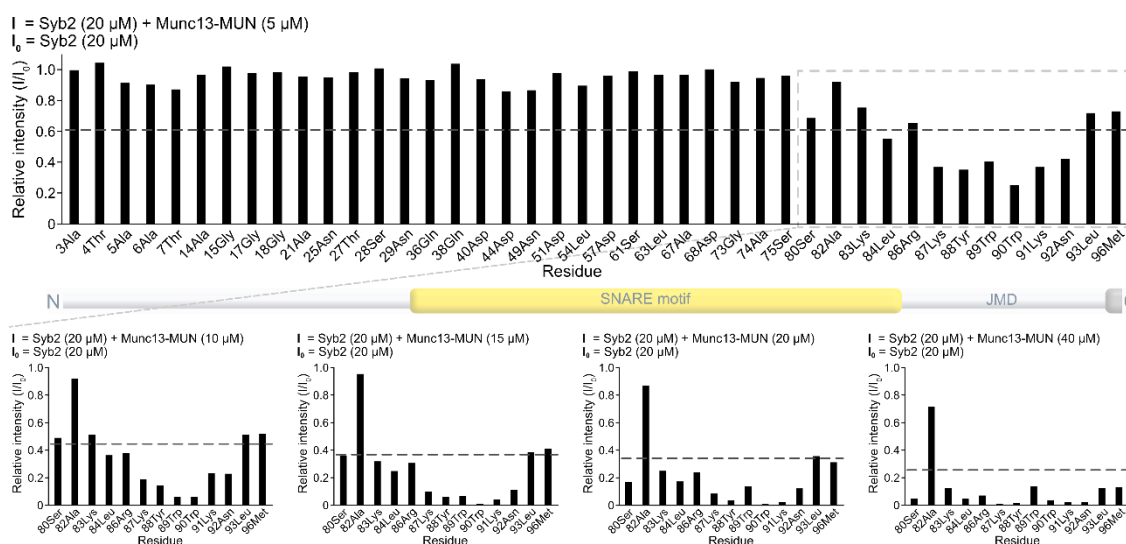


**Figure 4.20:** Quantification of relative cross-peak intensities ( $I/I_0$ ) upon the addition of increasing concentrations of Munc13-MUN highlights substantial cross-peak broadening exclusively in the C-terminal JMD of Syb2, which intensifies with higher concentrations of Munc13-MUN. In contrast, the relative intensities of the N-terminal residues remain largely unaffected. Detailed diagrams illustrating these relative intensities under the addition of higher concentrations of Munc13-MUN can be found in **Appendix Fig. 20**. A grey dashed line indicates the cut-off, calculated as the average of relative peak intensities minus the standard deviation. Relative intensities below this threshold denote significant cross-peak broadenings.

Indeed, when quantifying relative cross-peak intensities, the signal intensities of the N-terminal part remain largely unaffected, staying close to a relative intensity of 1.0 and only a slight and insignificant reduction in the overall intensity was observed. This suggests that the N-terminal region is largely unaffected by binding and is likely not involved in the binding interaction, remaining unbound and flexible (**Fig. 4.20**). In contrast, the C-terminal part, precisely the JMD, shows a significant reduction in relative peak intensity, which becomes increasingly pronounced with higher concentration of Munc13-MUN (**Fig. 4.20**).

Especially the central region of the JMD, around residues K87 to N92, is affected by cross-peak broadening, indicating that these residues are particularly involved in the binding of Syb2 to the MUN domain. This is consistent with the results of Wang *et al.* (2019), who co-crystallized a C-terminal Syb2 peptide (Residues 75-92) with the MUN domain [123]. There, the residues between K87 and N92 were, with high electron density, well resolved as a short, almost  $\alpha$ -helical peptide, which binds into a small hydrophobic pocket in the C-terminal part of the MUN domain through the two tryptophan residues W89 and W90 [123]. The remaining residues could not be resolved due to insufficient electron density, suggesting high flexibility in these regions, likely because they are not or only insignificantly involved in the binding process. This correlates with our results, which reveal that the N-terminal residues do not display line broadening, suggesting that they are unlikely to be involved in Munc13-MUN binding, independent of the added concentration, and instead demonstrate high flexibility (**Appendix Fig. 20**).

An exception to this is serine at position 80, which exhibits significant peak broadening when higher concentrations of Munc13-MUN are added. This suggests that this residue, likely due to its polar side chain, participates in binding to the MUN domain, albeit to a lesser extent than the central JMD region. The binding of serine-80 may not be nonspecific, as this side chain is part of a short hydrophilic stretch (residues 78-80) of Syb2, which could potentially interact with a polar patch of Munc13-MUN, which are generously distributed across the MUN domain [123]. Unfortunately, the lack of assignments for residues 78 and 79 prevents us from providing detailed cross-peak broadening analysis for these residues.

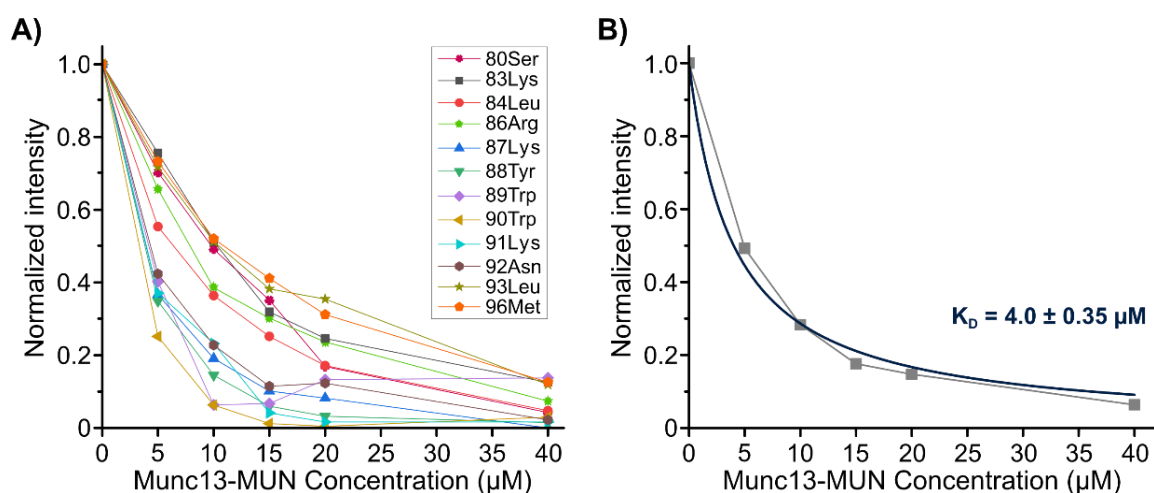


**Figure 4.21: A)** Plots of normalized intensities at each Munc13-MUN concentration for residues exhibiting notable line broadening upon Munc13-MUN addition. Intensities were normalized to their respective maximum values. **B)** The relative intensities were averaged, plotted, and fitted using a standard one-to-one protein-ligand binding model with the function  $y = \frac{1-x}{b+x}$  to calculate  $K_D$ , resulting in  $4.0 \pm 0.35 \mu\text{M}$ .

The hydrophobic alanine at position 82, on the other hand, does not appear to be involved in the interaction with Munc13-MUN, as the peak intensity of this side chain shows hardly any indication of cross-peak broadening. This observation likely extends to A81 as well; however, the lack of assignment for this residue prevents us from making a definite statement about its involvement.

To assess the binding affinity of the measured Syb2 construct towards the MUN domain of Munc13-1, we determined the relative peak intensities for every individual residue which showed significant cross-peak broadening along the increasing concentration of Munc13-MUN. We then calculated the average intensity for each concentration point and fitted the data using a standard one-to-one protein-ligand binding model (**Fig. 4.21**).

The overall fitting of the significantly line broadened cross-peak intensities resulted in a  $K_D$ -value of  $4.0 \pm 0.35 \mu\text{M}$ , suggesting a moderate binding affinity of Syb2 towards Munc13-MUN.

### 4.6.2. Tryptophane residues of Syb2 C-terminal JMD critical for Munc13-MUN interaction

To deepen our understanding and lay the groundwork for future complex engineering, we closely examined the interaction between the two protein constructs. Given that the two tryptophan residues, W89 and W90, at the core of Syb2's JMD, experience significant line broadening, indicating their likely importance for binding to the hydrophobic pocket of Munc13-MUN, we conducted NMR experiments with alanine mutations introduced to each tryptophan individually and to both simultaneously to assess their impact on binding.

In general, the  $^1\text{H}$ - $^{15}\text{N}$ -HSQC spectrum of Syb2<sup>W89A</sup> exhibited no significant changes in the overall cross-peak dispersion compared to the wild-type, suggesting that the substitution of alanine for tryptophan does not alter the overall structure of Syb2 (**Fig. 4.22 A**). However, the altered sequence led to changes in the chemical environment of residues near the mutation site, resulting in notable cross-peak shifts for some JMD residues towards the center of the spectrum. This indicates that the modest level of structure originally present in the JMD was affected. Moreover, these peak shifts hindered clear peak reassignment, prompting us to label the newly emerged peaks as 97-100 (**Fig. 4.22 A, B**).

The addition of  $40 \mu\text{M}$  Munc13-MUN resulted in significant line broadening of the cross-peaks corresponding to the C-terminal JMD for Syb2<sup>W89A</sup>, indicating that binding is still possible. Comparing the relative extent of cross-peak broadening to wild-type Syb2 under the addition of  $40 \mu\text{M}$  Munc13-MUN, however, the data suggest that binding was weakened. The N-terminal part remained largely unaffected, as relative changes in cross-peak intensity were insignificant and remained close to 1.0 (**Fig. 4.22 B**).

A similar spectrum and relative intensity profile can be observed for Syb2<sup>W90A</sup> upon the addition of  $40 \mu\text{M}$  Munc13-MUN (**Fig. 4.23 A**). The cross-peak dispersion remained narrow, and several cross-peaks corresponding to the C-terminal JMD shifted towards the center of the spectrum, making clear reassignment challenging. Interestingly, the remaining cross-peaks of the JMD exhibited diminished clarity and began to overlap with each other, indicating a relaxation of the preexisting structure in the wild-type.

## Results

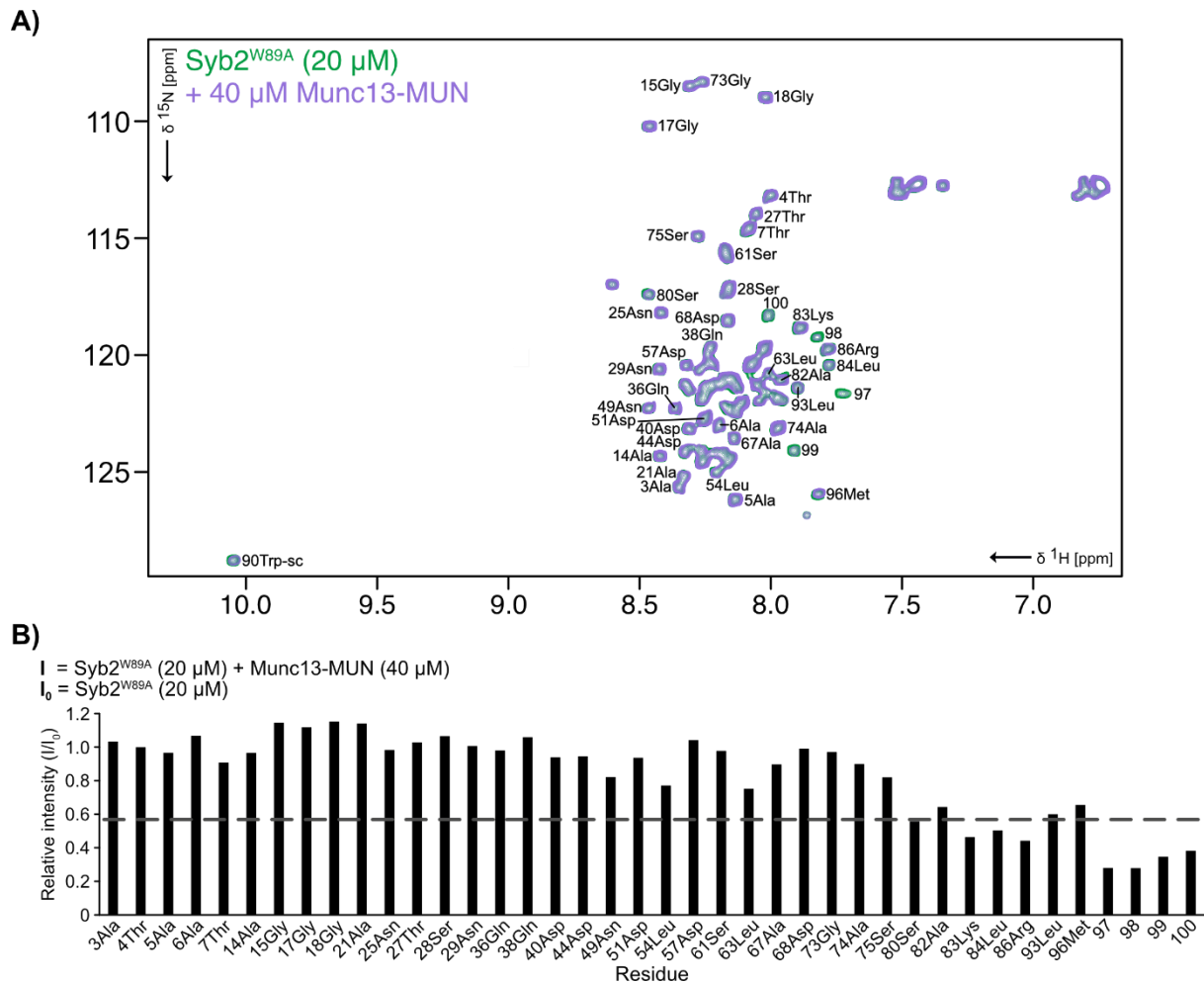


**Figure 4.22:**  $^1\text{H}$ - $^{15}\text{N}$ -HSQC spectra of  $\text{Syb2}^{\text{W89A}}$  (20  $\mu\text{M}$ ) before (green) and after the addition of Munc13-MUN (40  $\mu\text{M}$ , violet). The altered sequence at the JMD causes changes in chemical environments, resulting in peak shifts and making distinct assignments challenging, leading to the numbering of peaks instead. Line broadening was observed for the cross-peaks in the region corresponding to  $\text{Syb2}$ 's JMD. **B)** Quantification of relative cross-peak intensities ( $I/I_0$ ) upon the addition of Munc13-MUN reveals significant cross-peak broadening in the C-terminal JMD of  $\text{Syb2}^{\text{W89A}}$ . Newly emerged and numbered cross-peaks, likely representing residues of the JMD as well, also demonstrate significant line broadening. A grey dashed line indicates the cut-off, calculated as the average of relative peak intensities minus the standard deviation. Relative intensities below this threshold denote significant cross-peak broadenings.

The N-terminal part remained largely unaffected by the addition of the MUN domain, showing no significant cross-peak broadening, only a slight general decrease in relative intensity, possibly attributable to the overall increase in complex size. Only the C-terminal cross-peaks exhibited significant line broadening, suggesting that binding to Munc13-MUN through the JMD is still maintained (**Fig. 4.23 B**). However, upon comparing the relative peak intensities of the C-terminal region for  $\text{Syb2}^{\text{W90A}}$  to those of  $\text{Syb2}^{\text{W89A}}$ , we observed that cross-peak broadening is less pronounced, indicating a weaker binding of  $\text{Syb2}^{\text{W90A}}$  to Munc13-MUN compared to  $\text{Syb2}^{\text{W89A}}$ . This suggests that the tryptophan at position 90 plays a more crucial role in the binding than the tryptophan residue at position 89.



## Results

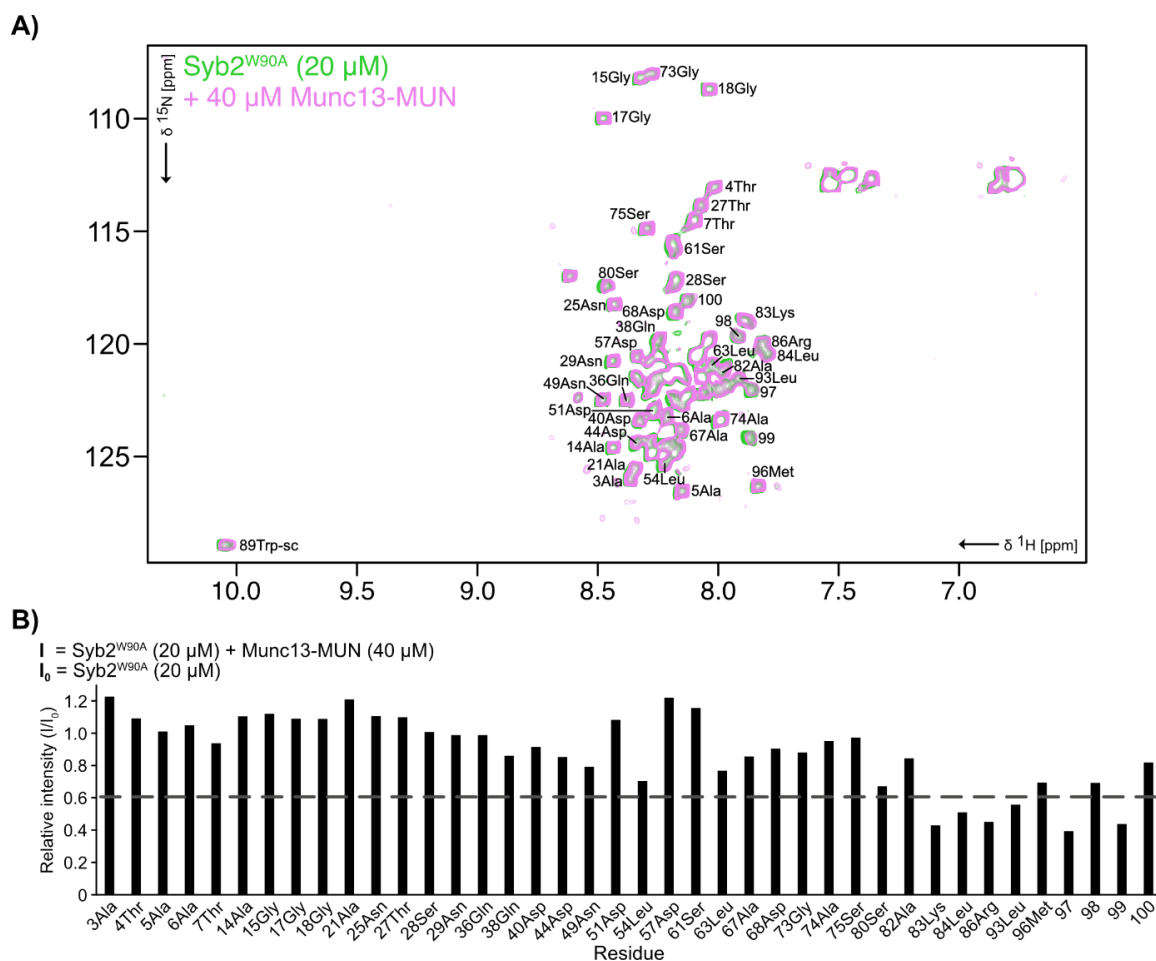


**Figure 4.23:**  $^1\text{H}$ - $^{15}\text{N}$ -HSQC spectra of  $\text{Syb2}^{\text{W90A}}$  (20  $\mu\text{M}$ ) before (mint) and after the addition of Munc13-MUN (40  $\mu\text{M}$ , pink). The altered sequence at the JMD causes changes in chemical environments, resulting in peak shifts and making distinct assignments challenging, leading to the numbering of peaks instead. Cross-peaks of the JMD exhibited diminished clarity and began to overlap with each other. **B)** Quantification of relative cross-peak intensities ( $I/I_0$ ) upon the addition of 40  $\mu\text{M}$  Munc13-MUN indicates considerable cross-peak broadening in the C-terminal JMD of  $\text{Syb2}^{\text{W90A}}$ . Only two of the newly emerged and numbered cross-peaks, presumably representing residues of the JMD, also exhibit significant line broadening. A grey dashed line indicates the cut-off, calculated as the average of relative peak intensities minus the standard deviation. Relative intensities below this threshold denote significant cross-peak broadenings.

Substantial disruption of binding was only observed when both tryptophan residues were substituted by alanine in  $\text{Syb2}^{\text{WWAA}}$ . The  $^1\text{H}$ - $^{15}\text{N}$ -HSQC spectrum for this construct closely resembles that of both  $\text{Syb2}^{\text{W89A}}$  and  $\text{Syb2}^{\text{W90A}}$  (**Fig. 4.24 A**). Upon addition of 40  $\mu\text{M}$  Munc13-MUN, the relative cross-peak intensity remained close to 1.0 for nearly all parts of  $\text{Syb2}^{\text{WWAA}}$ , indicating minimal line broadening (**Fig. 4.24 B**). Only a few cross-peaks in the C-terminal region exhibited slight, albeit significant, line broadening, suggesting that binding, albeit very weak, is still occurring. This could possibly be attributed to the earlier discussed interaction of Syb2 with the polar patch of Munc13-MUN, potentially allowing for a very weak interaction between Syb2 and the MUN domain. Interestingly, one newly emerged peak could be identified and numbered. More new peaks were not found, possibly due to overlap of the newly emerged peaks with the existing signals.

## Results

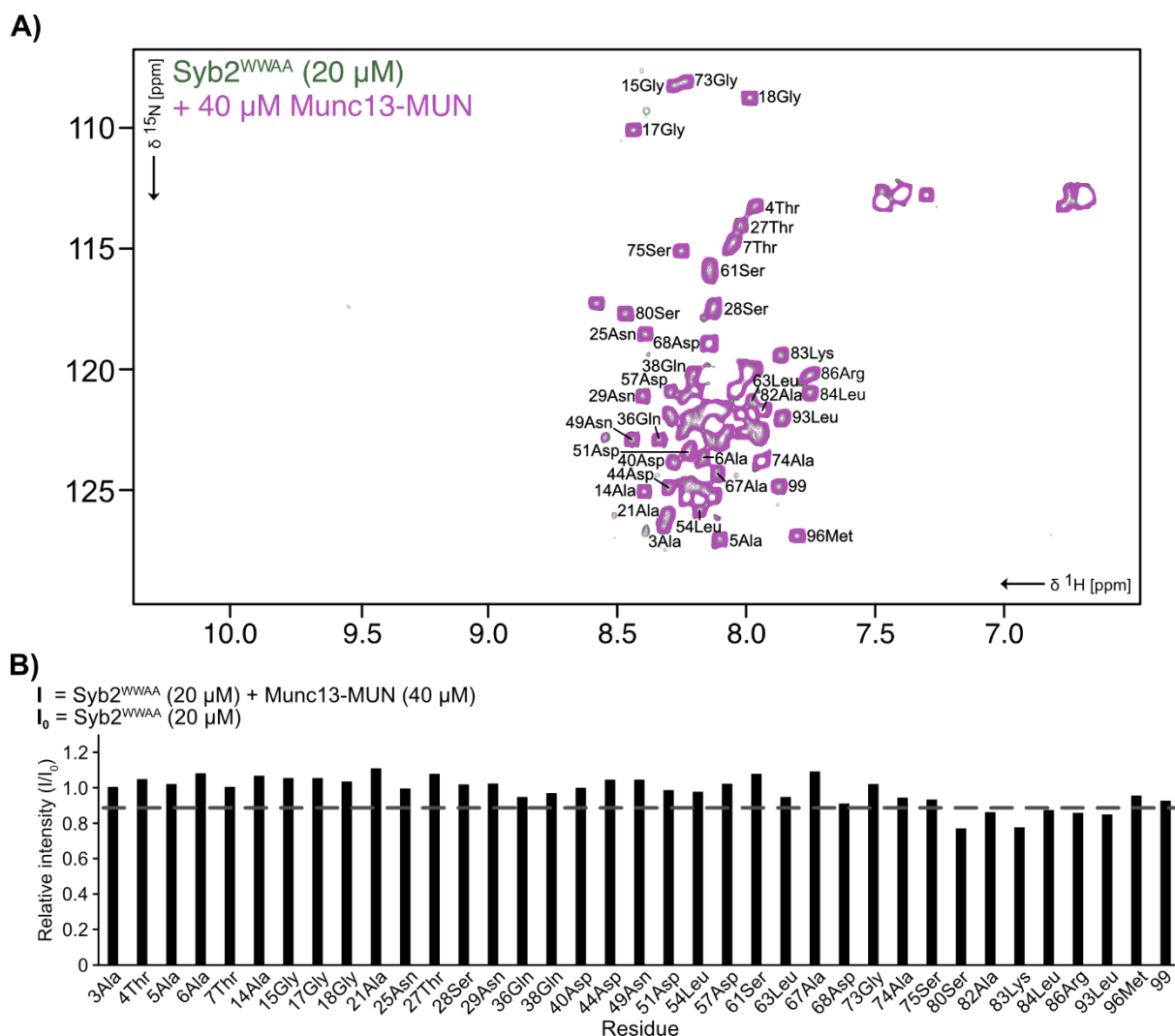


**Figure 4.24: A)**  $^1\text{H}$ - $^{15}\text{N}$ -HSQC spectra of  $\text{Syb2}^{\text{WVAA}}$  (20  $\mu\text{M}$ ) before (dark-green) and after the addition of Munc13-MUN (40  $\mu\text{M}$ , purple). The altered sequence at the JMD causes changes in chemical environments, resulting in peak shifts and making distinct assignments challenging, leading to the numbering of peaks instead. **B)** Quantification of relative cross-peak intensities ( $I/I_0$ ) upon the addition of 40  $\mu\text{M}$  Munc13-MUN reveals only minor or negligible line broadening of the C-terminal cross-peaks corresponding to  $\text{Syb2}$ 's JMD. Cross-peaks corresponding to the N-terminal part of  $\text{Syb2}$  remain largely unaffected by the addition of Munc13-MUN. A grey dashed line indicates the cut-off, calculated as the average of relative peak intensities minus the standard deviation. Relative intensities below this threshold denote significant cross-peak broadenings.

Summarizing the results,  $\text{Syb2}$  binds to the MUN domain of Munc13-1 through its C-terminal JMD with moderate binding affinity. The two tryptophan residues located in the center of the JMD, along with the directly neighboring residues, play a crucial role in the binding process, as evidenced by their significant line broadening with increasing addition of Munc13-MUN and the mutational analysis. Serine at position 80 also exhibits notable line broadening, possibly due to its involvement in a hydrophilic stretch of  $\text{Syb2}$ , which may interact with a polar patch of Munc13-MUN.

Individually, each tryptophan residue is capable of sustaining the binding of  $\text{Syb2}$  to the MUN domain of Munc13-1, albeit to a lesser extent compared to both tryptophan together. Additionally, it appears that tryptophan at position 90 plays a more pivotal role in binding than the tryptophan at position 89, as evidenced by the significantly reduced cross-peak broadening observed for  $\text{Syb2}^{\text{W90A}}$  compared to  $\text{Syb2}^{\text{W89A}}$ , indicating weaker binding of  $\text{Syb}^{\text{W90A}}$  compared to  $\text{Syb2}^{\text{W89A}}$ .

Alanine substitution of both tryptophan residues resulted in greatly reduced line broadening, indicating the abolition of binding.

The N-terminal part does not appear to be involved in the binding of Syb2 to Munc13-MUN, as indicated by the absence of line broadening or peak shifting in the cross-peaks, suggesting unrestricted internal movement of the N-terminal part of Syb2.

### 4.6.3. The C-terminal JMD of Syb2 shows weak binding to Munc18-1

In the context of the synaptic vesicle fusion site, the interaction between Syb2 and Munc13-MUN facilitates a close alignment with the Stx1:Munc18-1 complex situated on the presynaptic membrane. This alignment enables the subsequent formation of the template complex, where Munc18-1 binds both Stx1 and Syb2 [122, 264]. Investigations of the binding between Munc18-1 and Syb2, conducted by us and others, have revealed that the interaction is primarily mediated by the C-terminal part of Syb2, as indicated by cross-peak broadening (**Appendix Fig. 21 A, B**) [127]. Interestingly, the affected peaks partially coincide with the same region of Syb2 that has been identified as crucial for binding to the MUN domain of Munc13-1 [127]. This could suggest two possibilities: either the JMD exhibits promiscuity, and binding of that region to both Munc13-1 and Munc18-1 is nonspecific, or a handover mechanism occurs during the formation of the template complex. In this scenario, Syb2 initially binds to Munc13-MUN and is then positioned until it is transferred and binds to Munc18-1. The fact that the peak for W89 is more broadened than the peak for W90 during the binding of Syb2 to Munc18-1, while the opposite is observed during the binding of Syb2 to Munc13-MUN at comparable concentration ratios, suggests that the binding could potentially occur simultaneously (**Fig. 4.20** and **Appendix Fig. 21**). Assuming the angled positions of the residues in an alpha-helix relative to each other, it is possible that Syb2 is bound by two different proteins from two sides at the same region. In addition to the cross-peaks of the JMD being affected by line broadening, however, some of the cross-peaks of the SNARE motif also exhibit a notable decrease in intensity, although not significant, suggesting a weak interaction of the SNARE motif of Syb2 with Munc18-1 (**Appendix Fig. 21 B**). Additionally, there were no notable cross-peak shifts observed across the spectrum following the addition of Munc18-1 but only cross-peak broadening, indicating a slow to intermediate exchange rate.

Conversely, these measurements have only been conducted with the addition of Munc18-1 alone. However, in the context of synaptic vesicle fusion, Munc18-1 is known to form a complex with Stx1 on the presynaptic membrane before forming the template complex in which Syb2 binds to Munc18-1. Therefore, we investigated the interaction of Syb2 with the Stx1B:Munc18-1 complex (**Fig. 4.25 A, B**). Due to the tendency of Munc18-1 to aggregate during purification, we had to maintain a lower concentration for these measurements, with both the Stx1B:Munc18-1 complex and Syb2 set at a concentration of 10  $\mu$ M. To compensate for that, we extended the measurement time from 40 scans to 160 scans.

Similar to observations with the addition of Munc13-MUN, significant line broadening occurred for the cross-peaks corresponding to the JMD. However, there was no notable relative intensity

## Results

decrease for the SNARE motif compared to measurements with only Munc18-1. Interestingly, cross-peak broadening in the JMD was notably reduced compared to when Munc18-1 was added alone, even at a higher concentration ratio (2:1 Syb2:Munc18-1 shows more JMD broadening compared to 1:1 Syb2:(Munc18-1:Stx1B), **Fig. 4.25** and **Appendix Fig. 21**). This suggests that Syb2 binding to Munc18-1 might be enhanced without Stx1B present.

Although no significant cross-peak shifts were observed, a generally stronger relative intensity decrease for Syb2 was noted, expected due to the increased complex size compared to the  $^{15}\text{N}$ -labeled protein, albeit less pronounced than with Munc13-MUN [263].

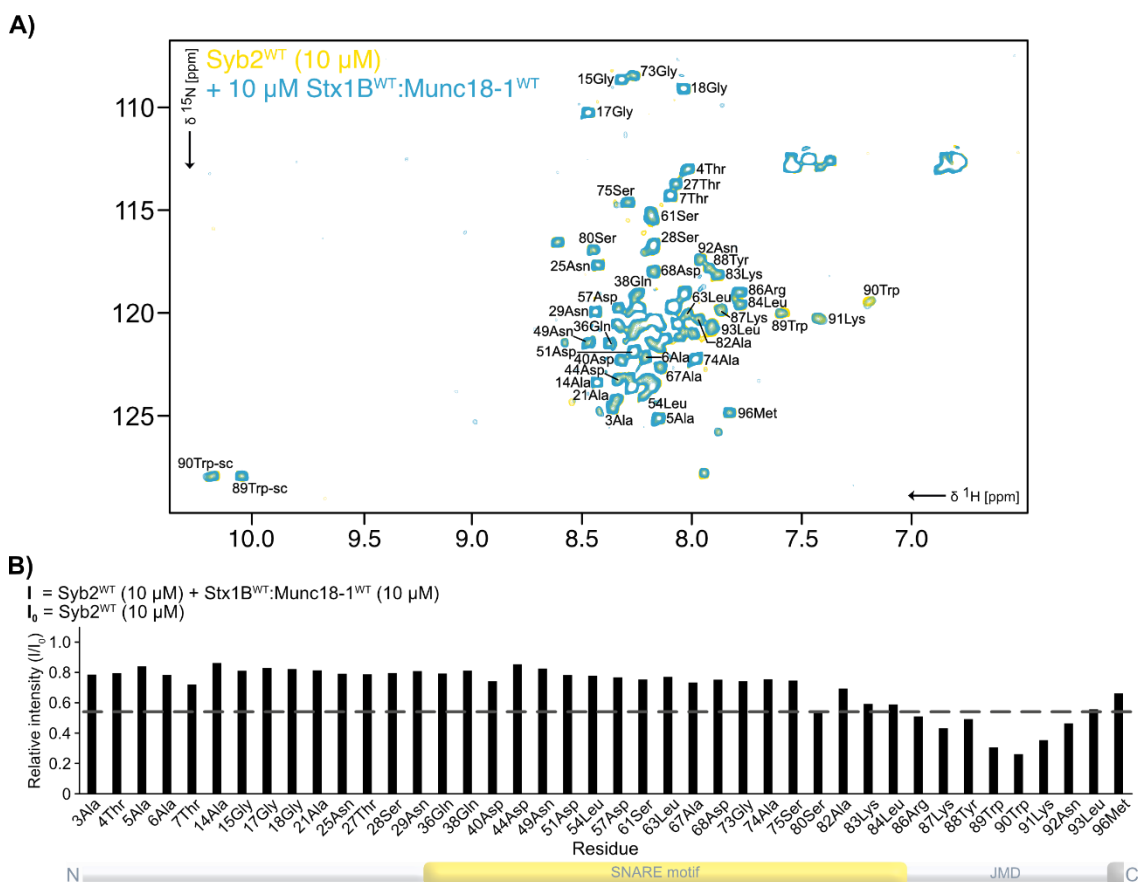


**Figure 4.25: A)**  $^1\text{H}$ - $^{15}\text{N}$ -HSQC spectra of Syb2<sup>WT</sup> (10  $\mu\text{M}$ ) before (yellow) and after the addition of the Stx1B<sup>WT</sup>:Munc18-1<sup>WT</sup> complex (10  $\mu\text{M}$ , light-blue). No significant cross-peak shifts were observed, but rather cross-peak broadening, particularly evident for the cross-peaks corresponding to the JMD of Syb2<sup>WT</sup>. **B)** Quantification of relative cross-peak intensities ( $I/I_0$ ) of Syb2<sup>WT</sup> upon the addition of 10  $\mu\text{M}$  Stx1B<sup>WT</sup>:Munc18-1<sup>WT</sup> complex reveals overall decrease of the cross-peak intensities and significant line broadening in the C-terminal JMD of Syb2. A grey dashed line indicates the cut-off, calculated as the average of relative peak intensities minus the standard deviation. Relative intensities below this threshold denote significant cross-peak broadenings.

# Results

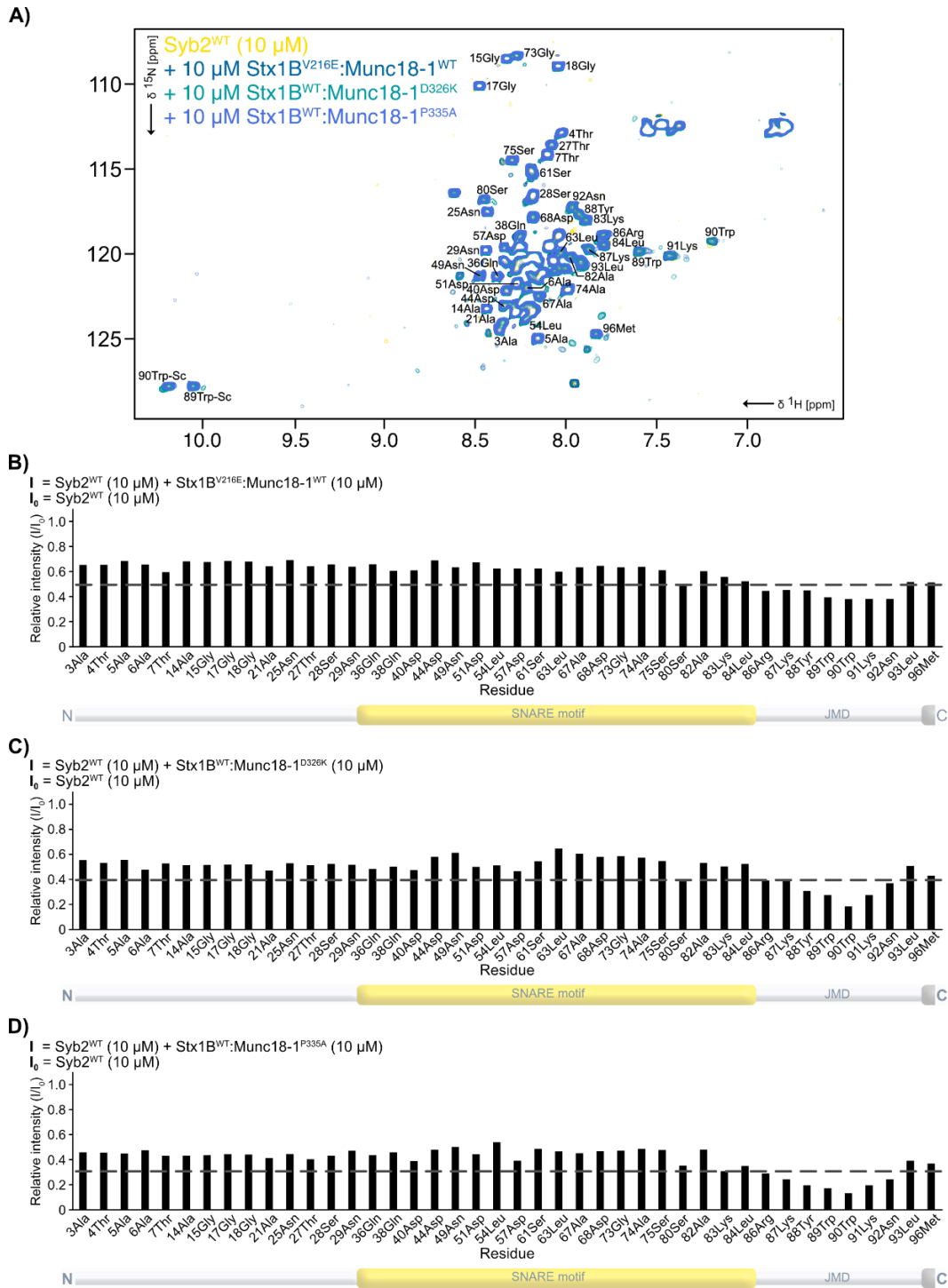


**Figure 4.26: A)**  $^1\text{H}$ - $^{15}\text{N}$ -HSQC spectra of  $\text{Syb2}^{\text{WT}}$  ( $10 \mu\text{M}$ ) before (yellow) and; after the addition of the  $\text{Stx1B}^{\text{V216E}}:\text{Munc18-1}^{\text{WT}}$  complex ( $10 \mu\text{M}$ , blue); after the addition of the  $\text{Stx1B}^{\text{WT}}:\text{Munc18-1}^{\text{D326K}}$  complex ( $10 \mu\text{M}$ , teal); after the addition of the  $\text{Stx1B}^{\text{WT}}:\text{Munc18-1}^{\text{P335A}}$  complex ( $10 \mu\text{M}$ , sky-blue). None of the recorded spectra exhibit significant differences compared to the  $\text{Syb2}^{\text{WT}}$  spectrum in terms of cross-peak dispersion and peak characteristics. Only cross-peak broadening is observed for the peaks corresponding to the JMD of Syb2. **B)-D)** Quantification of relative cross-peak intensities ( $I/I_0$ ) upon the addition of; **B)**  $10 \mu\text{M}$   $\text{Stx1B}^{\text{V216E}}:\text{Munc18-1}^{\text{WT}}$  complex; **C)**  $10 \mu\text{M}$   $\text{Stx1B}^{\text{WT}}:\text{Munc18-1}^{\text{D326K}}$  complex, **D)**  $10 \mu\text{M}$   $\text{Stx1B}^{\text{WT}}:\text{Munc18-1}^{\text{P335A}}$  complex. Diagrams depict an overall decrease in cross-peak intensity, with the least pronounced decrease observed for the  $\text{Stx1B}^{\text{V216E}}:\text{Munc18-1}^{\text{WT}}$  complex and the most pronounced for the  $\text{Stx1B}^{\text{WT}}:\text{Munc18-1}^{\text{P335A}}$  complex. Significant cross-peak broadening is evident upon the addition of all three mutant complexes, with the least significant broadening observed for the addition of the  $\text{Stx1B}^{\text{V216E}}:\text{Munc18-1}^{\text{WT}}$  complex and the most significant for the addition of the  $\text{Stx1B}^{\text{WT}}:\text{Munc18-1}^{\text{P335A}}$  complex. A grey dashed line indicates the cut-off, calculated as the average of relative peak intensities minus the standard deviation. Relative intensities below this threshold denote significant cross-peak broadenings.

As we did not gain sufficient insight into the binding of Syb2 to the Stx1B:Munc18-1 complex, we tried to enhance the binding of Syb2 to Munc18-1 by inducing the unfolding of the furred loop of Munc18-1, thereby exposing the binding region for the SNARE motif of Syb2. This would allow Syb2 to align next to the SNARE motif of Stx1, forming the template complex [69, 124, 142]. To achieve this, we introduced various mutations on both Munc18-1, including Munc18-1<sup>D326K</sup> and Munc18-1<sup>P335A</sup>, and on Stx1B, such as Stx1B<sup>V216E</sup>, as previously proposed and employed in other studies [69, 141, 178].

When repeating the measurements with the Stx1B<sup>V216E</sup>:Munc18-1 complex, cross-peaks of the JMD exhibited significant line broadening yet again (**Fig. 4.26 A, B**). Additionally, the previously observed general relative intensity decrease was further enhanced (**Fig. 4.26 B**). However, a distinct relative intensity-decrease for the cross-peaks corresponding to the SNARE motif was still not apparent.

This trend continued further for the measurements with Stx1B:Munc18<sup>D326K</sup> and Stx1B:Munc18<sup>P335A</sup> (**Fig. 4.26 A, C** and **D**). While line broadening for the cross-peaks of the JMD indeed became increasingly pronounced, no significant changes were observed for the SNARE motif region.

However, overall, the relative intensity decreased more strongly, particularly evident in the interaction of Syb2 with Stx1B:Munc18<sup>P335A</sup> (**Fig. 4.26 C, D**). This suggests that the introduction of different mutations might have enhanced the overall binding of Syb2 to the Stx1B:Munc18-1 complex to a certain degree, but it does not provide a definitive answer regarding the exact binding regions, especially in regards of the SNARE motif of Syb2, apart from the JMD.

$I$  = Syb2 + Stx1B:Munc18-1 Mutant Complex  
 $I_0$  = Syb2 + Stx1B:Munc18-1 Wild-Type Complex

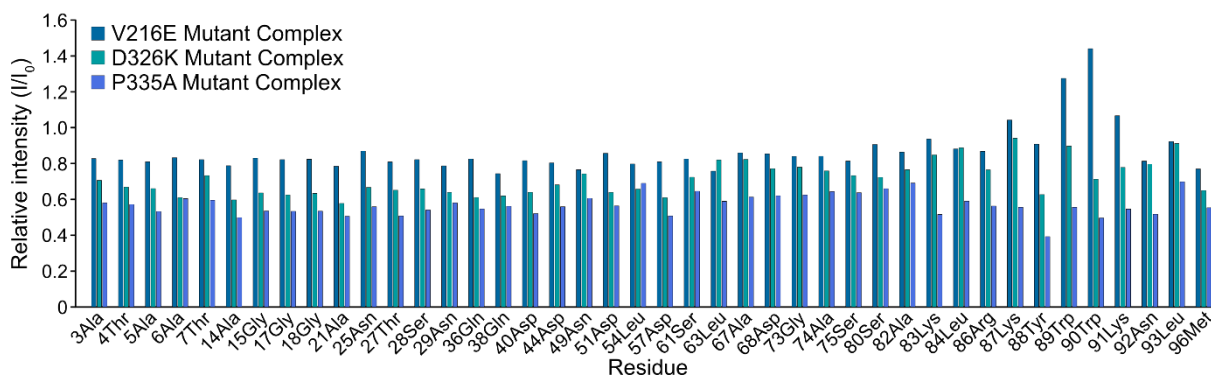


**Figure 4.27:** Relative intensities of Syb2 in interaction with the mutant complexes set in relation to the relative intensities of Syb2 in interaction with the Stx1B<sup>WT</sup>:Munc18-1<sup>WT</sup> complex. While the interaction of Syb2 with the Stx1B<sup>WT</sup>:Munc18-1<sup>P335A</sup> complex exhibited a notable decrease in intensities, particularly for the N-terminal residues and the residues corresponding to the C-terminal JMD, there were no distinct differences observed in the interaction of Syb2<sup>WT</sup> with the Stx1B<sup>WT</sup>:Munc18-1<sup>D326K</sup> complex, except for an overall reduction in cross-peak intensity. Conversely, Syb2's interaction with the Stx1B<sup>V216E</sup>:Munc18-1<sup>WT</sup> complex appeared diminished compared to the interaction with the wild-type complex, as indicated by relative intensity values exceeding 1.0, especially in the C-terminal JMD of Syb2.

Strikingly, upon comparing the relative intensities of Syb2 between the addition of the wild-type complex and the addition of the mutant complexes, it was notable that the cross-peak broadening of the JMD of Syb2 was significantly reduced in the measurements with Stx1B<sup>V216E</sup>:Munc18-1. This

is evidenced by the relative intensity values associated with the JMD, resulting in a value greater than 1.0 (**Fig. 4.27**). For the measurements with the Stx1B:Munc18-1<sup>D326K</sup> complex, only slight reductions were observed, whereas with the Stx1B:Munc18<sup>P335A</sup> complex, cross-peak broadenings were significantly pronounced (**Fig. 4.27**).

These results suggest that the interaction of Syb2 with the Stx1B:Munc18-1 complex is significantly enhanced only by the introduction of the Munc18-1<sup>P335A</sup> mutation. However, interaction is reduced when the Stx1B<sup>V216E</sup> mutation is introduced compared to the wild-type complex.

In conclusion, the C-terminal JMD region of Syb2 primarily engages with Munc18-1, yet this region also overlaps with the crucial binding site for Munc13-MUN, implying a potential promiscuity or handover mechanism during complex formation, possibly with a simultaneous binding of Munc18-1 and Munc13-MUN to Syb2. Furthermore, while a slight cross-peak broadening in the SNARE motif was evident in <sup>15</sup>N-Syb2 measurements with Munc18-1 alone, this effect was not consistently observed in interactions with the Stx1B:Munc18-1 complex. Moreover, the binding of Syb2 to Munc18-1 significantly increased when Stx1B was present, as indicated by more pronounced line broadening. Inducing the unfolding of Munc18-1's furred loop enhances Syb2 binding, notably with the Munc18-1<sup>P335A</sup> mutation. However, Stx1B<sup>V216E</sup> diminishes binding of Syb2 to the Munc18-1:Stx1B complex.

#### **4.7. Structural analysis of the SNARE complex formation machinery *via* XL-MS**

While NMR provided detailed insights into the binding interfaces and structural behavior of Syb2 in combination with Munc13-MUN and Munc18-1, certain results remained inconclusive, leaving gaps in our understanding of the interactions within the SNARE complex formation machinery as a whole. The observed impact on the JMD of Syb2 upon addition of both Munc13-MUN and Munc18-1 individually raised questions about the specificity and timescale of the binding between Syb2 and Munc13-MUN and Munc18-1, respectively. Moreover, we lacked insight into the interactions from the perspective of the unlabeled proteins. Although we observed cross-peak broadening in specific regions of Syb2, indicating binding, we were unable to ascertain which regions were affected by Munc13-MUN and Munc18-1. While existing models and structures could provide some insight, they may not fully represent the interactions under our experimental conditions. Therefore, simultaneous structural analysis of all participating proteins could offer valuable insights into their interactions. One method that provides this capability is cross-linking mass spectrometry (XL-MS). In recent years, XL-MS has emerged as a powerful tool for studying the three-dimensional structure of proteins and protein interactions. It allows for the simultaneous extraction of information regarding both the connectivity and structure of proteins and protein complexes [232, 265, 266]. Cross-linking reagents are typically small molecules equipped with two reactive groups, enabling the covalent linkage of amino acid residues. Following proteolytic digestion of the protein mixture, mass spectrometry is utilized to identify the cross-linked peptides. This method relies on the spatial proximity of the two amino acid residues for successful conjugation, thereby imposing a distance

constraint on the protein assembly. Such constraints are crucial for structural analysis and the identification of protein-protein interactions [232, 265, 267].

In the Freund Lab, we have been employing XL-MS to pinpoint interaction sites within protein complexes and unveil the structural arrangements of multi-protein complexes. For that, we collaborated with the mass spectrometry core facility at the Leibniz Forschungsinstitut für Molekulare Pharmakologie (FMP), overseen by Prof. Dr. Fan Liu [268]. We conducted the sample preparation in-house and dispatched the processed samples to the FMP for analysis, subsequently receiving the results.

However, this infrastructural setup is quite cumbersome, as the laboratories are located in different areas and the samples must first be sent to the mass spectrometry core facility of the FMP. Furthermore, the core facility is not only utilized by our laboratory but also by other labs that require their samples to be analyzed there. All of this leads to a very time-consuming issue, where long waiting times can occur until results are received. Additionally, experiment optimizations are also difficult or very slow to implement as a result.

For this reason, there has been a longstanding endeavor to implement the cross-linking method in our laboratory, especially considering the excellent equipment of the mass spectrometry division of the BioSupraMol core facility at the Freie Universität Berlin [269].

Being part of the same Collaborative Research Centre (CRC) 958 "Scaffolding of Membranes - Molecular Mechanism and Cellular Functions" Prof. Dr. Fan Liu has graciously agreed to share her workflow and the necessary software support with us as part of fostering good scientific exchange. It was then up to us to integrate and establish the cross-linking mass spectrometry workflow in our laboratories, employing the SNARE complex formation machinery as experimental model.

### **4.7.1. Detailed workflow of cross-linking mass spectrometry using the bottom-up approach**

Chemical XL-MS experiments can be conducted in two primary ways: the 'bottom-up' and 'top-down' approaches [270]. In the 'top-down' approach, cross-linked proteins are directly fragmented inside the mass spectrometer, eliminating the need for enzymatic digestion. This method offers the advantage of bypassing the separation of reacted proteins from the cross-linking reaction mixture before mass spectrometric analysis, as this is achieved through 'gas phase purification' within the mass spectrometer [265].

However, the top-down approach has several limitations. Analyzing large protein assemblies can be challenging because intact proteins or complexes may be too large to be efficiently ionized and fragmented in the mass spectrometer, leading to incomplete or ambiguous data. This approach also requires extremely high resolution and sensitivity to distinguish between the various fragments of large proteins, a capability that current mass spectrometers may struggle to achieve for very large complexes. Additionally, the efficiency of fragmentation is often lower for large, intact proteins compared to smaller peptides generated in the bottom-up approach. This can result in fewer identifiable fragments and a less comprehensive understanding of the protein's structure [271, 272].



## Results

Interpreting the data from top-down experiments is more complex and computationally intensive than bottom-up methods. The data analysis software must be capable of handling the larger and more complex datasets generated by this approach. Moreover, in top-down XL-MS, the cross-linking sites may not be as comprehensively covered as in bottom-up approaches, potentially limiting the ability to map interactions accurately within large protein complexes [273, 274].

Because of that, the majority of XL-MS studies typically follow the 'bottom-up' approach, where cross-linked proteins undergo enzymatic digestion, and the resulting peptide mixtures are analyzed using liquid chromatography-tandem mass spectrometry (LC-MS/MS). The positions of the cross-linked amino acids, along with the length of the cross-linker, impose distance constraints on the 3D structure of the protein or protein complex. By integrating these sparse distance constraints and using them as a foundation for computational modeling, XL-MS can help to infer protein 3D structures and delineate protein interfaces [270].

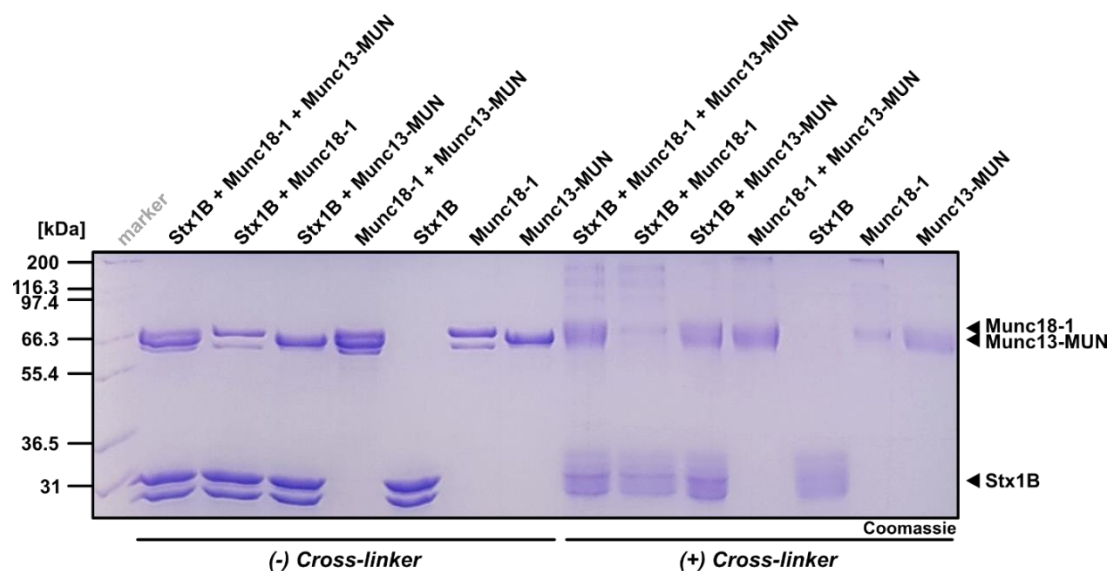


**Figure 4.28:** Coomassie-stained SDS-PAGE of analyzed proteins before and after cross-linking (unmodified full-size Coomassie-stained SDS-PAGE in **Appendix Fig. 22**). Addition of a cross-linker induces blurred bands in SDS-PAGE due to variations in protein masses caused by different numbers of cross-linkers bound to the protein. Additionally, high running complex-bands above 100 kDa are evident.

MS analysis of cross-linked and digested peptides offers several advantages: Firstly, the mass of the protein or protein complex under scrutiny is theoretically unlimited since enzymatic digestion occurs post cross-linking reaction, and MS analysis is conducted at the peptide level. Secondly, MS analysis is swift and requires only small protein amounts. Finally, the protein's 3D structure and flexibility are accurately represented as the cross-linking reaction can be conducted in a native-like environment. This method allows for the study of membrane proteins, post-translational modifications, and splicing variants [270].

The availability of numerous cross-linking reagents with various specificities and a broad range of spacer distances enables the design of precise experiments tailored to the specific protein system under investigation.

In our approach, we adhered to the 'bottom-up' methodology. We cross-linked proteins of the SNARE complex formation machinery using disuccinimidyl sulfoxide (DSSO) or disuccinimidyl dibutyric urea (DSBU), followed by quenching the reaction with Tris (**Fig. 4.28**). SDS-PAGE allowed us to track the successful cross-linking of proteins. Typically, proteins without cross-links display sharp bands in SDS-PAGE. However, upon adding the cross-linker, the bands become blurred (**Fig. 4.28**). This occurs because the masses of the proteins vary slightly, depending on the number of intramolecular cross-linkers bound to each protein molecule. Additionally, high-running complex bands are visible. These could comprise heteromolecular complexes, with the potential for homo-dimer formation as well.

Subsequently, the cross-linked proteins were denatured and linearized by adding 6 M urea, while any possible disulfide bonds were reduced using DTT. To prevent the re-formation of disulfide bonds, free thiol groups on cysteine residues were then alkylated using iodoacetamide.

The processed proteins were sequentially digested with endoproteinase Lys-C and trypsin. Both enzymes cleave proteins on the C-terminal side of lysine, and, in the case of trypsin, also arginine residues. This results in various peptide species: intermolecular cross-linked peptides, where the peptides derive from two different proteins; intramolecular cross-linked peptides, where the peptides derive from the same protein; and mono-linked peptides, where a peptide is bound to a cross-linker but is not linked to a second peptide (in rare cases, the cross-linker even connects two residues within the same peptide, **Fig. 4.29**).

Subsequently, the resulting peptides were purified using StageTips, eluted, dried, resuspended and analyzed by LC-MS/MS. Within the LC system, the peptides are separated using a C18 reversed-phase column by their hydrophobicity. Shorter peptides, which typically have lower charge states, are less hydrophobic and therefore elute earlier in the gradient. In contrast, longer peptides exhibit higher hydrophobicity and are more likely to carry multiple charges, causing them to elute later as the hydrophobicity of the mobile phase increases (**Appendix Fig. 23**). This separation is vital for resolving overlapping peptide signals and reducing sample complexity, thereby enhancing the detection and identification of cross-linked peptides.

The separated peptides are subsequently introduced into the mass spectrometer through an electrospray ionization source and subjected to MS/MS analysis (described in **Chapter 3.4.5.1, Fig. 4.29**) [232].

The identification of cross-linked peptides processes in a similar manner to linear peptides. For linear peptides, measured peptide masses are matched against a protein sequence database. The fragmentation spectrum (MS/MS spectrum) is then utilized to determine the peptide sequence that best corresponds to the observed fragment signals from among these candidates. To apply the same workflow to cross-linked peptides, all potential cross-linked peptides must be predicted by performing an *in silico* digestion of all proteins and generating all possible pairwise combinations of peptides. Any peptide containing a residue capable of cross-linking in the actual experiment must be considered. Pairing results in  $\frac{n^2+n}{2}$  possible cross-links for n peptides. This quadratic problem poses a challenge for search algorithms and evaluating any match between a spectrum and a

candidate peptide pair due to the high risk of random matches in a large database. However, this problem is simplified for the analysis of protein complexes, as only those proteins present in the sample need to be considered [232, 270].

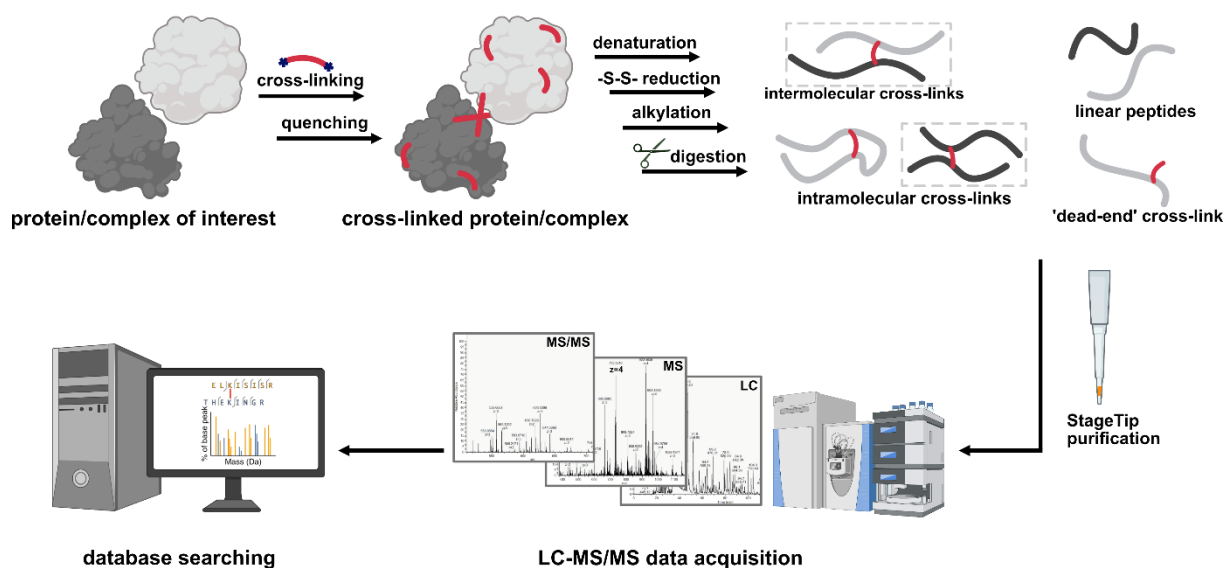


**Figure 4.29:** Schematic overview of the general cross-linking mass spectrometry workflow. Proteins of interest are first cross-linked. After quenching, the cross-linked proteins are denatured, reduced, alkylated and digested. The resulting peptides are then purified through StageTips and analyzed by LC-MS/MS. The resulting data are analyzed for cross-link identification.

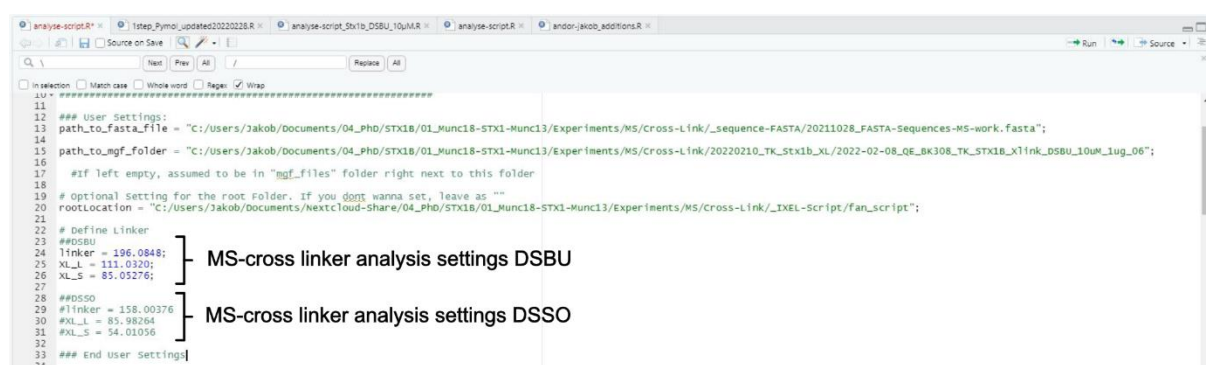
In the recent years, many algorithms and programs emerged to identify cross-links in proteins and in multi-protein complexes [275-280]. For this work, we utilized the data analysis algorithm XlinkX v2.0 developed by Prof. Dr. Fan Liu, an advancement of the XlinkX search engine [242, 281]. The previous version, XlinkX v1.0, was employed in workflows integrating MS-cleavable cross-linkers and a dual fragmentation strategy using sequential collision-induced dissociation (CID) and electron transfer dissociation (ETD) MS/MS to identify cross-links against full-proteome databases [281]. This approach relied heavily on high-quality MS<sup>3</sup> spectra for confident sequencing, limiting its applicability to ETD-enabled instruments and a specific set of MS-cleavable cross-linkers. To overcome these limitations, XlinkX v2.0 was developed, introducing innovative MS acquisition strategies and data analysis algorithms suitable for MS/MS and MS<sup>3</sup> fragmentation approaches on Lumos or Orbitrap Fusion instruments. It also implemented an intensity-based precursor mass determination strategy, enabling the identification of cross-links even with non-ideal fragmentation patterns. Details about the operating principle can be found in Liu et. al (2017) [242].

#### 4.7.2. DSSO and DSBU: choosing, analyzing, and evaluating cross-linkers

The discussed analysis strategies are broadly applicable to MS-cleavable cross-linkers with distinctive fragmentation patterns [238, 282]. Recently, MS-cleavable cross-linkers have become more prominent in structural protein studies and interaction networks due to the increased complexity of substrates, leading to larger peptide datasets. Identifying cross-linked spectra is challenging because each product involves two peptides, exponentially increasing the potential

cross-links for a given precursor mass. This growth complicates specific identification [283]. Additionally, co-fragmentation of linked peptides in the same MS/MS spectrum can reduce fragmentation efficiency, hindering identification [284]. To mitigate this, MS-cleavable cross-linkers should have labile covalent bonds, ensuring preferred fragmentation over the peptide backbone during collisional activation. This characteristic is particularly useful for data-dependent analyses, leveraging the unique fragment ion signatures in CID experiments.

In our studies, we utilized the MS-cleavable cross-linkers disuccinimidyl sulfoxide (DSSO) and disuccinimidyl dibutyric urea (DSBU). To do this, we expanded the script of the XlinkX v2.0 search algorithm to include an additional option for identifying cross-links with DSBU, while DSSO was already available (**Fig. 4.30**).



```

11 *****
12 ## User Settings:
13 path_to_fasta_file = "c:/Users/Jakob/Documents/04_PhD/STX1B/01_Munc18-STX1-Munc13/Experiments/MS/Cross-Link/_Sequence-FASTA/20211028_FASTA-Sequences-MS-work.fasta";
14
15 path_to_mgf_folder = "c:/Users/Jakob/Documents/04_PhD/STX1B/01_Munc18-STX1-Munc13/Experiments/MS/Cross-Link/20220210_TK_STX1B_XL/2022-02-08_QE_BK308_TK_STX1B_XL1nk_DSBU_10uM_lug_06";
16
17 #if left empty, assumed to be in "mgf_files" folder right next to this folder
18
19 # optional setting for the root folder. if you dont wanna set, leave as ""
20 rootLocation = "c:/Users/Jakob/Documents/nextcloud-share/04_PhD/STX1B/01_Munc18-STX1-Munc13/Experiments/MS/Cross-Link/_IXEL-Script/fan_script";
21
22 # Define Linker
23 ##DSBU
24 linker = 196.0848;
25 XL_L = 111.0320;
26 XL_S = 85.05276;
27
28 ##DSSO
29 linker = 158.00376;
30 #XL_L = 85.98264;
31 #XL_S = 54.01056;
32
33 ## End user Settings
34

```

**Figure 4.30:** Excerpt of the modified XlinkX v2.0 search algorithm script displaying the user settings, allowing configuration of the file paths for the .FASTA-file and the Mascot Generic Format (.MGF)-file. Additionally, users can specify the cross-linkers used in the experiments. Here, the masses (total mass and fragment masses after MS cleavage, XL\_L = long fragment, XL\_S = short fragment) for the DSBU cross-linker were added, enabling the search engine to identify peptides cross-linked *via* DSBU. Script is executed in R (R-Studio v.1.4, Posit PBC (Boston, USA)).

While XL-MS studies with DSSO are best conducted using a combined MS/MS-MS<sup>3</sup> acquisition approach – where CID-MS/MS at low collision energy cleaves the cross-linker to generate signature ions of both cross-linked peptides, followed by MS<sup>3</sup> fragmentation of these ions via CID and/or ETD to fragment the peptide backbone – DSBU allows for simpler MS/MS acquisition. DSBU can simultaneously generate cross-linker and peptide backbone fragments in a single MS/MS step [242, 285, 286]. This capability enables XL-MS studies with DSBU to be conducted on any high-resolution mass spectrometer with tandem MS capabilities. Yet, DSSO can be used under these conditions as well.

DSSO and DSBU contain two N-hydroxysuccinimide (NHS) ester functional groups and two symmetric MS-labile bonds (MS-cleavable C-S bond adjacent to the sulfoxide for DSSO, MS-cleavable N-C bond adjacent to the keto-group, **Fig. 4.31**). The NHS ester reacts efficiently with primary amine groups to form stable amide bonds. This reaction targets lysine residues, and possibly the N-terminus of proteins. DSSO and DSBU have a spacer length of 10.3 Å and 12.5 Å respectively, making them well suited for detecting protein interaction interfaces of protein complexes and generating informative distance constraints (**Fig. 4.31**) [238, 239].

Using MS/MS, the cross-linked peptides generate characteristic fragmentation patterns, appearing as doublet signals under collisional dissociation. The DSBU cross-linker produces distinctive fragment ion patterns attributed to a mass increase of 85 u (short fragment) or 111 u (long fragment) at the cross-linked peptides in CID-MS/MS experiments (**Appendix Fig. 23 A**). Consequently, fragmentation of DSBU cross-linked peptides shows two doublets with a difference of 26 u each as cleavage occurs at either of the two NH–C=O bonds in the central urea moiety. This results in both peptides being modified with short and long fragments of the linker in MS/MS spectra, producing two doublet signals (**Fig. 4.32 C** and **Appendix Fig. 23 B**) [239, 284].

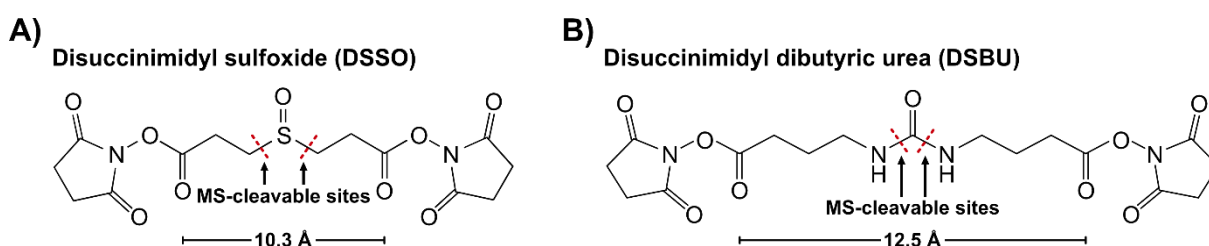


**Figure 4.31:** Molecular structure and linker length of the MS-cleavable cross-linkers **A)** disuccinimidyl sulfoxide (DSSO) and **B)** disuccinimidyl dibutyric urea (DSBU). MS cleavage leads to the creation of a short and a long fragment, creating a unique fragment pattern in the MS/MS spectrum.

Similarly, DSSO-cross-linked peptides can be distinguished based on their unique fragmentation patterns in MS/MS spectra and facilitate automated data analysis. During CID analysis of an interpeptide cross-link, cleavage of one C–S bond adjacent to the sulfoxide yields a pair of peptide fragments: one is an alkene (+54 u, short fragment) and the other is modified with sulfenic acid, losing a water molecule (+86 u, long fragment) (**Appendix Fig. 24 B**). Fragmentation of DSSO cross-linked peptides results in two doublets with a difference of 32 u each, due to the cleavage of either of the two symmetric C–S bonds (**Appendix Fig. 24 A**). In this respect, the DSSO cross-linker generates fragmentation patterns similar to those of the DSBU cross-linker (**Appendix Fig. 25 A**) [238, 284].

The characteristic fragment ion patterns of the DSBU linker simplify the identification of cross-linked species from complex mixtures and greatly reduce the potential of identifying false-positive cross-links. Consequently, these signature ions facilitate straightforward and automated identification (**Fig. 4.32**).

Moreover, by directly calculating the masses of connected peptides from the masses of these signature ions, the search space for potential cross-linked products can be significantly reduced compared to approaches employing non-cleavable reagents [282].

We assessed the efficacy of these two cross-linkers under various protein concentrations, considering that protein yield can vary significantly between different proteins and purification runs. For this, we used Stx1B as a model protein due to its abundant and evenly distributed lysine residues throughout its amino acid sequence, and cross-linked it at concentrations ranging from 5  $\mu$ M to 40  $\mu$ M (**Fig. 4.33**).

## Results

Notably, the number of cross-links generated by DSSO was consistently significantly higher than that of DSBU across all protein concentrations tested. Additionally, the number of identified cross-links increased with higher protein concentration for both cross-linkers (**Fig. 4.33 A**).

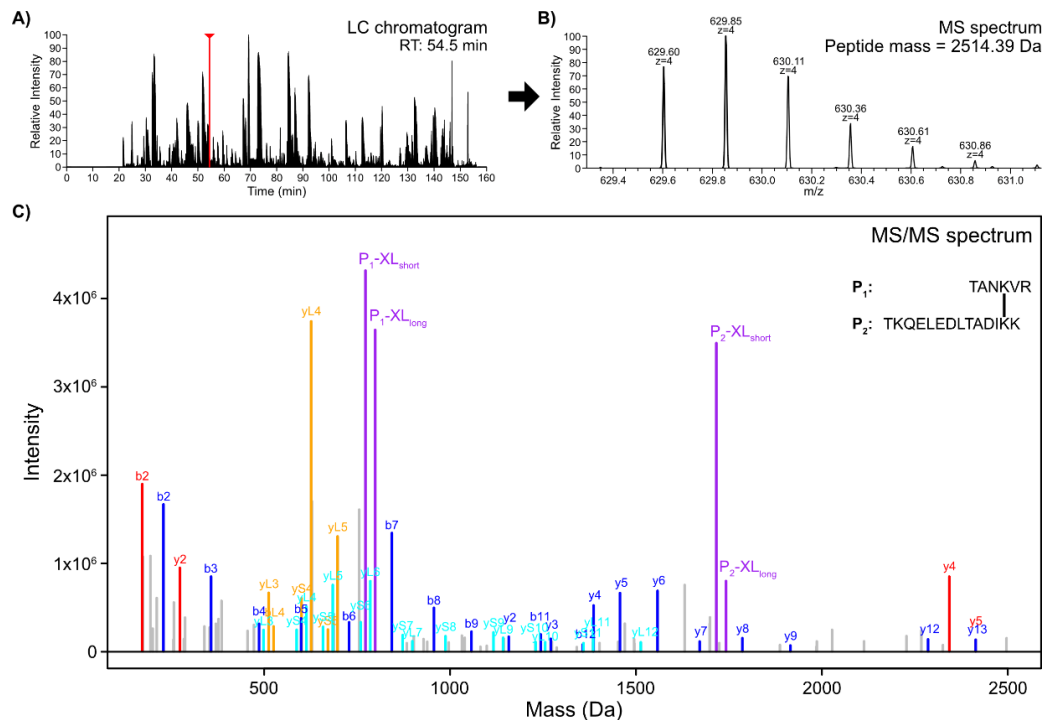


**Figure 4.32:** **A)** Exemplary LC chromatogram of an LC-MS/MS run displaying the separation of peptides over a 160-minute gradient, with eluted peptides measured *via* MS. **B)** MS spectrum of a parent peptide ion with a peptide mass of 2514.40 Da and charge state 4+, along with corresponding isotope signals, eluted at a retention time of 54.5 min. **C)** MS/MS spectrum confirming the interpeptide cross-link between K87 and K81 of Stx1B. All peaks are charge deconvoluted. Characteristic b- and y-fragment ions resulting from cleavage of peptide P<sub>1</sub> and P<sub>2</sub> are labeled in red and blue, respectively. Signature peaks of peptides P<sub>1</sub> and P<sub>2</sub> resulting from the cleavage of the DSSU cross-linker are labeled purple (XL<sub>short</sub>/XL<sub>long</sub> indicates whether the peptide contains the shorter or longer arm of DSSU after cleavage). Characteristic b- and y-fragment ions resulting from backbone cleavage of peptide P<sub>1</sub> or peptide P<sub>2</sub> and additional cleavage of the DSSU cross-linker are labeled in orange and cyan, respectively.

Upon closer analysis of the identified cross-links and the lysine residues involved, we noted instances where cross-links occurred between the same lysine residues. These instances were unmistakably attributed to homo-dimers. As Stx1B is not particularly known to form homo-dimers, it can be assumed that these are probably nonspecific and could also arise from aggregation. Interestingly, for DSSO, the number of cross-links between the same lysine appeared to be independent of protein concentration, whereas for DSBU, this number increased with higher protein concentration (**Fig. 4.33 B**).

Furthermore, there were cross-links observed with a significant overlength according to the 3D structure (PDB: 3C98). The maximum possible distance for a cross-link Ca-Ca bond is typically calculated as the sum of the linker length plus twice the length of the lysine side chain ( $2 \times 6.4 \text{ \AA} = 12.8 \text{ \AA}$ ), with an additional tolerance ranging between 2-5  $\text{\AA}$ . Given that DSSO and DSBU have fixed lengths of 10.3  $\text{\AA}$  and 12.5  $\text{\AA}$  respectively, this would result in a total maximum range of 28.1  $\text{\AA}$  for DSSO and 30.3  $\text{\AA}$  for DSBU [242, 287].

Considering that we measured the length of the recorded cross-links based on an existing crystal structure and recognizing that the actual structure may vary slightly due to molecular dynamics under solvent conditions, here we only considered cross-links with a distance of  $\geq 29$  Å for DSSO and  $\geq 31$  Å for DSBU as overlength cross-links. These typically occur between lysine residues at two opposite ends of the 3D protein structure and likely represent cross-links from two different Stx1B molecules and could be therefore also considered as rather nonspecific (identified cross-links were mapped onto the Stx1A isoform used as our reference 3D model for Stx1B (PDB: 3C98, **Appendix Fig. 26**).

Once again, we noticed that the number of overlength cross-links appeared to be unrelated to protein concentration for DSSO, whereas for DSBU, this number increased with higher protein concentration (**Fig. 4.33 C**). These findings suggest that DSSO exhibits higher cross-linking efficiency, albeit with a tendency towards nonspecificity. Consequently, we opted to proceed with DSBU, with the possibility of revisiting DSSO should analysis with DSBU yield an insufficient number of cross-links.

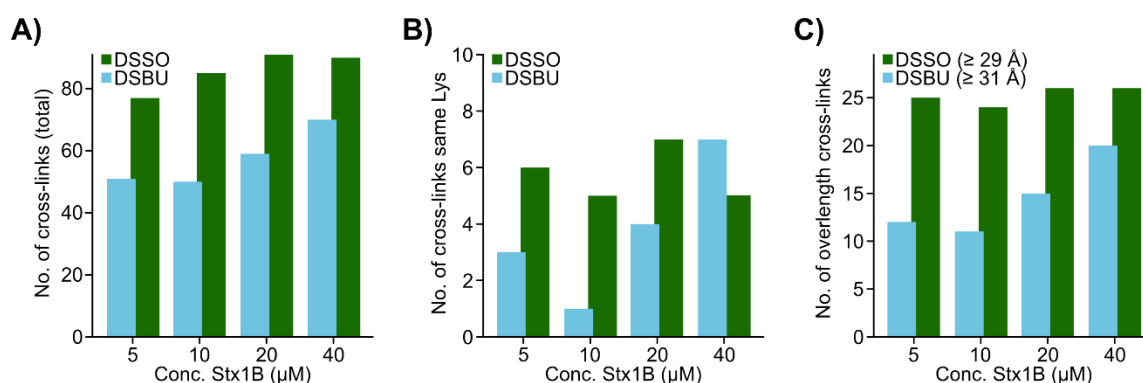


**Figure 4.33: A)** Comparison of the total numbers of identified cross-links when using DSSO or DSBU applied onto different protein concentrations of Stx1B ranging from 5  $\mu\text{M}$  to 40  $\mu\text{M}$ . **B)** Number of cross-links that were identified to link the same lysine when using DSSO or DSBU at different concentrations of Stx1B ranging from 5  $\mu\text{M}$  to 40  $\mu\text{M}$ . **C)** Number of cross-links that were identified with an overlength when using DSSO or DSBU at different concentrations of Stx1B ranging from 5  $\mu\text{M}$  to 40  $\mu\text{M}$ .

To ensure the validity of our cross-links and the integrity of our constructs during the cross-linking procedure, we examined the distance distribution of the identified cross-links and compared it to a random distribution of distances. Considering the distance restraint imposed by the DSBU cross-linker, we anticipated a clear shift in the distance distribution towards shorter distances compared to a random distribution.

For Stx1B, we observed a slight shift towards shorter distances in the distribution (**Fig. 4.34 A**). However, considering the relatively small size of the Stx1B molecule and its compact, globular structure, it becomes evident that the distances between lysine residues are generally short. Therefore, the random cross-link distance distribution also tends to show short distances. Furthermore, the majority of the measured cross-links stayed below the upper limit of the distance constraint of DSBU of 30.3 Å.



In regards of the overlength cross-links, which were found to exceed the maximum distance constraint, some of them are located within flexible regions of the measured proteins, such as the furled loop and an unstructured region in Munc18-1's domain 3a or the linker region as well as the C-terminal part of Stx1B behind the SNARE motif (**Appendix Fig. 26** and **Appendix Fig. 27**). Therefore, these overlength cross-links could be rationalized as capturing possible structural conformations (**Fig. 4.34 B**). This becomes particularly evident when examining the cross-link distance distribution in Munc13-MUN. The MUN domain has an elongated, rod-like shape, with almost no flexible regions, resulting in only a very few cross-links that exceed the upper limit of the 30.3 Å distance constraint (**Fig. 4.34 C**).

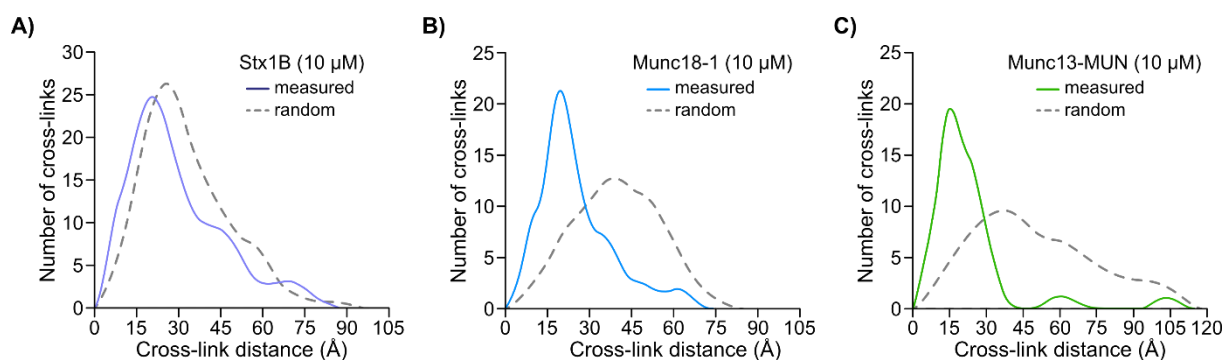


**Figure 4.34:** Measured DSBU cross-link distance distribution compared to theoretical random distance distribution (cross-linking of all available lysine residues without distance constraint, gray dashed line) for **A)** Stx1B, **B)** Munc18-1 and **C)** Munc13-MUN. Identified cross-links were mapped onto solved crystal structures of each individual protein and the distances were measured (**Appendix Fig. 26 A**) and **Appendix Fig. 27 A), B)**). The measured distance distribution is shifted towards shorter distances compared to respective random distance distribution due to distance constraint of the used cross-linker.

Combining the findings, it appears that both cross-linkers, DSSO and DSBU, effectively facilitate cross-linking even at low concentrations. While DSBU consistently yielded fewer identified cross-links compared to DSSO, the results suggest that DSSO may exhibit some level of nonspecificity, potentially making DSBU the preferred choice for specific experiments. Furthermore, cross-link distance distributions confirm that the identified cross-links are not random but adhere to the distance constraint imposed by DSBU.

#### 4.7.3. XL-MS reveals interaction sites between C-terminus and SNARE motif of Syb2 and Munc13-MUN

To further investigate the interaction between Syb2 and the orchestrating protein Munc13-MUN, complementing the insights obtained from NMR studies, we cross-linked Syb2 with Munc13-MUN. To map the identified cross-links, we superimposed the solved NMR structure of Syb2 (Ellena *et al.* (2009), PDB: 2KOG) with the short C-terminal peptide of Syb2 within the crystal structure of Munc13-MUN (Wang *et al.* (2019), PDB: 6A30) [110, 123]. The alignment was conducted using W89 and W90 of Syb2 as fixed points, as these residues were identified as crucial for Syb2's interaction with Munc13-MUN in our NMR experiments (**Chapter 4.6.2** and **Appendix Fig. 28**). Although the backbones of these residues align, the side chains of W89 and W90 of Syb2 exhibit



different rotations. However, this area appears to be relatively unstructured, as the defined alpha-helical region surrounding this part experiences a kink and serves as a rotation point for the different states observed in the recorded NMR structures from Ellena *et al.* (2009, **Appendix Fig. 29**) [110]. All shown cross-links mapped onto the structures have been identified in at least two experiments. The XL-MS measurements confirmed the initial findings of the C-terminal interaction sites between Syb2 and Munc13-MUN, identifying two cross-links in this region. Both cross-links fell within the distance constraint of DSBU, with one measuring 16.1 Å and the other 21.5 Å (C $\alpha$ -C $\alpha$ , **Fig. 4.35**). This highlights the significance of these areas as potential primary interaction sites between Syb2 and the MUN domain of Munc13-1. Furthermore, seven cross-links were found between K52 of Syb2 and lysine residues from different regions of Munc13-MUN. These cross-links all exceed the distance constraint of the DSBU cross-linker, suggesting conformational variation compared to the superimposed structures (**Fig. 4.35**). Given the inherent flexibility of the numerous unstructured regions of Syb2, typical of an IDP, these identified cross-links likely captured various conformational states, confirming notable structural flexibility in Syb2. This flexibility allows the structured SNARE motif of Syb2 to associate to the MUN-domain at different positions.

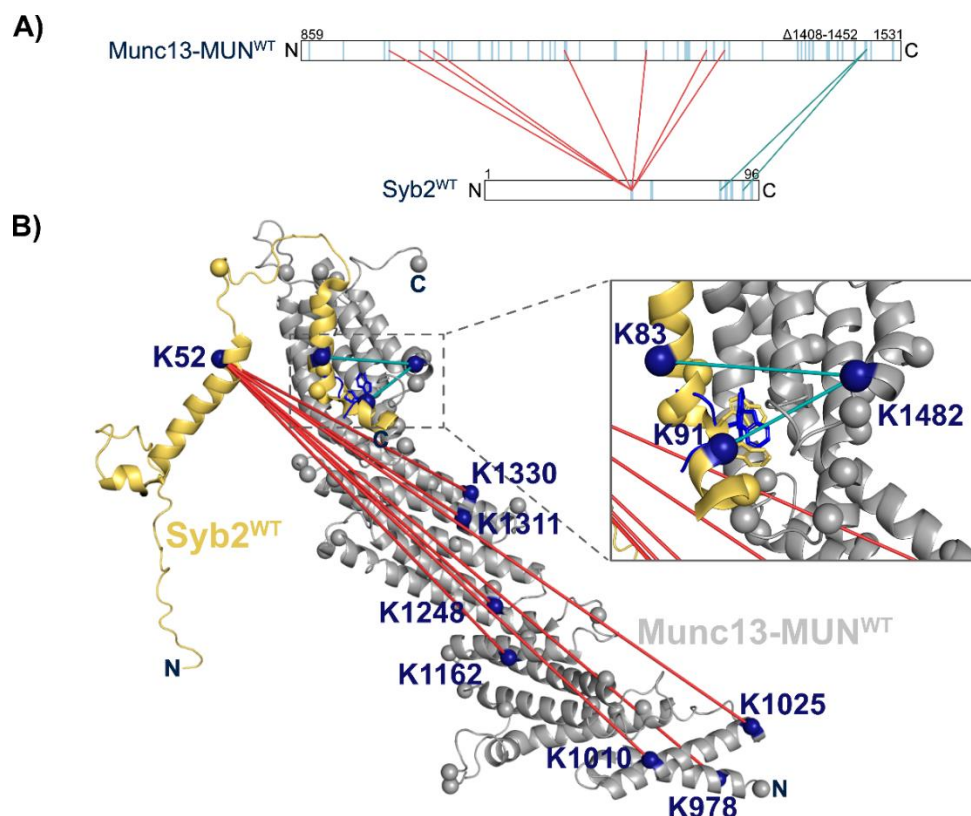


**Figure 4.35: A)** Cross-link map shows the sequence positions of identified intermolecular cross-links between Syb2<sup>WT</sup> and Munc13-MUN<sup>WT</sup>. Lysine residues within the sequence are marked in light blue. Intermolecular cross-links that exceed the distance constraint when mapped onto the structures are colored in red, while those within the distance constraint are colored in teal. XiNET Cross-Linker Viewer was used to create the cross-link map [288]. **B)** Identified cross-links are mapped onto the superimposed structures of Syb2<sup>WT</sup> (PDB: 2KOG) and Munc13-MUN (PDB: 6A30). Lysine residues within the structures are marked as spheres and cross-linked lysine residues are colored in dark blue. Inset provides a close-up view onto the superimposed structures of the Syb2 peptide (PDB: 6A30, blue) and Syb2 (PDB: 2KOG, gold), along with the identified cross-links between the C-termini of Munc13-MUN and Syb2. Intermolecular cross-links that exceed the distance constraint are colored in red, while those within the distance constraint are colored in teal (cross-link length can be found in **Appendix Table 7.3**).

## Results

Remarkably, all lysine residues of Munc13-MUN cross-linked to K52 of Syb2 displayed a consistent orientation inwardly within the curved structure of Munc13-MUN. This suggests that the region surrounding K52 likely orientates toward concave side of the MUN domain (**Fig. 4.35 B**).

Interestingly, no cross-link has been identified for K59 of Syb2, which is positioned at a highly flexible region.

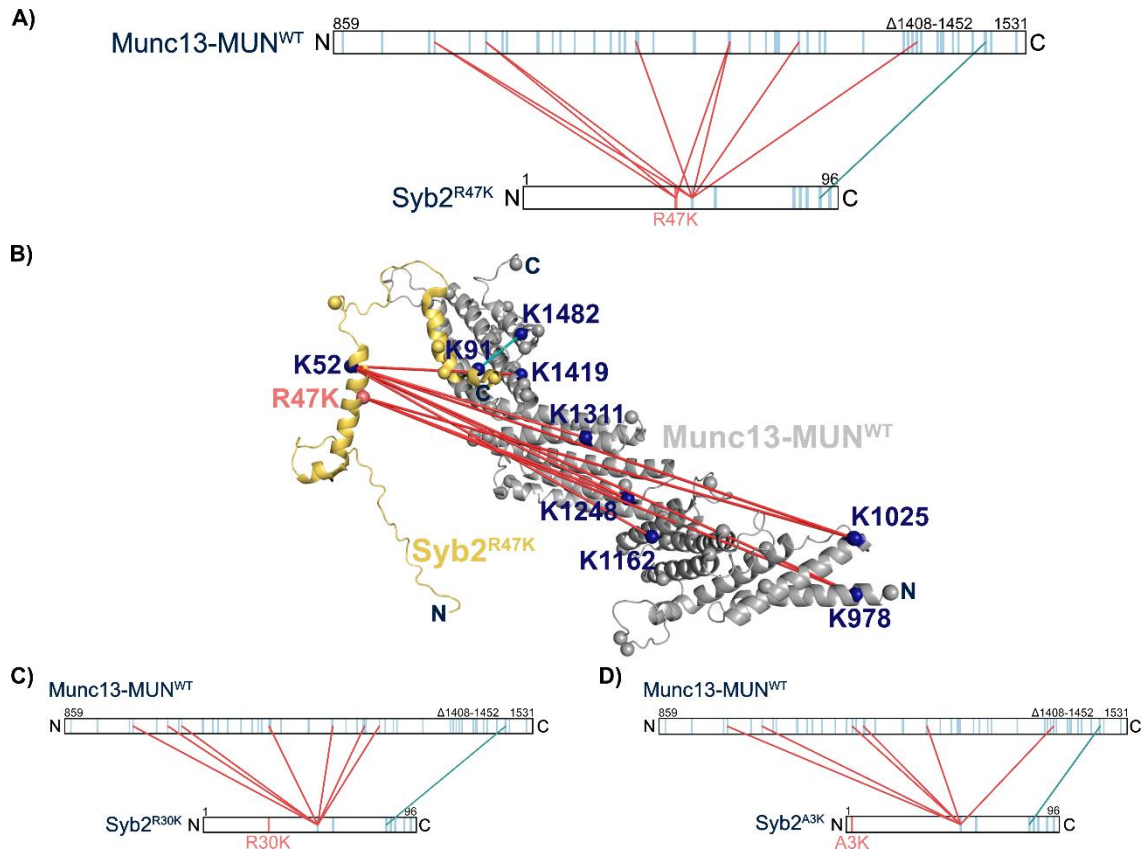


**Figure 4.36:** **A)** Cross-link map shows the sequence positions of the identified intermolecular cross-links between Syb2<sup>R47K</sup> and Munc13-MUN<sup>WT</sup>. Lysine residues within the sequence are marked in light blue. The newly introduced lysine residue at position 47 is marked in lilac. Intermolecular cross-links that exceed the distance constraint when mapped onto the structures are colored in red, while those within the distance constraint are colored in teal. XiNET Cross-Linker Viewer was used to create the cross-link map [288]. **B)** Identified cross-links are mapped onto the superimposed structures of Syb2 (PDB: 2KOG, position of R47K mutation is indicated) and Munc13-MUN (PDB: 6A30). Lysine residues within the structures are marked as spheres and those involved in cross-linking are colored in dark blue. The newly introduced lysine residue at position 47 is colored in lilac. Intermolecular cross-links that exceed the distance constraint are colored in red, while those within the distance constraint are colored in teal (cross-link length can be found in **Appendix Table 7.3**). **C) – D)** Cross-link map shows the sequence positions of the identified intermolecular cross-links between **C)** Syb2<sup>R30K</sup> and Munc13-MUN<sup>WT</sup> as well as **D)** Syb2<sup>A3K</sup> and Munc13-MUN<sup>WT</sup>. Lysine residues within the sequence are marked in light blue. The newly introduced lysine residue at position 30 and 3 are marked in lilac. Intermolecular cross-links that exceed the distance constraint when mapped onto the structures are colored in red, while those within the distance constraint are colored in teal (structures can be found in **Appendix Fig. 30**). XiNET Cross-Linker Viewer was used to create the cross-link maps [288].

Having pinpointed the interaction sites of the C-terminal region and the SNARE motif of Syb2 with Munc13-MUN, our understanding is limited regarding the N-terminal segment of Syb2. This is due to the absence of lysine residues within this highly unstructured region, which, however, are crucial for cross-links and deducing conformational orientations and interaction sites. To address this gap, we sought to broaden our perspective by incorporating new lysine residues into the N-terminal

region. For that, we introduced new lysine residues individually at positions 47, 30 and 3, substituting arginine or alanine residues *via* site-directed mutagenesis. This approach provides an additional cross-linking probe in the structured SNARE motif and two cross-linking probes in the unstructured region further up the N-terminal part, enabling a more comprehensive exploration of possible interaction sites while also preserving side chain characteristics, at least at positions 47 and 30.

In our measurements with Syb2<sup>R47K</sup> and Munc13-MUN, we identified one less cross-link in the C-terminal region between Syb2 and the MUN domain, as well as one less cross-link connecting K52 of Syb2 with the MUN domain (**Fig. 4.36 A, B**). Additionally, we also discovered a new cross-link between Syb2 K52 and Munc13-MUN K1482, likely indicating the considerable flexibility of the disordered Syb2 protein. Moreover, we found three cross-links for the newly introduced lysine residue at position 47, connecting to the same lysine residues that are cross-linked to K52 of Syb2. This suggests a certain structural rigidity in the SNARE motif, which keeps both residues in close proximity, allowing them to cross-link to the same lysine residues on the side of Munc13-MUN.

In regards of Syb2<sup>R30K</sup> and Syb2<sup>A3K</sup>, the overall cross-link distribution was similar to the wild-type and Syb2<sup>A47K</sup>, however, no additional cross-links have been found for the introduced lysine residues at position 30 and 3, suggesting that the unstructured N-terminal region is not involved in any interaction with Munc13-MUN (**Fig. 4.36 C, D**).

The XL-MS analysis with Syb2 constructs and Munc13-MUN confirmed a C-terminal interaction between the two proteins. Additionally, multiple cross-links between Syb2's K52 and various regions of the MUN domain were consistently observed. The cross-linked lysine residues of the MUN domain are oriented inwardly within its arch-shaped structure, suggesting that Syb2 adopts different structural conformations, all directed towards the concave side of Munc13-MUN. Furthermore, lysine mutations revealed that the unstructured N-terminal region of Syb2 does not participate in any interaction with the MUN domain.

#### **4.7.4. Syb2 SNARE motif aligns to domain 3a binding groove and domain 1 of Munc18-1**

We then turned our attention to the other orchestrating protein, Munc18-1. Our NMR results revealed weak interactions between the two proteins, particularly in the C-terminal region of Syb2. However, based on the crystal structure of the homologous protein complex Vps33:Nyv1 in *Chaetomium thermophilum*, where Nyv1 (the homolog of Syb2) binds with its SNARE motif into the binding groove of Vps33 (the homolog of Munc18-1), we anticipated a notable decrease in relative signal intensity for residues within the SNARE motif, which, however, we did not observe [119, 122, 124, 127].

Remarkably, XL-MS measurements revealed eight cross-links between Syb2 K52 and lysine residues of two distinct regions of Munc18-1, which are assigned to domain 1 and domain 3a, along with one cross-link between Syb2 K59 and a lysine residue in domain 3a (**Fig. 4.37 A**). Interestingly, however, no cross-links between Munc18-1 and the C-terminal region of Syb2 were observed.

## Results

We mapped the identified cross-links on the recently published crystal structure of the Munc18-1:Stx1A:Syb2 complex by Stepien *et al.* (2022), revealing Syb2's interaction with the unfurled loop region between helix 11 and helix 12 of Munc18-1 of domain 3a, akin to the homologues complex structure of Vps33:Nyv1 (**Fig. 4.37 B**) [69, 122]. The six cross-links between Syb2 K52 and K59 fell within the distance constraint of DSBU, ranging from 13.5 Å to 21.6 Å (C $\alpha$ -C $\alpha$ ), indicating a precise fit for Syb2's SNARE motif binding to this region.

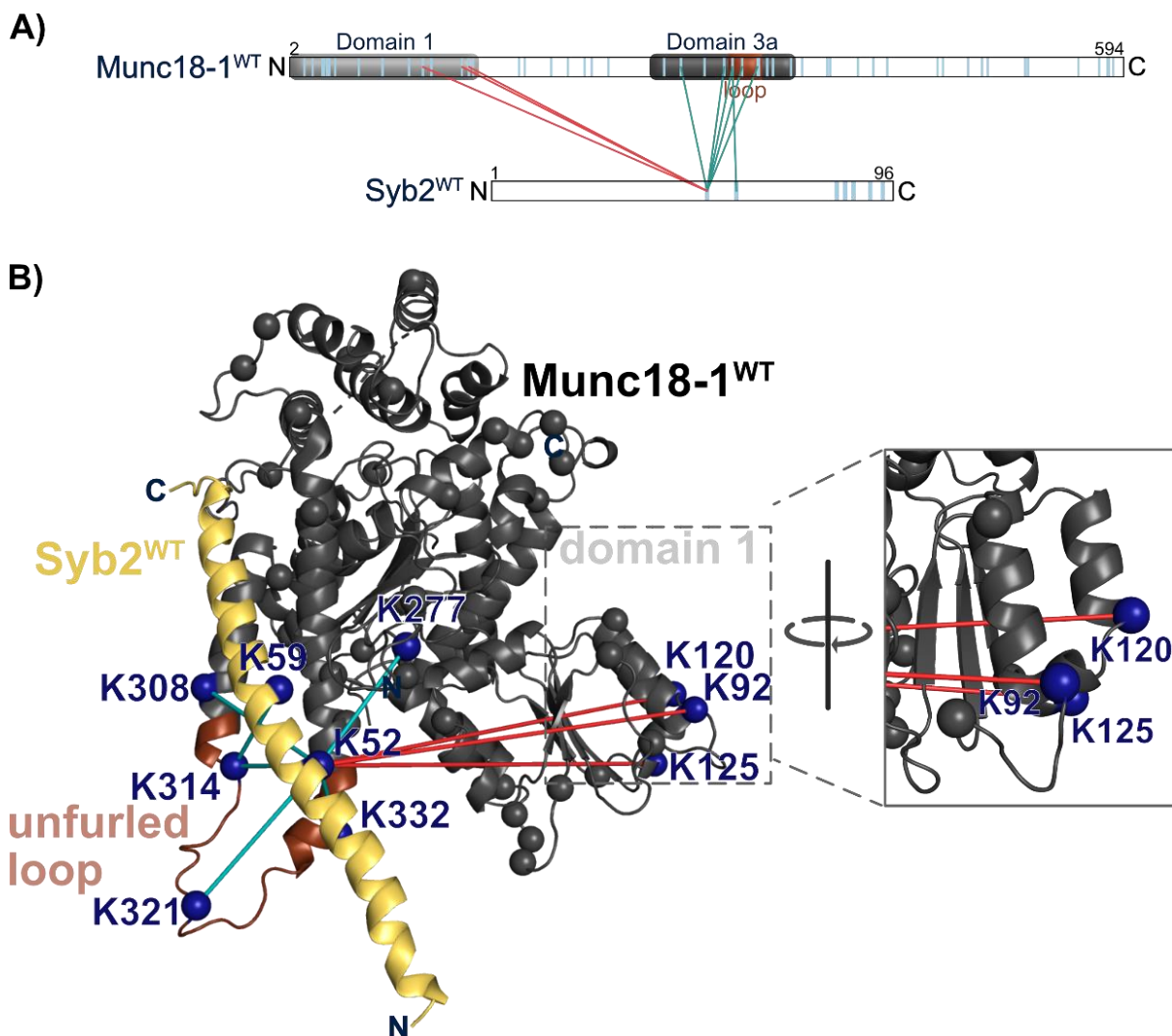


**Figure 4.37: A)** Cross-link map shows the sequence positions of the identified intermolecular cross-links between Syb2<sup>WT</sup> and Munc18-1<sup>WT</sup>. Lysine residues within the sequence are marked in light blue. Domain 1 and domain 3a of Munc18-1 are highlighted with grey tones, the position of the loop is shown in brown. Intermolecular cross-links that exceed the distance constraint when mapped onto the structures are colored in red, while those within the distance constraint are colored in teal. XINET Cross-Linker Viewer was used to create the cross-link map [288]. **B)** Identified cross-links are mapped onto the EM structure of the Munc18-1:Stx1A:Syb2 complex (here only showing Munc18-1 (black) and Syb2 (gold), PDB: 7UDC). The missing segment of the unfurled loop (brown) was modeled using MoMa-LoopSampler (Barozet *et al.* (2022) [289]). Lysine residues within the structures are marked as spheres and those involved in cross-linking are colored in dark blue. Intermolecular cross-links that exceed the distance constraint are colored in red, while those within the distance constraint are colored in teal (cross-link length can be found in **Appendix Table 7.3**). Inset shows a detailed view of the helices within Munc18-1's domain 1, featuring lysine residues implicated in cross-linking with Syb2.

Interestingly, three cross-links suggest a potential secondary binding site of Syb2 to Munc18-1's domain 1 (**Fig. 4.37 B**). However, considering previous data and models, this interaction site could be deemed secondary or possibly an artifact, given that the expected primary binding site at the furled loop region of Munc18's domain 3a is already occupied [69, 84, 122]. Nonetheless, XL-MS experiments with Syb2 and Munc13-MUN have demonstrated the binding flexibility of the SNARE motif region of Syb2, enabling it to align with different regions, potentially leading to nonspecific binding to Munc18-1's domain 1. Furthermore, this domain structurally forms a two-helix binding groove similar to that of helix 11 and helix 12 within domain 3a of Munc18-1 where the SNARE motif of Syb2 could align (**Fig. 4.37 B**). Moreover, the existence of a natural second binding site cannot be ruled out, as it could provide an additional tethering mechanism, where Syb2 on the synaptic vesicle side binds to Munc18-1 on the presynaptic membrane side, which in turn binds to Stx1. This argument gains support from the exclusive involvement of lysine residues from these two regions in cross-linking with Syb2, contrasting with the absence of cross-links with other lysine residues of Munc18-1, despite their abundance, suggesting a degree of specificity.

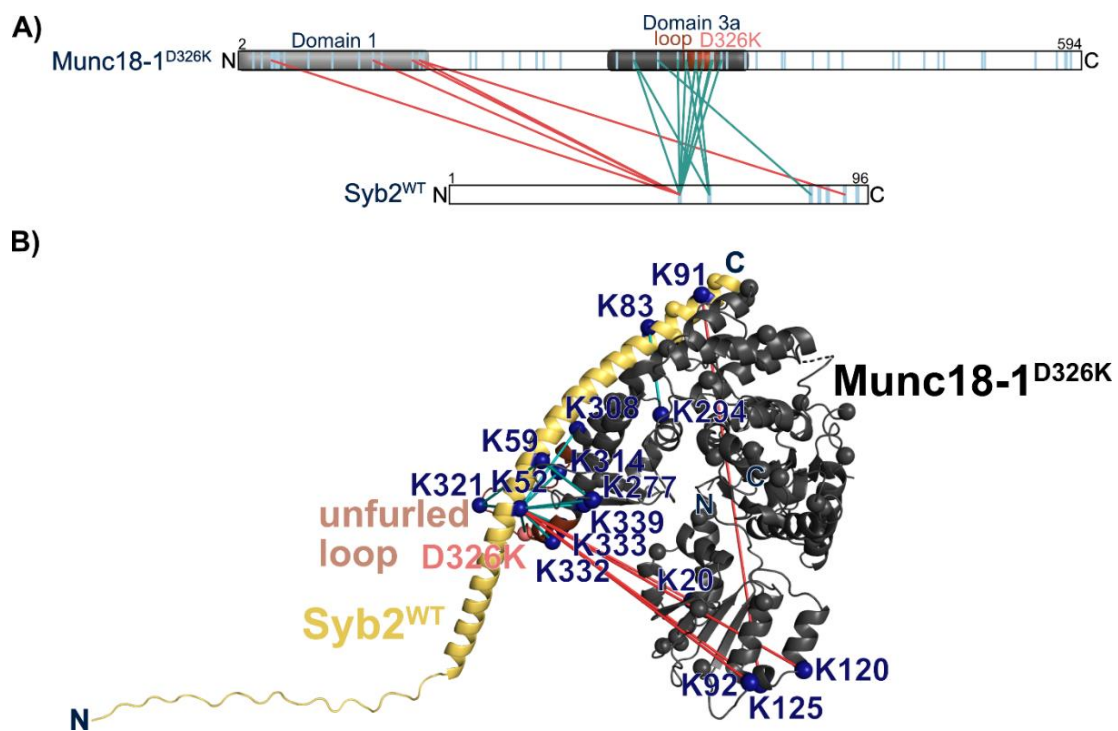


**Figure 4.38: A)** Cross-link map shows the sequence positions of the identified intermolecular cross-links between Syb2<sup>WT</sup> and Munc18-1<sup>D326K</sup>. Lysine residues within the sequence are marked in light blue. Domain 1 and domain 3a of Munc18-1 are highlighted with grey tones, the position of the loop is shown in brown. The introduced mutant lysine residue at position 326 is marked in lilac. Intermolecular cross-links that exceed the distance constraint when mapped onto the structures are colored in red, while those within the distance constraint are colored in teal. XiNET Cross-Linker Viewer was used to create cross-link map [288]. **B)** Identified cross-links are mapped onto the EM structure of the Munc18-1:Stx1A:Syb2 complex (here only showing Munc18-1 (black (PDB: 7UDC, position of D326K mutation is indicated), the missing part of the unfurled loop (brown) was modeled using MoMa-LoopSampler (Barozet *et al.* (2022) [289]) and Syb2 (gold, PDB: AF-P63027-F1). The Syb2 structure displayed here is an AlphaFold 2 structure, superimposed with the Syb2 of the original EM structure to highlight the involvement of the C-terminal part in cross-linking (**Appendix Fig. 31**). Lysine residues within the structures are marked as spheres and those involved in cross-linking are colored in dark blue. Intermolecular cross-links that exceed the distance constraint are colored in red, while those within the distance constraint are colored in teal (cross-link length can be found in **Appendix Table 7.3**).



In the EM structure of the Syb2:Stx1A:Munc18-1 complex, Stepien *et al.* (2022) employed functional mutants Stx1A<sup>LEAA</sup> and Munc18-1<sup>P335A</sup> to alter the conformations of the involved proteins, promoting the unfurling of the loop within Munc18-1's domain 3a and thus enhancing the binding of Syb2 to Munc18-1 [69]. This was supported by our XL-MS experiments with Syb2 and Munc18-1<sup>D326K</sup>, another functional mutation within the loop, inducing the opening of the furled loop [127, 290]. These experiments revealed a notably higher number of cross-links between Syb2 and Munc18-1<sup>D326K</sup> compared to the wild-type counterpart, with 17 cross-links detected between Syb2<sup>WT</sup> and Munc18-1<sup>D326K</sup>, including two more to domain 1 and six additional cross-links to domain 3a of Munc18-1. Remarkably, we also observed two cross-links between the C-terminal part of Syb2 and Munc18-1, one towards domain 1 (K125) and another towards the backside of domain 3a (K294). This suggests that the forced opening of the furled loop facilitates a more efficient alignment of Syb2 within the binding groove between helix 11 and helix 12 of domain 3a of Munc18-1 (**Fig. 4.38 A**).

To map all identified cross-links, including those between the C-terminal part of Syb2 and Munc18-1, we aligned the full-length AlphaFold 2 structure of Syb2 (PDB: AF-P63027-F1) with the Syb2 fragment shown in the EM structure from Stepien *et al.* (2022 [69], PDB: 7UDC) using the lysine residues K52 and K59 as anchor points, as these residues are primary anchor points for the cross-links (**Appendix Fig. 31**).

All cross-links between Syb2<sup>WT</sup> and domain 3a of Munc18-1<sup>D326K</sup> fall within the distance constraint of DSBU, ranging from 12.6 Å to 26.3 Å (C $\alpha$ -C $\alpha$ ). This includes a cross-link between K52 of Syb2 and the introduced D326K mutation of Munc18-1, confirming the correct integration of that mutant residue (**Fig. 4.38 B**). Cross-links toward domain 1 exceed the distance constraint of DSBU in this binding model, strongly suggesting the additional binding site for Syb2 to Munc18-1 at this domain as mentioned before (**Fig. 4.38 B**).

In these experiments with Syb2 and Munc18-1, however, cross-linking was performed without Munc18-1's primary interaction partner, Stx1. According to the crystal structure from Burkhardt *et al.* (2008 [140], PDB: 3C98), the interaction between Stx1A and Munc18-1 maintains the loop of domain 3a in its furled conformation (**Fig. 1.9**) [140]. Alignment of the crystal structure from Burkhardt *et al.* (2008 [140], PDB: 3C98) and EM structure from Stepien *et al.* (2022 [69], PDB: 7UDC) showed that a furled loop would hinder Syb2 binding between helix 11 and 12 as structures overlap (**Appendix Fig. 31**).

In the light of this, we pondered whether addition of Stx1B was indeed affecting the interaction between Munc18-1 and Syb2. Our hypothesis proposed that the loop within domain 3a of Munc18-1 folds back onto helices 11 and 12, thus obstructing the interaction with Syb2 and potentially guiding Syb2 towards the newly discovered interaction site in domain 1 of Munc18-1.

Interestingly, XL-MS experiments conducted in the presence of all three proteins – Syb2, Munc18-1, and Stx1B – revealed no significant alterations in the interaction region between Syb2 and Munc18-1 at first glance. Intermolecular cross-links between Syb2 and Munc18-1's domain 1 and domain 3a persisted, indicating that domain 3a remained accessible for the interaction

(**Fig. 4.39 A**). However, there were notably fewer cross-links between Syb2 and Munc18-1, with only five in total: two towards domain 1 and three towards domain 3a of Munc18-1. Additionally, K59 and the C-terminal part of Syb2 were no longer involved in cross-linking (**Fig. 4.39 A, B**). Distinctly, for the interaction between Syb2 and domain 3a of Munc18-1, only lysine residues on helix 11 (K308 and K314) and K321 on the loop (the lysine residue closest to helix 11) were involved. However, none of the lysine residues on helix 12, which had previously participated in cross-linking with Syb2, nor K277 of Munc18-1, which is situated deeper within the structure of Munc18-1 and close to helix 12, were involved in cross-linking anymore. This suggests that there might be suboptimal alignment of Syb2 towards domain 3a with the furled loop, allowing for cross-linking with the lysine residues on the surface of the Munc18-1 structure in that region but not proper alignment of Syb2 between helix 11 and 12, as would occur with an unfurled loop. This indicates that the interaction between Munc18-1<sup>WT</sup> and Syb2<sup>WT</sup> indeed maintains the loop in its furled conformation, and an additional Syb2 is unable to properly align with that region.

Furthermore, we observed only one cross-link between Syb2 (K52) and Stx1B (K87). This one falls within the distance constraint, with a length of 22.5 Å (C $\alpha$ -C $\alpha$ ), but unexpectedly, it connects between helix H<sub>b</sub> of Stx1B and Syb2, rather than linking the SNARE motifs of Stx1B and Syb2 as would be anticipated in the context of a template complex formation. This implies that the interaction between Munc18-1 and Stx1B effectively prevents Stx1B from engaging with Syb2 and suggests only a nonspecific alignment of Syb2 in this case (**Fig. 4.39 B**).

Regarding the interaction of Munc18-1 and Stx1B, 17 cross-links have been identified between the two proteins. Interestingly, while the cross-linked lysine residues are distributed throughout the entire sequence of Stx1B, lysine residues from three regions of Munc18-1 are more frequently involved: domain 1 and domain 3a (similar to the interaction with Syb2), and additionally the C-terminal part of domain 2 (**Fig. 4.39 A**). In the context of the complex structure, this observation is quite logical, given that domain 1 and domain 3a flank Stx1B, which is bound between them. Most of the identified cross-links fall within the distance constraint, with two interesting exceptions: one being between Stx1B K251 and Munc18-1 K120 (36.7 Å (C $\alpha$ -C $\alpha$ )), connecting the C-terminus of Stx1B and domain 1 of Munc18-1. In the crystal structure, both regions are still in proximity to each other and the overlength cross-link possibly reflects a conformational flexibility of the C-terminus of Stx1B. The other one involves K526 of Munc18-1, which connects to three different lysine residues of Stx1B, K54 and K55 of the helix H<sub>a</sub> and K139 of the helix H<sub>c</sub>. All these three cross-links displayed an overlength in the realm of 44.7 Å to 46.2 Å (C $\alpha$ -C $\alpha$ ). Considering K526's location within a flexible region of Munc18-1, it's probable that these cross-links arise due to the substantial flexibility in this area, possibly capturing conformations where the loop is closer to the helices of Stx1B (**Fig. 4.39 B**), originally missing parts of this flexible region in this crystal structure were modeled using MoMa-LoopSampler (Barozet *et al.* (2022) [289])).

It is worth noting that no cross-links were found from Munc18-1 K526 to helix H<sub>b</sub> and also not with the SNARE motif of Stx1B. This is sensible since these two helices are positioned away from the interaction interface, thus providing further validation for the identified cross-links.

## Results

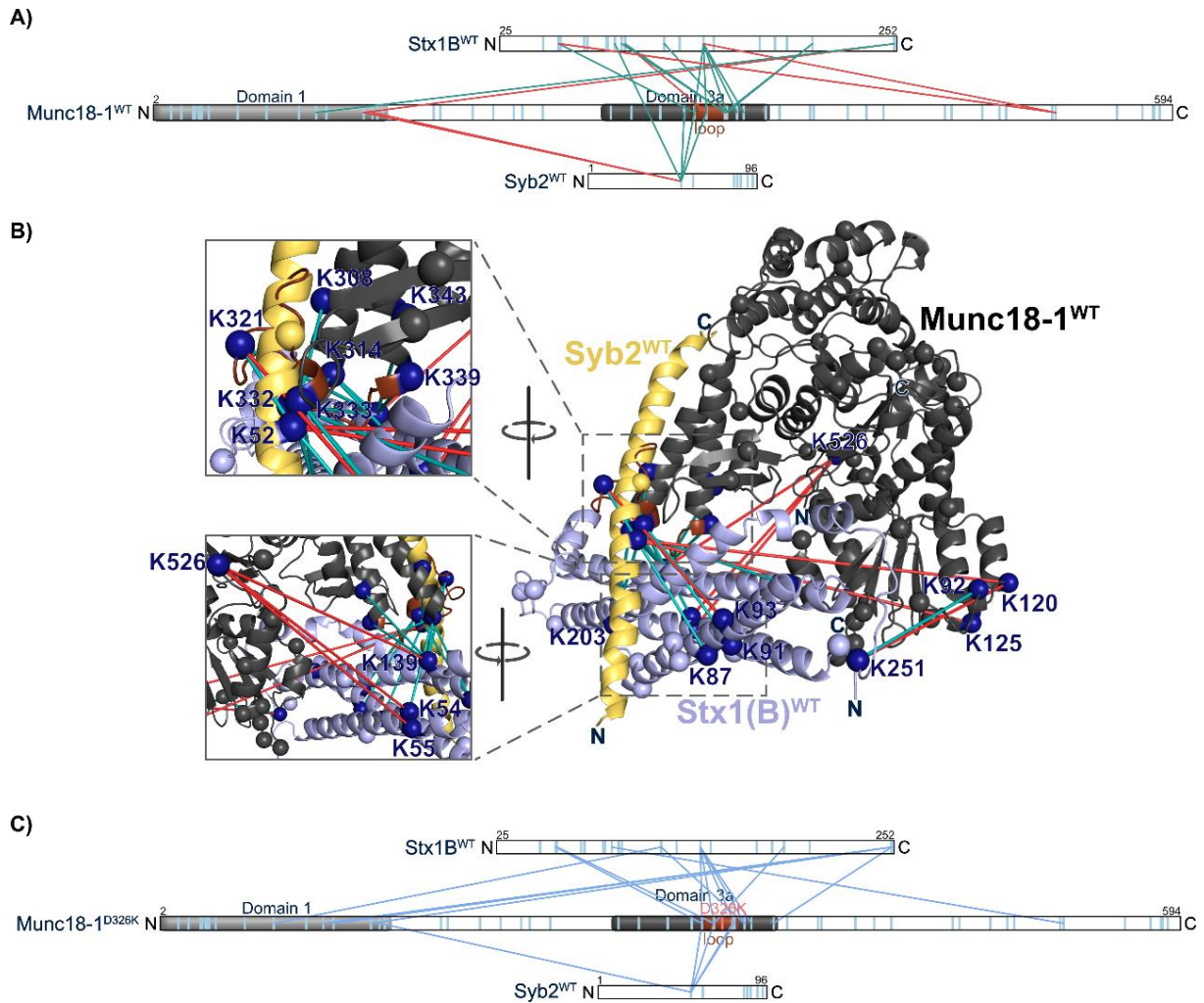


**Figure 4.39: A)** Cross-link map shows the sequence positions of the identified intermolecular cross-links between Syb2<sup>WT</sup>, Munc18-1<sup>WT</sup> and Stx1B<sup>WT</sup>. Lysine residues within the sequence are marked in light blue. Intermolecular cross-links that exceed the distance constraint when mapped onto the structures are colored in red, while those within the distance constraint are colored in teal. Domain 1 and domain 3a of Munc18-1 are highlighted with grey tones, the position of the loop is shown in brown. XiNET Cross-Linker Viewer was used to create the cross-link map [288]. **B)** Identified cross-links are mapped onto the crystal structure of the Stx1:Munc18-1 complex (PDB: 3C98) and EM structure of Syb2 (PDB: 7UDC), which was added by the alignment of the structures of Munc18-1 from the EM structure and the crystal structure (**Appendix Fig. 32**). Missing parts within the structure were modeled using MoMa-LoopSampler (Barozet *et al.* (2022) [289]). The sequence of the Stx1A chain in the crystal structure was adjusted to match the sequence of Stx1B. The insets show a detailed view of Munc18-1's furled loop within domain 3a, overlaid with Syb2 (top), and the backside of the interaction interface of domain 3a (bottom). Lysine residues within the structures are shown as spheres and those involved in cross-linking are colored in dark blue. Intermolecular cross-links that exceed the distance constraint are colored in red, while those within the distance constraint are colored in teal (cross-link length can be found in **Appendix Table 7.3**). **C)** Cross-link map shows the sequence positions of the identified intermolecular cross-links between Syb2<sup>WT</sup>, Munc18-1<sup>D326K</sup> and Stx1B<sup>WT</sup>. Lysine residues within the sequence are marked in light blue and intermolecular cross-links between lysine residues are colored in light purple. Domain 1 and domain 3a of Munc18-1 are highlighted with grey tones, the position of the loop is shown in brown. The introduced mutant lysine residue at position 326 is marked in lilac. XiNET Cross-Linker Viewer was used to create the cross-link map [288].

We attempted to enhance Syb2 binding to the Stx1B:Munc18-1 complex by employing the Munc18-1<sup>D326K</sup> mutation once again, aiming to unfold the furled loop and expose the binding groove between helices 11 and 12 of Munc18-1<sup>D326K</sup> for Syb2<sup>WT</sup>. This approach aimed to potentially capture



more cross-links between the SNARE motifs of Syb2 and Stx1B, indicative of a side-by-side alignment resembling template complex formation. However, XL-MS data revealed that the utilization of the D326K mutation did not significantly enhance Syb2 binding. The number of cross-links between Syb2<sup>WT</sup> and domain 3a of Munc18-1<sup>D326K</sup> remained reduced compared to the measurements without Stx1B (totaling only 4 cross-links), with lysine residues from helix 12 and the buried K277 still excluded (**Fig. 4.39 C**). This strongly suggests that Syb2 still fails to bind properly to the Stx1B:Munc18-1 complex, even with the D326K mutation (**Fig. 4.39 C**). Furthermore, no cross-links between Syb2 and Stx1B were detected, indicating the absence of a side-to-side alignment and the continued inaccessibility of Stx1B for early SNARE complex formation.

Upon examining the aligned crystal and EM complex structures from Burkhardt *et al.* (2008) and Stepien *et al.* (2022), it becomes apparent that a complete unfurling of the loop triggered by the D326K mutation of Munc18-1 would not be feasible in the interaction with Stx1B, unless a crucial conformational change occurs within Stx1B. This is because an unfurled loop would overlap with the linker region of Stx1B (**Appendix Fig. 32 C**). Therefore, it could be inferred that the binding of Syb2 to domain 3a was not successful in this case, as the loop might not fully unfurl due to the presence of Stx1B.

Interestingly, a new cross-link between Munc18-1<sup>D326K</sup> and Stx1B<sup>WT</sup> was identified, involving K321 (Munc18-1) and K188 (Stx1B, **Appendix Fig. 32 D**). This particular cross-link exhibits significant overlength of 55.5 Å (C $\alpha$ -C $\alpha$ ), suggesting that it would have only formed if there were some conformational changes bringing the loop and the beginning of the SNARE motif closer together. This implies that the loop may not remain completely furled upon the utilization of the D326K mutation and might partially unfurl. However, it cannot unfurl completely due to structural blockage by Stx1B, which consequently hinders proper Syb2 binding as well.

In summary, our XL-MS experiments uncovered two Syb2 binding sites on Munc18-1. One resides within Munc18-1's domain 3a, between helix 11 and 12, consistent with previous findings [69, 124]. Additionally, cross-links hint to a secondary binding site in Munc18-1's domain 1. The D326K mutation of Munc18-1, known to trigger loop opening, notably enhanced binding of Syb2 to domain 3a. However, the addition of Stx1B limited Syb2's binding to Munc18-1, indicating that Stx1B maintains the loop of Munc18-1 in its furled state, hindering proper Syb2 alignment. This hindrance persisted even with the Munc18-1 D326K mutation in the presence of Stx1B, indicating that the loop cannot fully unfurl without significant conformational changes in Stx1B. Moreover, only one cross-link was detected between Syb2 and Stx1B, and no cross-links were found between their SNARE motifs. This suggests that Stx1B, when interacting with Munc18-1, remains inaccessible to Syb2 for early SNARE complex formation. Other factors may be required to facilitate the opening of Stx1B's conformation, allowing access to its SNARE motif for SNARE complex formation.

#### 4.7.5. Cross-links indicate conformational changes in the binding sites between Munc18-1 and Stx1B mutants

We then compared the intermolecular cross-link profiles of Munc18-1 and Stx1B between the measurements with and without Syb2 to determine if the addition of Syb2 affects their interaction and potentially their conformation (**Fig. 4.39** and **Fig. 4.41**). Yet, no significant differences were observed in the intermolecular cross-links between Munc18-1 and Stx1B between measurements, suggesting that the addition of Syb2 does not alter the binding conformation of the Stx1B:Munc18-1 complex. Nonetheless, 25 cross-links between Munc18-1 and Stx1B from the measurement without Syb2 were additionally identified (eight more than in the measurement with Syb2, **Fig. 4.41 B**). Most of these new cross-links were situated within the expected interaction interface and fell within the distance constraints, leaving domain 1 and domain 3a of Munc18-1 as hotspot domains for cross-linking with Stx1B (**Fig. 4.41 A, C**).

However, a few cross-links displayed significant overlength. Two of these were already known from the measurement with Syb2, involving Munc18-1's K526, situated in a flexible region, and Stx1B's K54 as well as K139, with lengths of 45.9 Å and 44.7 Å (C $\alpha$ -C $\alpha$ ), respectively (**Fig. 4.41 C**). This suggests that the flexible region containing K526 can indeed adopt conformations closer to the interaction interface with Stx1B than indicated by the crystal structure. Another cross-link, also observed in the measurement with Syb2, involves Stx1B's K251 and Munc18-1's K120 (36.7 Å (C $\alpha$ -C $\alpha$ )), further highlighting the flexibility of Stx1B's C-terminus. This flexibility is further underpinned by three newly identified overlength cross-links, involving the aforementioned C-terminal K251 of Stx1B and Munc18-1's K356 (55.7 Å (C $\alpha$ -C $\alpha$ )) as well as K584 (51.1 Å (C $\alpha$ -C $\alpha$ )) and even with K308 of domain 3a (57.3 Å (C $\alpha$ -C $\alpha$ )). All these findings strongly indicate a high degree of flexibility in the C-terminus of Stx1B. However, these results need to be considered in perspective as we utilized a C-terminally truncated Stx1B construct in these measurements, lacking the JMD and TMR of Stx1B which would normally anchor it into a membrane, potentially reducing its flexibility in its natural environment. In the artificial, membrane-free, and buffer-only environment where the cross-linking was performed, an unspecific flexibility of the truncated C-terminal end is conceivable.

Besides these findings, there were no clear indications of a substantial conformational change in both measurements, with and without Syb2. This suggests that Syb2, within the context of the Stx1B:Munc18-1 complex, does not induce the opening of the closed conformation of the complex or initiate a template complex formation on its own.

We then shifted our focus to the Stx1B<sup>L221P</sup> and Stx1B<sup>E210K</sup> mutants to investigate whether these mutations induced any detectable conformational changes that could lead to potential alterations in binding conformations. Our ITC experiments had already indicated reduced binding affinities between Munc18-1 and the Stx1B mutants, particularly evident for the E210K mutant, despite both mutations are not found within the binding interface of Stx1 and Munc18-1 (as per the crystal structure of the Stx1A:Munc18-1 complex (PDB: 3C98) [140], **Chapter 4.4.1**). This discrepancy suggests the possibility of allosteric effects within Stx1B's structure. The number of intermolecular

## Results

cross-links between Munc18-1 and the Stx1B mutants appeared comparable to those with the wild-type (total count 25), with Stx1B<sup>E210K</sup> showing two cross-links more (total count 27) and Stx1B<sup>L221P</sup> three fewer (total count 22).<sup>(1)</sup> Initially, no significant differences were observed in the domains involved in cross-linking. On Munc18-1's side, domain 1 and domain 3a were predominantly involved in cross-linking with both Stx1B<sup>L221P</sup> and Stx1B<sup>E210K</sup>, while on Stx1B's side, cross-linked lysine residues were distributed throughout the entire sequence, akin to the wild-type (**Fig. 4.41 A** and **4.42 A**).

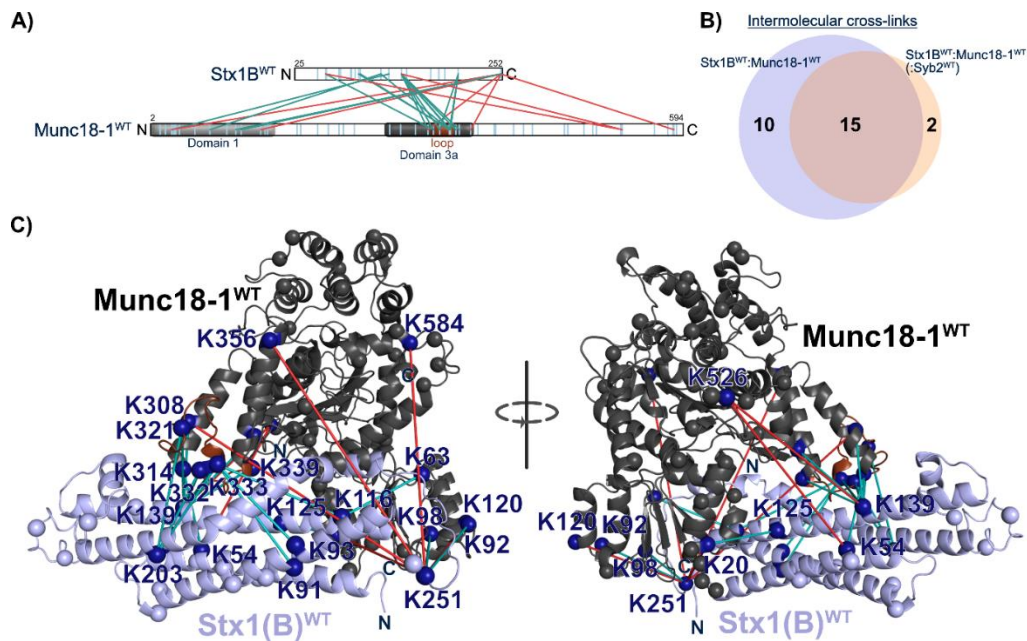


**Figure 4.40:** **A)** Cross-link map shows the sequence positions of the identified intermolecular cross-links between Munc18-1<sup>WT</sup> and Stx1B<sup>WT</sup>. Lysine residues within the sequence are marked in light blue. Intermolecular cross-links that exceed the distance constraint when mapped onto the structures are colored in red, while those within the distance constraint are colored in teal. Domain 1 and domain 3a of Munc18-1 are highlighted with grey tones, the position of the furled loop is shown in brown. XiNET Cross-Linker Viewer was used to create the cross-link map [288]. **B)** Venn diagram illustrates the count of individually identified intermolecular cross-links obtained from the XL-MS measurements of Stx1B<sup>WT</sup> and Munc18-1<sup>WT</sup> with (**Fig. 4.39 A**) and without Syb2, as well as the overlapping count of identical intermolecular cross-links detected in both measurements. **C)** Identified cross-links are mapped onto the crystal structure of the Stx1:Munc18-1 complex (PDB: 3C98). Missing parts within the structure were modeled using MoMa-LoopSampler (Barozet *et al.* (2022) [289]). The sequence of the Stx1A chain in the crystal structure was adjusted to match the sequence of Stx1B. Lysine residues within the structures are shown as spheres and those involved in cross-linking are colored in dark blue. Intermolecular cross-links that exceed the distance constraint are colored in red, while those within the distance constraint are colored in teal (cross-link length can be found in **Appendix Table 7.3**).

Comparing the identified cross-links between the mutants and the wild-type revealed 14 identical cross-links found in all measurements, with substantial overlaps of identical cross-links observed when comparing two measurements individually (**Appendix Fig. 33** and **Fig. 4.41 B**). The count of 19 overlapping intermolecular cross-links was observed between the measurements conducted with Stx1B<sup>WT</sup> and Stx1B<sup>E210K</sup>, whereas only 16 identical cross-links were identified for Stx1B<sup>WT</sup> and Stx1B<sup>L221P</sup> (**Fig. 4.41 B**). This observation is unsurprising, given the higher total number of intermolecular cross-links found for Stx1B<sup>WT</sup> and Stx1B<sup>E210K</sup> compared to Stx1B<sup>L221P</sup>.

(1) Note that for the measurements with Stx1B<sup>WT</sup> and Stx1B<sup>E210K</sup>, cross-links were found at least twice in different XL-MS measurements. For L221P, only a single XL-MS measurement has been performed here.

## Results

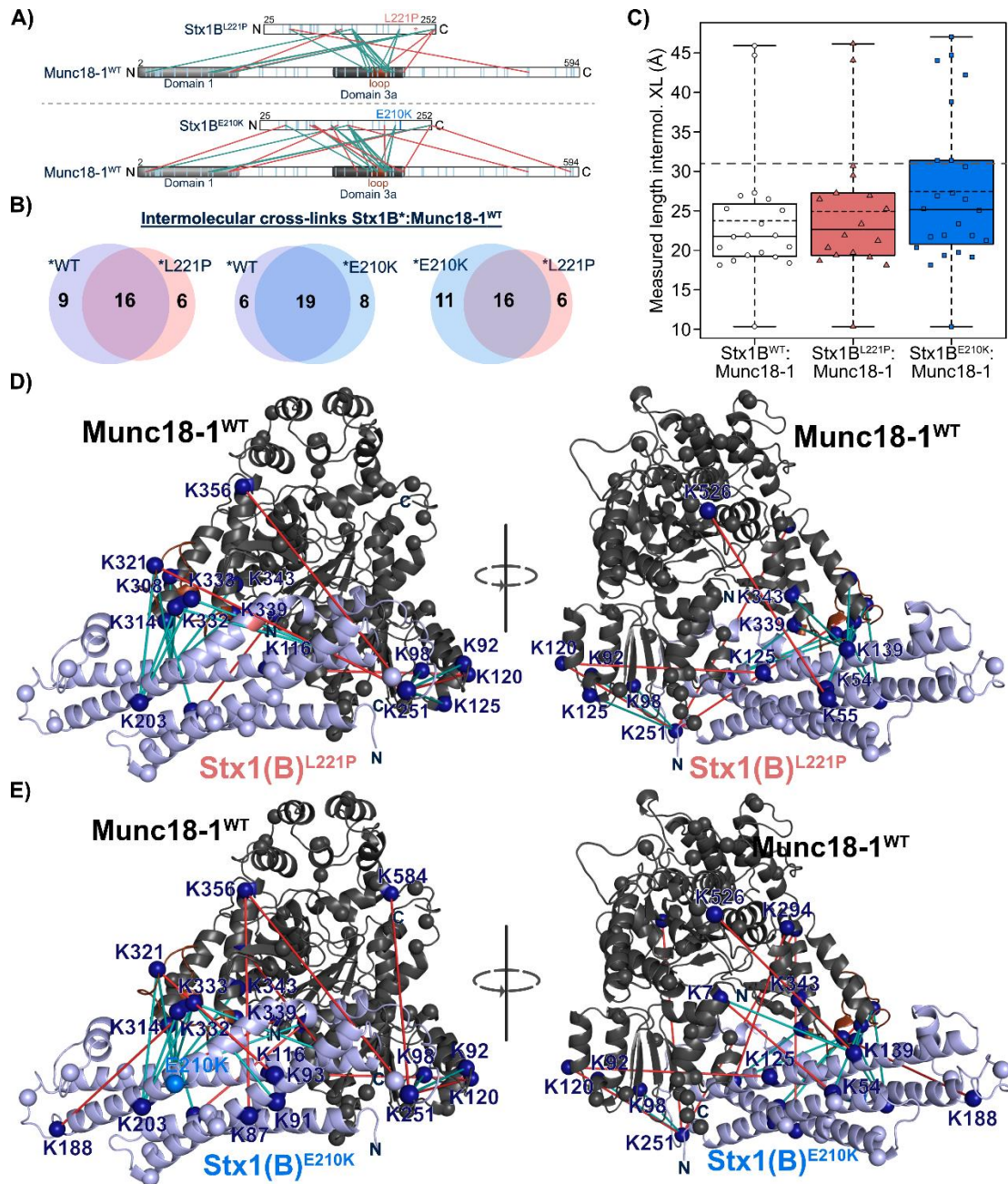


**Figure 4.41:** **A)** Cross-link maps illustrate intermolecular cross-links between Munc18-1<sup>WT</sup> and Stx1B<sup>L221P</sup> (top) and Stx1B<sup>E210K</sup> (bottom). Lysine residues are marked in light blue. Intermolecular cross-links that exceed the distance constraint when mapped onto the structures are colored in red, while those within the distance constraint are colored in teal. Munc18-1 domain 1 and domain 3a are shaded in grey, and the furled loop is shown in brown. Positions of the L221P mutation (salmon) and E210K mutation (blue) in Stx1B are labeled. Cross-link maps were generated using XiNET Cross-Linker Viewer [288]. **B)** Venn diagrams show counts of intermolecular cross-links and overlap from XL-MS measurements of Stx1B<sup>WT</sup> (purple), Stx1B<sup>L221P</sup> (salmon), and Stx1B<sup>E210K</sup> (blue) with Munc18-1<sup>WT</sup>. **C)** Box plots display the length dispersion of intermolecular cross-links between Stx1B wild-type and mutants, and Munc18-1. Overlength cross-links involving the C-terminal K251 of Stx1B were omitted (box plot with all data point in **Appendix Fig. 33 B)**). Median and average values are indicated as straight and dashed line, respectively. Grey dashed line indicates maximum distance constraint. Data were analyzed and plotted using OriginPro-2023 (OriginLab Corporation). **D)-E)** Identified cross-links from measurements with Stx1B<sup>L221P</sup> (**D)**) and Stx1B<sup>E210K</sup> (**E)**) are mapped onto the crystal structure of the Stx1:Munc18-1 complex (PDB: 3C98), with missing parts modeled using MoMa LoopSampler [289]. The sequence of the Stx1A chain in the crystal structure was adjusted to match the sequence of Stx1B. Lysine residues are represented as spheres, with cross-linking residues in dark blue. Lysine residues within the structures are shown as spheres and those involved in cross-linking are colored in dark blue. Intermolecular cross-links that exceed the distance constraint are colored in red, while those within the distance constraint are colored in teal (cross-link length can be found in **Appendix Table 7.3)**.

Furthermore, 16 identical intermolecular crosslinks were identified in the measurements with Stx1B<sup>E210K</sup> and Stx1B<sup>L221P</sup>. As a result, there was also a considerable number of unique intermolecular cross-links, potentially suggesting the emergence of new binding sites due to structural changes. We speculated that structural changes could facilitate the creation of these new cross-links as potential binding sites draw closer together. Consequently, these distinct cross-links might appear longer when mapped onto the crystal structure of the wild-type complex conformation (PDB: 3C98).

Alternatively, it is possible that these newly identified cross-links also simply integrate into the already discovered binding interfaces and were just not identified in measurements with the wild-type, which in turn means that no substantial conformational changes have occurred. These would be characterized by not exceeding the distance constraint.

This was notably observed in the measurement with Stx1B<sup>L221P</sup> where most intermolecular cross-links appeared to be within the distance constraints and showed no substantial overlength, similar to the wild-type, when mapped onto the Stx1:Munc18-1 crystal structure (**Fig. 4.41 D**).

For the measurement with Stx1B<sup>WT</sup> (ignoring the overlength cross-links derived from the flexible C-terminus of Stx1B), only two cross-links showed a significant overlength, which were found between K526 (Munc18-1) and K139 as well as K54 (both Stx1B) that have been discussed before (**Fig. 4.40 C**).

Two overlength cross-links for the measurement with Stx1B<sup>L221P</sup> were found between K526 (Munc18-1) and K55 (Stx1B) with a length of 46.2 Å (C $\alpha$ -C $\alpha$ ), as well as K120 (Munc18-1) and K125 (Stx1B) with a length of 44.1 Å (C $\alpha$ -C $\alpha$ ). The former cross-link is similar to one of the overlength cross-links found in the measurement with Stx1B<sup>WT</sup> and can be attributed to the flexible region harboring K526 of Munc18-1 (**Fig. 4.41 D**). The latter is a newly identified cross-link between Stx1B's helix H<sub>c</sub> and a helix of Munc18-1's domain 1 (**Fig. 4.41 D**). This may suggest a conformational change induced by the mutation. However, no other indications can be found, making the interpretation difficult. Other newly identified cross-links mainly occurred within the interaction interface and did not exceed the distance constraint. Interestingly, two of these new cross-links involved K116 (Stx1B) and K332 as well as K339 (both Munc18-1). Both mapped cross-links traverse through the SNARE motif, particularly close to the L221P mutation (**Fig. 4.41 D**). This suggests that steric hindrance might have prevented their formation in the wild-type structure. However, the L221P mutation, potentially altering the helix course in the SNARE motif due to the helix-breaking properties of proline, made these lysine residues more accessible for cross-link formation.

In summary, most of the newly discovered intermolecular cross-links in the measurement with Stx1B<sup>L221P</sup> did not suggest significant conformational changes. They were located within the interaction interface and did not exceed the distance constraints, indicating minor conformational alterations (**Fig. 4.41 D**). The distance distribution, median, and average cross-link length remained similar to the wild-type, suggesting that the binding conformation is not much influenced by the L221P mutation (**Fig. 4.41 C**).<sup>(1)</sup>

Strikingly, this was notably different for the measurements with Stx1B<sup>E210K</sup>. Median and average intermolecular cross-link length were considerably higher compared to the measurements with Stx1B<sup>WT</sup> and Stx1B<sup>L221P</sup>, displaying new cross-links with longer distances, when mapped onto the wild-type crystal structure (PDB: 3C98, **Fig. 4.41 C, D**).

One of these longer cross-links, already identified in measurements with Stx1B<sup>WT</sup>, occurred between K526 (Munc18-1) and K54 (Stx1B) with a length of 44.7 Å (Cα-Cα). This overlength cross-link is likely due to the flexible region containing K526 of Munc18-1, potentially capturing a conformation where this region is close to Stx1B, falling below the distance constraint. This trend echoes the one observed in all measurements involving the Stx1B:Munc18-1 complex.

Another overlength cross-link that has already been found in the measurement with Stx1B<sup>L221P</sup>, but not in the measurement with the wild-type is between K120 (Munc18-1) and K125 (Stx1B, 44.1 Å, Cα-Cα). This cross-link could imply a change in the binding conformation. However, while hardly any other indications were observed in the measurement with Stx1B<sup>L221P</sup>, many indications of a conformational change can be found in the measurements with Stx1B<sup>E210K</sup>.

To begin with, there is the longest intermolecular cross-link identified in the measurements with Stx1B<sup>E210K</sup>, spanning between K356 (Munc18-1, domain 3a) and K87 (Stx1B, helix H<sub>b</sub>) with a length of 47.0 Å (Cα-Cα, **Fig. 4.41 E**). This suggests a shift of helix H<sub>b</sub> towards helix 12 in domain 3a of Munc18-1. This is likely only possible if the SNARE motif, which is bound to the H<sub>abc</sub> domain, pivots away. Assuming that the E210K mutation promotes such an opening, as suggested by our ITC experiments, such a conformational change is conceivable. Additionally, another noteworthy overlength intermolecular cross-link was found between K294 (Munc18-1) and K116 (Stx1B), spanning 38.8 Å (Cα-Cα, **Fig. 4.41 E**), providing further support for the notion of a potential shift in the entire H<sub>abc</sub> domain of Stx1B.

Two additional cross-links indicating a change in binding conformation are the cross-links between K333 (Munc18-1, domain 3a, loop) and K188 (Stx1B, linker region or start of the SNARE motif) with a length of 42.0 Å (Cα-Cα), and between K321 (Munc18-1, domain 3a, loop) and K93 (Stx1B, helix H<sub>b</sub>) with a length of 31.4 Å (Cα-Cα, **Fig. 4.41 E**). These cross-links imply the opening of the furled loop, which could occur if the SNARE motif pivots away due to the E210K mutation, triggering the opening of Stx1B's closed conformation. This movement could create space for the furled loop of Munc18-1 to open, bringing the involved lysine residues closer together.

(1) For plotting the box plots, overlength cross-links involving Stx1B's K251 were excluded to provide a clearer representation of overlength cross-links potentially associated solely with substantial binding conformational changes, as cross-links with K251 likely arose due to unspecific flexibility of the truncated C-terminal end as discussed before. Box Plot including all cross-links can be found in **Appendix Fig. 33 B**.



Additionally, the latter cross-link implies a shift of Stx1B's helix H<sub>b</sub> toward Munc18-1's helix 12, similar to the previously described cross-link.

The most compelling cross-links, indicating alterations in binding conformation, are situated on the rear side of the binding interface between Stx1B and Munc18-1 domain 3a. These cross-links involve K7 (Munc18-1) and both K54 and K139 (Stx1B). Each cross-link scratches the maximum distance constraint, measuring 31.4 Å (C $\alpha$ -C $\alpha$ ) and 30.6 Å (C $\alpha$ -C $\alpha$ ), respectively. Interestingly, these cross-links were absent in measurements with Stx1B<sup>WT</sup> or Stx1B<sup>L221P</sup>, likely because the lysine residues were slightly too distant in the buffer environment to cross-link with each other. Connecting the buried N-terminal helix of Munc18-1 with helices H<sub>a</sub> and H<sub>c</sub> of Stx1B, these cross-links strongly suggest an inward shift of the H<sub>abc</sub> domain into the buried region of Munc18-1. Consequently, this would also create space for the unfurling of the Munc18-1 loop, when the SNARE motif pivots away. This would allow for the alignment of the SNARE motifs of Syb2 and Stx1B for early template complex formation.

In summary, the XL-MS measurements with Munc18-1 and Stx1B<sup>E210K</sup> suggested significant alterations in the binding conformation of the Stx1B:Munc18-1 complex compared to Stx1B<sup>WT</sup> and Stx1B<sup>L221P</sup>. While Stx1B<sup>L221P</sup> only showed possible minor conformational changes within the interaction interface, Stx1B<sup>E210K</sup> displayed a notable increase in median and average intermolecular cross-link lengths, caused by new cross-links with longer distances. This shift was significant enough to include points previously classified as outliers within the box plot's whiskers. Notably, several overlength cross-links were identified, suggesting a potential shift in the entire H<sub>abc</sub> domain of Stx1B closer to Munc18-1. Furthermore, two cross-links suggested a possible opening of the furled loop, likely facilitated by the E210K mutation-induced movement of the SNARE motif away from Stx1B's H<sub>abc</sub> domain (driven by charge repulsion as suggested in **Chapter 4.4.1**), and subsequent opening of its closed conformation. The alteration in the binding conformation is further supported by cross-links indicating a shift of the H<sub>abc</sub> domain towards the buried region of Munc18-1. Consequently, this movement could additionally allow for the unfurling of the Munc18-1 loop, enabling the alignment of SNARE motifs for early template complex formation. Overall, our results strongly suggest a substantial alteration in the binding conformation between Munc18-1 and the Stx1B<sup>E210K</sup> mutant compared to the wild-type complex.

## 5. Discussion

### 5.1. Advances in understanding the molecular mechanism of the SNARE complex formation machinery and the role of Stx1B E210K and L221P SNAREopathic mutations

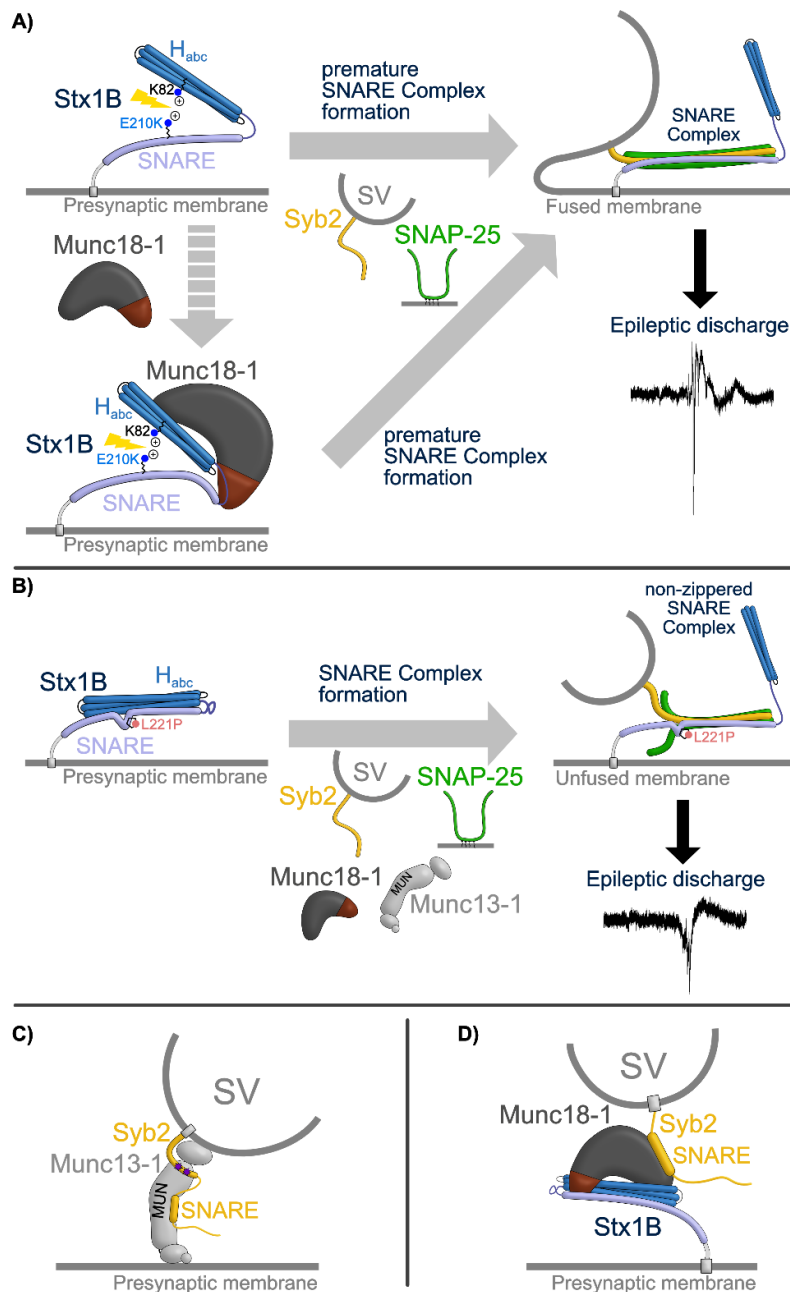


**Figure 5.1:** Main conclusions and hypothetical model derived from our results for the SNARE complex formation machinery. **A)** Stx1B<sup>E210K</sup> causes a charge repulsion between the its H<sub>abc</sub> domain and SNARE motif, inducing an open conformation and affecting binding to Munc18-1. This leads to premature SNARE complex formation, impacting neural circuits and resulting in epilepsy. **B)** The L221P mutation of Stx1B affects the structural integrity of its SNARE motif, destabilizing the SNARE complex and hindering proper formation. This results in less efficient vesicle fusion and neurotransmitter release, leading to impaired signal transmission and ultimately epilepsy. **C)** The SNARE motif of Syb2 aligns with the concave side of the MUN domain of Munc13-1, while the C-terminal JMD interacts with the C-terminal region of the MUN domain, with both tryptophan residues serving as key anchor points. **D)** The SNARE motif of Syb2 can also bind to domain 1 of Munc18-1, potentially serving as an additional binding site during vesicle docking.



Our findings add valuable insights into the current model of the SNARE complex formation machinery (**Fig. 1.11**). Particularly in relation to the SNAREopathic effects of the two Stx1B mutations, E210K and L221P, which seem to disrupt the vesicle fusion mechanism through distinct mechanisms.

Stx1B<sup>E210K</sup> primarily affects its interaction with the orchestrating protein Munc18-1. This mutation disrupts a salt bridge between the H<sub>abc</sub> domain and the SNARE motif within Stx1B and likely induces charge repulsion, prompting a shift from the closed to the open conformation, and significantly reducing its binding affinity to Munc18-1. As a result, Munc18-1's regulation of the autoinhibited, closed state of Stx1B is compromised, making it possibly more prone to premature SNARE complex formation and neurotransmission (**Fig. 5.1 A**). Additionally, the E210K mutation exhibits a gain-of-function effect by accelerating vesicle fusion.

In contrast, Stx1B<sup>L221P</sup> directly affects the stability of the SNARE complex, likely by interfering with its correct formation. The proline substitution disrupts the structural integrity of the SNARE motif, possibly compromising the watertight seal of the hydrophobic core of the SNARE complex, thereby reducing the overall stability. This instability leads to a significant reduction in synaptic vesicle fusion efficiency (**Fig. 5.1 B**). The L221P mutation also shows reduced binding affinity to Munc18-1, though less pronounced than the E210K mutation.

These conclusions for the Stx1B<sup>E210K</sup> and Stx1B<sup>L221P</sup> mutants suggest that both mutations potentially disrupt the delicate balance of signal transduction in the nervous system, leading to the development of epilepsy.

For the other molecular components involved in SNARE complex formation, we found strong evidence of an interaction between the juxtamembrane domain (JMD) of Syb2 and the C-terminal region of the MUN domain of Munc13-1, with both tryptophan residues in the JMD of Syb2 acting as key anchor points. Additionally, we observed that the SNARE motif of Syb2 likely aligns with the concave side of the Munc13-MUN (**Fig. 5.1 C**). Together, these interactions may facilitate the proper orientation of Syb2 for SNARE complex formation.

Furthermore, beyond the primary binding site for the Syb2 SNARE motif at the furled loop region of Munc18-1's domain 3a, where both the Syb2 and Stx1B SNARE motifs would align to form the template complex, we identified an additional binding site in domain 1 of Munc18-1. This secondary site may play a supplementary role in synaptic vesicle docking (**Fig. 5.1 D**).

### **5.2. Evaluating the molecular impact of Stx1B<sup>E210K</sup> and Stx1B<sup>L221P</sup> mutations on the SNARE complex formation machinery**

CD spectroscopy analysis of the individual Stx1B proteins revealed similar thermal stability and a predominantly helical structure for the wild-type protein and its mutant counterparts. However, the mutations influenced helicity differently. Stx1B<sup>E210K</sup> showed increased helical content, indicated by more pronounced minima, while Stx1B<sup>L221P</sup> exhibited less pronounced minima, suggesting reduced helical content compared to the wild-type. While this result was expected for the L221P

mutant, as proline is known for its helix-disrupting characteristics, it was surprising for the E210K mutant [247, 248].

The argument that lysine has a high helix-forming propensity is certainly plausible, and the increase in helical content is further supported by the  $n\pm 3,4$  rule, where the newly introduced lysine can form a helix-stabilizing interaction with aspartic acid located three positions away (**Appendix Fig. 9**) [291]. However, it has to be mentioned that glutamic acid also has a very high helical propensity, even higher than that of lysine, and is commonly found in  $\alpha$ -helices [245, 291]. Therefore, the differences observed may not necessarily arise from a higher helical content of the protein itself but could also be due to slight variations in concentrations during the measurements. Nonetheless, the results were consistent across all measurements.

Another possible explanation is provided by a size exclusion analysis conducted during T. Werk's master's thesis project (2024), which I supervised. Gel filtration of the individual proteins revealed that Stx1B<sup>L221P</sup> has a similar elution profile to the wild-type, whereas Stx1B<sup>E210K</sup> shows an earlier elution, indicating a species with a higher molecular weight [292]. Based on the idea that the E210K mutation causes a charge repulsion to an opposing lysine residue, the resulting binding disruption of the H<sub>abc</sub> domain to the SNARE motif would probably lead to an open conformation of Stx1B. A free SNARE motif could result in nonspecific oligomerization with other free SNARE motifs, leading to high molecular weight species, which are not identifiable in SDS-PAGE as multimers fall apart there. The formation of multimers could cause previously less structured SNARE motifs to adopt a strong  $\alpha$ -helical structure, thereby increasing the helical content. Furthermore, it remains unclear how the linker region of Stx1B<sup>E210K</sup> behaves in this case. It is possible that this region also adopts a more helical structure, which would similarly increase the helical content.

It should also be noted that the differences in the spectra are relatively small. We observed a difference of approximately 4 mdeg for each minimum between Stx1B<sup>E210K</sup> and Stx1B<sup>WT</sup> and about 2 mdeg for each minimum between Stx1B<sup>L221P</sup> and Stx1B<sup>WT</sup>. Much more significant differences were seen in samples with the InDel mutation of Stx1B, which showed a difference of approximately 60 mdeg for each minimum compared to the wild-type when only the H<sub>abc</sub> domains were examined, and a difference of nearly 30 mdeg for each minimum when looking at the H<sub>abc</sub>-SNARE constructs [178]. Therefore, putting the results into perspective, while the E210K and L221P mutations do cause differences in the helical structure, these differences are minor.

The observations of varying degrees of helicity also extend to the investigations of the SNARE complexes formed with the wild-type and mutant proteins (**Fig. 4.3 A**). Here, the same tendencies are observed, with the L221P mutant reducing the helical content and the E210K mutant increasing it.

It is striking that the E210K mutation still seems to increase the helical content, as the SNARE motifs should already be in a helical formation, as shown in crystal structures of SNARE complexes [45]. The aforementioned  $n\pm 3,4$  rule may come into play here, allowing for additional stabilization of the helical structure. For the SNARE complex formed with L221P, the reduced helicity aligns with the helix-breaking characteristics of proline, which is not overcome by the formation of the helical

SNARE complex. The inability to form an  $\alpha$ -helical conformation might also affect the other SNARE motifs of Syb2 and SNAP-25, which present as IDPs when not in complex.

However, these differences in the helical content are also relatively minor, with variations of approximately 1 mdeg to 3 mdeg.

More significant are the differences in thermal stability, where the SNARE complex formed with the L221P mutant is significantly less stable than both the wild-type SNARE complex and the one formed with the E210K mutant, which show similar melting temperatures (**Fig. 4.3 B), C**). We suspect that the L221P mutation interferes with the water-tight sealing of the hydrophobic core near the zero layer, allowing water molecules to infiltrate the buried region of the SNARE complex. This influx of water disrupts hydrophobic interactions and dissolves the ionic interactions within the zero layer.

Despite all this, the melting temperature, with  $T_M = 75.72 \pm 0.86$  °C, is still very high and well above normal physiological conditions. However, it is likely that this reduced thermal stability also translates into physiological impairment. It is conceivable that the L221P mutation affects the docking mechanism of synaptic vesicles, causing the half-zipped SNARE complexes, which keep the synaptic vesicles in a release-ready state, to dissolve. As a result, it may prevent the buildup or reduces the size of the RRP, which is normally important for rapid neurotransmission, high-frequency signaling, synaptic plasticity, and the overall performance of neural circuits. Its affection has been shown for other mutants of Stx1B and other proteins of the SNARE complex formation machinery [123, 141, 178, 293]. And in a cellular environment where NSF and SNAPs strongly favor complex disassembly, a high stability and integrity of the complex is likely required to prevent these factors from easily disassembling it [293, 294].

In this regard, it would be interesting to see how a proline mutation would affect SNARE complex formation and stability if it were located further C-terminal to the zero layer, in the positive layer region of the SNARE complex. An earlier study has shown that N- to C-terminal zippering must break through the zero layer to achieve a stable SNARE complex [123]. As the proline residue of the L221P mutant resides in the negative layer region, it might prevent successful SNARE complex formation at the presynaptic membrane, as the mutation could hinder the zippering process from reaching the zero layer (**Fig. 4.4**). If a proline mutation would be located further C-terminal, it might still allow for SNARE complex assembly, and such a mutation might not be associated with SNAREopathies.

The reduced stability of the SNARE complex formed with L221P was also observed in the SDS-PAGE from the SNARE complex formation assay. The band intensity of the SNARE complex was significantly reduced, while the band intensity increased for the unbound individual proteins (**Fig. 4.2**). This clearly indicates that a SNARE complex formed with L221P is unable to sustain the SDS environment, in contrast to the wild-type and E210K counterparts. The weak point introduced by the L221P mutation likely allows the SDS buffer to effectively dissolve the complex.

Interestingly, an additional band for the t-SNARE complex was visible in the SNARE complex formation assay with the wild-type SNARE motif, which was significantly less intense for both

mutants. Earlier studies have shown that Stx1 form a complex with SNAP-25, which is thought to prepare a platform at the presynaptic membrane awaiting the arrival of Syb2 for form the ternary SNARE complex with the assistance of Munc18-1 [81, 295, 296]. Strikingly, both the E210K and L221P mutations seem to render the SNARE motif of Stx1B incapable of forming this t-SNARE complex with SNAP-25 or reduce its stability, making it not SDS-stable.

For the L221P mutant, the reason could be similar to the destabilized ternary SNARE complex; the introduction of the proline residue might disturb the helical alignment of the SNARE motifs by disrupting the conformation of the  $\alpha$ -helix in the SNARE motif of Stx1B. On the other hand, the E210K mutation is particularly intriguing as it does not interfere with the stability or integrity of the ternary SNARE complex. Furthermore, the position of this mutation neither directly substitutes a hydrophobic layer residue nor does the side chain point inward into the buried region of the SNARE complex. This suggests that the binary complex of Stx1B and SNAP-25 adopts a structure very different from the ternary complex, where position E210 plays a more central role in the interaction between the SNARE motifs of Stx1B and SNAP-25. Unfortunately, no solved structure of the synaptic t-SNARE complex exists, only a study by Jakhanwal *et al.* on the Stx1:SNAP25:Munc18-1 complex where cross-links indicate that the structure of the Stx1:SNAP-25:Munc18-1 complex is different from that of the binary Stx1:Munc18-1 complex and that Stx1 likely adopts an open conformation [296].

#### 5.4. The Critical Role of the K82-E210 Salt Bridge in Stx1B's Binding to Munc18-1

The critical role of the salt bridge between K82 and E210 of Stx1B was confirmed by experiments of T. Werk (2024), where we inverted only the charge of the side chain at position 82, creating Stx1B<sup>K82E</sup> as a control mutant [292]. Pull-down assays and ITC experiments revealed a similarly reduced binding towards Munc18-1 as observed with Stx1B<sup>E210K</sup>, with binding affinity in the micromolar range [292]. This strongly indicates that the intramolecular charge repulsion between the residues at positions 82 and 210 is indeed responsible for the reduced binding to Munc18-1, underscoring the importance of that salt-bridge.

Experiments focusing on the neighboring lysine residue at position 83 of Stx1B have shown no rescue effect on the E210K mutation. On the contrary, the binding of Stx1B<sup>E210K,K83E</sup> to Munc18-1 was completely abolished (**Fig. 4.12**). Only the Stx1B<sup>KKEE</sup> mutant, which involves the crucial position 82, could rescue the binding. Strikingly, Stx1B<sup>E210K,K83E</sup> revealed also a lower thermal stability compared to the rescue mutant and a significantly reduced helicity, indicating a structural affection of Stx1B by this mutant. This was surprising as we did not find any evidence of structural stability involvement of lysine at position 83, neither from the Stx1A crystal structure nor in an AlphaFold 3 complex prediction, as it points away from any potentially opposing intramolecular residues (**Fig. 4.11** and **Fig. 5.3**).

Interestingly, when we performed ITC measurements with Stx1B<sup>K83E</sup> in the context of T. Werk's master thesis (2024), however, the binding affinity towards Munc18-1 was found to be as diminished as for Stx1B<sup>K82E</sup>, displaying a  $K_D$ -value of  $35.8 \pm 3.90 \mu\text{M}$  [292]. Since the K83E mutation

did not lead to a rescue effect in the context of the E210K mutant, it can be assumed that the K83E mutation might follow a different mechanism that also disrupts binding to Munc18-1. This could explain why the binding of Stx1B<sup>E210K,K83E</sup> to Munc18-1 is completely diminished; when two binding-weakening mutations act through different mechanisms, their combined effect can completely abolish binding. The structural influence of the simultaneous mutations was also reflected in a substantially reduced helical content and significantly reduced thermal stability (Fig. 4.13).

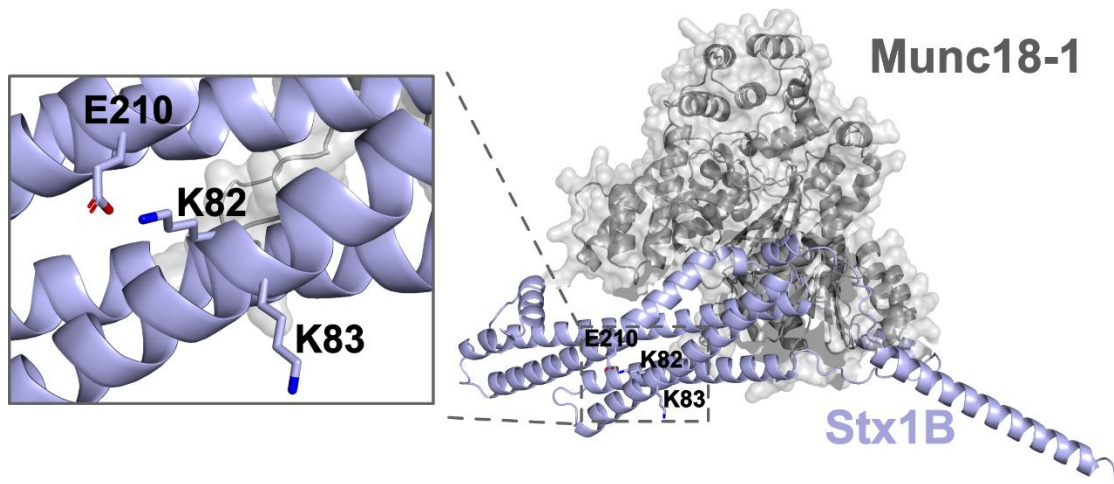


**Figure 5.3: A)** AlphaFold 3 structure of the Stx1B:Munc18-1 complex [297]. The model shows a similar structure to the Stx1A:Munc18-1 crystal structure (PDB: 3C98, Fig. 4.11). The lysine residue at position 83 is not involved in a salt bridge-interaction and points away from possible interaction partners.

Given the assumption that the charge repulsion in the epilepsy-relevant Stx1B<sup>E210K</sup> mutant potentially prevents the autoinhibitory H<sub>abc</sub> domain from binding to the SNARE motif, it is conceivable that Stx1B<sup>E210K</sup> maybe adopts an open conformation. Therefore, a functional comparison with the LE/AA mutant of Stx1, which is known to facilitate an open conformation of Stx1, would be interesting in this context [66]. The LE/AA mutant can partially mitigate the severe phenotypes observed in *C. elegans* lacking Unc13, the invertebrate homolog of Munc13-1. Furthermore, it bypasses the requirement of Munc13-1, but not Munc18-1 for liposome fusion [298, 299]. Additionally, the Stx1 LE/AA mutation has been shown to increase the vesicular release probability in mice [300]. This suggests that the energy barriers to SNARE complex formation are lowered by LE/AA mutation, likely due to the constant availability of the SNARE motif in its triggered open conformation, bypassing the necessary conformational changes facilitated by the orchestrating proteins Munc18-1 and Munc13-1 under wild-type conditions [84]. If Stx1B<sup>E210K</sup> functions similarly, it is understandable why this mutant triggers SNAREopathies, as bypassing highly controlled mechanisms can affect the delicate balance of signal transduction in the nervous system.

In this context, it should be emphasized that the binding mode between Stx1B<sup>E210K</sup> and Munc18-1 differs significantly from that of the wild-type and Stx1B<sup>L221P</sup>. The latter two exhibit enthalpy-driven binding, whereas the interaction between Stx1B<sup>E210K</sup> and Munc18-1 is driven by entropy. This

means the binding process is mainly associated with an increase in disorder within the system, typically due to significant hydrophobic interactions. When hydrophobic regions come together, water molecules that were previously ordered around these surfaces are released into the bulk solvent, increasing entropy [301]. This aligns with the fact that binding can induce favorable conformational changes, bringing previously distant regions into proximity. This conformational flexibility could also contribute to the entropy increase [302, 303].

Based on this and the known data, we can speculate about the exact nature of the binding process between Munc18-1 and Stx1B<sup>E210K</sup>. One possibility is that Stx1B<sup>E210K</sup>, initially in an open conformation due to charge repulsion, is forced into a closed conformation by Munc18-1. This could result in the formation of a hydrophobic core between the SNARE motif and the H<sub>abc</sub> domain, displacing water molecules and increasing entropy. Alternatively, a conformational change might occur in Munc18-1, where the furled loop unfolds and aligns with the free SNARE motif of the open conformation of Stx1B<sup>E210K</sup>. Apart from this, another entirely different binding conformation is also conceivable. To explore this, we need more detailed structural information to provide a direct impression of the binding conformations. One method to achieve this is cross-linking mass spectrometry, which will be discussed in more detail later on.

### **5.5. Evaluating the functional integration and the impact of Stx1B mutants in zebrafish models**

A particularly compelling argument for the functionality of the constructed Stx1B<sup>E210K,K82E</sup> mutant is that the rescue effect also succeeded in our *in vivo* experiments with zebrafish larvae. This success demonstrates that the rescue mechanism functions effectively in a natural synaptic environment, not just in the artificial *in vitro* conditions.

Zebrafish (*Danio rerio*) were chosen for their high genetic homology with humans, transparent bodies, and ease of genetic manipulation. Furthermore, they have only simple breeding and maintenance requirements, exhibit high fertility, and display rapid external development [304-306]. Because of these advantages, zebrafish have become increasingly popular as a model for investigating various human diseases, including cancer, cardiovascular disease, and metabolic disorders, but especially neurodevelopmental disorders over the past two decades [307, 308].

Despite their simplicity, the zebrafish central nervous system includes several conserved subcortical and cortical structures, with neurons and connections similar to those in humans. The zebrafish brain is divided into the forebrain, midbrain, and hindbrain/spinal cord, with further subdivisions forming structures like the pallium, subpallium, thalamus, and cerebellum [309]. Additionally, most neurotransmitters and the neuropeptidergic system are highly similar between zebrafish and humans, making them an excellent model for investigating human neurological diseases [310]. For this reason, the findings obtained from experiments with zebrafish can likely be well extrapolated to humans.

In epilepsy research, zebrafish offer several key benefits, including the ability to conduct high-throughput behavioral analysis using automated video tracking systems, perform

electroencephalographic (EEG) or local field potential (LFP) recordings in both larval and adult fish, and carry out *in vivo* brain imaging with activity-dependent bioluminescent/fluorescent reporters [256-260].

Zebrafish have gained further prominence as models for specific diseases due to advancements in gene editing tools like TALENs and CRISPR/Cas9, enabling targeted mutations efficiently [311, 312]. The availability of extensive gene expression data and numerous mutant and transgenic strains further enhances their utility in neurobiological research [313]. Their transparency and small brain size make them ideal for monitoring brain activity with techniques like calcium imaging and two-photon microscopy [314]. Additionally, zebrafish are valuable for neurobehavioral studies, as larvae display quantifiable behaviors that can be monitored through video tracking. While larval models are useful, it is important to consider their developing neural systems, which may limit some aspects of neurological disorder studies. Adult zebrafish, with fully developed and complex brain functions, could also offer significant benefits [315].

In this work, we used the *To2* transposon system to introduce human Stx1B<sup>WT</sup>, Stx1B<sup>L221P</sup>, Stx1B<sup>E210K</sup>, and Stx1B<sup>E210K,K82E</sup> into zebrafish genomes, with successful integration confirmed by mCherry fluorescence. This system offers several advantages, including efficient and stable transgenesis, versatility in accommodating large DNA fragments, and minimal position effects. This system is highly efficient for inserting transgenes into the zebrafish genome, facilitating stable integration and high germline transmission rates [316]. Transgenes introduced *via* the *To2* system are stably integrated, leading to consistent and heritable gene expression. It can accommodate large DNA fragments, allowing for the introduction of complete gene constructs, including regulatory elements that ensure proper expression in the appropriate tissues [317]. Additionally, as a non-viral method, it avoids potential complications associated with viral vectors, such as immune responses or insertional mutagenesis [316].

However, the *To2* transposon system also presents challenges such as random integration, potential mosaicism, risk of insertional mutagenesis, possible transgene silencing, and variability in transgene copy number [318]. Random integration can sometimes disrupt endogenous genes or regulatory elements, potentially causing unwanted mutations or gene expression changes that could confound experimental results [318]. Transgene microinjection at one-cell stage can result in mosaicism, where only a subset of cells contains the transgene, complicating analyses and requiring additional generations to establish stable, fully transgenic lines [244]. While less common than with viral vectors, there is still a risk of insertional mutagenesis, where the integration disrupts essential genes, potentially leading to deleterious phenotypes or lethality [317]. Additionally, the number of transgene copies integrated into the genome can vary, leading to differences in expression levels between individual transgenic lines [316]. In this regard, also cis-regulatory elements near the integration sites might have an effect on the transcriptional activity [319].

To check whether the integration of the foreign human Stx1B constructs had any impact on the healthy development of the zebrafish, the larvae were examined at 3 and 5 days post-fertilization (dpf) for morphological abnormalities and epileptiform activities using local field potential (LFP)

recordings. All transgenic zebrafish larvae exhibited normal development with no visible morphological abnormalities, including heart and swim bladder development, indicating that the introduction of the human Stx1B variants did not adversely affect the overall physical development of the zebrafish. This suggests that the genetic modifications were successfully integrated and expressed without causing detrimental morphological effects, which is a crucial consideration when assessing the viability and potential impact of these genetic interventions *in vivo*. Thus, it can be assumed that the random integration did not disrupt crucial endogenous genes or regulatory elements, at least for the larvae that survived and continued to develop.

In terms of neurological function, LFP recordings at 5 dpf revealed that almost all larvae injected with human Stx1B<sup>WT</sup> exhibited baseline activity with close to none epileptiform events, indicating no adverse neurological impact, meaning that the introduction of the wild-type human Stx1B does not negatively impact the neurological function of zebrafish larvae. However, it is important to note that these experiments were conducted against the background of the endogenous Stx1B wild-type gene. Although the expression of the constructs can be confirmed by mCherry fluorescence, it remains debatable how well the expressed human Stx1B constructs integrate into the SNARE complex formation machinery of the zebrafish larvae. It is possible that while the constructs introduced by the *ToI2* transposon system are expressed, they may not be functionally integrated at the synapse.

However, based on the neurological (dys)functions observed in zebrafish expressing the mutant human Stx1B constructs, the functional integration into the SNARE complex formation machinery of the zebrafish is indeed likely. Larvae expressing Stx1B<sup>L221P</sup> exhibited the highest number of ictal discharges, characterized by mild but frequent seizures. In contrast, larvae expressing Stx1B<sup>E210K</sup> showed fewer but significantly stronger seizures, often accompanied by aftershock events. The Stx1B<sup>E210K,K82E</sup> mutant displayed rescue effects, with seizure activity similar to wild-type, characterized by low amplitude and short duration. Nevertheless, it could be argued that the neurological abnormalities might have arisen from poor genetic integration of the human Stx1B constructs by the *ToI2* transposon system. Given the statistical comparison to the wild-type, however, this seems unlikely. It is more probable that the mutant human constructs negatively impact the SNARE complex formation machinery in the zebrafish larvae.

To further understand these dynamics, it would be interesting to investigate how the expression of human Stx1B constructs, both wild-type and mutants, affects the expression of endogenous Stx1B. This raises questions about whether endogenous expression remains constant, is reduced, or is increased. Additionally, exploring whether the human Stx1B and endogenous Stx1B constructs compete for integration into the SNARE complex formation machinery, or if one is preferentially incorporated due to certain factors, is worthwhile. Measurements with the mutant human constructs showed some individuals that did not exhibit any epileptic discharges during the measurement period, possibly because the endogenous wild-type Stx1B partially compensates (**Appendix Fig. 17**). However, it must be noted that the measurement time frame is relatively short, meaning that seizing events could have been missed. Extending the measurement time is also



inadvisable, as the implanted electrode could cause trauma, increasing artificial seizing events unrelated to the mutant effects.

A method to reduce the concentration of endogenous Stx1B is the usage of morpholinos. In an earlier study by Schubert *et al.* (2014), zebrafish experiments were also conducted regarding mutations of Stx1B [181]. In this study, a functional knockdown of *stx1b* was achieved by the application of morpholinos, mimicking a loss-of-function by interfering with protein expression. A 50% reduction in Stx1b led to abnormal behaviors and LFP events at 5 dpf, including a lack of touch response in 40% of larvae, increased jaw and pectoral fin movements, and myoclonus-like jerks [181]. LFP recordings from the optic tectum showed that *stx1b* knockdown induced paroxysmal events in 45% of morphants, averaging 12.9 events per 10 min with a mean duration of 100 milliseconds. These events included polyspiking discharges and high-frequency oscillations (HFOs). A moderate temperature increase to 31.5 °C induced seizures in both morphants and controls, but morphants were more sensitive, showing a higher frequency and duration of paroxysmal events [181].

Co-injection of wild-type human Stx1B also *via* the *To/2* transposon system rescued the epileptic phenotype, reducing both the number and duration of paroxysmal events. Conversely, human Stx1B<sup>V216E</sup> did not rescue the phenotype, with similar seizure activity observed in both the knockdown and mutant groups. These results indicate that the observed phenotypes are due to *stx1b* knockdown and not off-target MO effects [181].

Nonetheless, it must be emphasized that morpholinos are no longer considered state of the art and are avoided in modern studies due to their numerous off-target effects, which can erode the validity of experimental conclusions [320]. The most optimal approach would be to directly edit the genome to mutate the endogenous Stx1B accordingly. Modern gene-editing methods such as CRISPR/Cas9 are suitable for this purpose. However, generating stable lines takes a considerable amount of effort and time, which is why we opted for the simpler implementation of expressing human Stx1B *via* the *To/2* transposon system for these experiments.

Observing how zebrafish with a *stx1b*-null background behave when they receive the human Stx1B constructs *via* the *To/2* transposon system would be quite informative. However, generating individuals with a pure *stx1b*-null background poses significant challenges, as they do not survive beyond 10 dpf due to their inability to feed. Therefore, a stable mutant line must always be maintained as a parental heterozygous population.

This approach was applied for the assessment of behavioral function through touch response experiments at 3 dpf. The touch response in zebrafish is a simple, quantifiable behavior that provides valuable insights into neurological function, seizure activity, and the effects of genetic mutations and potential antiepileptic drugs, making it a useful tool for epilepsy research. This non-invasive and ethical approach facilitates high-throughput screening and developmental studies [307]. The touch response in zebrafish is mediated by mechanosensory neurons, specifically Rohon-Beard neurons in the dorsal spinal cord and trigeminal sensory neurons in the head, which detect mechanical stimuli and relay this information to the central nervous system [321, 322].

Epileptic seizure zebrafish models often show no touch response because seizures disrupt normal neuronal activity and sensory processing. During seizures, the excessive and abnormal electrical activity in the brain can impair the function of sensory neurons and neural circuits responsible for touch perception, leading to a diminished or absent response to tactile stimuli [307].

Larvae injected with Stx1B<sup>WT</sup> showed a significant increase in the proportion of touch-responsive larvae in a *stx1b*-null background, from around 75% to around 87.3%, indicating partial rescue of sensory and motor functions. This strongly suggests that the wild-type construct is compatible with the zebrafish's nervous system and is integrated into the SNARE complex formation machinery, restoring neurotransmitter release. Interestingly, larvae expressing Stx1B<sup>L221P</sup> showed a similar partial rescue effect, while those injected with Stx1B<sup>E210K</sup> exhibited no significant rescue effect and slightly increased non-responsive larvae.

The fact that Stx1B<sup>L221P</sup> also partially restores motor response function indicates that this Stx1B construct functionally integrates into the neurotransmitter release machinery. However, its function restoration is counterintuitive, given that Stx1B<sup>L221P</sup> exhibited the highest number of ictal discharges and has been characterized as a dysfunctional mutant in other experiments in this study. Nevertheless, it must be noted that the nature of the touch response test allows only a binary outcome: either a touch response is present or not. Fine distinctions, such as the distance individuals swim after the touch or whether they remain responsive immediately after the initial touch, are not considered in this assessment. Therefore, it is possible that while Stx1B<sup>L221P</sup> restores the touch response, it may not be as effective in fully restoring motor functions compared to Stx1B<sup>WT</sup>. A more detailed examination with an adjusted experimental approach might be appropriate to investigate this further.

Since Stx1B<sup>E210K</sup> behaves significantly differently in the touch response compared to the L221P mutation, it is evident that both mutants affect the SNARE complex formation machinery in distinct ways. For the E210K mutant, it appears that it cannot restore the function of the SNARE complex formation machinery. The reason could either be that it is not compatible with the other zebrafish proteins in the machinery, which is unlikely, or that it is not properly integrated into the presynaptic functional apparatus. Given the nature of the E210K mutant with its intramolecular charge repulsion, it is quite possible that the free SNARE motif leads to oligomerization, resulting in a non-functional clustering of the protein, which cannot maintain neurotransmitter release.

The Stx1B<sup>E210K,K82E</sup> mutant, on the other hand, partially rescued the negative effect of Stx1B<sup>E210K</sup>, reducing the proportion of non-responsive larvae to about 20%. This clearly suggests that the negative effect of the E210K mutant is not due to poor integration into the presynaptic sites but rather caused by the specific alteration of its functional properties, which are partially mitigated by the rescue mutation.

In conclusion, the Stx1B<sup>WT</sup> and Stx1B<sup>E210K,K82E</sup> mutants were effective in rescuing both neurological and motor sensory functions to near wild-type levels *in vivo*. The Stx1B<sup>L221P</sup> mutant induced frequent mild seizures but partially compensated for sensory and motor deficits. The Stx1B<sup>E210K</sup> mutant caused strong, intense seizures with limited rescue of motor sensory function. The study

underscores the utility of zebrafish as a model for epilepsy research, providing insights into the neurological impact of specific Stx1B mutations and potential avenues for therapeutic intervention.

### 5.3. Functional impacts of Stx1B mutations on SNARE complex formation and membrane fusion

Plausibly, the reduced stability of the SNARE complex caused by the L221P mutation also translates into a diminished capability to facilitate membrane fusion, as shown in the liposome fusion assay. Fusion reactions conducted with Stx1B<sup>SNARE-L221P</sup> reached a lower signal intensity compared to the wild-type within the measured time frame, indicating that the mutant SNARE motif facilitates liposome membrane fusion less efficiently. Surprisingly, experiments conducted with Stx1B<sup>SNARE-E210K</sup> achieved a higher signal intensity compared to the wild-type within the same time frame (**Fig. 4.6**). Notably, the E210K mutant reaches a linear saturation plateau much faster, while the wild-type and L221P mutant still show an increase in signal intensity. This indicates that the reaction with the E210K mutant seems to be completed, whereas the reactions with the other two are still ongoing within the measured time frame. It would have been interesting to see how much further the signal intensity would increase for the wild-type and the L221P mutant to determine if the signal intensity achieved by the E210K mutant would be surpassed by its counterparts. This would indicate whether relatively more liposomes would have fused, albeit at a slower rate.

The less effective SNARE complex formation and the resulting slower liposome fusion were evident in the kinetic quantification. Both the half-maximum fusion time and the initial fusion velocity indicated that the L221P mutant displayed significantly less effective liposome fusion compared to the wild-type and the E210K mutant. This suggests that vesicle fusion with the presynaptic membrane in axon terminals is also less effective and slower due to the L221P mutation in Stx1B. The slowed vesicle fusion could lead to a lower release of neurotransmitters, causing the action potential on the postsynaptic side to be smaller, triggered too late, or not triggered at all, thus affecting neuronal communication [323].

In contrast, an apparent gain-of-function effect of the E210K SNARE complex formation was evident in the kinetic quantification. Both the half-maximum fusion time and the initial fusion velocity showed that the E210K mutant displayed more efficient liposome fusion compared to the wild-type, although the differences were not significant. A gain-of-function effect in synaptic neurotransmission can be harmful, as it could lead to excessive release of neurotransmitters, disrupting the balance between excitatory and inhibitory signals in the brain. This disruption can cause hyperexcitability of neurons, potentially resulting in epilepsy. Additionally, heightened activity can lead to cellular stress, neurodegeneration, and cognitive impairments due to abnormal functioning and connectivity of synapses [324-326].

In an earlier study, Lammertse *et al.* have shown that a homozygous Munc18-1<sup>L446F</sup> mutation, which leads to a severe form of epileptic encephalopathy, increases vesicular release probability and the degree of short-term depression [326]. These features have also been observed for Stx1B<sup>V216E</sup>, another SNAREopathic mutation, in an earlier study of ours, indicating that a gain-of-function

mutation may be present there as well [178]. While Munc18-1<sup>L446F</sup> also results in enhanced Ca<sup>2+</sup> neurotransmitter release, unlike Stx1B<sup>V216E</sup>, it is notable that both mutants alter short-term plasticity, a feature also observed in Munc18-1<sup>+/-</sup> neurons [73]. Notably, individuals who are heterozygous for the Munc18-1<sup>L446F</sup> mutation do not exhibit any disease symptoms [326]. This highlights the complex nature of gain-of-function mutations and their varied impact on synaptic function and neurological health.

In light of these findings, it would be intriguing to perform experiments in mouse neurons with the Stx1B mutations investigated here. By doing so, it may be possible to determine if these mutations influence the RRP, vesicular release probability (P<sub>vr</sub>), paired-pulse ratio (PPR), and excitatory postsynaptic current (EPSC), as we did in our earlier study [178]. Additionally, it would be valuable to observe their impact on the cellular protein levels of interaction partners, particularly Munc18-1. However, the question remains as to why Stx1B<sup>E210K</sup> exhibits a gain-of-function effect on liposome fusion. While we have attempted to explain this through a possible clustering effect caused by the E210K mutation, we lack evidence to confirm that it is indeed related to membrane interaction. In this context, it might be conceivable to conduct another experiment where the formation of SNARE complexes is performed in the absence of membranes, as done in other studies [69, 84, 123, 145]. A FRET assay could be conducted in such a setup, with donor and acceptor FRET labels attached to the C-terminus of two SNARE motifs, such as Stx1B and Syb2, to measure the speed of SNARE complex formation. If no differences are found in the kinetics between the mutant and Stx1B, it is likely that membrane interaction plays an important role.

Another question we need to address at this point is the stability of the ΔN-SNARE complex formed with the L221P mutant. Based on the crystal structure of the SNARE complex, the truncated N-terminus of Syb2 coincides with the affected L221P mutation site of Stx1B (**Fig. 5.2**). In contrast, the E210K mutation site is located further N-terminal and does not overlap with this region. Therefore, it is reasonable to assume that the stability and, consequently, the functionality of the ΔN-SNARE complex might already be compromised, which in turn could lead to less effective liposome fusion. This hypothesis could be tested by strategically positioning FRET labels to measure the stability of the complex. Nonetheless, it is evident that the L221P mutation significantly impacts the stability and functionality of SNARE complexes.

It should be noted that we monitored liposome fusion solely through lipid mixing, assuming that complete membrane fusion occurred. However, it is possible that only hemifusion took place, where only the outer leaflets of the lipid bilayers merge, allowing lipid exchange while keeping the inner layers distinct and separate [113, 116, 327]. Thus, performing a liposome fusion assay focused on content fusion might be plausible. This method detects the mixing of internal vesicle contents, providing direct evidence of full membrane fusion and offering a more accurate indicator of functional fusion events relevant for processes like neurotransmitter release [328].

However, setting up a content mixing assay is more complex, requiring the encapsulation of fluorescent dyes or other markers within the vesicles. Additionally, it may not be as sensitive to the initial steps of the fusion process, potentially missing early fusion intermediates detectable by lipid

mixing assays, which would not allow for precise initial fusion velocity measurements, as obtained from lipid mixing in our experiments [328, 329]. Therefore, for a comprehensive understanding, it might be useful to use both assays in tandem or even simultaneously [329]. Lipid mixing assays elucidate initial fusion kinetics, while content mixing assays confirm the occurrence of complete fusion events.

On another note, it would be worthwhile to test whether the application of liposomes of different sizes affects membrane fusion. Specifically, it might be insightful to place the  $\Delta$ N-SNARE complex onto a giant unilamellar vesicle (GUV) and the full-length Syb2 construct onto a small unilamellar vesicle (SUV) to mimic the membrane curvature conditions at the presynapse.

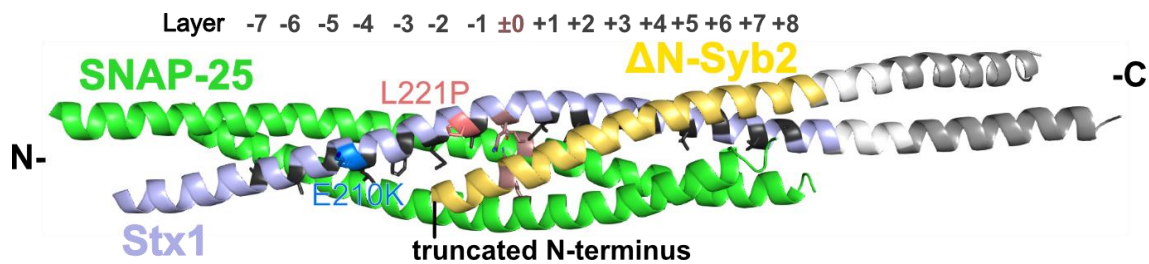


**Figure 5.2:** Possible model of a  $\Delta$ N-SNARE complex based on the crystal structure of the SNARE complex (PDB: 3HD7). The truncated N-terminal end of Syb2 still includes the stabilizing zero layer and overlaps with the L221P mutation site of Stx1B. E210K is not located within the interaction region.

In the assay described in this work, we only used the SNARE-TMR constructs of Stx1B, which lack the  $H_{abc}$  domain. Therefore, it would also be interesting to see how the full-length constructs of Stx1B wild-type and mutants behave. These full-length membrane proteins were purified during the master's thesis of A. Reklos (2023), which I supervised [330]. Interestingly, the full-length membrane proteins were significantly easier to handle than their SNARE-TMR construct counterparts. It can be assumed that the cytoplasmic  $H_{abc}$  domain significantly increased the solubility of the full-length Stx1B protein in aqueous buffers [330].

When using the full-length constructs, it would be necessary to reconsider the experimental design, as the prior formation of the  $\Delta$ N-SNARE complex might exclude any effects regarding the  $H_{abc}$  domain from the outset, probably leading to similar experimental outcomes. In this context, only the efficiency of the formation of the  $\Delta$ N-SNARE complex would differ, which would not be particularly interesting for our investigations, as  $\Delta$ N-SNARE complex formation does not reflect natural SNARE complex formation. Here, conclusions could only be drawn about whether the formation of the  $\Delta$ N-SNARE complex is influenced by an affected  $H_{abc}$  domain binding to the SNARE motif. It is conceivable that if the E210K mutation disrupts the  $H_{abc}$  domain binding to the SNARE motif, it could lead to a faster  $\Delta$ N-SNARE complex formation due to the abolition of the autoinhibitory effect of the  $H_{abc}$  domain.

In a newly designed assay adapted for the full-length constructs, the inclusion of the orchestrating proteins Munc18-1 and Munc13-1 should be considered, as has been done in earlier studies [69, 123, 167]. In this setup, no  $\Delta$ N-SNARE complex would be pre-formed. Instead, the focus would be

on the complex formation of Stx1B with Munc18-1, where the MUN domain of Munc13-1 would catalyze the SNARE complex formation.

Based on the data from the pull-down assays and ITC measurements, however, we would directly encounter another phenomenon: the reduced binding affinity of the Stx1B mutants to Munc18-1, particularly evident for the E210K mutation. Both experiments have demonstrated that the binding to Munc18-1, whether endogenous from mouse brain or recombinant, is significantly affected by the Stx1B mutations, with a ~20-fold reduction in binding affinity for Stx1B<sup>L221P</sup> and a ~100-fold reduction for Stx1B<sup>E210K</sup> compared to the wild-type. Reduced binding affinities of epilepsy-related Stx1B mutations have been observed before in our earlier study, with Stx1B<sup>G226R</sup> displaying a ~60-fold decrease and a ~5-fold decrease for Stx1B<sup>V216E</sup>, but none appear to influence binding affinity as strongly as the E210K mutation [178]. This is particularly interesting as both the L221P and E210K mutations are not located in the direct interaction interface between Stx1B and Munc18-1, whereas the G226R and V216E mutations are. Therefore, it is likely that there must be an indirect effect on the binding caused by these two mutants.

The rescue of binding affinity towards Munc18-1 by the charge reversion mutant Stx1B<sup>E210K,K82E</sup> strongly suggests that the salt bridge between the glutamic acid residue at position 210 and the lysine residue at position 82 is crucial for binding to Munc18-1. This importance likely stems from the essential role of the salt bridge in maintaining the stable binding of the H<sub>abc</sub> domain to the SNARE motif in the closed conformation of the wild-type. This correlation is logical since Munc18-1 primarily binds Stx1B in its autoinhibited state, functioning as a chaperone for Stx1B [140, 145, 331]. Therefore, it is conceivable that the proline mutation in Stx1B<sup>L221P</sup> also leads to a sufficiently strong conformational change, affecting the specific binding between Stx1B and Munc18-1.

In this context, it would be sensible to assess how these mutations affect the equilibrium between the open and closed conformations of Stx1B, both with and without the addition of Munc18-1, and whether the mutations favor the open conformation. To achieve this, FRET labels could be attached to opposing positions on the H<sub>abc</sub> domain and the SNARE motif, allowing fluorescence intensity and FRET efficiency to be measured, as demonstrated in a study by Lee *et al.* [144].

Furthermore, it might be interesting to examine whether the binding affinities of the H<sub>abc</sub> domain to the SNARE motif are indeed affected by the mutations. This could be done using ITC or NMR spectroscopy with <sup>15</sup>N labeling of the H<sub>abc</sub> domain, as the SNARE motif is likely to be unstructured, which would result in a poorly resolved NMR spectrum. The NMR analysis of the closed conformation of Stx1 by Chen *et al.* could be used as a foundation [332]. We initiated these experiments in the master's thesis project of A. Reklós (2023) but were unable to obtain a well-resolved NMR spectrum of the H<sub>abc</sub> domain [330]. This was likely due to the use of a construct of the H<sub>abc</sub> domain that included the linker region at its C-terminal end. This linker region is known to exhibit some flexibility, as it undergoes conformational changes for the SNARE complex formation [70]. This flexibility was likely even more pronounced when the SNARE motif was not attached, as it typically binds to the H<sub>abc</sub> domain. As a result, the spectrum showed many overlapping peaks in the center, making it difficult to assign or detect clear indications of SNARE

binding. Peak shifts that occurred were mostly due to different pH levels of the measured samples [330]. Therefore, it would be worth repeating the experiments with a shorter construct omitting the linker region and stricter control of the pH.

## 5.6. Insights and limits of investigating the interaction of Syb2 and Munc13-MUN via NMR

While the interaction between Stx1B and Munc18-1 provides the crucial platform for SNARE complex formation and introduces the necessary energy barriers through conformational changes essential for an orderly and finely tuned neurotransmitter release, it represents only one part of the SNARE complex formation machinery. The other part is characterized by the SNARE protein Syb2 and the orchestrating protein Munc13-1. While Syb2 provides the anchor point to the vesicle membrane, Munc13-1 bridges both, the presynaptic and the vesicle membrane with its peripheral C<sub>1</sub>, C<sub>2</sub>B and C<sub>2</sub>C domains (**Fig. 1.11**). In contrast, the MUN domain is attributed with functional relevance for SNARE complex formation. Here we analyzed the interactions between Syb2 and Munc13-MUN via NMR spectroscopy. The spectra of <sup>15</sup>N-labeled Syb2 are characteristic of an intrinsically disordered protein (IDP) but suggest a partially structured region in the C-terminal JMD. IDPs present several challenges in NMR spectroscopy due to their lack of a stable, well-defined structure. As in the recorded <sup>1</sup>H-<sup>15</sup>N-HSQC spectra of <sup>15</sup>N-labeled Syb2, they often have numerous overlapping cross-peaks in the center of the spectra because their amino acid residues experience a not well defined chemical environment, making it difficult to assign cross-peaks to specific residues accurately [261].

We improved the quality of the spectrum by lowering the measurement temperature to reduce chemical exchange and thus avoid cross-peak broadening of Syb2. Additionally, we decreased the pH to enhance protonation. However, many overlapping cross-peaks remained in the center of the spectra, making it difficult to completely transfer assignments from Ellena *et al.* (BMRB entry 16514) [110].

In their experiments, Ellena *et al.* measured full-length Syb2 in dodecylphosphocholine (DPC) micelles and found two transient helical segments which were flanked by natively disordered regions, while the transmembrane region (TMR) forms a third more stable  $\alpha$ -helix. The N-terminal transient helical segment was likely induced by the interaction with the membrane-mimicking detergent DPC [110].

These results were also confirmed by a later study of Koo *et al.* who also used a shorter construct of Syb2, lacking the TMR [262]. They showed that the addition of DPC caused general increase in signal intensity and the occurrence of additional, as well as more pronounced, helical segments, including a part of the N-terminal SNARE motif.

In our binding experiments, we did not add detergents, as our Syb2 construct does not include the TMR. Moreover, we focused on the C-terminal binding of Syb2 to Munc13-MUN, which has been suggested by other studies [123, 127].

In order to obtain a full assignment of all cross-peaks, we could have attempted a complete assignment using  $^{13}\text{C}$ - $^{15}\text{N}$  labeling. However, the overall coverage provided by the transferred assignments seemed sufficient for the experiments as the C-terminal part was well covered. Additionally, assigning peaks for IDPs is particularly challenging due to the numerous peak overlaps caused by their unrigid structure.

Another approach to improve the limited resolution in the  $^1\text{H}$  dimension would be a 2D-carbon-detected  $^{13}\text{C}$ - $^{15}\text{N}$ -CON measurement, as the  $^{13}\text{C}$  carbonyl offers better resolution. This method also allows for the detection of proline residues, which is particularly advantageous for Syb2, given its high number of proline residues, especially in the N-terminal region.

Analysis of the cross-peak intensities of  $^{15}\text{N}$ -labeled Syb2 indicated that the C-terminal JMD of Syb2 is primarily responsible for binding to the Munc13-MUN domain. We tracked the binding through Syb2 cross-peak broadening in the presence of Munc13-MUN. The reasons we observed only cross-peak broadening of Syb2 instead of cross-peak shifts could be due to the substantial size of the binding partner, Munc13-MUN, which is nearly six times larger, resulting in slower tumbling rates and increased transverse relaxation rates of the nuclei, leading to broader cross-peaks in the NMR spectrum [333]. Additionally, the binding is likely characterized by an intermediate exchange, indicating a moderate binding strength. This was confirmed by titration experiments, which revealed an intermediate binding affinity in the micromolar range.

It is important to note, however, that determining the  $K_D$  value using titration experiments in NMR is typically done through cross-peak shifts rather than cross-peak broadening, as cross-peak intensities can be influenced not only by binding but also by changes in the dynamics of the molecule. Alternative methods such as ITC, could be used to confirm the obtained  $K_D$  values. Yet, this method of determining affinity through cross-peak intensities in NMR has also been used in other studies [145, 178]. The advantage of determining affinity through NMR is the precise identification of the residues affected by binding, which allows for the deduction of the binding site for the labeled protein.

In the studies by Ma *et al.* (2011) and also our previous studies, the interactions between the SNARE motif of Stx1A and Munc13-MUN were primarily investigated [145, 178]. However, based on the current interaction models for the SNARE complex formation machinery, these findings should be viewed with caution, as no recent data support a direct interaction between the SNARE motif of Stx1B and the MUN domain. Since the measurements were conducted with isolated components rather than within the broader context of the entire machinery, it is possible that the observed binding was nonspecific [294]. Nevertheless, a direct, albeit likely very transient, interaction cannot be completely ruled out.

To potentially detect cross-peak shifts in the interaction between Syb2 and Munc13-MUN, one could deuterate the samples. This would extend the relaxation times, possibly allowing for the visibility of the complex [334].



Alanine substitution of the tryptophan residues at positions 89 and 90 in the JMD of Syb2 *via* site directed mutagenesis showed that both are critical for binding to Munc13-MUN, with W90 being more crucial than W89.

It would also be interesting to identify the binding site in Munc13-MUN. In NMR, we can only see the cross-peaks of the labeled interaction partner, but not the unlabeled one. While we could <sup>15</sup>N label Munc13-MUN, the size of Munc13-MUN would result in a very crowded NMR spectrum, making assignment extremely time-consuming. Nonetheless, it would be interesting to see if a specific region of the MUN domain is affected or if various interaction sites are detected, which could inform us about specificity.

Interestingly, in a review by J. Rizo, (2022) on the molecular mechanisms underlying neurotransmitter release, the interaction between the JMD of Syb2 and Munc13-MUN is described as likely nonspecific since the JMD is highly promiscuous and expected to interact strongly with the membrane due to its proximity [109, 127, 294]. This sequence, which includes five basic and three aromatic residues and is located near the TMR, is likely to interact with the synaptic vesicle membrane through its abundant basic and hydrophobic residues *in vivo*.

Supporting this, a study found that membrane fusion requires destabilization of the bilayer by the conserved JMD of Syb2, which disrupts the lipid structure. The ability of the JMD to be replaced by another membrane-disrupting peptide underscores its crucial role in SNARE-mediated fusion and suggests that membrane-destabilizing peptides are a common feature in biological membrane fusion [115]. This raises the question of whether this sequence is more prone to nonspecific protein interactions in the absence of a membrane [127].

The crystal structure of the MUN domain bound to a Syb2 JMD peptide suggested that this interaction aids in forming the template complex [123]. However, molecular modeling shows that the peptide's C-terminus is oriented away from the vesicle membrane, indicating that the observed binding mode is probably incompatible with anchoring Syb2 to the vesicle [294]. Nonetheless, regardless of the exact binding orientation, an interaction in this manner would make sense, as the benefit of this assembly pathway is that it prevents the formation of antiparallel SNARE complexes and 2:1 Stx1:SNAP-25 heterodimers [168, 294].

The promiscuous binding nature of the C-terminal JMD of Syb2 is further evidenced by its unexpected interaction with Munc18-1, as cross-peak broadening was also observed for the C-terminal region in the <sup>1</sup>H-<sup>15</sup>N-HSQC spectra of <sup>15</sup>N-labeled Syb2 in the presence of Munc18-1. Based on current models and crystal structures of this and homologous complexes, we would have expected cross-peak broadening corresponding to the N-terminal SNARE motif of Syb2 [69, 84, 119, 124].

Under our experimental conditions, where there is no spatial anchoring of the C-terminal part of Syb2, the JMD might displace the SNARE motif from its usual binding site at Munc18-1, as the SNARE motif binding might be even more transient. We also attempted to determine the binding affinity *via* cross-peak broadening, similar to our approach with Munc13-MUN. However, since we are not convinced that the JMD is the primary interaction site of Syb2 with Munc18-1, we have

reservations about the validity of these results. In this context, it might be worthwhile to conduct measurements with a shorter Syb2 construct that does not incorporate the JMD. Alternatively, the tryptophan-to-alanine substitution mutants could be used here as well to see if a weakening of the JMD interaction allows the SNARE motif interaction to become more apparent.

Given this, the results of the binding experiments using various Stx1B and Munc18-1 mutations to open the furled loop of Munc18-1 in the Stx1B complex and to enhance binding with Syb2 should be interpreted with caution. It appears that rather than the SNARE motif, the JMD of Syb2 is still the primary region interacting with Munc18-1. Nonetheless interestingly, only the Munc18-1<sup>P335A</sup> mutation enhanced the binding of Syb2 to the Stx1B:Munc18-1 complex, while the D326K mutation of Munc18-1 in the complex had almost no effect. This suggests that only the P335A mutation effectively opens the furled loop, allowing for efficient binding of Syb2, assuming that the JMD also binds within the furled loop region of Munc18-1.

Furthermore, the Stx1B<sup>V216E</sup> mutation did not have the expected effect of triggering the opening of the furled loop. On the contrary, the V216E mutation seemed to prevent binding to the Stx1B complex, contradicting our earlier hypothesis. This indicates that the V216E mutation may have an additional effect beyond merely opening the furled loop of Munc18-1.

To investigate such transient interactions in NMR, a large excess of the unlabeled titrant, about 10 to 50 times the concentration of the analyte, would be beneficial, as weak bindings result in many analyte proteins remaining unbound, leaving any molecular binding event averaged out in the spectrum [335]. However, neither Munc13-MUN nor Munc18-1 are suitable for high concentrations *in vitro*, as they tend to aggregate at higher concentrations. Further reducing the concentration of the analyte (Syb2, in this case) is also not ideal, as it can compromise spectrum quality. Additionally, low concentrations are not practical for ensuring binding interactions.

### **5.7. Unveiling protein interaction networks and structural dynamics: Insights from cross-linking mass spectrometry**

Another approach to characterize interaction sites and structural conformation is cross-linking mass spectrometry (XL-MS), which we successfully implemented and optimized in our laboratories. This workflow followed a 'bottom-up' approach, involving the cross-linking of intact proteins, enzymatic digestion, and mass spectrometric analysis to identify cross-linked peptides. By using cross-linkers like DSSO and DSBU, we were able to identify interaction sites and establish distance constraints, which were particularly useful for assessing conformational flexibility when cross-links exhibited overlength. When the cross-links spanned greater distances than expected based on known structures, it suggested that the protein or complex was adopting different or more extended conformations, highlighting regions of flexibility within the structure. These overlength cross-links provided insights into how the proteins may shift or expand beyond their static conformations.

Interestingly, DSSO demonstrated higher cross-linking count than DSBU. This outcome was unexpected, given that both cross-linkers feature the same amine-reactive N-hydroxysuccinimide (NHS) ester head-group at each end. Moreover, the DSBU spacer is slightly longer than that of

DSSO, which might suggest that DSBU could more effectively reach certain lysine residues that are slightly too far apart for the DSSO cross-linker. However, given that both cross-linkers have the same reactive groups at their ends, it is unlikely that the observed differences are due to variations in reactivity. On the other hand, the spacers of the two cross-linkers have different chemical structures for MS-based fragmentation, which could lead to differences in detection, with one potentially being better detected than the other. This variation in detection efficiency might explain the slight difference in the number of unique cross-links identified.

A study by M. Matzinger *et al.* (2022), which benchmarked different cross-linkers and workflows using a large synthetic peptide library based on sequences from 38 proteins of the *E. coli* ribosomal complex, found that this difference in detecting cross-linked peptides using different cross-linkers is notably dependent on the search engine-software used [336]. Their findings showed that the cross-linking search engine MS Annika performs very well with DSSO, identifying an average of 632 cross-links, compared to 558 for DSBU [336]. In contrast, the search engine MeroX favored DSBU, identifying an average of 767 cross-links, compared to 658 for DSSO [336].

Interestingly, when they tested the XlinkX search engine, the predecessor to the XlinkX v2.0 search engine used in this study, they found more DSBU cross-links, averaging 562 counts, compared to DSSO cross-links, which averaged 526 counts. Additionally, it is important to note that the FDR for DSBU was significantly higher than for DSSO, whereas, in the other search engines, the FDR was similar for both cross-linkers [336].

This strongly suggests that the differences we observed between the two cross-linkers are not due to their cross-linking efficiency but could rather stem from the software-specific analysis. In this context, it would be prudent to analyze our MS data using other search engines as well.

Cross-linking studies of Syb2 and Munc13-MUN have shown that the C-terminus and SNARE motif of Syb2 are involved in interactions with Munc13-MUN. Notably, the C-terminal interaction of Syb2 aligns with initial NMR findings, and the distance constraints provided by the DSBU cross-linker support the placement of Syb2's C-terminal JMD relative to the crystallized C-terminal peptide of Syb2, which was previously identified as binding to Munc13-MUN in the work of Wang *et al.* (2019) [123]. This evidence challenges the argument that the C-terminal binding is promiscuous, at least in part, as the XL-MS results further suggest that the binding of Syb2's JMD is confined to the C-terminal region of the MUN domain, with no cross-links detected in other regions.

In contrast, the SNARE motif of Syb2 formed multiple cross-links with different regions of the MUN domain, suggesting a less specific binding pattern. However, these cross-links consistently align the SNARE motif along the concave side of the Munc13-MUN structure, suggesting a pre-orientation of the SNARE motif for later alignment in the formation of the template complex.

One of the regions involved in cross-linking with the SNARE motif of Syb2 is the area around the NF motif on helix 6 of the MUN domain of Munc13-1. The cross-linked lysine residue 1162, located on the same helix near the NF motif, and lysine residue 1248 on the opposing helix 8 are in close proximity. This could suggest that the NF motif might play a role in the correct alignment of the SNARE motif of Syb2 for subsequent SNARE complex formation. However, the fact that this region

is not exclusively involved in cross-linking warrants a more critical view. Yet, it is still possible that this region binds the SNARE motif with higher affinity than others. To further investigate, it would be valuable to perform XL-MS experiments using the Munc13-MUN<sup>NFAA</sup> mutant, which involves an alanine substitution of the NF motif and has been shown to be unable to drive SNARE complex formation and sustain neurotransmission [70, 167]. If no cross-links are found in this region with the mutant, it could strongly indicate that the NF motif is indeed involved in aligning the Syb2 SNARE motif.

Interestingly, all the cross-links originating from the SNARE motif of Syb2 were formed exclusively from the lysine side chain at position 52, despite there being another lysine side chain just seven positions away at K59. According to the NMR structure we used here, K59 is located outside a helical region, in an unstructured area. This could suggest that the region around K59 does not come close enough to the MUN domain for cross-linking. However, given the short distance between K52 and K59, it seems unlikely that this is the sole reason why no cross-links were found between K59 and the MUN domain.

A possible explanation lies in the sequence of Syb2 and how it influences tryptic digestion. Trypsin cleaves proteins after lysine and arginine residues, but when these residues are adjacent to each other or followed by proline, missed cleavages often occur, leading to incomplete digestion. This can result in peptides that are either too short or too long, both of which hinder detection [337]. For example, in Syb2, the arginine residue at position 56 is only three amino acids away from K59, creating a short cross-linked peptide. The detectability of this peptide depends on the length of the opposing peptide to which it is cross-linked. Short peptides tend to adopt low charge states, resulting in low protonation, which can be problematic for identifying cross-linked peptides. In MS2, this often leads to fragments that adopt no charge, making them undetectable. This, in turn, produces poor MS2 spectra, significantly reducing the identification accuracy of cross-linked peptides. Furthermore, they also produce fewer fragment ions during MS/MS, reducing identification accuracy. On the other hand, overly long peptides can ionize inefficiently, produce complex fragmentation patterns, and adopt multiple charge states, further complicating detection. This issue is particularly important when cross-linking regions rich in arginine and lysine residues. While lysine provides essential side-chain targets for cross-linking, too many closely spaced lysine and arginine residues can be counterproductive for detection after tryptic digestion. This is evident in the limited number of cross-links detected between the C-terminal ends of Syb2 and the MUN domain of Munc13. Despite the abundance of lysine residues in both regions, only one or two cross-links were detected in various measurements. This could be due to the generation of peptides that are either too short or too numerous, lowering signal intensity and making detection more difficult. Conversely, having too few or no lysine residues in regions of interest can also be a limitation. To address this, we introduced lysine residues into the N-terminal part of Syb2 to create reactive groups for our cross-linkers, allowing us to investigate whether the N-terminal region interacts with Munc13-MUN. The results indicated that it does not.

However, it's important to note that the absence of detected cross-links does not necessarily mean they were not formed during sample preparation. For instance, positioning a lysine residue at position 3 (Syb2<sup>A3K</sup>) results in a very short tripeptide after tryptic digestion. As mentioned earlier, such short peptides can be difficult to detect due to their size, making them possibly challenging to identify.

In the case of the Syb2<sup>R30K</sup> mutant, there are no other lysine or arginine residues before the introduced lysine, except for an arginine at position 31. This means that tryptic digestion would produce a peptide that is 30 or 31 amino acids long. Cross-linking further increases the size of the peptide and detecting such long peptides in mass spectrometry is challenging due to their high retention time, lower ionization efficiency and complex fragmentation patterns, which complicate detection and data analysis [338].

All of these points highlight the importance of an even distribution of lysine residues for efficient XL-MS analysis, especially when using cross-linkers with NHS esters that preferentially react with lysine residues, combined with tryptic digestion to generate cross-linked peptides [339]. This can be problematic when studying proteins that do not meet these criteria, necessitating alternative strategies, such as using cross-linkers like sulfosuccinimidyl 2-(m-azido-o-nitrobenzamido)ethyl-1,3'-dithiopropionate (SDA). SDA is a photoactivatable cross-linker that, upon UV light exposure, reacts nonspecifically with various amino acids, including aromatic residues like tyrosine and phenylalanine, as well as the protein backbone, while also having a thiol-reactive end, enabling cross-linking without the need for lysine residues [340]. Additionally, other enzymatic cleavage reactions can be used to generate peptides independently of the presence of arginine or lysine residues. For example, chymotrypsin, which cleaves C-terminally of aromatic amino acids like tyrosine, phenylalanine, and tryptophan, or the endoproteinase Glu-C, which cleaves after glutamic acid and aspartic acid residues, can be employed [341].

One of the key strengths of XL-MS is its ability to identify and characterize both sides of interaction sites in a single measurement, eliminating the need for additional experiments with isotope labeling of each interaction partner, as long as distinct partners are involved. However, when analyzing homodimers, isotope labeling of half of the sample is advantageous, as it can be difficult to distinguish intramolecular cross-links from intermolecular ones. If labeling is not possible, the analysis must rely solely on distance restraints.

Furthermore, direct modeling based solely on XL-MS data can be challenging, particularly when using NHS esters that preferentially react with lysine residues, which are commonly used in cross-linking. There are disadvantages in targeting lysine residues as their side chains are highly flexible, meaning the structural information obtained from these experiments is less rigid. For example, cross-linkers with spacer lengths of about 8 Å might bridge C $\alpha$ -C $\alpha$  distances of up to approximately 27 Å [284].

Another point to consider is that the interaction sites and possible conformations of interaction partners identified from cross-linking data present a mosaic-like picture composed of the sum of all identified cross-links. For example, while we can determine that the central SNARE motif of Syb2

interacts with various regions of the MUN domain of Munc13-1, we cannot definitively say whether this represents a single 1:1 binding interaction between the molecules. It's possible that Syb2 exhibits conformational flexibility, with different conformations being observed where the C-terminal JMD is anchored to the C-terminal part of the MUN domain, allowing the SNARE motif to interact with different areas of the MUN domain. Alternatively, we might be observing a scenario where multiple Syb2 molecules simultaneously bind their SNARE motifs to different regions of the MUN domain (**Fig. 5.4**).

The same uncertainty applies to the interaction between Munc18-1 and Syb2, where we identified two distinct binding sites for Syb2 on Munc18-1 (**Fig. 4.37**). However, we cannot say with certainty whether this represents a 1:1 binding interaction, where either domain 3a or domain 1 of Munc18-1 is engaged, or if it involves a 2:1 binding scenario in which both identified binding sites are occupied simultaneously by Syb2. Based on data from other studies and homolog structures, it is likely that the binding site in domain 3a is preferred [69, 122, 124, 264]. The second binding site is possibly only engaged when the primary binding site is occupied.

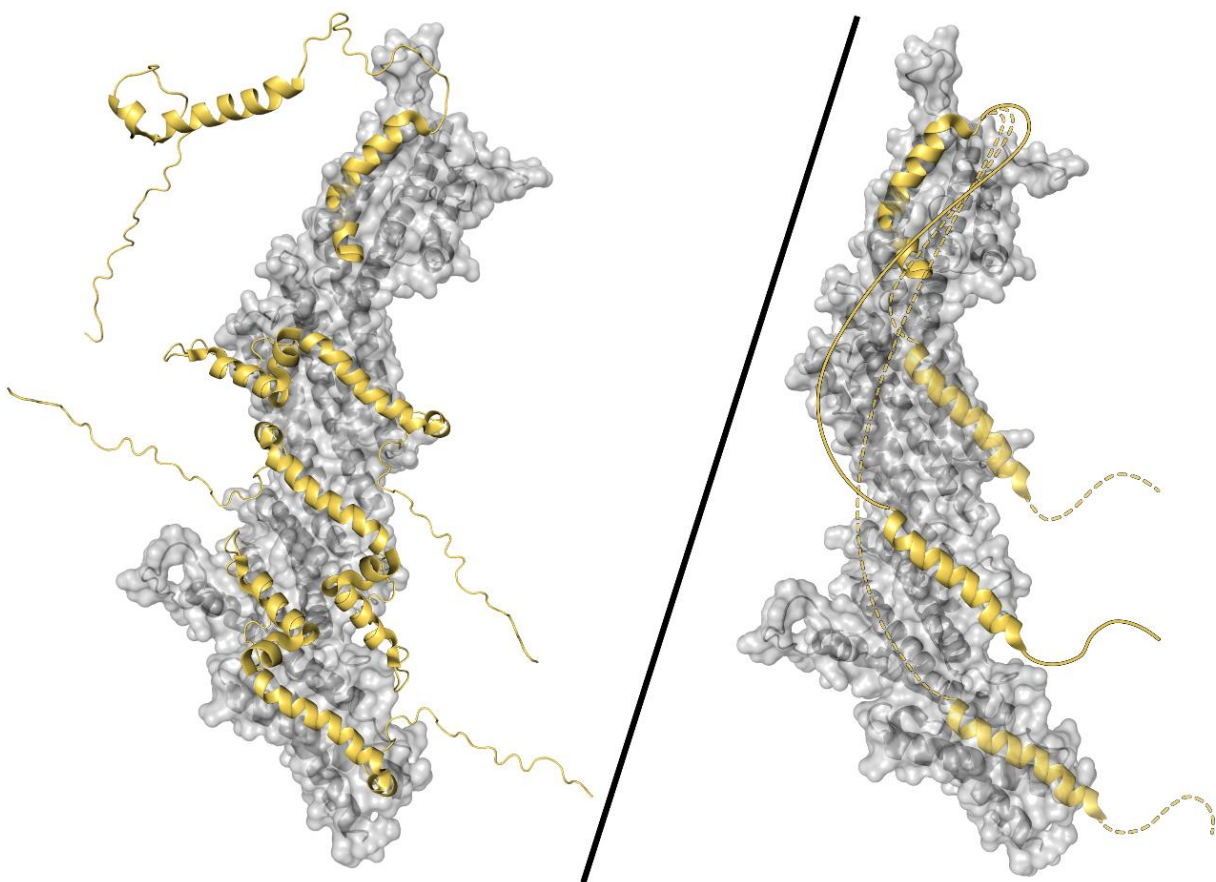


**Figure 5.4:** Conceptual alternative models of how Syb2 (gold, PDB: 2KOG) could interact with Munc13-MUN (grey, PDB: 6A30), based on the XL-MS data. One potential scenario is that a single Syb2 molecule interacts with the MUN domain of Munc13-1, with the JMD engaging the C-terminal part of Munc13-MUN while the SNARE motif flexibly interacts with various regions of the MUN domain (left). Alternatively, multiple Syb2 molecules could interact with the MUN domain of Munc13-1, where, for example, the JMD of one Syb2 molecule interacts with the C-terminal part of Munc13-MUN, while additional Syb2 molecules bind their respective SNARE motifs to different regions of Munc13-MUN (right).

One approach to address the challenge of identifying preferred or primary binding sites versus secondary ones *via* XL-MS could be to quantify the MS1 signal intensities of cross-linked peptides. In theory, preferred binding sites should result in significantly more cross-links, leading to a higher abundance of peptides derived from these sites. However, it is important to consider the obstacles previously discussed regarding the detection of cross-linked peptides. Even if one interaction site is more favored and generates more cross-linked peptides, if these peptides are harder to detect than those from a less preferred binding site, the results could be skewed, leading to ambiguous conclusions.

The comparison between NMR spectroscopy and XL-MS data is particularly noteworthy. While NMR results primarily indicate an interaction of the C-terminal JMD of Syb2 with both Munc13-MUN and Munc18-1, XL-MS data suggest a significant involvement of the SNARE motif of Syb2. This implies that the interaction of the SNARE motif with the orchestrating proteins Munc18-1 and Munc13-MUN may be too transient to be detected by NMR spectroscopy. Additionally, it suggests that XL-MS might be more effective in capturing these transient interactions, provided they are stable enough for the cross-linker to form a covalent bond [232].

The inability of random interactions to produce observable cross-links implies that transient interactions must be sufficiently long-lasting and prevalent within the population for cross-linking to occur, meaning there is a minimum threshold of structural stability required [232]. A recent study found that protein complexes with a  $K_D$  of around 25  $\mu\text{M}$  could be specifically cross-linked, whereas those with a  $K_D$  between 100  $\mu\text{M}$  and 300  $\mu\text{M}$  could not, suggesting the cross-linking affinity limit lies within this range [342]. Other studies have also demonstrated XL-MS's ability to effectively capture transient interactions [343-345].

A result that is reflected in both methods, NMR spectroscopy and XL-MS, is that the D326K mutation of Munc18-1 in the Stx1B:Munc18-1:Syb2 complex probably does not enhance the binding of Syb2. This suggests that, at least under our experimental conditions, this functional mutant does not, or does not sufficiently, fulfill its role in facilitating the furled loop opening, allowing for a more effective alignment of the SNARE motif of Syb2 between helix 11 and helix 12 of Munc18-1. One possible reason for this could be that the linker region of Stx1B in the complex obstructs the efficient opening of the furled loop. To address this, it might be insightful to combine this functional mutant with the disease-causing Stx1B<sup>E210K</sup> mutation, which we speculate also induces an open conformation of Stx1B. This combination might be compatible with the D326K mutation of Munc18-1, potentially allowing for more efficient binding of Syb2.

To our surprise, we discovered an additional binding site for the SNARE motif of Syb2 at the two helices of domain 1 of Munc18-1, which has not been previously reported in the literature (**Fig. 4.37**). However, we cannot be certain if this represents a specific binding site for Syb2 or if it is a more promiscuous interaction, where Syb2 primarily binds to the main binding site in the furled loop region of domain 3a in Munc18-1, and any remaining Syb2 binds to the next available site once the main one is occupied. One way to test whether Syb2 has a preference for the different identified binding sites could be by examining the MS1 signal intensities in the mass spectrum. In

theory, a main binding site should lead to significantly more cross-linked peptides, resulting in higher signal intensity. However, it is important to note that, as previously mentioned, different peptides ionize with varying efficiencies, which can affect signal intensity and should be interpreted with caution.

Further analysis of Stx1B mutants suggested significant conformational changes, particularly with the E210K mutant, which indicated an altered binding conformation in combination with Munc18-1. This assumption is based on several newly formed cross-links, which appeared with overlength when mapped onto the wild-type crystal structure of the Stx1:Munc18-1 complex, suggesting a structural alteration of the complex.

Overlength cross-links are often used to describe and infer structural dynamics and conformational changes in proteins and protein complexes [236, 346, 347]. They are frequently found in structurally dynamic or flexible regions of proteins, which was also observed in our samples. This is particularly evident in the cross-links involving K251 at the C-terminal end of our Stx1B constructs, which are dispersed and link to lysine side chains from various regions of Munc18-1. Modeling the complex with our constructs using AlphaFold 3 yielded a very low pLDDT score<sup>(1)</sup> (< 50) for the C-terminal end, indicating that the structure and conformation of this region can only be predicted with very low confidence, suggesting high flexibility [297]. This flexibility is reflected in the cross-links we identified (**Fig. 5.5**). A similar situation is observed with the unstructured region around K526. Cross-links originating from this lysine residue were consistently detected in various measurements, linking to lysine residues of the H<sub>abc</sub> domain. When mapped onto the crystal structure, these cross-links also appear overlength. Modeling of this region yielded a very low pLDDT score (< 50), indicating high dynamics in this area, which is further confirmed by our cross-links (**Fig. 5.5**).

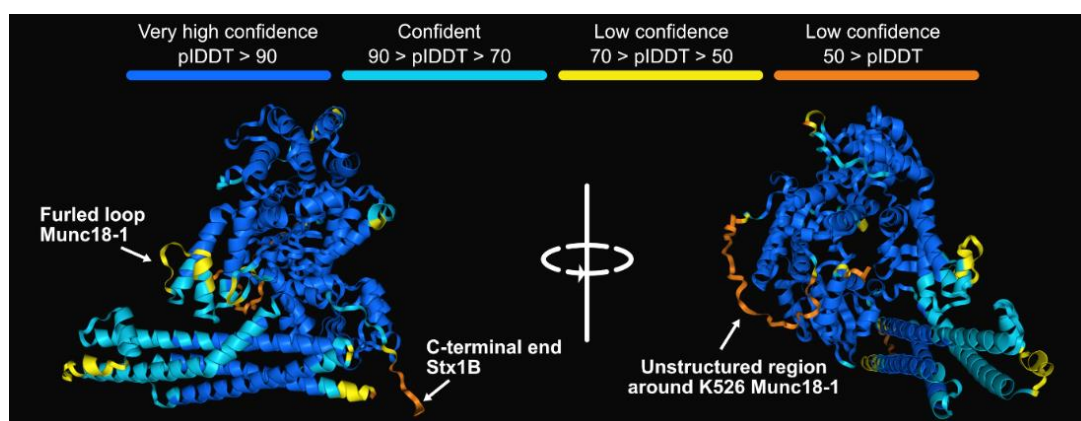


**Figure 5.5:** Modeling of the Stx1B:Munc18-1 complex using the amino acid sequences of the Stx1B and Munc18-1 constructs *via* AlphaFold 3 [297]. The color code represents the pLDDT score of the modeled structure.

Therefore, it is fair to say that newly identified cross-links in measurements with Stx1B<sup>L221P</sup>, and especially with Stx1B<sup>E210K</sup>, which appear overlength when mapped onto the crystal structure, likely indicate a conformational change.

(1) The pLDDT (Predicted Local Distance Difference Test) score is a measure used to assess the confidence of protein structure predictions, particularly in models generated by AI tools. It evaluates how well the predicted structure matches the expected local geometry of the protein. A higher pLDDT score (close to 100) indicates high confidence in the accuracy of the predicted structure, while a lower score (below 50) suggests low confidence and indicates regions of the protein that are likely flexible or poorly predicted.



Particularly noteworthy are the overlength cross-links involving K321 and K332 from the furled loop region of Munc18-1, linking to lysine residues of the SNARE motif and the H<sub>abc</sub> domain of Stx1B<sup>E210K</sup>, as well as K54 and K139 on the backside of the H<sub>abc</sub> domain of Stx1B<sup>E210K</sup>, which link to K7 of Munc18-1. Such connections can essentially only be explained by a conformational change. The furled loop of Munc18-1 also showed a low pIDDT score between 50 and 70, further supporting this interpretation.

While some overlength cross-links can be explained by altered conformations, others make little sense, even in such models. For instance, cross-links between K125 of Stx1B<sup>E210K/L221P</sup> and K120 of Munc18-1, or between K87 of Stx1B<sup>E210K</sup> and K356 of Munc18-1, are challenging to interpret. These cross-links could result from non-specific interactions or technical artifacts. Even with a false discovery rate (FDR) of 2%, there remains the possibility of misinterpretation and false positives. XL-MS as an experimental method inherently involves some level of error. Additionally, data interpretation errors can occur if structural models are inaccurate or if the databases used are incomplete, leading to potential misinterpretations of the cross-linking data [232]. Cross-linking can potentially introduce structural artifacts, such as capturing proteins in rare or non-functional conformations or causing unintended protein-protein interactions. However, these issues have not been significantly observed experimentally. While cross-linking might induce conformational changes, extensive agreement between XL-MS data and high-resolution structures suggests that such artifacts are not common. Potential errors, such as protein aggregation or misinterpretation during data analysis, must be carefully managed, but overall, XL-MS remains a reliable method for obtaining structural information [232-234, 348].

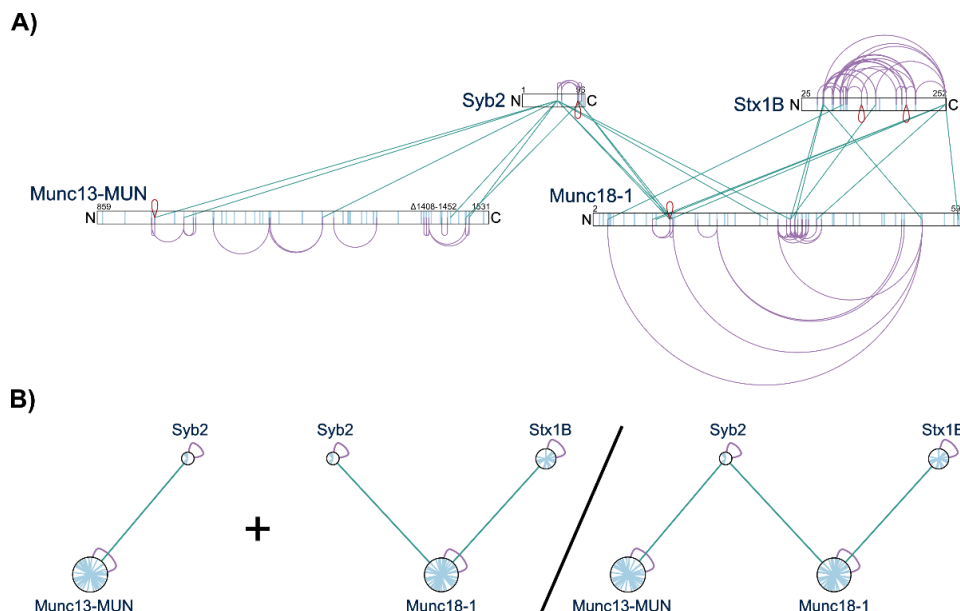


**Figure 5.6: A)** Cross-link map from the XL-MS measurement of Munc13-MUN, Syb2, Munc18-1, and Stx1B. Syb2 forms intermolecular cross-links with both Munc13-MUN and Munc18-1, but no intermolecular cross-links are observed between Munc13-MUN and Munc18-1. Stx1B only forms intermolecular cross-links with Munc18-1. Cross-link map was generated using XiNET Cross-Linker Viewer [288]. **B)** Intermolecular cross-links of Syb2 between Munc13-MUN and Munc18-1 could be interpreted as Syb2 simultaneously binding to both proteins, acting as a bridging protein in the complex machinery (right). However, it is also possible that the cross-link map reflects independent, non-simultaneous interactions between Syb2 and Munc13-MUN, as well as Syb2 and Munc18-1.

When it comes to tracking multistep mechanisms like SNARE complex formation, XL-MS presents challenges due to its time-scale limitations. While XL-MS can capture conformational changes at a single time point, it becomes difficult to track multiple, consecutive changes, especially when these depend on the involvement of different proteins at various stages. If all participants are added simultaneously, XL-MS cannot retrospectively determine which protein interacted first or last, making it challenging to identify key intermediate conformations.

We attempted to track the main components of the SNARE complex formation machinery using XL-MS. However, instead of producing a complex network with cross-connections between all participants, we observed a linear interaction chain, with Munc18-1 and Syb2 at the center (**Fig. 5.6**). This could be interpreted as Syb2 binding simultaneously to both Munc18-1 and Munc13-MUN, or as separate bindings where Syb2 interacts with either Munc13-MUN or Munc18-1, which then binds Stx1B. Since we only capture a snapshot of the interactions, it is difficult to conclusively interpret a multistep mechanism.

One possible approach could be time-resolved XL-MS during sample preparation, where reagents are introduced at specific time points during the reaction, or by comparing different setups with varying compositions of the components. This method could potentially map the progression of structural changes over time. However, whether this approach would yield a complete picture remains uncertain.

In summary, XL-MS is a powerful tool for characterizing structures, conformations, and conformational changes, as well as for identifying interaction sites. However, the method has limitations when it comes to resolving dynamic, multistep processes and capturing temporal conformational changes. While XL-MS provides valuable insights, its results can be affected by artifacts and misinterpretations. Therefore, it is beneficial to combine XL-MS with other structural characterization methods such as NMR, cryo-EM, or molecular dynamics simulations to fully resolve and understand structures and mechanisms.

## 6. Outlook

In addition to the improvements and expansions of the experiments discussed in **Chapter 4**, there are many other factors worth investigating further. One area of interest lies in exploring the molecular impact of other SNAREopathic mutations of Stx1B. Particularly intriguing are missense mutations, which involve a substitution of a single amino acid side chain, such as Stx1B<sup>V88F</sup> or Stx1B<sup>C144F</sup> [182]. These mutations could have a targeted effect on protein structure or interactions, in contrast to mutations that lead to early truncation, resulting in the loss of entire domains or structural regions, which naturally limits their interactions.

This investigation into SNAREopathic mutations could be extended to other SNARE proteins such as Syb2 and SNAP-25, as well as the orchestrating proteins Munc18-1 and Munc13-1. Examining how these mutations affect the molecular mechanisms in these proteins could provide a deeper understanding of their roles. As the number of known SNAREopathic mutations continues to grow, a more mechanistic understanding of the pathogenesis, particularly when shared principles exist among mutations in different SNAREopathy genes, would be a significant step toward the development of rational therapies.

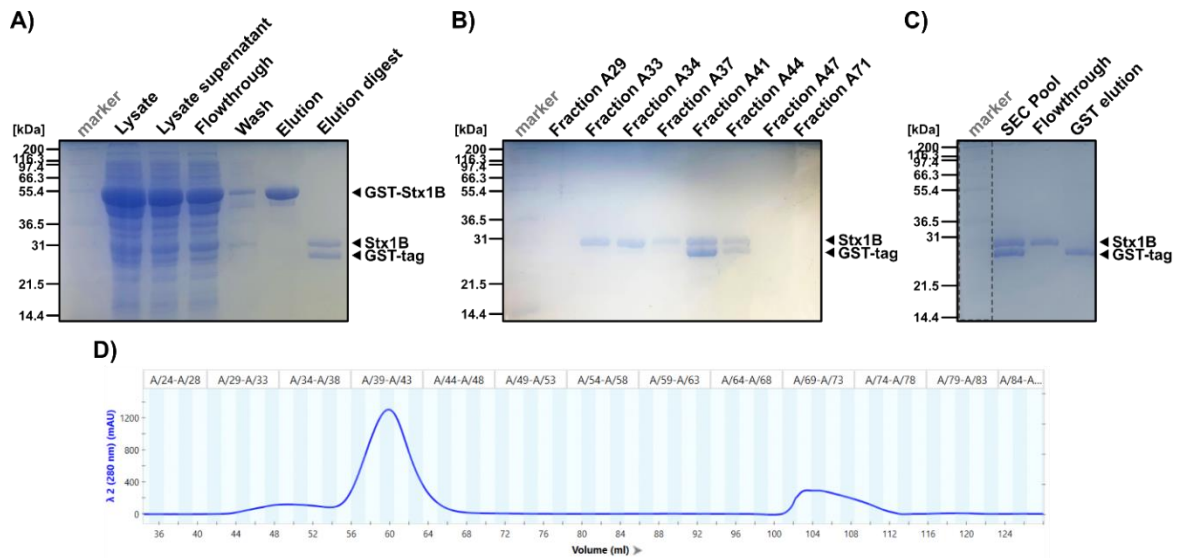
Moreover, despite the comprehensive work presented here, many factors of the neurotransmitter release machinery have yet to be explored. One area of future study would be the influence of mutations on other key components of this machinery, such as Synaptotagmin-1 and Complexin, which likely help form and stabilize a primed state with a partially zippered SNARE complex.

Another unexplored area is the molecular mechanism behind the incorporation of SNAP-25 into the SNARE complex. While the formation of the template complex involving Stx1, Syb2, and Munc18-1 is well characterized, the specific step at which SNAP-25 is incorporated remains unclear. Several studies have examined potential interactions between SNAP-25 and various binding partners, offering conflicting results and it remains elusive when and how SNAP-25 integrates into the complex [83, 84, 296]. Resolving these discrepancies is critical to fully understanding SNARE complex formation.

Furthermore, a still unresolved issue is how Munc13-1, through its MUN domain, promotes the transition of Stx1 from a closed conformation within the Stx1 complex to an open conformation, thus driving SNARE complex formation. This likely involves transient interactions with the other components of the SNARE machinery, like the linker region of Stx1 or Munc18-1, which are difficult to capture. The goal would be to catch this transition state during the opening of the Stx1:Munc18-1 complex. Introducing mutations that weaken the interaction between Stx1 and Munc18-1 and promote conformational changes, such as those investigated in this and previous studies, could help destabilize the closed conformation [178]. Also, combining these mutations in Stx1B or Munc18-1 may make it easier to stabilize the transition state for experimental interrogation. Ultimately, constructing a quaternary complex comprising Stx1:Munc18-1:Syb2:Munc13-MUN would be the ideal outcome, enabling us to understand the conformation changes necessary for SNARE complex formation and neurotransmitter release.

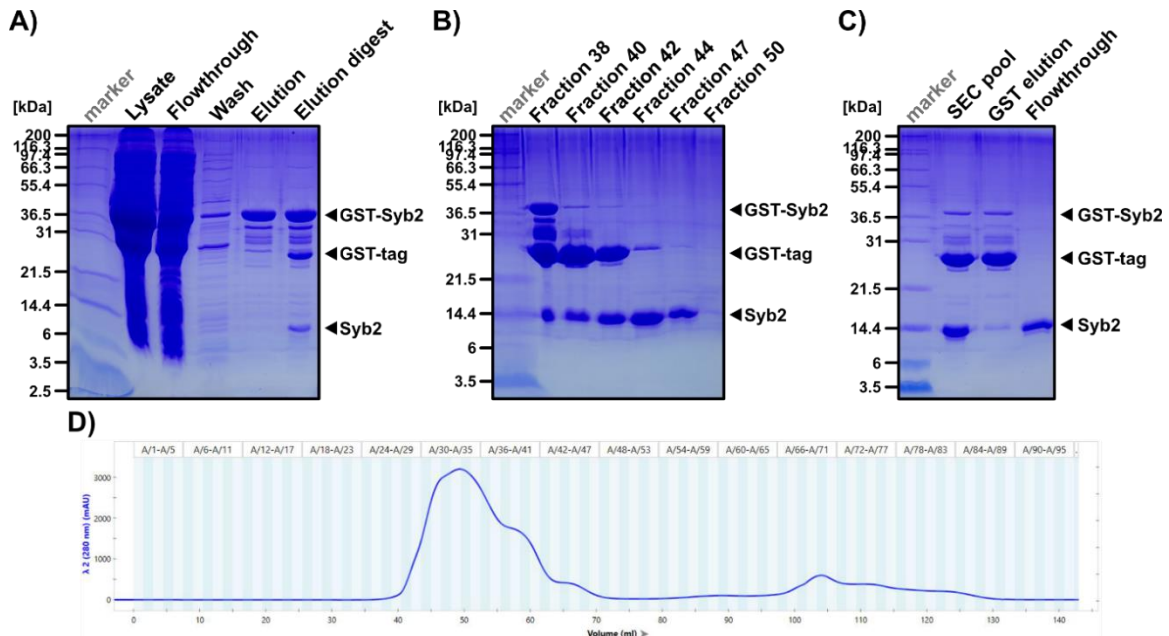
## 7. Appendix

### Appendix Figure 1



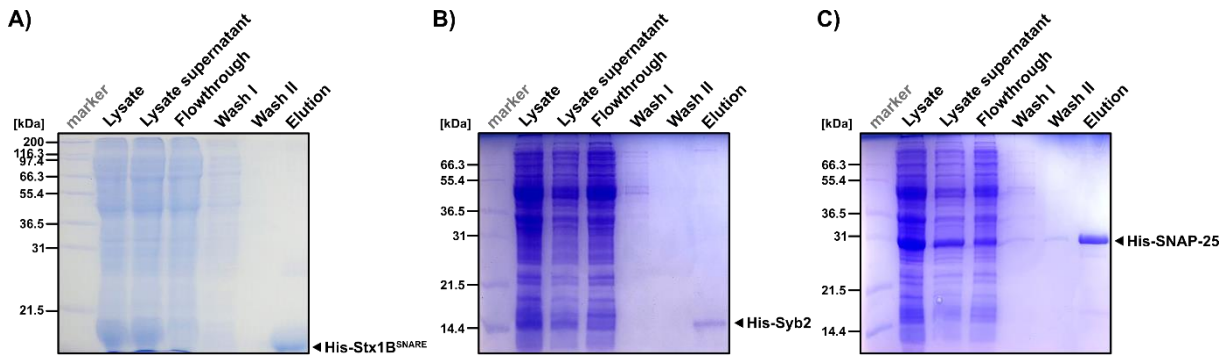
**Appendix Figure 1:** Representative SDS-PAGEs and size exclusion chromatography (SEC) chromatogram for the purification of the GST-Stx1B constructs. **A)** GST/4B FPLC affinity purification of the Stx1B construct through its GST-tag. **B)** SDS-PAGE of the eluted fractions corresponding to the SEC chromatogram in D). **C)** SDS-PAGE displaying GST-tag removal after pooling respective SEC fractions resulting in the purified, tag-free Stx1B protein construct of interest. **D)** SEC chromatogram displaying elution fractions of Stx1B indicated by UV absorption-peaks (plotted with ChromLab v6.0.0.34 (Bio-Rad Laboratories, Inc.)).

### Appendix Figure 2



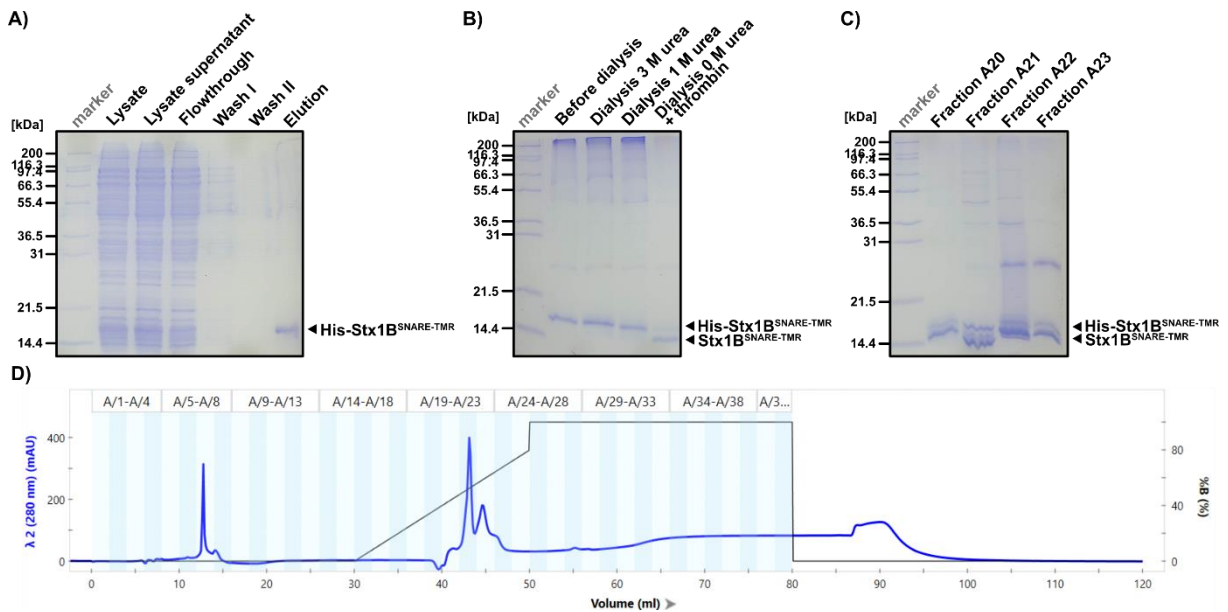
**Appendix Figure 2:** Representative SDS-PAGEs and size exclusion chromatography (SEC) chromatogram for the purification of the GST-Syb2 constructs. **A)** GST/4B FPLC affinity purification of the Syb2 construct through its GST-tag. **B)** SDS-PAGE of the eluted fractions corresponding to the SEC chromatogram in D). **C)** SDS-PAGE displaying GST-tag removal after pooling respective SEC fractions resulting in the purified, tag-free Syb2 protein construct of interest. **D)** SEC chromatogram displaying elution fractions of Syb2 indicated by UV absorption-peaks (plotted with ChromLab v6.0.0.34 (Bio-Rad Laboratories, Inc.)).

Appendix Figure 3



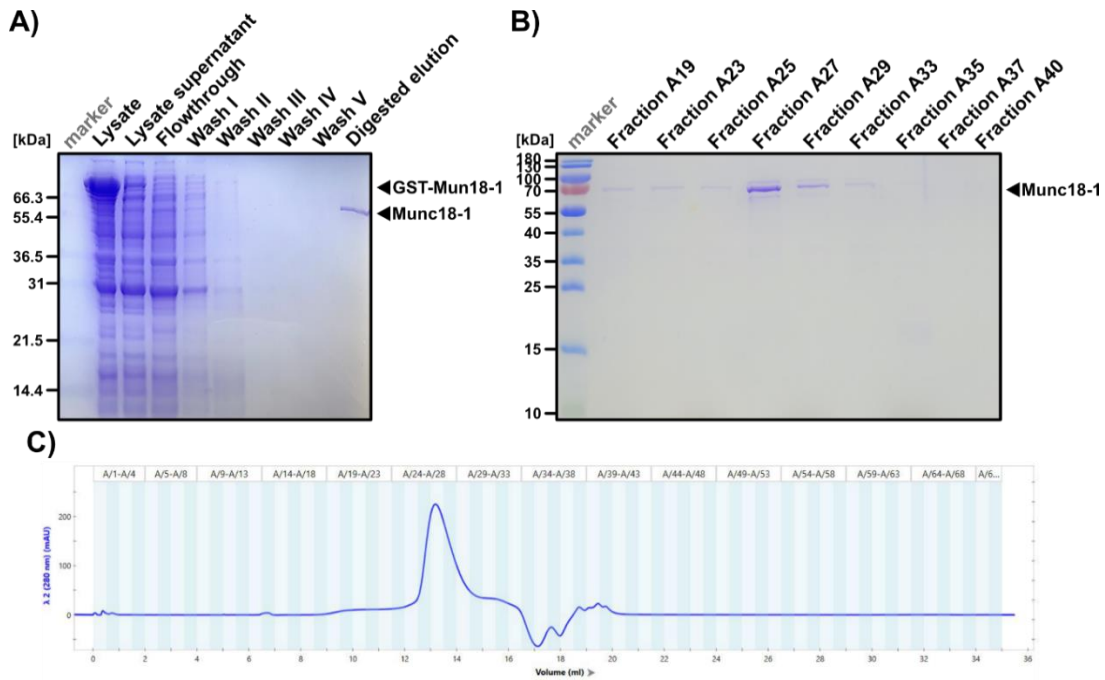
**Appendix Figure 3:** **A)** Representative SDS-PAGE for the Ni-NTA FPLC affinity purification of the Stx1B-SNARE construct through its His-tag. **B)** Representative SDS-PAGE for the Ni-NTA FPLC affinity purification of the Syb2 construct through its His-tag. **C)** Representative SDS-PAGE for the Ni-NTA FPLC affinity purification of the SNAP-25 constructs through its His-tag.

Appendix Figure 4



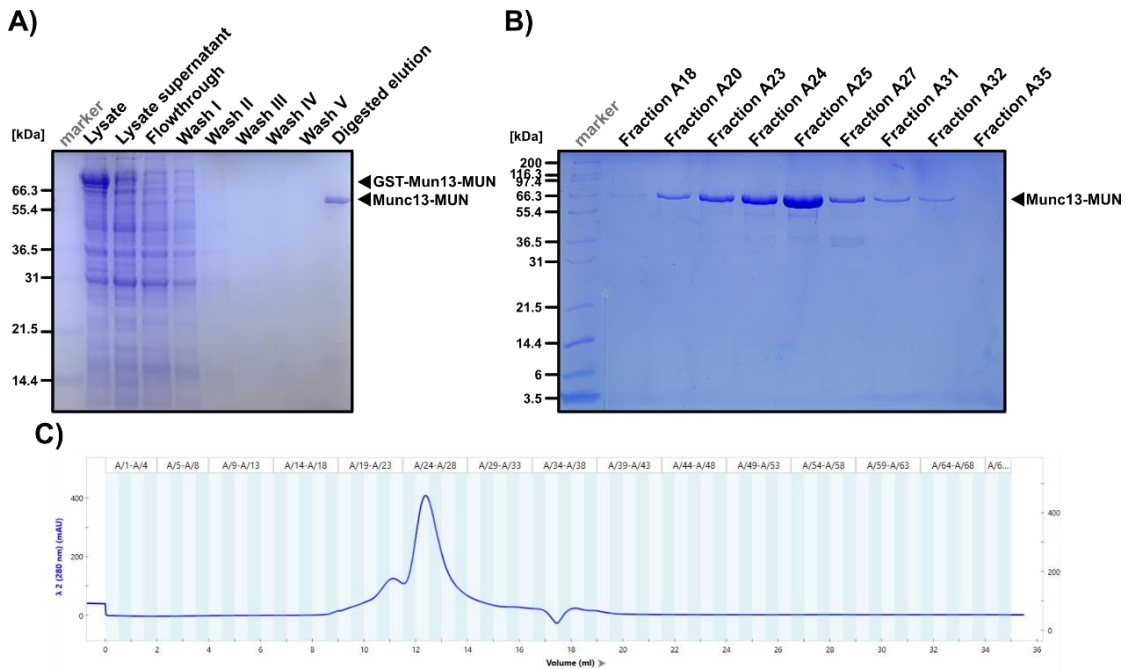
**Appendix Figure 4:** Representative SDS-PAGEs and ion exchange chromatography chromatogram for the purification of the His-Stx1B<sup>SNARE-TMR</sup> constructs. **A)** Ni-NTA FPLC affinity purification of the Stx1B<sup>SNARE-TMR</sup> construct through its His-tag. **B)** SDS-PAGE of samples taken from the stepwise dialysis to reduce urea concentration and introduction of 1% CHAPS with thrombin digestion to cleave the His-tag. **C)** SDS-PAGE of the eluted fractions corresponding to the ion exchange chromatography chromatogram in D). **D)** Ion exchange chromatography chromatogram displaying NaCl-gradient and elution fractions of Stx1B<sup>SNARE-TMR</sup> through UV absorption-peaks (plotted with ChromLab v6.0.0.34 (Bio-Rad Laboratories, Inc.)).

Appendix Figure 5



**Appendix Figure 5:** Representative SDS-PAGEs and size exclusion chromatography (SEC) chromatogram for the purification of the GST-Munc18-1 constructs. **A)** GST/4B Beads affinity purification of the Munc18-1 construct through its GST-tag. **B)** SDS-PAGE of the eluted fractions corresponding to the SEC chromatogram in C). **C)** SEC chromatogram displaying elution fractions of Munc18-1 through UV absorption-peaks (plotted with ChromLab v6.0.0.34 (Bio-Rad Laboratories, Inc.)).

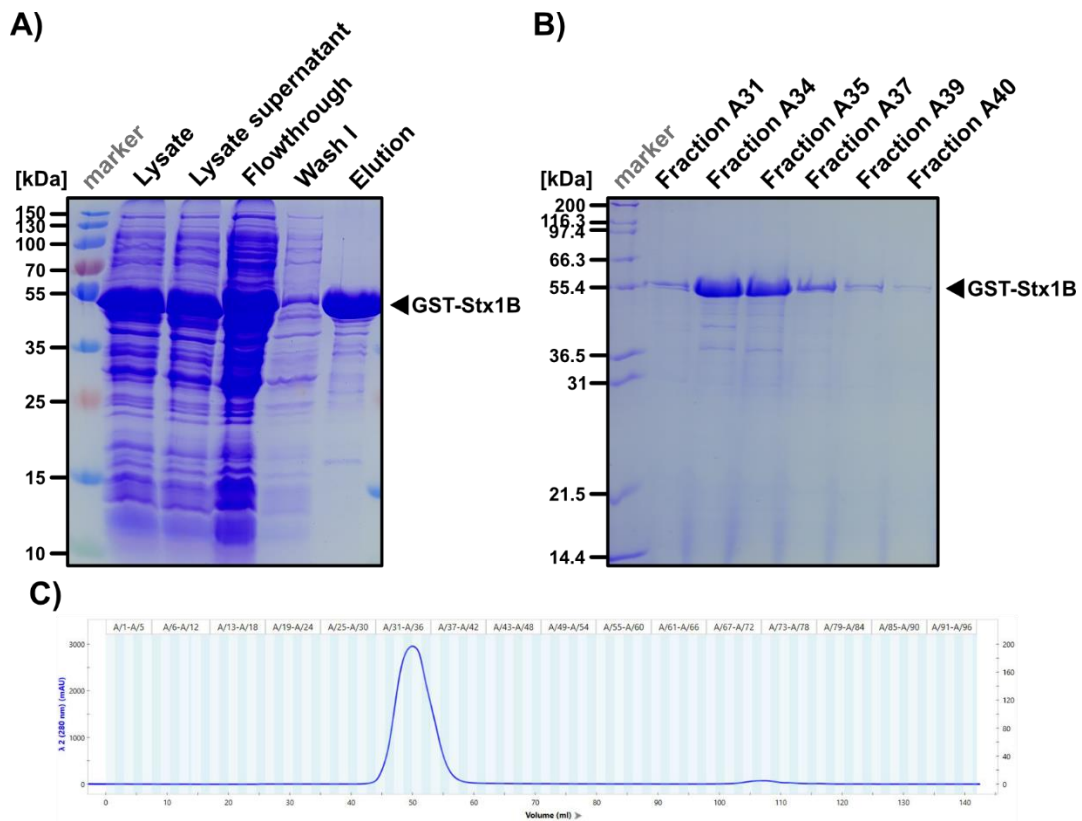
Appendix Figure 6



**Appendix Figure 6:** Representative SDS-PAGEs and size exclusion chromatography (SEC) chromatogram for the purification of the GST-Munc13-MUN constructs. **A)** GST/4B Beads affinity purification of the Munc18-MUN construct through its GST-tag. **B)** SDS-PAGE of the eluted fractions corresponding to the SEC chromatogram in C). **C)** SEC chromatogram displaying elution fractions of Munc13-MUN through UV absorption-peaks (plotted with ChromLab v6.0.0.34 (Bio-Rad Laboratories, Inc.)).

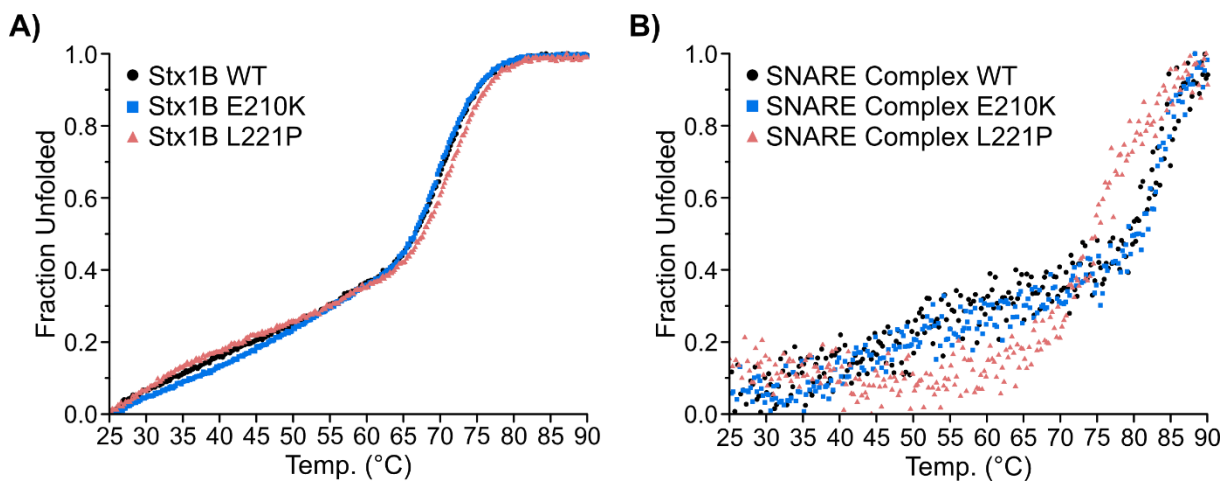


## Appendix Figure 7



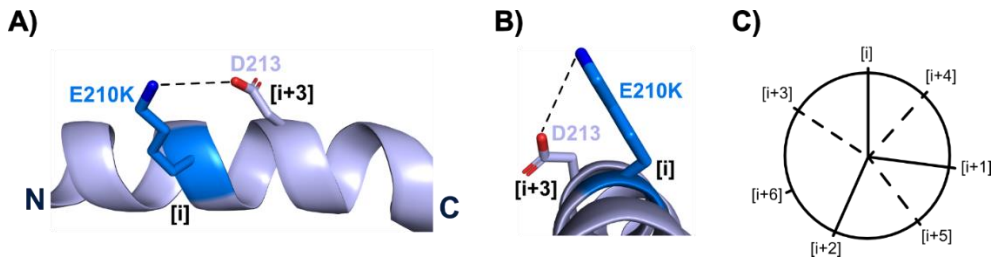
**Appendix Figure 7:** Representative SDS-PAGEs and size exclusion chromatography (SEC) chromatogram for the purification of the GST-Stx1B fusion protein constructs. **A)** GST/4B FPLC affinity purification of the GST-Stx1B fusion protein construct through its GST-tag. **B)** SDS-PAGE of the eluted fractions corresponding to the SEC chromatogram in C). **C)** SEC chromatogram displaying elution fractions of GST-Stx1B through UV absorption-peaks (plotted with ChromLab v6.0.0.34 (Bio-Rad Laboratories, Inc.)).

## Appendix Figure 8



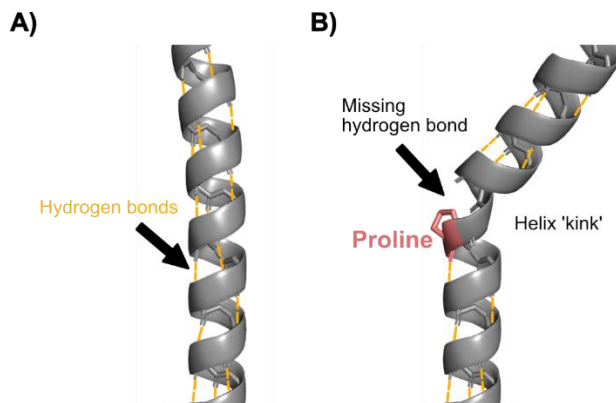
**Appendix Figure 8:** Complete normalized fraction unfolded spectra plotted from 25 °C to 90 °C of: **A)** Stx1B<sup>WT</sup> (black), Stx1B<sup>E210K</sup> (blue) and Stx1B<sup>L221P</sup> (salmon). **B)** SNARE complexes formed with SNAP-25, Syb2 and Stx1B SNARE<sup>WT</sup> (SNARE complex WT, black), Stx1B SNARE<sup>E210K</sup> (SNARE complex E210K, blue) or Stx1B SNARE<sup>L221P</sup> (SNARE complex L221P, salmon).

Appendix Figure 9



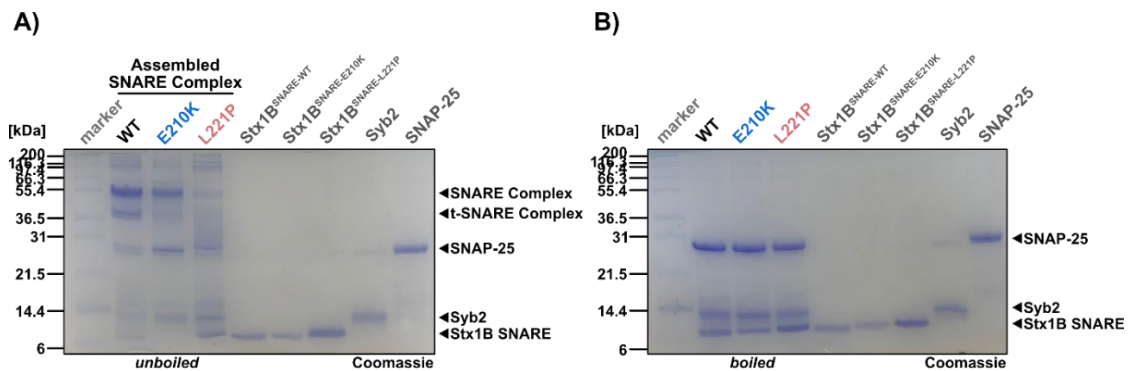
**Appendix Figure 9:** **A)** Crystal Structure of a fragment of the Stx1B SNARE helix displaying residues at position 210 and 213. The Stx1B's E210K mutation allows for a hydrogen bond to form lysine and aspartic acid, potentially enhancing helical structure and stability. **B)** Based on the helical wheel pattern's side-chain interactions, where residues at positions [i+3] and [i+4] orientate on the same side of the helix with the residue at position [i], the negatively charged aspartic acid is positioned three places after the introduced lysine, possibly enhancing stability. **C)** Helical wheel. The projection of the  $\alpha$ -helix illustrates the interrelationships of the amino acid residues. Each amino acid covers a sector of  $100^\circ$ . The hydrogen-bonded residues 1 and 5 are spatially close to each other, being parts of consecutive turns. The same applies to residues 1 and 4 (so-called "n+/-3,4 criterion").

Appendix Figure 10



**Appendix Figure 10:** **A)** Stabilization scheme in  $\alpha$ -helix. Helical structure is stabilized by backbone hydrogen bonds. **B)** Introduction of a proline impedes backbone hydrogen interaction within an  $\alpha$ -helix, causing a kink in the helical conformation or complete disruption (figure adapted from Reiersen *et al.* (2001) [248]).

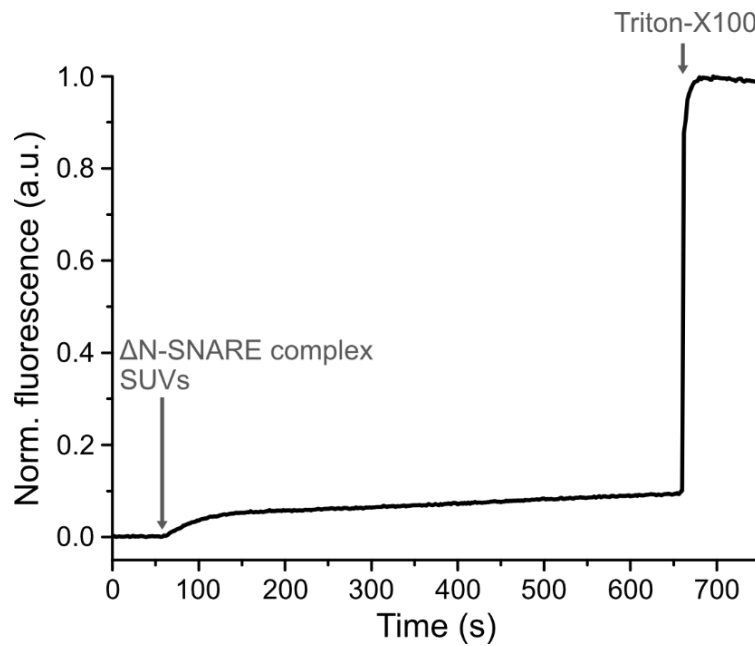
Appendix Figure 11



**Appendix Figure 11:** Unmodified full-size Coomassie-stained SDS-PAGE of: **A)** Assembled SNARE complexes using Stx1BWT, Stx1BE210K and Stx1B<sup>L221P</sup> with Syb2 and SNAP-25. All samples were not boiled prior to loading on the gel. Mark12 Unstained Standard was used as protein ladder. **B)** For loading control, all samples were boiled before gel loading. Boiling caused the SDS-stable SNARE complex to dissociate, revealing bands corresponding to individual components. Mark12 Unstained Standard was used as protein ladder.

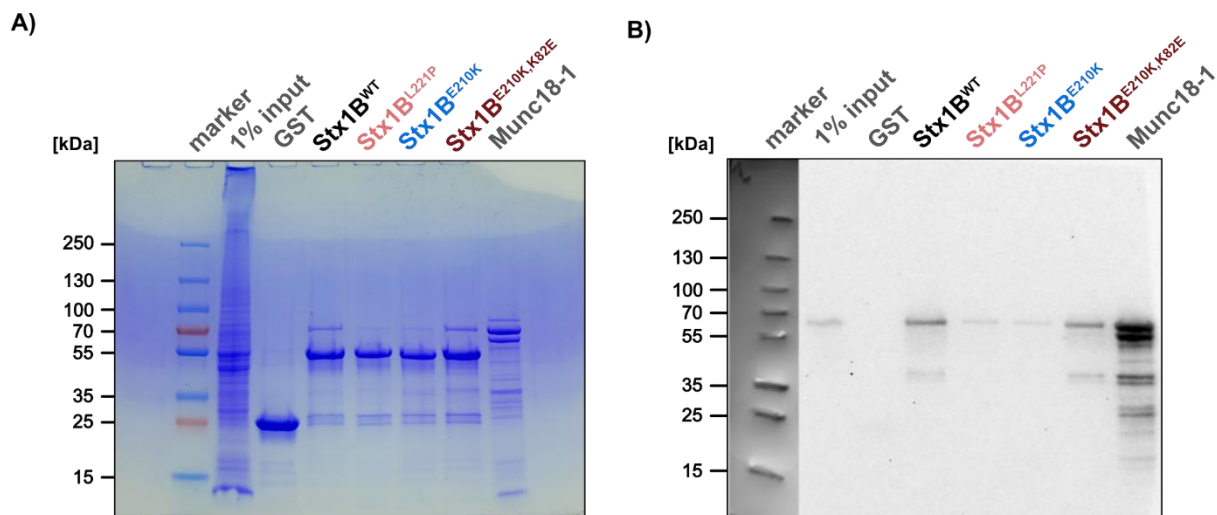


**Appendix Figure 12**



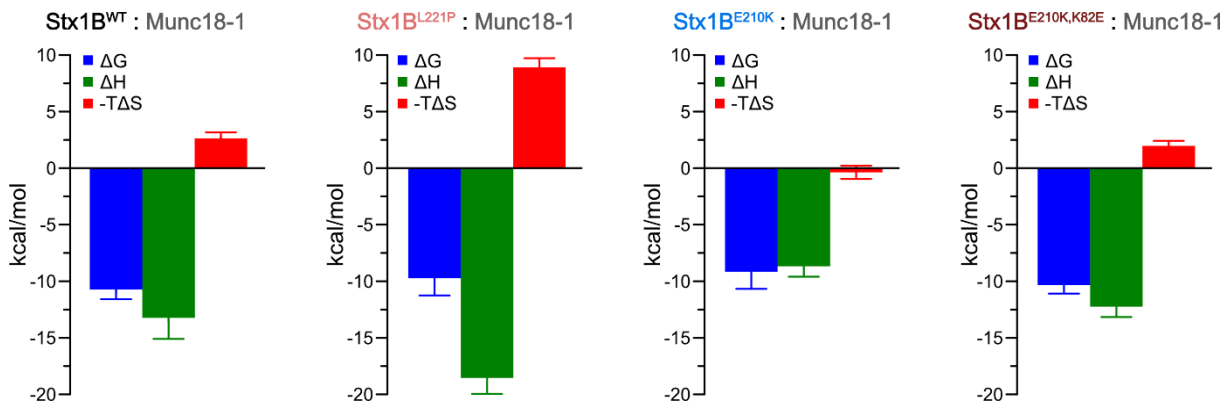
**Appendix Figure 12:** Representative fluorescence diagram of a complete vesicle fusion assay run, monitoring vesicle fusion through lipid mixing, normalized to the maximum value. Small unilamellar vesicles (SUVs) with reconstituted with FRET fluorophores and full-length Syb2 were held in the measurement cuvette under constant stirring for 60 s to check for content leakage. After 60 s, SUVs reconstituted with the pre-formed  $\Delta$ N-SNARE complex were added to initiate vesicle fusion. Vesicle fusion was monitored for 600 s and was stopped by the addition of Triton X-100, which led to the dissolution of the vesicles and release of individual compartment, resulting in a sudden increase in fluorescence of the donor fluorophore to the maximum value.

**Appendix Figure 13**



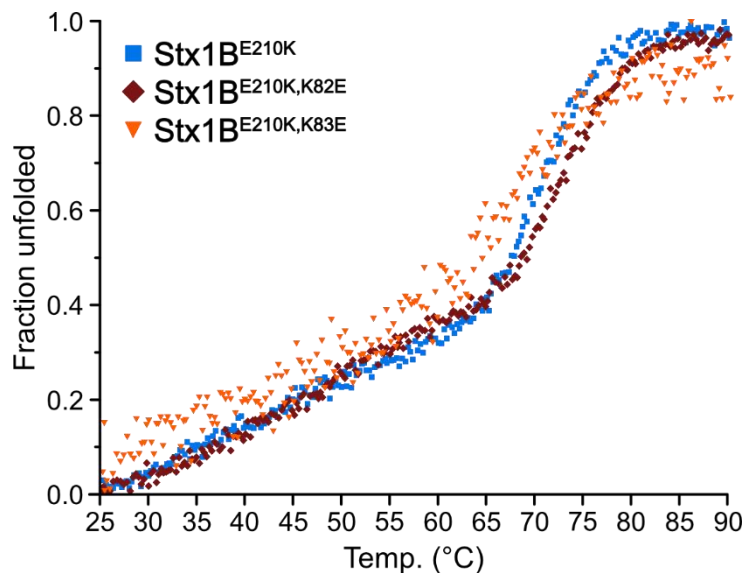
**Appendix Figure 13: A)** Full-size Coomassie-stained SDS-PAGE of the pull-down assay. Recombinant expressed and purified Munc18-1 was loaded into the last well as an additional control for the viability of the Munc18-1 antibody. The sample used here has been subject to multiple freeze-thaw cycles and therefore looks degraded. **B)** Full-size western blot of the pull-down assay. The protein ladder was subsequently edited into the western blot post-capture to enhance visibility since it was only very faintly visible in the original after blotting, The additional control used for the Munc18-1 antibody was successful. Even degraded bands were detected by the antibody. Notably, Munc18-1 seem to have a distinct degrading pattern as some degradation bands were visible for both, the Munc18-1 of the mouse brain lysate and the recombinant Munc18-1.

## Appendix Figure 14



**Appendix Figure 14:** Binding signature plots depicting the interaction of Stx1B<sup>WT</sup>, Stx1B<sup>L221P</sup>, Stx1B<sup>E210K</sup>, and Stx1B<sup>E210K,K82E</sup> with Munc18-1. Stx1B<sup>WT</sup>, along with the Stx1B<sup>L221P</sup> and Stx1B<sup>E210K,K82E</sup> mutants, exhibit comparable thermodynamic parameters, suggesting an enthalpy-driven interaction characterized by hydrogen bonding and van der Waals interactions. This interaction is further associated with substantial conformational changes, as indicated by the unfavorably positive temperature-entropy product. The interaction of Stx1B<sup>E210K</sup> with Munc18-1 exhibits a more entropy-driven interaction comprising of hydrogen bonding as well as hydrophobic interactions as indicated by the negative or favorable binding enthalpy ( $\Delta H$ ) and entropy factor ( $-T\Delta S$ ) [213].

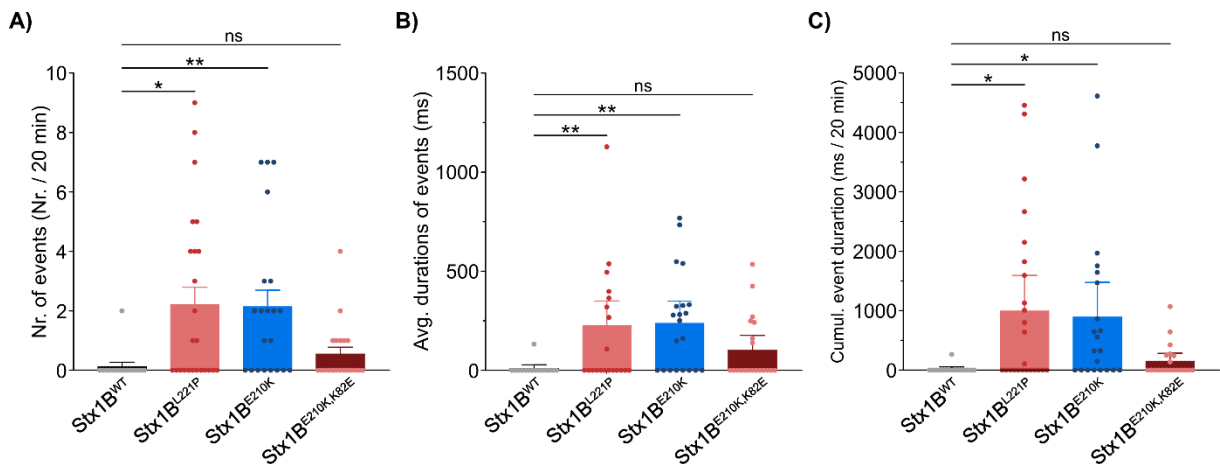
## Appendix Figure 15



**Appendix Figure 15:** Representative normalized fraction unfolded spectra plotted from 25 °C to 90 °C (full spectrum) of Stx1B<sup>E210K</sup> (blue), Stx1B<sup>E210K,K82E</sup> (brown) and Stx1B<sup>E210K,K83E</sup> (orange).

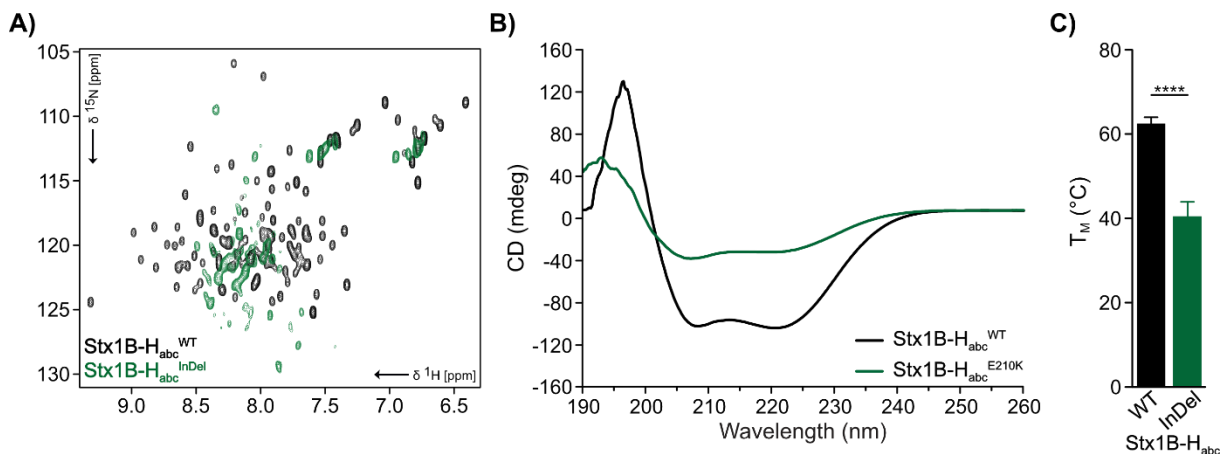


## Appendix Figure 17



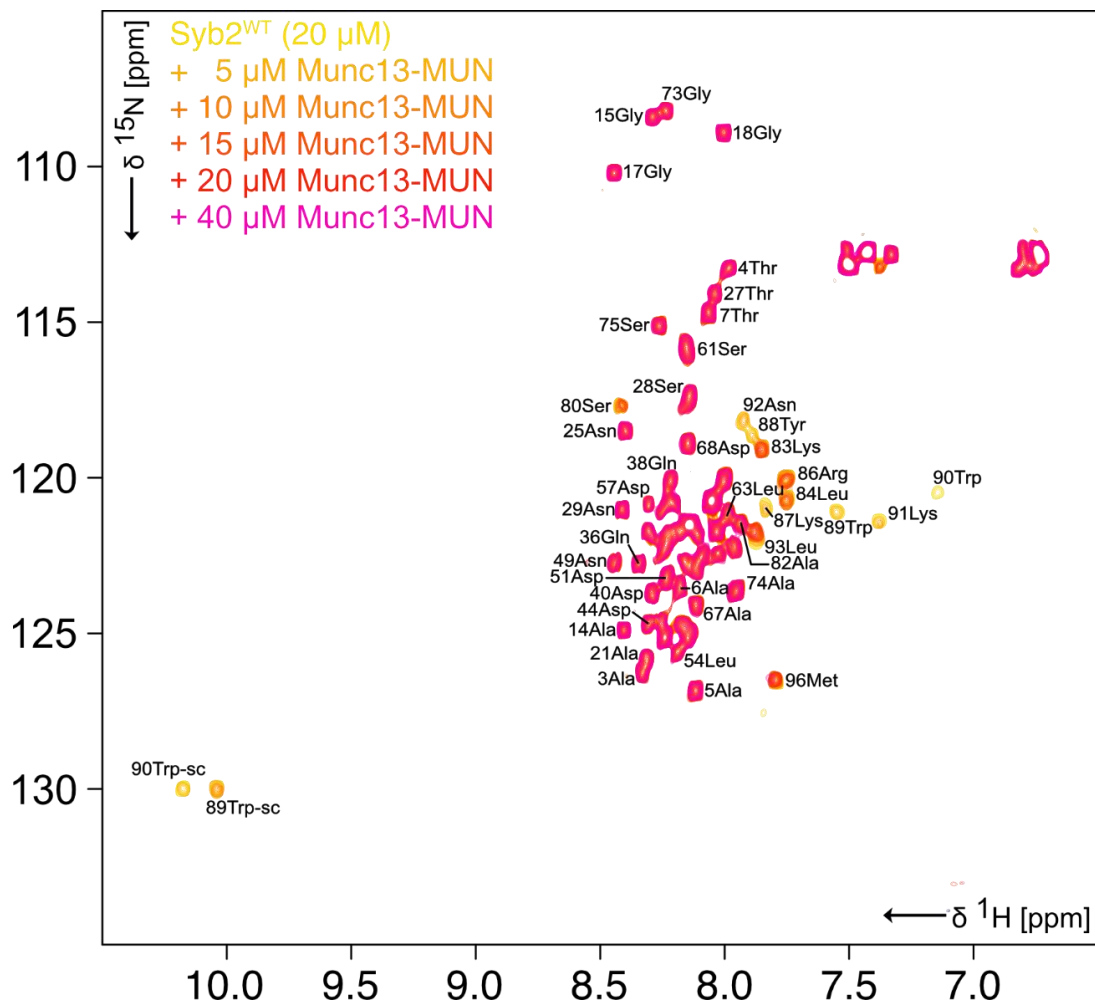
**Appendix Figure 17:** Quantification of all 20-minute LFP recordings. **A)** Number of epileptiform discharge events in larvae expressing different human Stx1B wild-type and mutants. Sample size: Stx1B<sup>WT</sup>, n = 15; Stx1B<sup>L221P</sup>, n = 24; Stx1B<sup>E210K</sup>, n = 21; Stx1B<sup>E210K,K82E</sup>, n = 20. A significant difference between Stx1B<sup>WT</sup> and Stx1B<sup>E210K</sup> (Kruskal-Wallis test,  $^{***}p < 0.01$ ) as well as Stx1B<sup>L221P</sup> (Kruskal-Wallis test,  $^{*}p < 0.05$ ) was observed, but none to Stx1B<sup>E210K,K82E</sup>, indicating that this mutant rescues the number of events back to WT level. **B)** Mean duration of discharge events in the measured zebrafish larvae (sample size similar to A)). Similar to the number of events, a significant difference between Stx1B<sup>WT</sup> and Stx1B<sup>E210K</sup> (Kruskal-Wallis test,  $^{**}p < 0.01$ ) as well as Stx1B<sup>L221P</sup> (Kruskal-Wallis test,  $^{*}p < 0.01$ ) was observed, but none to Stx1B<sup>E210K,K82E</sup>, indicating that this mutant rescues the average duration of events back to WT level. **C)** Cumulative duration of epileptiform events in the measured zebrafish larvae (sample size similar to A)). A significant difference between Stx1B<sup>WT</sup> and Stx1B<sup>E210K</sup> (Kruskal-Wallis test,  $^{*}p < 0.05$ ) as well as Stx1B<sup>L221P</sup> (Kruskal-Wallis test,  $^{*}p < 0.05$ ) was observed. Stx1B<sup>E210K,K82E</sup> exhibited a substantial reduction in the overall seizing time compared to the other mutants.

## Appendix Figure 18



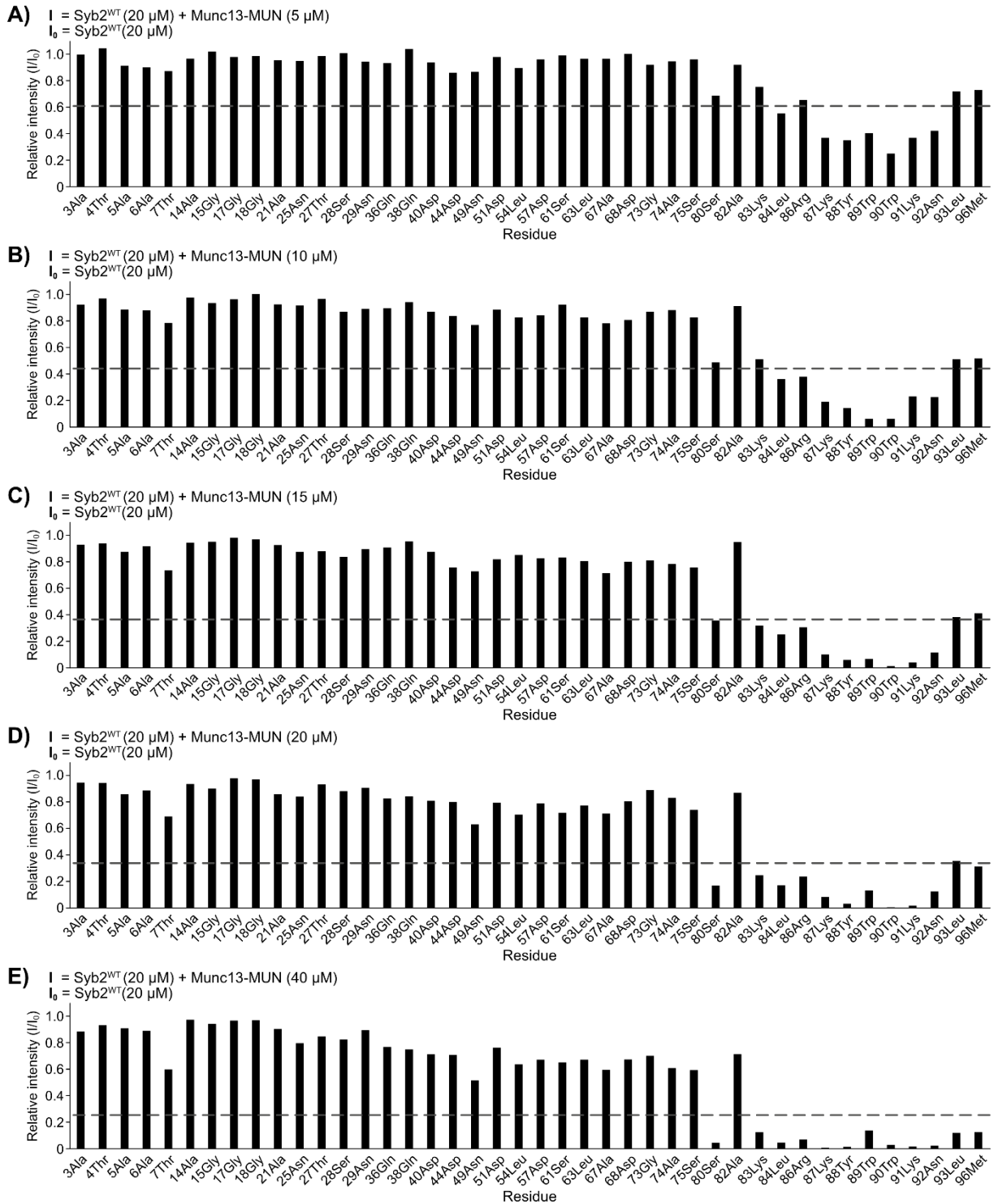
**Appendix Figure 18:** (Figure adapted from Vardar, Gerth, **Schmitt et al.** (2020) [178]) **A)**  $^1\text{H}$ - $^{15}\text{N}$ -HSQC spectra of wild-type (black) and InDel (green) H<sub>abc</sub> domain of Stx1B. The spectrum of the wild-type construct is well dispersed while the spectrum of the InDel mutant shows signs of an intrinsic disordered protein. **B)** Far-UV CD spectra of Stx1B-H<sub>abc</sub><sup>WT</sup> (black) and Stx1B-H<sub>abc</sub><sup>InDel</sup> (green) constructs. While the wild-type constructs display a well pronounced spectrum, characteristic for an  $\alpha$ -helical structure, helicity is largely reduced for the InDel mutant construct. **C)** Melting temperatures of Stx1B-H<sub>abc</sub><sup>WT</sup> and Stx1B-H<sub>abc</sub><sup>InDel</sup> constructs ( $\pm$  SEM, n = 3, t-test,  $^{****}p < 0.001$ , two tailed).

Appendix Figure 19



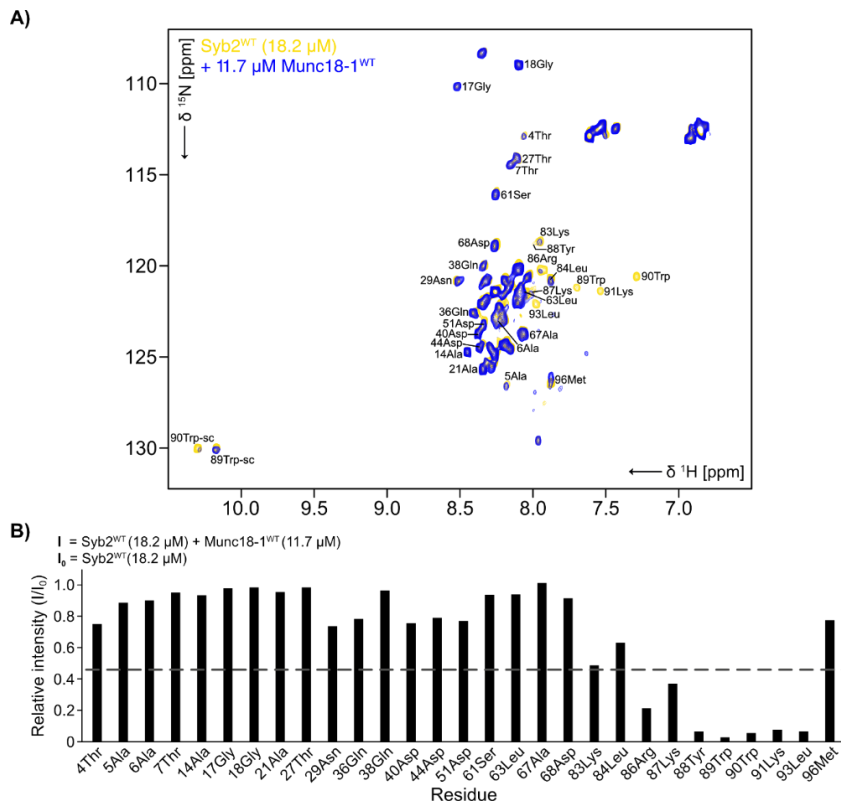
**Appendix Figure 19:**  $^1\text{H}$ - $^{15}\text{N}$ -HSQC spectra of Syb2<sup>WT</sup> (20  $\mu\text{M}$ ) before (yellow) and after the addition of 5  $\mu\text{M}$  (light-orange), 10  $\mu\text{M}$  (orange), 15  $\mu\text{M}$  (red-orange), 20  $\mu\text{M}$  (red) and 40  $\mu\text{M}$  (pink) Munc13-MUN. Cross-peaks corresponding to the C-terminal JMD exhibit increasing cross-peak broadening with higher concentrations of Munc13-MUN.

Appendix Figure 20



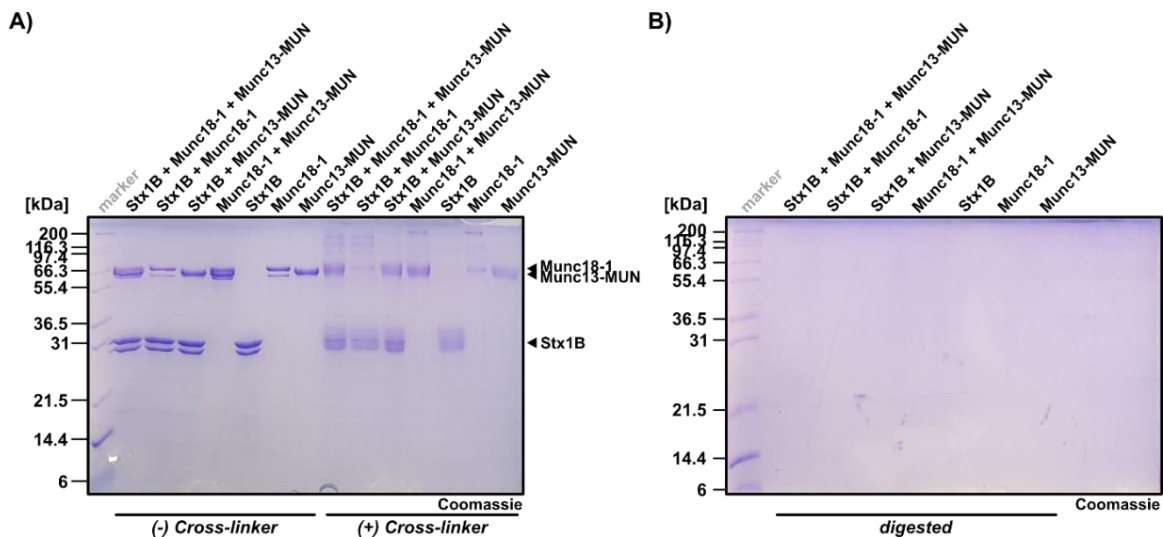
**Appendix Figure 20:** Quantification of the relative cross-peak intensities ( $I/I_0$ ) of Syb2 upon the addition of **A)** 5  $\mu\text{M}$  Munc13-MUN, **B)** 10  $\mu\text{M}$  Munc13-MUN, **C)** 15  $\mu\text{M}$  Munc13-MUN, **D)** 20  $\mu\text{M}$  Munc13-MUN, and **E)** 40  $\mu\text{M}$  Munc13-MUN. While the relative cross-peak intensities corresponding to the N-terminal part remain largely unaffected by the addition of Munc13-MUN, the cross-peaks corresponding to the C-terminal JMD display significant line broadening, intensifying with increasing concentrations of Munc13-MUN. A grey dashed line indicates the cut-off, calculated as the average of relative peak intensities minus the standard deviation. Relative intensities below this threshold denote significant cross-peak broadenings.

Appendix Figure 21



**Appendix Figure 21: A)**  $^1\text{H}$ - $^{15}\text{N}$ -HSQC spectra of Syb2<sup>WT</sup> (18.2  $\mu\text{M}$ ) before (yellow) and after the addition of Munc18-1<sup>WT</sup> (11.7  $\mu\text{M}$ , blue). No significant cross-peak shifts were observed, but rather cross-peak broadening, particularly evident for the cross-peaks corresponding to the JMD of Syb2<sup>WT</sup>. **B)** Quantification of relative cross-peak intensities ( $I/I_0$ ) of Syb2 upon the addition of 11.7  $\mu\text{M}$  Munc18-1<sup>WT</sup> complex reveals significant decrease of the cross-peak intensities for the residues corresponding to the C-terminal JMD of Syb2. Additionally, subtle cross-peak broadening can be observed for the cross-peaks corresponding to the residues of the SNARE motif, although not significant. A grey dashed line indicates the cut-off, calculated as the average of relative peak intensities minus the standard deviation. Relative intensities below this threshold denote significant cross-peak broadenings.

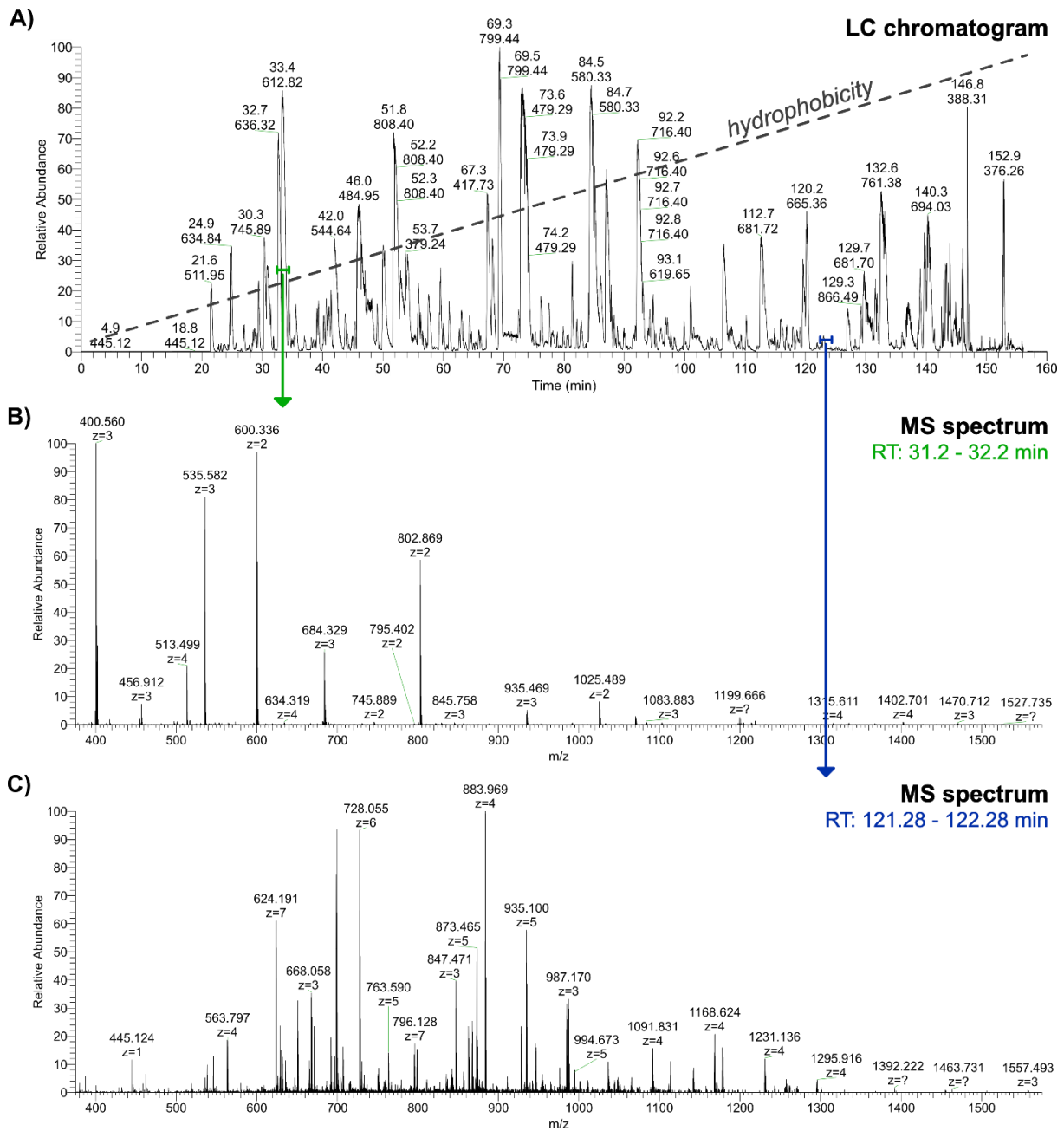
Appendix Figure 22



**Appendix Figure 22: A)** Full-size Coomassie-stained SDS-PAGE of analyzed proteins before and after cross-linking. **B)** Full-size Coomassie-stained SDS-PAGE of analyzed proteins before and after cross-linking and after digestion using endoproteinase LysC and trypsin. No protein bands are detectable.



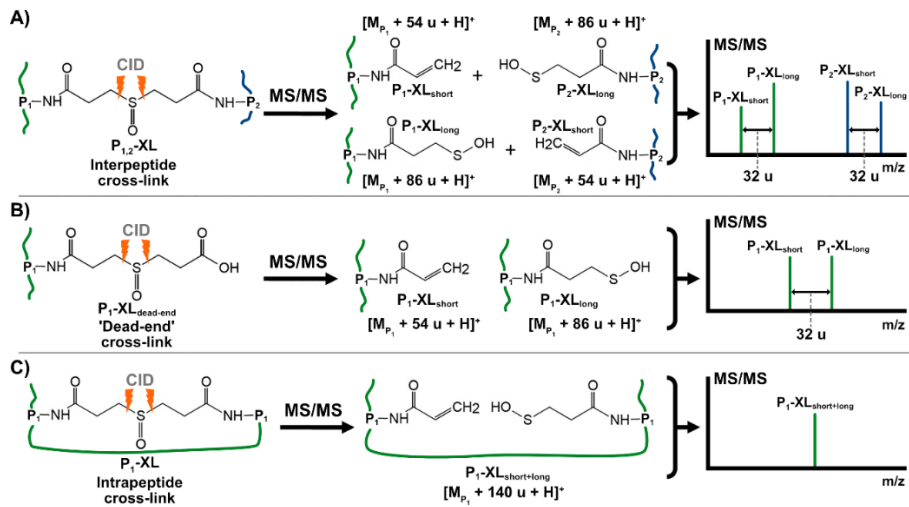
## Appendix Figure 23



**Appendix Figure 23:** **A)** Representative LC chromatogram of an LC-MS/MS run displaying the separation of peptides over a 160-minute gradient with increasing hydrophobicity of the mobile phase. Shorter peptides often elute early due to their lower hydrophobicity, while longer peptides often elute later due to their higher hydrophobicity. The separation of peptides allows for sequential introduction of peptides into the mass spectrometer, enhancing detection and identification of peptides in the complex mixture. **B)** Exemplary summed MS spectrum recorded at the retention between 31.2 min and 32.2 min. The spectrum displays peaks with low  $m/z$  ratios, indicating the presence of shorter peptides. These shorter peptides typically exhibit lower mass and smaller surface area, resulting in lower charge states. **C)** Exemplary summed MS spectrum recorded at the retention between 121.28 min and 122.28 min. The spectrum displays peaks with high  $m/z$  ratios, indicating the presence of longer peptides. Cross-linked peptides exhibit a charge state of 4+ or higher due to the involvement of two lysine side chains and two amine groups of the N-termini.

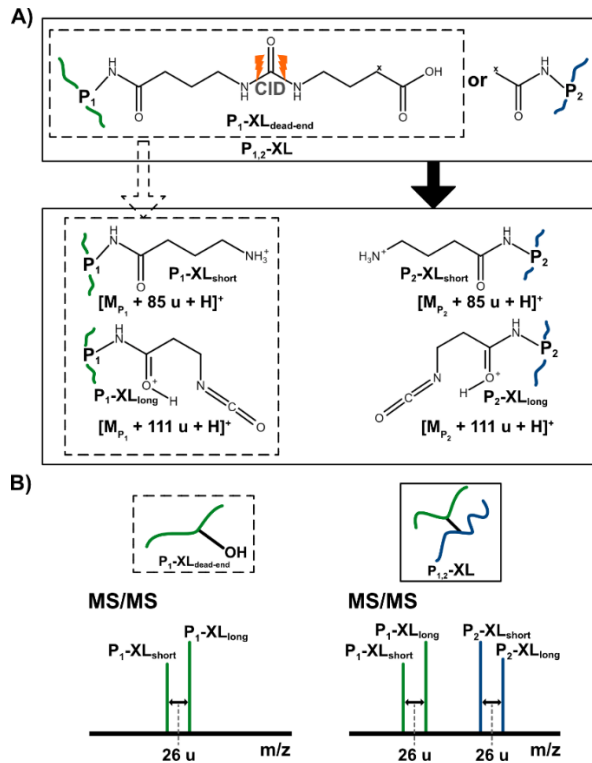


Appendix Figure 24



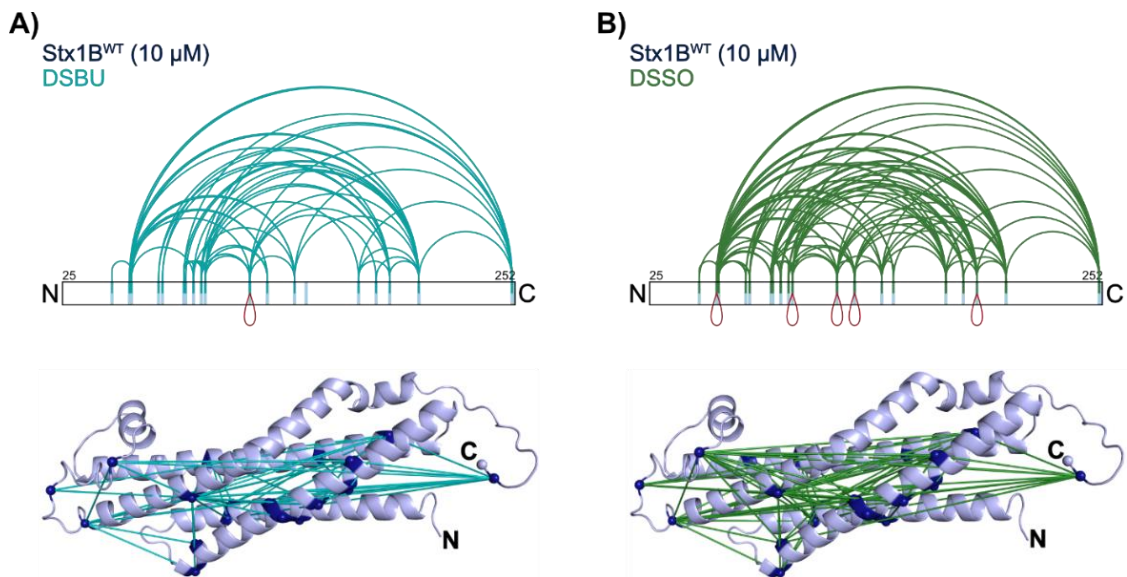
**Appendix Figure 24:** Fragmentation scheme of DSSO cross-linked peptides after cleavage under CID conditions. **A)** Fragmentation pattern of an interpeptide cross-link. DSSO cleaves into a short and a long fragment with different masses adding to the mass of the attached peptides  $P_1$  and  $P_2$ . This results in two doublet peak-signals in the MS/MS spectrum. **B)** Fragmentation pattern of a 'dead-end' cross-link. DSSO cleaves into a short and a long fragment with different masses adding to the mass of the attached peptide  $P_1$ . This results in one doublet peak-signals in the MS/MS spectrum. **C)** Fragmentation pattern of an intrapeptide cross-link. DSSO cleaves into a short and a long fragment but results in only one peak-signal in the MS/MS spectrum, as both fragments are attached to the same peptide (figure adapted from A. Kao (2011) [238]).

Appendix Figure 25



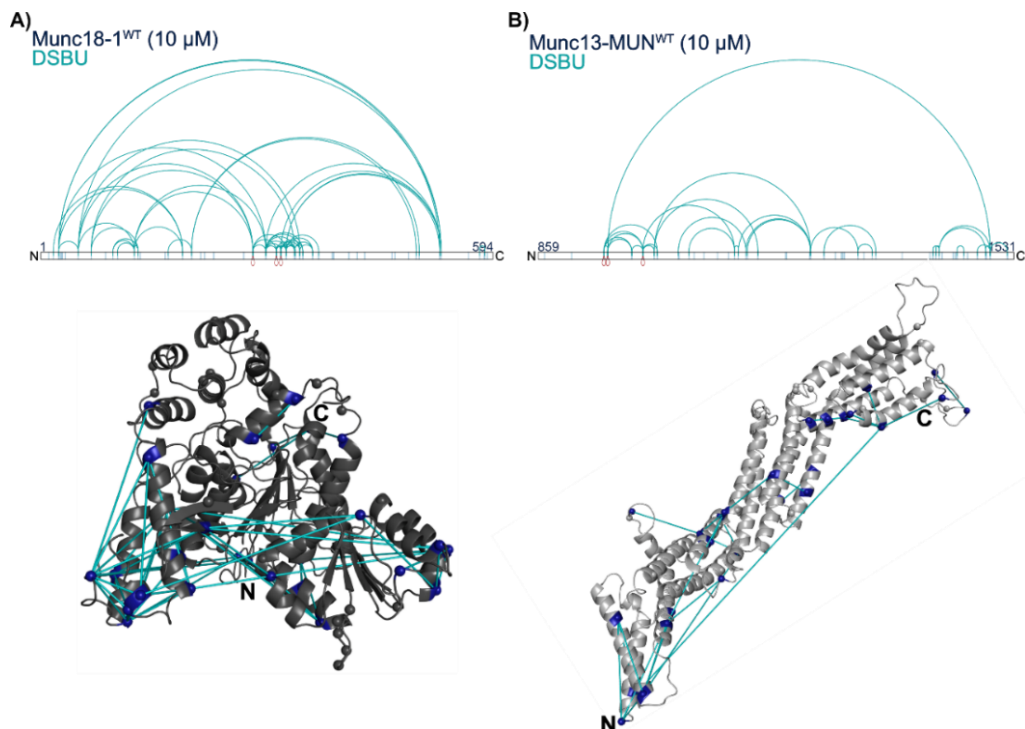
**Appendix Figure 25:** **A)** Fragmentation scheme of DSBU cross-linked peptides after cleavage under CID conditions. DSBU cleaves into a short and a long fragment with different masses adding to the mass of the attached peptides  $P_1$  and  $P_2$ . **B)** Doublet peak-signals with a difference of 26 u are visible in the MS/MS spectrum, indicating the presence of a cross-linker. 'Dead-end' cross-links will give one doublet, while two doublets are indicative of an interpeptide cross-link (figure adapted from A. Sinz (2017) [284]).

## Appendix Figure 26



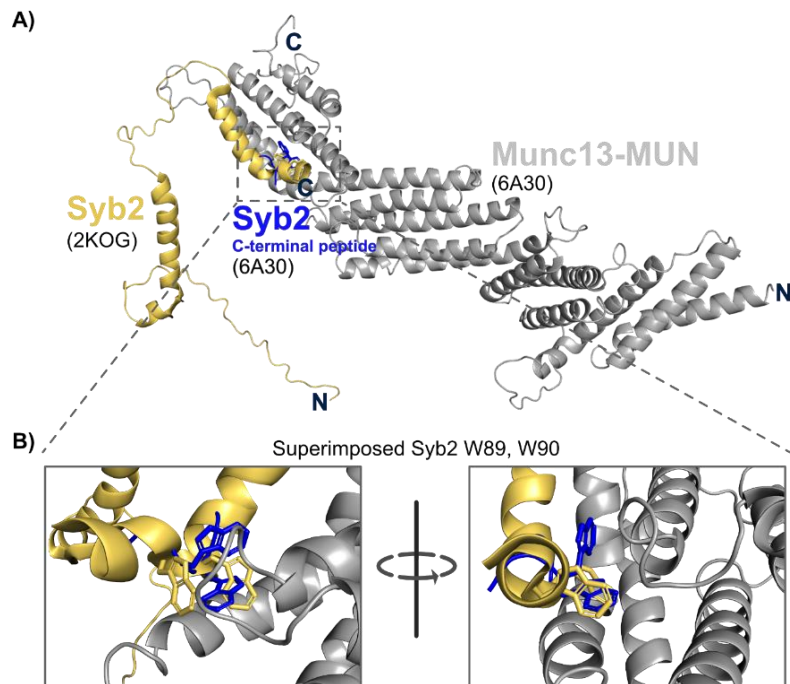
**Appendix Figure 26:** Cross-linking mass spectrometry analysis of Stx1B utilizing **A)** DSBU (teal) or **B)** DSSO (dark green) as cross-linker. Linkage map (top) shows the sequence position of all observed cross-linked lysine pairs within Stx1B. Self-links (identified cross-links between the same lysine residue) are colored red. XiNET Cross-Linker Viewer was used to create the cross-link map [288]. Identified cross-links are mapped onto the crystal structure of Stx1A (homolog of Stx1B) to visualize cross-link distances within a 3D structure. The sequence, particularly the lysine positions in the crystal structure of Stx1A, was adjusted to match that of Stx1B (PDB: 3C98). Lysine residues within the structures are marked as spheres and cross-linked lysine residues are colored in dark blue.

## Appendix Figure 27



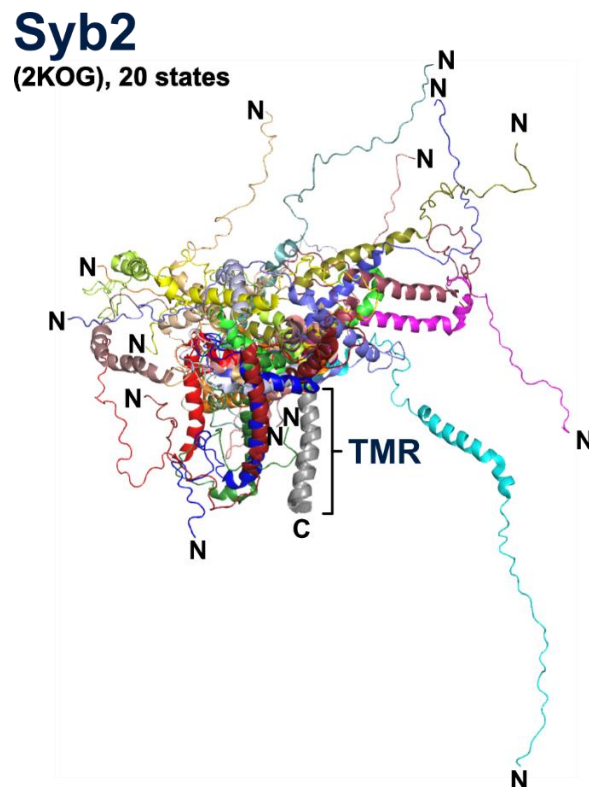
**Appendix Figure 27:** Cross-linking mass spectrometry analysis of **A)** Munc18-1<sup>WT</sup> and **B)** Munc13-MUN<sup>WT</sup> utilizing DSBU as cross-linker. Linkage map (top) shows the sequence position of all observed cross-linked lysine pairs within **A)** Munc18-1<sup>WT</sup> and **B)** Munc13-MUN<sup>WT</sup>. Self-links (identified cross-links between the same lysine residue) are colored red. XiNET Cross-Linker Viewer was used to create the cross-link maps [288]. Identified cross-links are mapped onto the crystal structure of **A)** Munc18-1<sup>WT</sup> (PDB: 3C98) and **B)** Munc13-MUN<sup>WT</sup> (PDB: 6A30). Lysine residues within the structures are marked as spheres and cross-linked lysine residues are colored in dark blue.

## Appendix Figure 28



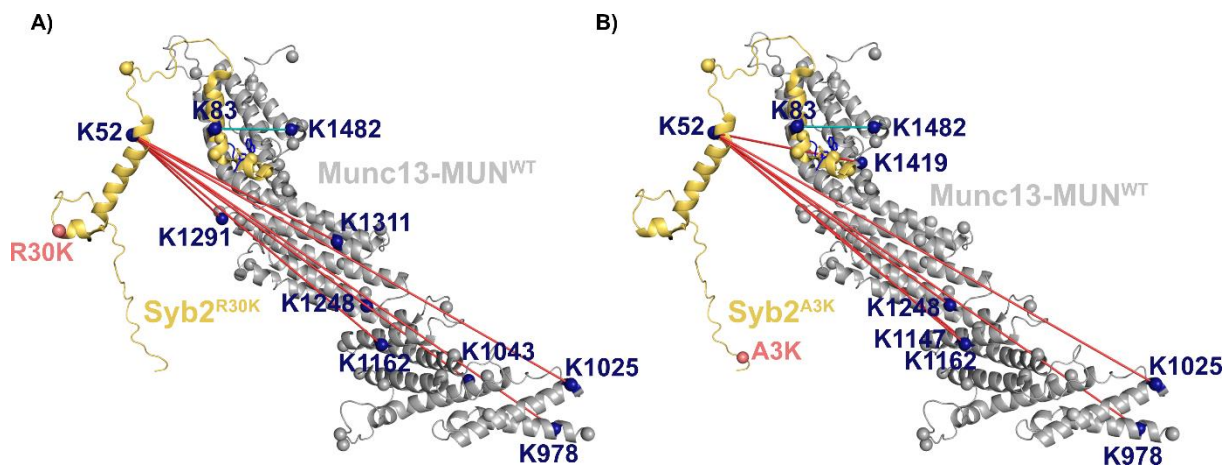
**Appendix Figure 28:** **A)** Superimposition of the NMR structure of Syb2 (gold, PDB: 2KOG) and the C-terminal peptide of Syb2 within the crystal structure of Munc13-MUN (blue and grey, PDB: 6A30). **B)** Close-up of the alignment region in Syb2 highlighting the two tryptophan residues W89 and W90 as anchor points for the alignment. Although the backbone of these residues aligns, the side chains display distinct rotations.

## Appendix Figure 29



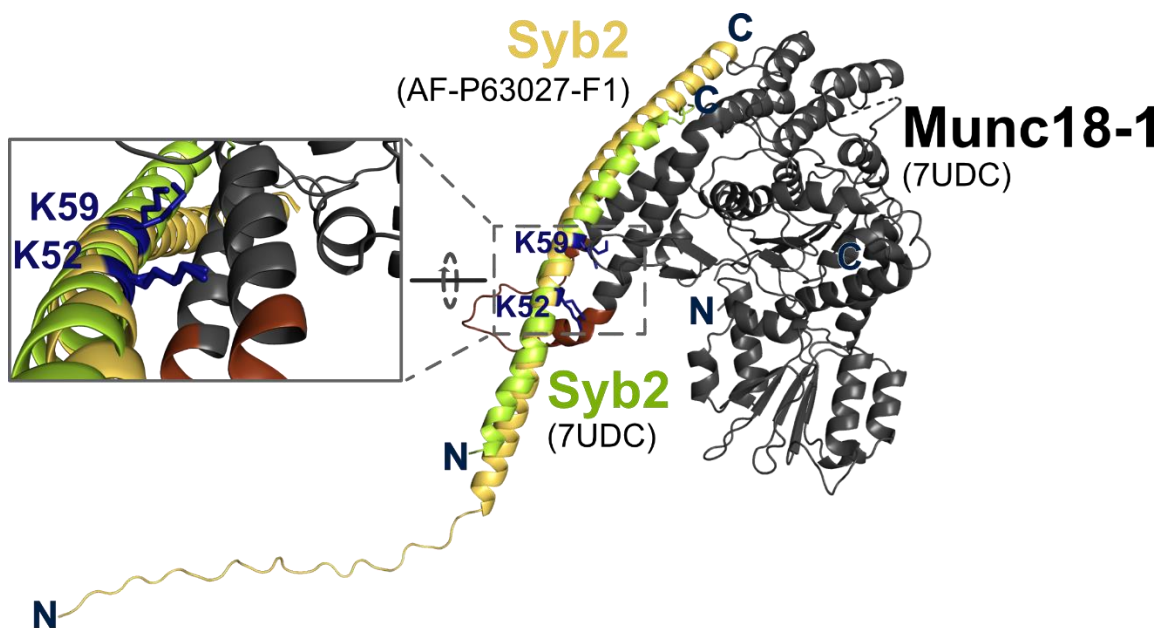
**Appendix Figure 29:** Twenty lowest energy structures of Syb2 (1-116) in DPC micelles recorded by NMR. Transmembrane region (TMR) is superimposed and the N-terminal part shows high structural flexibility. Only the juxtamembrane domain and a part of the SNARE motif adopts a helical conformation [110].

## Appendix Figure 30



**Appendix Figure 30:** Identified cross-links are mapped onto the superimposed structures of **A)** Syb2<sup>R30K</sup> **B)** Syb2<sup>A3K</sup> (PDB: 2KOG) and Munc13-MUN (PDB: 6A30). Lysine residues within the structures are marked as spheres and cross-linked lysine residues are colored in dark blue. Inset provides a close-up view onto the superimposed structures of the Syb2 peptide (PDB: 6A30, blue) and Syb2 (PDB: 2KOG, gold), along with the identified cross-links between the C-termini of Munc13-MUN and Syb2. Intermolecular cross-links that exceed the distance constraint are colored in red, while those within the distance constraint are colored in teal (cross-link length can be found in Appendix Table 7.3).

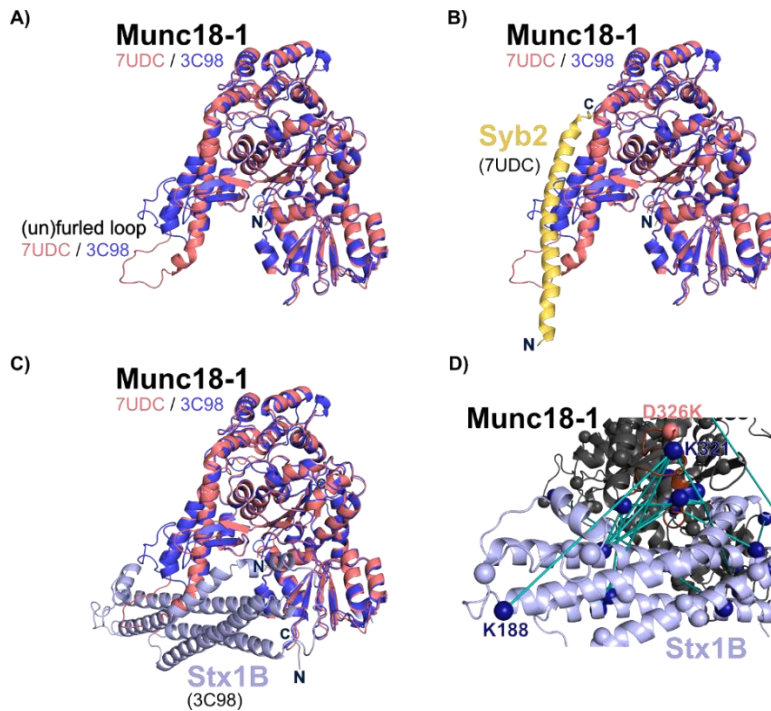
## Appendix Figure 31



**Appendix Figure 31:** Superimposition of the AlphaFold 2-modeled structure of Syb2 (gold, PDB: AF-P63027-F1) and the Syb2 fragment depicted in the EM structure of the Syb2:Stx1A:Munc18-1 complex (lime and black, PDB: 7UDC, here only showing Syb2 and Munc18-1). Inset displays a detailed view of the aligned Syb2 helices, with lysine residues K52 and K59 serving as reference points. The missing segment of the unfurled loop (brown) was reconstructed using MoMa-LoopSampler (Barozet *et al.* (2022) [289]).

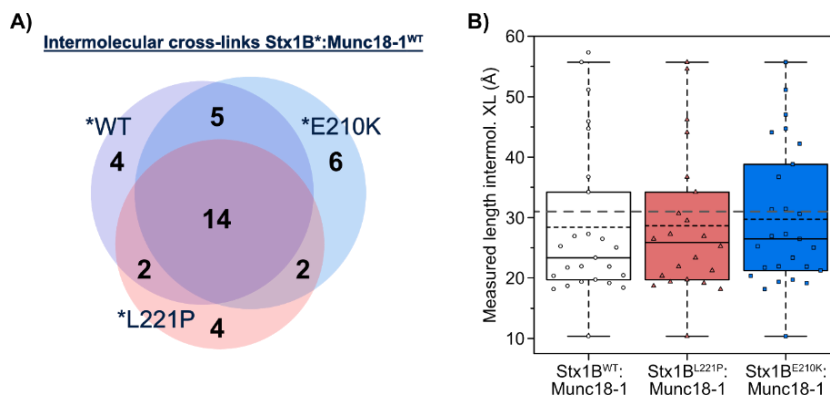


Appendix Figure 32



**Appendix Figure 32:** **A)** Superimposition of the EM structure of Munc18-1 (Stepien *et al.* (2022 [69], PDB: 7UDC), colored in rose), with the unfurled loop capable of binding Syb2, and the crystal structure of Munc18-1 (Burkhardt *et al.* (2008 [140], PDB: 3C98), colored in blue) with the furled loop, binding Stx1 in its closed conformation. The missing part of each loop was modeled using MoMa-LoopSampler (Barozet *et al.* (2022) [289]). **B)** Superimposed Munc18-1 structures with Syb2 from the EM complex structure (Stepien *et al.* (2022 [69], PDB: 7UDC), colored in gold). Overlaying reveals a potential hindrance to their interaction caused by the furled loop, as evidenced by the overlapping of both structures. **C)** Superimposed Munc18-1 structures with Stx1B from the crystal structure of the Stx1:Munc18-1 complex (Burkhardt *et al.* (2008 [140], PDB: 3C98), colored in light blue). The structure of the unfurled loop collides with the SNARE motif of Stx1B, which implies that a complete unfurling of the loop is only possible by significant conformational changes. **D)** Mapped cross-links between Stx1B and Munc18-1<sup>D326K</sup> revealed one cross-link between K321 (Munc18-1) and K188 (Stx1) which showed overlength, implying a conformational change of the furled loop.

Appendix Figure 33



**Appendix Figure 33:** **A)** Venn diagram shows the counts of intermolecular cross-links between Stx1B and Munc18-1, highlighting the overlap of identical cross-links from XL-MS measurements of Stx1B<sup>WT</sup> (purple), Stx1B<sup>L221P</sup> (salmon), and Stx1B<sup>E210K</sup> (blue). **B)** Box plots display the length dispersion of intermolecular cross-links between Stx1B wild-type and mutants, and Munc18-1, including the unspecific overlength cross-links involving K251 of Stx1B. Median and average values are indicated as straight and dashed line, respectively, within the boxes. Grey dashed line indicates maximum distance constraint. Data were analyzed and plotted using OriginPro-2023 (OriginLab Corporation).

## Appendix

**Table 7.1:** Detailed statistical data Stx1B wild-type and Mutant constructs

<b>Figure</b>	<b>Parameter measured</b>	<b>Genotype</b>	<b>Number of Experiments</b>	<b>Mean</b>	<b>SEM</b>	<b>Median</b>	<b>Statistical test</b>	<b>Adjusted p-value (vs. WT)</b>
<b>4.1 C)</b>	$T_M$	WT	3	69.42 °C	0.31 °C	69.52 °C	Student's t-test	> 0.05 (n.s.)
		E210K	3	69.08 °C	0.54 °C	69.19 °C		
		L221P	3	70.56 °C	0.49 °C	70.65 °C		
<b>4.3 C)</b>	$T_M$	WT	3	83.54 °C	0.56 °C	83.63 °C	Student's t-test	> 0.05 (n.s.)
		E210K	3	83.81 °C	0.46 °C	83.89 °C		
		L221P	3	75.72 °C	0.86 °C	75.83 °C		
<b>4.7 B)</b>	Half-maximum fusion time	WT	6	60.61 s	9.78 s	57.65 s	Shapiro-Wilk-test, Student's t-test	> 0.05 (n.s.), ( $< 0.01$ vs. L221P)
		E210K	9	48.96 s	6.32 s	49.90 s		
		L221P	7	84.88 s	5.75	89.58 s		
<b>4.7 D)</b>	Initial fusion velocity	WT	6	0.018 a.u./s	0.003 a.u./s	0.016 a.u./s	Welch-test	> 0.05 (n.s.), ( $< 0.05$ vs. L221P)
		E210K	9	0.024 a.u./s	0.004 a.u./s	0.02 a.u./s		
		L221P	7	0.010 a.u./s	0.001 a.u./s	0.01 a.u./s		
<b>4.8 D)</b>	Western blot band intensity	WT	3	1.0	-	-	-	-
		L221P	3	0.29	0.07	0.36		
		E210K	3	0.39	0.12	0.35		
		E210K, K82E	3	0.74	0.06	0.79		
<b>4.10</b>	$K_D$	WT	3	9.9 nM	1.6 nM	11.5 ± 5.4 nM	-	-
		L221P	3	216.2 nM	7.2 nM	220 ± 34 nM		
		E210K	3	2.3 μM	0.4 μM	2.4 ± 0.7 μM		
		E210K, K82E	3	25.2 nM	2.2 nM	23 ± 7 nM		

## Appendix

<b>4.12</b>	K <sub>D</sub>	E210K, K82E	3	25.2 nM	2.2 nM	23 ± 7 nM	-	-
		E210K, K83E	3	No binding	No binding	No binding		
		E210K, K82E, K82E	3	17.5 nM	2.4 nM	17.5 ± 3.2 nM		
<b>4.13</b>	T <sub>M</sub>	E210K	3	69.08 °C	0.55 °C	68.91 °C		-
		E210K, K82E	3	72.96 °C	0.18 °C	72.81 °C		
		E210K, K83E	3	66.65 °C	0.35 °C	66.71 °C		
<b>4.16 A)</b>	Number of seizure events per 20 min (only seizure positive)	WT	1	2	0	2	Mann-Whitney-test	-
		L221P	12	4.42	0.72	4		
		E210K	13	3.46	0.66	2		
		E210K, K82E	7	1.57	0.42	1		
<b>4.16 B)</b>	Duration of discharge (only seizure positive)	WT	1	133 ms	0 ms	133 ms	Kruskal-Wallis-test	-
		L221P	12	453 ms	75 ms	390 ms		
		E210K	13	383 ms	56 ms	323 ms		
		E210K, K82E	7	289 ms	54 ms	249 ms		
<b>4.16 C)</b>	Cumulative duration of epileptiform events per 20 min (only seizure positive)	WT	1	265 ms	0 ms	265 ms	One-way ANOVA test	-
		L221P	12	1991 ms	409 ms	1709 ms		
		E210K	13	1442 ms	379 ms	863 ms		
		E210K, K82E	7	433 ms	123 ms	270 ms		

## Appendix

<b>4.17</b>	% of larvae with touch response	Wild-type zebrafish population	4	100%	0%	100%	Binomial exact test	
		Nmd zebrafish population	4	75.5%	1.4%	76.5%		-
		WT population	4	87.3%	2.5%	87.7%		< 0.0001 vs. 75%
		L221P population	3	91.2%	4.6%	94.7%		< 0.001 vs. 75%
		E210K population	4	72.7%	4.3%	76.5%		> 0.05 vs. 75%
		E210K, K82E population	5	80.9%	4.2%	82.0%	< 0.01 vs. 75%	
<b>4.41 C)</b>	Length of intermolecular XL Stx1B:Munc18-1	WT	Number of XL = 20	23.77 Å	1.87 Å	21.79 Å	-	
		L221P	Number of XL = 18	24.91 Å	2.08 Å	22.61 Å	-	-
		E210K	Number of XL = 24	28.09 Å	2.10 Å	25.14 Å	-	-
<b>Appendix Fig. 14</b>	$\Delta G$	WT	3	-10.7	1.9	-11.0	-	
		L221P	3	-9.8	2.8	-9.3	-	-
		E210K	3	-8.35	2.3	-7.9	-	-
		E210K, K82E	3	-10.4	0.9	-10.8	-	-
	$\Delta H$	WT	3	-13.2	2.4	-13.5	-	
		L221P	3	-18.6	2.2	-17.9	-	-
		E210K	3	-7.93	1.2	-8.2	-	-
		E210K, K82E	3	-12.3	1.03	11.9	-	-
	$-T\Delta S$	WT	3	2.45	0.7	2.5	-	
		L221P	3	8.81	1.1	8.5	-	-
		E210K	3	-0.42	0.5	-0.22	-	-
		E210K, K82E	3	2.23	0.2	1.9	-	-



## Appendix

<b>Appendix Fig. 17 A)</b>	Number of seizure events per 20 min	WT	15	0.13	0.13	0.0	Kruskal-Wallis-test	
		L221P	24	2.21	0.59	0.5		< 0.05
		E210K	21	2.14	0.55	2.0		< 0.01
		E210K, K82E	20	0.55	0.22	0.0		> 0.05
<b>Appendix Fig. 17 B)</b>	Duration of discharge	WT	15	9 ms	9 ms	0 ms	Kruskal-Wallis-test	
		L221P	24	266 ms	60 ms	54 ms		< 0.01
		E210K	21	237 ms	54 ms	251 ms		< 0.01
		E210K, K82E	20	101 ms	36 ms	0 ms		> 0.05
<b>Appendix Fig. 17 C)</b>	Cumulative duration of epileptiform events per 20 min	WT	15	18 ms	18 ms	0 ms	One-way ANOVA test	
		L221P	24	996 ms	288 ms	54 ms		< 0.05
		E210K	21	893 ms	279 ms	327 ms		< 0.05
		E210K, K82E	20	152 ms	63 ms	0 ms		> 0.05
<b>Appendix Fig. 18 C)</b>	T <sub>M</sub>	WT	3	62.31 °C	1.69 °C	62.61 °C	Student's t-test	
		InDel	3	41.70 °C	2.86 °C	41.92 °C		< 0.0001
<b>Appendix Fig. 33 B)</b>	Length of intermolecular XL Stx1B:Munc18-1	WT	Number of XL = 25	27.21 Å	2.63 Å	23.34 Å	-	
		L221P	Number of XL = 22	27.71 Å	2.59 Å	22.85 Å	-	
		E210K	Number of XL = 27	28.39 Å	2.44 Å	26.44 Å	-	

## Appendix

**Table 7.2:** Detailed statistical NMR data

<b>Figure</b>	<b>Protein</b>	<b>Number of assigned Peaks</b>	<b>Mean relative intensity</b>	<b>Stdev.</b>	<b>Cutoff</b>
<b>4.20 and Appendix Fig. 20</b>	<sup>15</sup> N-Syb2 <sup>WT</sup> (20 μM) + Munc13-MUN (5 μM)	42	0.832	0.225	0.606
	<sup>15</sup> N-Syb2 <sup>WT</sup> (20 μM) + Munc13-MUN (10 μM)	42	0.729	0.285	0.444
	<sup>15</sup> N-Syb2 <sup>WT</sup> (20 μM) + Munc13-MUN (15 μM)	42	0.685	0.319	0.365
	<sup>15</sup> N-Syb2 <sup>WT</sup> (20 μM) + Munc13-MUN (20 μM)	42	0.659	0.319	0.338
	<sup>15</sup> N-Syb2 <sup>WT</sup> (20 μM) + Munc13-MUN (40 μM)	42	0.590	0.335	0.255
<b>4.22</b>	<sup>15</sup> N-Syb2 <sup>W89A</sup> (20 μM) + Munc13-MUN (40 μM)	40	0.825	0.255	0.570
<b>4.23</b>	<sup>15</sup> N-Syb2 <sup>W89A</sup> (20 μM) + Munc13-MUN (40 μM)	40	0.864	0.258	0.606
<b>4.24</b>	<sup>15</sup> N-Syb2 <sup>WWAA</sup> (20 μM) + Munc13-MUN (40 μM)	37	0.976	9.091	0.885
<b>4.25</b>	<sup>15</sup> N-Syb2 <sup>WT</sup> (10 μM) + Stx1B <sup>WT</sup> :Munc18-1 <sup>WT</sup> (10 μM)	42	0.695	0.153	0.541
<b>4.26 B)</b>	<sup>15</sup> N-Syb2 <sup>WT</sup> (10 μM) + Stx1B <sup>V218E</sup> :Munc18-1 <sup>WT</sup> (10 μM)	42	0.586	0.093	0.492
<b>4.26 C)</b>	<sup>15</sup> N-Syb2 <sup>WT</sup> (10 μM) + Stx1B <sup>WT</sup> :Munc18-1 <sup>D326K</sup> (10 μM)	42	0.490	0.094	0.396
<b>4.26 D)</b>	<sup>15</sup> N-Syb2 <sup>WT</sup> (10 μM) + Stx1B <sup>WT</sup> :Munc18-1 <sup>P335A</sup> (10 μM)	42	0.401	0.097	0.304
<b>Appendix Fig. 21</b>	<sup>15</sup> N-Syb2 <sup>WT</sup> (18.2 μM) + Munc18-1 <sup>WT</sup> (11.7 μM)	29	0.696	0.249	0.448

## Appendix

**Table 7.3:** Intermolecular Cross-links length

<i>Figure</i>	<i>Proteins</i>	<i>Position lysine A (protein)</i>	<i>Position lysine B (protein)</i>	<i>Length</i>
<b>4.35 B)</b>	Syb2 <sup>WT</sup> (1-96) Munc13-MUN (859-1531, Δ1408-1452)	52 (Syb2 <sup>WT</sup> )	978 (Munc13-MUN)	132.5 Å
		52 (Syb2 <sup>WT</sup> )	1010 (Munc13-MUN)	112.7 Å
		52 (Syb2 <sup>WT</sup> )	1025 (Munc13-MUN)	126.4 Å
		52 (Syb2 <sup>WT</sup> )	1162 (Munc13-MUN)	84.7 Å
		52 (Syb2 <sup>WT</sup> )	1248 (Munc13-MUN)	75.2 Å
		52 (Syb2 <sup>WT</sup> )	1311 (Munc13-MUN)	60.3 Å
		52 (Syb2 <sup>WT</sup> )	1330 (Munc13-MUN)	65.5 Å
		83 (Syb2 <sup>WT</sup> )	1482 (Munc13-MUN)	21.5 Å
<b>4.36 B)</b>	Syb2 <sup>R47K</sup> (1-96) Munc13-MUN (859-1531, Δ1408-1452)	91 (Syb2 <sup>WT</sup> )	1482 (Munc13-MUN)	16.1 Å
		R47K (Syb2 <sup>R47K</sup> )	978 (Munc13-MUN)	127.7 Å
		R47K (Syb2 <sup>R47K</sup> )	1025 (Munc13-MUN)	122.5 Å
		R47K (Syb2 <sup>R47K</sup> )	1248 (Munc13-MUN)	70.0 Å
		52 (Syb2 <sup>R47K</sup> )	978 (Munc13-MUN)	132.5 Å
		52 (Syb2 <sup>R47K</sup> )	1025 (Munc13-MUN)	126.4 Å
		52 (Syb2 <sup>R47K</sup> )	1162 (Munc13-MUN)	84.7 Å
		52 (Syb2 <sup>R47K</sup> )	1248 (Munc13-MUN)	75.2 Å
		52 (Syb2 <sup>R47K</sup> )	1311 (Munc13-MUN)	60.3 Å
52 (Syb2 <sup>R47K</sup> )	1419 (Munc13-MUN)	45.0 Å		
<b>4.37 A)</b>	Syb2 <sup>WT</sup> (1-96) Munc18-1 <sup>WT</sup> (2-594)	91 (Syb2 <sup>R47K</sup> )	1428 (Munc13-MUN)	16.1 Å
		52 (Syb2 <sup>WT</sup> )	92 (Munc18-1 <sup>WT</sup> )	56.8 Å
		52 (Syb2 <sup>WT</sup> )	120 (Munc18-1 <sup>WT</sup> )	63.4 Å
		52 (Syb2 <sup>WT</sup> )	125 (Munc18-1 <sup>WT</sup> )	58.4 Å
		52 (Syb2 <sup>WT</sup> )	277 (Munc18-1 <sup>WT</sup> )	18.4 Å
		52 (Syb2 <sup>WT</sup> )	308 (Munc18-1 <sup>WT</sup> )	21.6 Å
52 (Syb2 <sup>WT</sup> )	314 (Munc18-1 <sup>WT</sup> )	16.2 Å		

## Appendix

		52 (Syb2 <sup>WT</sup> )	321 (Munc18-1 <sup>WT</sup> )	21.1 Å
		52 (Syb2 <sup>WT</sup> )	332 (Munc18-1 <sup>WT</sup> )	13.5 Å
		59 (Syb2 <sup>WT</sup> )	314 (Munc18-1 <sup>WT</sup> )	14.5 Å
<b>4.38 B)</b>	Syb2 <sup>WT</sup> (1-96) Munc18-1 <sup>D326K</sup> (2-594)	52 (Syb2 <sup>WT</sup> )	20 (Munc18-1 <sup>D236K</sup> )	40.0 Å
		52 (Syb2 <sup>WT</sup> )	92 (Munc18-1 <sup>D236K</sup> )	56.2 Å
		52 (Syb2 <sup>WT</sup> )	120 (Munc18-1 <sup>D236K</sup> )	62.9 Å
		52 (Syb2 <sup>WT</sup> )	125 (Munc18-1 <sup>D236K</sup> )	57.9 Å
		52 (Syb2 <sup>WT</sup> )	277 (Munc18-1 <sup>D236K</sup> )	18.1 Å
		52 (Syb2 <sup>WT</sup> )	308 (Munc18-1 <sup>D236K</sup> )	22.0 Å
		52 (Syb2 <sup>WT</sup> )	314 (Munc18-1 <sup>D236K</sup> )	16.5 Å
		52 (Syb2 <sup>WT</sup> )	321 (Munc18-1 <sup>D236K</sup> )	21.5 Å
		52 (Syb2 <sup>WT</sup> )	D326K (Munc18-1 <sup>D236K</sup> )	20.1 Å
		52 (Syb2 <sup>WT</sup> )	332 (Munc18-1 <sup>D236K</sup> )	13.3 Å
		52 (Syb2 <sup>WT</sup> )	333 (Munc18-1 <sup>D236K</sup> )	12.8 Å
		52 (Syb2 <sup>WT</sup> )	339 (Munc18-1 <sup>D236K</sup> )	12.8 Å
		59 (Syb2 <sup>WT</sup> )	277 (Munc18-1 <sup>D236K</sup> )	15.9 Å
		59 (Syb2 <sup>WT</sup> )	314 (Munc18-1 <sup>D236K</sup> )	14.3 Å
		59 (Syb2 <sup>WT</sup> )	321 (Munc18-1 <sup>D236K</sup> )	26.3 Å
		83 (Syb2 <sup>WT</sup> )	294 (Munc18-1 <sup>D236K</sup> )	19.1 Å
		91 (Syb2 <sup>WT</sup> )	125 (Munc18-1 <sup>D236K</sup> )	78.1 Å
<b>4.39 B)</b>	Syb2 <sup>WT</sup> (1-96) Munc18-1 <sup>WT</sup> (2-594) Stx1B <sup>WT</sup> (25-252)	52 (Syb2 <sup>WT</sup> )	120 (Munc18-1 <sup>WT</sup> )	63.1 Å
		52 (Syb2 <sup>WT</sup> )	125 (Munc18-1 <sup>WT</sup> )	58.1 Å
		52 (Syb2 <sup>WT</sup> )	308 (Munc18-1 <sup>WT</sup> )	19.5 Å
		52 (Syb2 <sup>WT</sup> )	314 (Munc18-1 <sup>WT</sup> )	15.4 Å
		52 (Syb2 <sup>WT</sup> )	321 (Munc18-1 <sup>WT</sup> )	11.4 Å
		52 (Syb2 <sup>WT</sup> )	87 (Stx1B <sup>WT</sup> )	22.5 Å
		54 (Stx1B <sup>WT</sup> )	526 (Munc18-1 <sup>WT</sup> )	44.9 Å

## Appendix

		54 (Stx1B <sup>WT</sup> )	314 (Munc18-1 <sup>WT</sup> )	19.7 Å
		55 (Stx1B <sup>WT</sup> )	526 (Munc18-1 <sup>WT</sup> )	46.2 Å
		91 (Stx1B <sup>WT</sup> )	332 (Munc18-1 <sup>WT</sup> )	25.0 Å
		93 (Stx1B <sup>WT</sup> )	321 (Munc18-1 <sup>WT</sup> )	31.4 Å
		93 (Stx1B <sup>WT</sup> )	332 (Munc18-1 <sup>WT</sup> )	21.7 Å
		116 (Stx1B <sup>WT</sup> )	333 (Munc18-1 <sup>WT</sup> )	29.5 Å
		139 (Stx1B <sup>WT</sup> )	314 (Munc18-1 <sup>WT</sup> )	10.3 Å
		139 (Stx1B <sup>WT</sup> )	321 (Munc18-1 <sup>WT</sup> )	25.2 Å
		139 (Stx1B <sup>WT</sup> )	333 (Munc18-1 <sup>WT</sup> )	19.4 Å
		139 (Stx1B <sup>WT</sup> )	339 (Munc18-1 <sup>WT</sup> )	18.1 Å
		139 (Stx1B <sup>WT</sup> )	343 (Munc18-1 <sup>WT</sup> )	21.9 Å
		139 (Stx1B <sup>WT</sup> )	526 (Munc18-1 <sup>WT</sup> )	44.7 Å
		203 (Stx1B <sup>WT</sup> )	332 (Munc18-1 <sup>WT</sup> )	23.3 Å
		203 (Stx1B <sup>WT</sup> )	333 (Munc18-1 <sup>WT</sup> )	20.3 Å
		251 (Stx1B <sup>WT</sup> )	92 (Munc18-1 <sup>WT</sup> )	26.5 Å
		251 (Stx1B <sup>WT</sup> )	120 (Munc18-1 <sup>WT</sup> )	36.7 Å
<b>4.40 C)</b>	Stx1B <sup>WT</sup> (25-252) Munc18-1 <sup>WT</sup> (2-594)	54 (Stx1B <sup>WT</sup> )	314 (Munc18-1 <sup>WT</sup> )	19.7 Å
		54 (Stx1B <sup>WT</sup> )	526 (Munc18-1 <sup>WT</sup> )	45.9 Å
		91 (Stx1B <sup>WT</sup> )	332 (Munc18-1 <sup>WT</sup> )	25.0 Å
		93 (Stx1B <sup>WT</sup> )	332 (Munc18-1 <sup>WT</sup> )	21.7 Å
		116 (Stx1B <sup>WT</sup> )	332 (Munc18-1 <sup>WT</sup> )	26.9 Å
		116 (Stx1B <sup>WT</sup> )	63 (Munc18-1 <sup>WT</sup> )	20.4 Å
		125 (Stx1B <sup>WT</sup> )	20 (Munc18-1 <sup>WT</sup> )	18.4 Å
		139 (Stx1B <sup>WT</sup> )	308 (Munc18-1 <sup>WT</sup> )	18.7 Å
		139 (Stx1B <sup>WT</sup> )	314 (Munc18-1 <sup>WT</sup> )	10.3 Å
		139 (Stx1B <sup>WT</sup> )	321 (Munc18-1 <sup>WT</sup> )	25.2 Å
		139 (Stx1B <sup>WT</sup> )	332 (Munc18-1 <sup>WT</sup> )	21.9 Å
		139 (Stx1B <sup>WT</sup> )	333 (Munc18-1 <sup>WT</sup> )	19.4 Å

## Appendix

		139 (Stx1B <sup>WT</sup> )	339 (Munc18-1 <sup>WT</sup> )	18.1 Å
		139 (Stx1B <sup>WT</sup> )	343 (Munc18-1 <sup>WT</sup> )	21.9 Å
		139 (Stx1B <sup>WT</sup> )	526 (Munc18-1 <sup>WT</sup> )	44.7 Å
		203 (Stx1B <sup>WT</sup> )	321 (Munc18-1 <sup>WT</sup> )	27.3 Å
		203 (Stx1B <sup>WT</sup> )	332 (Munc18-1 <sup>WT</sup> )	23.3 Å
		203 (Stx1B <sup>WT</sup> )	333 (Munc18-1 <sup>WT</sup> )	20.3 Å
		251 (Stx1B <sup>WT</sup> )	98 (Munc18-1 <sup>WT</sup> )	19.1 Å
		251 (Stx1B <sup>WT</sup> )	120 (Munc18-1 <sup>WT</sup> )	36.7 Å
		251 (Stx1B <sup>WT</sup> )	20 (Munc18-1 <sup>WT</sup> )	34.2 Å
		251 (Stx1B <sup>WT</sup> )	308 (Munc18-1 <sup>WT</sup> )	57.3 Å
		251 (Stx1B <sup>WT</sup> )	356 (Munc18-1 <sup>WT</sup> )	55.7 Å
		251 (Stx1B <sup>WT</sup> )	584 (Munc18-1 <sup>WT</sup> )	51.1 Å
		251 (Stx1B <sup>WT</sup> )	92 (Munc18-1 <sup>WT</sup> )	26.5 Å
<b>4.41 D)</b>	Stx1B <sup>L221P</sup> (25-252) Munc18-1 <sup>WT</sup> (2-594)	54 (Stx1B <sup>L221P</sup> )	314 (Munc18-1 <sup>WT</sup> )	19.7 Å
		55 (Stx1B <sup>L221P</sup> )	526 (Munc18-1 <sup>WT</sup> )	46.2 Å
		116 (Stx1B <sup>L221P</sup> )	332 (Munc18-1 <sup>WT</sup> )	26.9 Å
		116 (Stx1B <sup>L221P</sup> )	333 (Munc18-1 <sup>WT</sup> )	29.5 Å
		116 (Stx1B <sup>L221P</sup> )	339 (Munc18-1 <sup>WT</sup> )	21.2 Å
		125 (Stx1B <sup>L221P</sup> )	120 (Munc18-1 <sup>WT</sup> )	44.1 Å
		139 (Stx1B <sup>L221P</sup> )	308 (Munc18-1 <sup>WT</sup> )	18.7 Å
		139 (Stx1B <sup>L221P</sup> )	314 (Munc18-1 <sup>WT</sup> )	10.3 Å
		139 (Stx1B <sup>L221P</sup> )	321 (Munc18-1 <sup>WT</sup> )	25.2 Å
		139 (Stx1B <sup>L221P</sup> )	333 (Munc18-1 <sup>WT</sup> )	19.4 Å
		139 (Stx1B <sup>L221P</sup> )	339 (Munc18-1 <sup>WT</sup> )	18.1 Å
		139 (Stx1B <sup>L221P</sup> )	343 (Munc18-1 <sup>WT</sup> )	21.9 Å
		203 (Stx1B <sup>L221P</sup> )	321 (Munc18-1 <sup>WT</sup> )	27.3 Å
		203 (Stx1B <sup>L221P</sup> )	332 (Munc18-1 <sup>WT</sup> )	23.3 Å
		203 (Stx1B <sup>L221P</sup> )	333 (Munc18-1 <sup>WT</sup> )	20.3 Å

## Appendix

		251 (Stx1B <sup>L221P</sup> )	98 (Munc18-1 <sup>WT</sup> )	19.1 Å
		251 (Stx1B <sup>L221P</sup> )	120 (Munc18-1 <sup>WT</sup> )	36.7 Å
		251 (Stx1B <sup>L221P</sup> )	125 (Munc18-1 <sup>WT</sup> )	30.7 Å
		251 (Stx1B <sup>L221P</sup> )	321 (Munc18-1 <sup>WT</sup> )	54.6 Å
		251 (Stx1B <sup>L221P</sup> )	356 (Munc18-1 <sup>WT</sup> )	55.7 Å
		251 (Stx1B <sup>L221P</sup> )	92 (Munc18-1 <sup>WT</sup> )	26.5 Å
<b>4.41 E)</b>	Stx1B <sup>E210K</sup> (25-252) Munc18-1 <sup>WT</sup> (2-594)	54 (Stx1B <sup>E210K</sup> )	7 (Munc18-1 <sup>WT</sup> )	31.4 Å
		54 (Stx1B <sup>E210K</sup> )	314 (Munc18-1 <sup>WT</sup> )	19.7 Å
		87 (Stx1B <sup>E210K</sup> )	356 (Munc18-1 <sup>WT</sup> )	47.0 Å
		91 (Stx1B <sup>E210K</sup> )	332 (Munc18-1 <sup>WT</sup> )	25.0 Å
		93 (Stx1B <sup>E210K</sup> )	321 (Munc18-1 <sup>WT</sup> )	31.4 Å
		93 (Stx1B <sup>E210K</sup> )	332 (Munc18-1 <sup>WT</sup> )	21.7 Å
		116 (Stx1B <sup>E210K</sup> )	294 (Munc18-1 <sup>WT</sup> )	38.8 Å
		116 (Stx1B <sup>E210K</sup> )	332 (Munc18-1 <sup>WT</sup> )	26.9 Å
		116 (Stx1B <sup>E210K</sup> )	339 (Munc18-1 <sup>WT</sup> )	21.2 Å
		125 (Stx1B <sup>E210K</sup> )	120 (Munc18-1 <sup>WT</sup> )	44.1 Å
		139 (Stx1B <sup>E210K</sup> )	7 (Munc18-1 <sup>WT</sup> )	30.6 Å
		139 (Stx1B <sup>E210K</sup> )	314 (Munc18-1 <sup>WT</sup> )	10.3 Å
		139 (Stx1B <sup>E210K</sup> )	321 (Munc18-1 <sup>WT</sup> )	25.2 Å
		139 (Stx1B <sup>E210K</sup> )	332 (Munc18-1 <sup>WT</sup> )	21.9 Å
		139 (Stx1B <sup>E210K</sup> )	333 (Munc18-1 <sup>WT</sup> )	19.4 Å
		139 (Stx1B <sup>E210K</sup> )	339 (Munc18-1 <sup>WT</sup> )	18.1 Å
		139 (Stx1B <sup>E210K</sup> )	343 (Munc18-1 <sup>WT</sup> )	21.8 Å
		139 (Stx1B <sup>E210K</sup> )	526 (Munc18-1 <sup>WT</sup> )	44.7 Å
		188 (Stx1B <sup>E210K</sup> )	332 (Munc18-1 <sup>WT</sup> )	42.2 Å
		203 (Stx1B <sup>E210K</sup> )	321 (Munc18-1 <sup>WT</sup> )	27.3 Å
		203 (Stx1B <sup>E210K</sup> )	332 (Munc18-1 <sup>WT</sup> )	23.3 Å
		203 (Stx1B <sup>E210K</sup> )	333 (Munc18-1 <sup>WT</sup> )	20.3 Å

## Appendix

		251 (Stx1B <sup>E210K</sup> )	98 (Munc18-1 <sup>WT</sup> )	19.1 Å
		251 (Stx1B <sup>E210K</sup> )	120 (Munc18-1 <sup>WT</sup> )	36.7 Å
		251 (Stx1B <sup>E210K</sup> )	356 (Munc18-1 <sup>WT</sup> )	55.7 Å
		251 (Stx1B <sup>E210K</sup> )	584 (Munc18-1 <sup>WT</sup> )	51.1 Å
		251 (Stx1B <sup>E210K</sup> )	92 (Munc18-1 <sup>WT</sup> )	26.5 Å
<b>Appendix Fig. 30 A)</b>	Syb2 <sup>R30K</sup> (1-96) Munc13-MUN (859-1531, Δ1408-1452)	52 (Syb2 <sup>R30K</sup> )	978 (Munc13-MUN)	132.5 Å
		52 (Syb2 <sup>R30K</sup> )	1025 (Munc13-MUN)	126.4 Å
		52 (Syb2 <sup>R30K</sup> )	1043 (Munc13-MUN)	107.5 Å
		52 (Syb2 <sup>R30K</sup> )	1162 (Munc13-MUN)	84.7 Å
		52 (Syb2 <sup>R30K</sup> )	1248 (Munc13-MUN)	75.2 Å
		52 (Syb2 <sup>R30K</sup> )	1291 (Munc13-MUN)	38.4 Å
		52 (Syb2 <sup>R30K</sup> )	1311 (Munc13-MUN)	60.3 Å
		83 (Syb2 <sup>R30K</sup> )	1428 (Munc13-MUN)	21.5 Å
<b>Appendix Fig. 30 B)</b>	Syb2 <sup>A3K</sup> (1-96) Munc13-MUN (859-1531, Δ1408-1452)	52 (Syb2 <sup>A3K</sup> )	978 (Munc13-MUN)	132.5 Å
		52 (Syb2 <sup>A3K</sup> )	1025 (Munc13-MUN)	126.4 Å
		52 (Syb2 <sup>A3K</sup> )	1147 (Munc13-MUN)	92.8 Å
		52 (Syb2 <sup>A3K</sup> )	1162 (Munc13-MUN)	84.7 Å
		52 (Syb2 <sup>A3K</sup> )	1248 (Munc13-MUN)	75.2 Å
		52 (Syb2 <sup>A3K</sup> )	1419 (Munc13-MUN)	45.0 Å
		83 (Syb2 <sup>A3K</sup> )	1482 (Munc13-MUN)	21.5 Å



## 8. References

1. R. Eckert, D.R., G. Augustine, *Tierphysiologie*. Vol. 2. 1993, Stuttgart, New York: Gerog Thieme Verlag. 724.
2. E. R. Kandel, J.H.S., T. M. Jessel, S. A. Siegelbaum, A. J. Hudspeth, *Principles of Neural Science*. Vol. 5th ed. 2013: McGraw-Hill Education.
3. B. Alberts, A.J., J. Lewis, M. Raff, K. Roberts, P. Walter, *Molecular Biology of the Cell*. Vol. 6th ed. 2014: Garland Science.
4. K. Munk, K.R., *Grundstudium Biologie - Zoologie*. 2002, Heidelberg, Berlin: Spektrum Akademischer Verlag GmbH. 28.
5. B. W. Connors, M.A.L., *Electrical synapses in the mammalian brain*. Annual Review of Neuroscience, 2004. **27**: p. 393 - 418.
6. M. Bennett, D.A.G., *Gap junctions, electrotonic coupling, and intercellular communication*. Neuroscience Research Program Bulletin, 1978. **16**(3): p. 1-486.
7. E. A. Pereda, *Electrical synapses and their functional interactions with chemical synapses*. Nat. Rev. Neurosci., 2014. **15**(4): p. 250-263.
8. J. E. Rash, K.G.V., N. Kamasawa, *Molecular and functional asymmetry at a vertebrate electrical synapse*. Neuron, 2013. **79**(5): p. 957-969.
9. M. Bennett, R.S.Z., *Electrical coupling and neuronal synchronization in the Mammalian brain*. Neuron, 2004. **41**(4): p. 495-511.
10. BioRender. 2024; Available from: [www.biorender.com](http://www.biorender.com).
11. T. C. Südhof, *Neurotransmitter release: the last millisecond in the life of a synaptic vesicle*. Neuron, 2013. **80**(3): p. 675-690.
12. D. L. Nelson, M.M.C., *Lehninger Principles of Biochemistry*. 7th Edition ed. 2017, New York: W. H. Freeman. 1328.
13. J. Del Castillo, B.K., *Quantal components of the end-plate potential*. J. Physiol., 1954. **123**: p. 560-573.
14. B. Katz, *Quantal mechanism of neural transmitter release*. Science, 1971. **173**: p. 123-125.
15. E. F. Stanley, *The calcium channel and the organization of the presynaptic transmitter release face*. Trends in Neurosciences, 1997. **20**: p. 404-409.
16. T. C. Südhof, *The presynaptic active zone*. Neuron, 2012. **75**: p. 11-25.
17. V. Haucke, E.N., S. J. Sigrist, *Protein scaffolds in the coupling of synaptic exocytosis and endocytosis*. Nat. Rev. Neuroscience, 2011. **12**: p. 127-138.
18. Z. H. Sheng, R.E.W., W. A. Catterall, *Physical link and functional coupling of presynaptic calcium channels and the synaptic vesicle docking/fusion machinery*. J. Bioenerg. Biomembr., 1998. **30**: p. 335-345.
19. T. Schikorski, C.F.S., *Morphological correlates of functionally defined synaptic vesicle populations*. Nat. Neurosci., 2001. **4**: p. 391-395.

## References

---

20. F. Schimmoller, I.S., S. R. Pfeffer, *GTPases, directors of vesicle docking*. J. Biol. Chem., 1998. **273**: p. 22161-22164.
21. I. Dulubova, X.L., J. Lu, I. Huryeva, A. Alam, R. Schneggenburger, T. C. Südhof, J. Rizo, *Munc13/RIM/Rab3 tripartite complex: from priming to plasticity?* EMBO J., 2005. **24**: p. 2839-2850.
22. A. G. Leenders, F.H.L.d.S., W. E. Ghijsen, M. Verhage,, *Rab3a is involved in transport of synaptic vesicles to the active zone in mouse brain nerve terminals*. Mol. Biol. Cell., 2001. **12**: p. 3095-3102.
23. O. M. Schluter, F.S., R. Jahn, C. Rosenmund, T. C. Südhof, *A complete genetic analysis of neuronal Rab3 function*. J. Neurosci., 2004. **24**: p. 6629-6637.
24. S. Nofal, U.B., D. Hof, U. Matti, J. Rettig, *Primed vesicles can be distinguished from docked vesicles by analyzing their mobility*. J. Neurosci., 2007. **27**: p. 1386-1395.
25. K. M. Misura, R.H.S., W. I. Weis, *Three-dimensional structure of the neuronal-Sec1-syntaxin 1a complex*. Nature, 2000. **404**: p. 355-362.
26. D. Kummel, S.S.K., D. T. Radoff, F. Li, C. G. Giraudo, F. Pincet, J. E. Rothman, K. M. Reinisch *Complexin cross-links prefusion SNAREs into a zigzag array*. Nat. Struct. Mol. Biol., 2011. **18**: p. 927-933.
27. K. D. Brewer, T.B., A. Cavalli, C. Camilloni, J. D. Swarbrick, J. Liu, A. Zhou, P. Zhou, N. Barlow, J. Xu, A. B. Seven, E. A. Prinslow, R. Voleti, D. Haussinger, A. M. Bonvin, D. R. Tomchick, M. Vendruscolo, B. Graham, T. C. Südhof, J. Rizo, *Dynamic binding mode of a Synaptotagmin-1-SNARE complex in solution*. Nat. Struct. Mol. Biol., 2015. **22**: p. 555-564.
28. Q. Zhou, Y.L., T. Bacaj, M. Zhao, A. Y. Lyubimov, M. Uervirojnangkoorn, O. B. Zeldin, A. S. Brewster, N. K. Sauter, A. E. Cohen, S. M. Soltis, R. Alonso-Mori, M. Chollet, H. T. Lemke, R. A. Pfuetzner, U. B. Choi, W. I. Weis, J. Diao, T. C. Südhof, A. T. Brunger, *Architecture of the synaptotagmin-SNARE machinery for neuronal exocytosis*. Nature, 2015. **525**: p. 62-67.
29. M. Zhao, S.W., Q. Zhou, S. Vivona, D. J. Cipriano, Y. Cheng, A. T. Brunger, *Mechanistic insights into the recycling machine of the SNARE complex*. Nature, 2015. **518**: p. 61-67.
30. R. Mohrmann, H.d.W., M. Verhage, E. Neher, J. B. Sorensen, *Fast vesicle fusion in living cells requires at least three SNARE complexes*. Science, 2010. **330**.
31. G. van den Bogaart, M.G.H., G. Bunt, D. Riedel, F. S. Wouters, R. Jahn, *One SNARE complex is sufficient for membrane fusion*. Nat. Struct. Mol. Biol., 2010. **17**.
32. *The Nobel Prize in Physiology or Medicine 2013*. 2013 [cited 2013 October 7].
33. D. Ungar, F.M.H., *SNARE Protein Structure and Function*. Annual Review of Cell and Developmental Biology, 2003. **19**: p. 493-517.
34. J. A. Williams, D.I.Y., *Physiology of the Gastrointestinal Tract - Stimulus-secretion Coupling in Pancreatic Acinar Cells*. 5 ed. 2012: ebook.
35. G. Karp, *Cell and Molecular Biology*. 4 ed. 2002: John Wiley & Sons. 866.
36. R. Flaumenhaft, *Molecular Basis of Platelet Granule Secretion*. Arteriosclerosis, Thrombosis, and Vascular Biology, 2003. **23**(7): p. 1152-1160.
37. S. Martens, H.T.M., *Mechanisms of membrane fusion: disparate players and common principles*. Nat. Rev. Mol. Cell Bio., 2008. **9**: p. 543-556.

## References

---

38. R. Jahn, R.H.S., *SNAREs—engines for membrane fusion*. Nat. Rev. Mol. Cell Bio., 2006. **7**(9): p. 631-643.
39. T. C. Südhof, J.E.R., *Membrane fusion: grappling with SNARE and SM proteins*. Science, 2009. **323**(5913): p. 474-477.
40. J. Rizo, T.C.S., *The membrane fusion enigma: SNAREs, Sec1/Munc18 proteins, and their accomplices—guilty as charged?* Annual Review of Cell and Developmental Biology, 2012. **28**: p. 279-308.
41. L. V. Chernomordik, M.M.K., *Mechanics of membrane fusion*. Nat. Struct. Mol. Biol., 2008. **15**(7): p. 675-683.
42. Y. A. C., R. H. Scheller, *SNARE-mediated membrane fusion*. Nat. Rev. Mol. Cell Bio., 2001. **2**: p. 98-106.
43. B. Liang, V.K., L. K. Tamm, *Prefusion structure of syntaxin-1A suggests pathway for folding into neuronal trans-SNARE complex fusion intermediate*. Proc. Natl. Acad. Sci., 2013. **110**(48): p. 19384-19389.
44. R. B. Sutton, D.F., R. Jahn, A. T. Brunger, *Crystal structure of a SNARE complex involved in synaptic exocytosis at 2.4 Å resolution*. Nature, 1998. **395**: p. 347-353.
45. A. Stein, G.-W., M. C. Wahl, R. Jahn, *Helical extension of the neuronal SNARE complex into the membrane*. Nature, 2009. **460**: p. 525-528.
46. D. Fasshauer, B.R.S., A. T. Brunger, R. Jahn, *Conserved structural features of the synaptic fusion complex: SNARE proteins reclassified as Q- and R-SNAREs*. Proc. Natl. Acad. Sci., 1998. **95**(26): p. 15781-15786.
47. Y. Lai, J.D., D. J. Cipriano, Y. Zhang, R. A. Pfuetzner, *Complexin inhibits spontaneous release and synchronizes Ca<sup>2+</sup>-triggered synaptic vesicle fusion by distinct mechanisms*. eLife, 2014. **3**(e03756).
48. N. Arora, T.F.J.M., *Decision to enter the secretory pathway: More than 20S or not 20S?* Nat. Cell Bio., 2013. **15**(4): p. 365-367.
49. D. Deak, Y.X., W. P. Chang, I. Dulubova, M. Khvotchev, X- Liu, T. C. Südhof, J. Rizo, *Munc18-1 binding to the neuronal SNARE complex controls synaptic vesicle priming*. J. Cell. Biol., 2009. **184**(4): p. 751-764.
50. R. Guan, H.D., J. Rizo, M. U. N. Binding, *Atomic structure of the syntaxin–SNAP-25–1 interaction complex*. Nature, 2008. **385**(15): p. 889-893.
51. J. Shen, D.C.T., F. Paumet, J. E. Rothman, T. J. Mella, *Selective activation of cognate SNAREpins by Sec1/Munc18 proteins*. Cell, 2007. **128**(1): p. 183-195.
52. T. Mishima, T.F., M. Sanada, T. Kofuji, M. Kanai-Azuma, K. Akagawa, *Syntaxin 1B, but Not Syntaxin 1A, Is Necessary for the Regulation of Synaptic Vesicle Exocytosis and of the Readily Releasable Pool at Central Synapses*. PLOS One, 2014. **9**(2): p. e90004.
53. J. Skolnick, M.G., H. Zhou, S. Singh, *AlphaFold 2: Why It Works and Its Implications for Understanding the Relationships of Protein Sequence, Structure, and Function*. J. Chem. Inf. Model, 2021. **61**(10): p. 4827-4831.
54. G. van den Bogaart, K.M., H. J. Risselada, ..., U. Diederichsen, R. Jahn, *Membrane protein sequestering by ionic protein-lipid interactions*. Nature, 2011. **479**(7374): p. 552-555.

## References

---

55. T. M. Khuong, R.L.P.H., S. Kuenen, A. Witkowska, ..., R. Jahn, G. van den Bogaart, P. Verstreken, *Synaptic PI(3,4,5)P3 is required for Syntaxin1A clustering and neurotransmitter release*. *Neuron*, 2013. **77**(6): p. 1097-1108.
56. R. Kang, J.W., P. Arstikaitis, H. Takahashi, ..., N. G. Davis, A. El-Husseini, *Neuronal palmitoyl-proteomics reveals dynamic synaptic palmitoylation*. *Nature*, 2008. **456**: p. 904-909.
57. G. R. Prescott, O.A.G., J. Greaves, L. H. Chamberlain, *Palmitoylation of the synaptic vesicle fusion machiner*. *Journal of Neurochemistry*, 2009. **110**: p. 1135-1149.
58. S. Blaskovic, M.B., F. G. van der Goot, *What does S-Palmitoylation do to membrane proteins?* *The FEBS Journal*, 2013. **280**: p. 2766-2774.
59. J. Charollais, F.G.v.d.G., *Palmitoylation of membrane proteins*. *Rev. Molec. Membr. Biol.*, 2009. **26**: p. 55-66.
60. D. H. Kweon, C.S.K., Y. K. Shin, *The membrane-dipped neuronal SNARE complex, a site directed spin labeling electron paramagnetic resonance study*. *Biochemistry*, 2002. **41**: p. 9264-9268.
61. C. S. Kim, D.H.K., Y. H. Shin, *Membrane topologies of neuronal SNARE folding intermediates*. *Biochemistry*, 2002. **41**(10928-10933).
62. D. Williams, J.V., I. Zaitsecam S. McLaughlin, J. E. Passin, *Evidence that electrostatic interactions between vesicle-associated membrane protein 2 and acidic phospholipids may modulate the fusion of transport vesicles with the plasma membrane*. *Mol. Biol. Cell.*, 2009. **20**: p. 4910-4919.
63. G. Vardar, A.S.-L., S. Zobel, T. Trimbuch, C. Rosenmund, *Syntaxin-1A modulates vesicle fusion in mammalian neurons via juxtamembrane domain dependent palmitoylation of its transmembrane domain*. *eLife*, 2022. **11**(e78182).
64. V. J. Starai, C.M.H., W. Wickner, *HOPS proofreads the trans-SNARE complex for yeast vacuole fusion*. *Mol. Biol. Cell.*, 2008. **19**(6): p. 2500-2508.
65. Y. Gao, S.Z., G. Gunderson, Z. Xi, L. Ma, G. Sirinakis, J. E. Rothman, Y. Zhang, *Single Reconstituted Neuronal SNARE Complexes Zipper in Three Distinct Stages*. *Science*, 2012. **337**(6100): p. 1340-1343.
66. I. Dulubova, S.S., S. Hill, M. Hosaka, I. Fernandez, T. C. Südhof, J. Rizo, *A conformational switch in Syntaxin during exocytosis: Role of Munc18*. *EMBO J.*, 1999. **18**(6): p. 4372-4382.
67. G. Vardar, A.S.-L., M. Brockmann, M. Weber-Boyvat, S. Zobel, V. W. A. Kumbol, T. Trimbuch, C. Rosenmund, *Reexamination of N-terminal domains of syntaxin-1 in vesicle fusion from central murine synapses*. *eLife*, 2021. **10**(e69498).
68. M. Margittai, D.F., R. Jahn, R. Langen, *The Habc Domain and the SNARE Core Complex Are Connected by a Highly Flexible Linker*. *Biochemistry*, 2003. **42**(14): p. 4009-4014.
69. K. P. Stepien, J.X., X. Zhang, X. C. Bai, J. Rizo, *SNARE assembly enlightened by cryo-EM structures of a synaptobrevin–Munc18-1–syntaxin-1 complex*. *Sci. Adv.*, 2022. **8**(eabo5272).
70. S. Wang, U.B.C., J. Gong, X. Yang, Y. Li, A. L. Wang, X. Yang, A. T. Brunger, C. Ma, *Conformational change of syntaxin linker region induced by Munc13s initiates SNARE complex formation in synaptic exocytosis*. *EMBO J.*, 2017. **36**(6): p. 816-829.

## References

---

71. M. Verhage, A.S.M., J. J. Plomp, ..., H. J. Geuze, T. C. Südhof, *Synaptic Assembly of the Brain in the Absence of Neurotransmitter Secretion*. Science, 2000. **287**(5454): p. 864-869.
72. I. Dulubova, M.K., S. Liu, I. Huryeva, T. C. Südhof, J. Rizo, *Munc18-1 binds directly to the neuronal SNARE complex*. Proc. Natl. Acad. Sci., 2007. **104**(8): p. 2697-2702.
73. R. F. G. Toonen, K.W., M. S. Sons, ..., J. J. Plomp, M. Verhage, *Munc18-1 expression levels control synapse recovery by regulating readily releasable pool size*. PNAS, 2006. **103**(48): p. 18332-18337.
74. P. Zhou, Z.P.P., X. Yang, Y. Zhang, C. Rosenmund, T. Bacaj, T. C. Südhof, *Syntaxin-1 N-peptide and Habc-domain perform distinct essential functions in synaptic vesicle fusion*. EMBO J., 2013. **32**(1): p. 159-171.
75. I. C. Bark, K.M.H., A. E. Ryabinin, M. C. Wilson, *Differential expression of SNAP-25 protein isoforms during divergent vesicle fusion events of neural development*. Proc. Natl. Acad. Sci. U.S.A., 1995. **92**.
76. G. R. Prescott, L.H.C., *Regional and developmental brain expression patterns of SNAP25 splice variants*. BMC Neurosci., 2011. **12**(35).
77. E. R. Chapman, S.A., N. Barton, R. Jahn, *SNAP-25, a t-SNARE which binds to both syntaxin and synaptobrevin via domains that may form coiled coils*. J. Biol. Chem., 2003. **269**(44): p. 27427-27432.
78. J. B. Sørensen, G.N., F. Varoqueaux, ..., E. Neher, *Differential Control of the Releasable Vesicle Pools by SNAP-25 Splice Variants and SNAP-23*. Cell, 2003. **114**: p. 75-86.
79. G. Ahnert-Hilger, A.M.-W., M. Höltje, *Synaptic vesicle proteins: targets and routes for botulinum neurotoxins*. Curr. Top. Microbiol. Immunol., 2013. **364**: p. 159–177.
80. K. R. Aoki, B.G., *Botulinum toxin type A and other botulinum toxin serotypes: a comparative review of biochemical and pharmacological actions*. Eur. J. Neurol., 2001. **8**: p. 21-29.
81. D. Dawidowski, D.S.C., *Munc18-1 and the Syntaxin-1 N-terminus Regulate Open-Closed States in a t-SNARE complex*. Structure, 2016. **34**(3): p. 392-400.
82. D. Milovanovic, R.J., *Organization and dynamics of SNARE proteins in the presynaptic membrane*. Front. Physiol., 2015. **6**(89).
83. R. V. K. Sundaram, H.J., F. Li, ..., J. E. Rothman, S. S. Krishnakumar, *Munc13 binds and recruits SNAP25 to chaperone SNARE complex assembly*. FEBS Lett., 2023. **595**(3): p. 279-309.
84. M. Magdziarek, A.A.B., K. P. Stepien, B. Quade, X. Liu, J. Rizo, *Re-examining how Munc13-1 facilitates opening of syntaxin-1*. Protein Science, 2020. **29**: p. 1440-1458.
85. F. Antonucci, I.C., G. Fossati, R. Tomasoni, E. Menna, M. Matteoli, *SNAP-25, a Known Presynaptic Protein with Emerging Postsynaptic Functions*. Front. Synaptic Neurosci., 2016. **8**(7).
86. C. Verderio, D.P., E. Pravettoni, ..., M. Matteoli, *SNAP-25 modulation of calcium dynamics underlies differences in GABAergic and glutamatergic responsiveness to depolarization*. Neuron, 2004. **41**(4): p. 599-610.
87. G. Kochlamazashvili, V.H., *A dual role of SNAP-25 as carrier and guardian of synaptic transmission*. EMBO Rep., 2013. **14**: p. 579-580.

## References

---

88. S. B. Condliffe, I.C., D. Pozzi, C. Verderio, M. Matteoli, *SNAP-25 regulates native voltage-gated calcium channels in glutamatergic neurons*. J. Biol. Chem., 2010. **285**: p. 24968–24976.
89. Z. Zhang, D.W., T. Sun, ..., W. Shin, L. G. Wu, *The SNARE proteins SNAP25 and synaptobrevin are involved in endocytosis at hippocampal synapses*. J. Neurosci., 2013. **33**(22): p. 9169-9175.
90. M. C. Galas, S.C.-G., S. Dirrig-Grosch, M. F. Bader, *Presence of dynamin–syntaxin complexes associated with secretory granules in adrenal chromaffin cells*. J. Neurochem., 2000. **75**: p. 1511-1519.
91. M. Okamoto, S.S., T. C. Südhof, *EHSH1/intersectin, a protein that contains EH and SH3 domains and binds to dynamin and SNAP-25. A protein connection between exocytosis and endocytosis?* J. Biol. Chem., 1999. **274**: p. 18446-18454.
92. H. Zhang, S.Z., Y. Zhu, J. Chen, G. Zhang, H. Chang, *An association study between SNAP-25 gene and attention-deficit hyperactivity disorder*. Eur. J. Paediatr., 2011. **15**: p. 48-52.
93. P. M. Thompson, S.E., M. P. Vawter, *SNAP-25 reduction in the hippocampus of patients with schizophrenia*. Prog. Neuropsychopharmacol. Biol. Psychiatry, 2003. **27**(411-417).
94. B. Etain, A.D., F. Mathieu, ..., M. Leboyer, S. Jamain, *A SNAP25 promoter variant is associated with early-onset bipolar disorder and a high expression level in brain*. Mol. Psychiatr., 2010. **15**(7): p. 748-755.
95. V. Rossi, R.P., M. Vacca, ..., T. Galli, F. Filippini, *VAMP subfamilies identified by specific R-SNARE motifs*. Biol. Cell, 2004. **96**: p. 251-256.
96. Hong, W., *SNAREs and traffic*. Biochim. Biophys. Acta, 2005. **1744**: p. 120-144.
97. F. A. Meunier, N.H., D. Corbin, C. Hu, *Fusogenic pairings of vesicle-associated membrane proteins (VAMPs) and plasma membrane t-SNAREs – VAMP5 as the exception*. PLoS One, 2010. **5**.
98. D. Ivanova, K.L.D., A. Gajhiye, ..., M. Trost, M. A. Cousin, *Control of synaptic vesicle release probability via VAMP4 targeting to endolysosomes*. Sci. Adv., 2021. **7**(18): p. 1-21.
99. D. Ivanova, M.A.C., *Synaptic vesicle recycling and the endolysosomal system: A reappraisal of form and function*. Front. Synaptic Neurosci., 2022. **14**.
100. X. Tian, J.T., J. Chen, *New insights regarding SNARE proteins in autophagosome-lysosome fusion*. Autophagy, 2021. **17**(2680-2688).
101. R. J. Advani, B.Y., R. Prekeris, K. C. Lee, J. Klumperman, R. H. Scheller, *VAMP-7 mediates vesicular transport from endosomes to lysosomes*. J. Cell Biol., 1999. **146**(4): p. 765-776.
102. E. Morrison, T.W., A. E. Zuchetti, M. Alvaro-Benito, ..., B. Brügger, C. Hivroz, C. Freund, *Dynamic palmitoylation events following T-cell receptor signaling*. Nat. Comm. Biol., 2020. **3**(368): p. 1-9.
103. Z. P. Pang, T.C.S., *Cell biology of Ca<sup>2+</sup>-triggered exocytosis*. Curr. Opin. Cell Biol., 2010. **22**: p. 496-505.
104. Y. Liu, Y.S., W. Lin, *The role of Synaptobrevin1/VAMP1 in Ca<sup>2+</sup>-triggered neurotransmitter release at the mouse neuromuscular junction*. J. Physiol., 2011. **589**: p. 1603-1618.
105. S. Takamori, M.H., K. Stenius, ..., F. Wieland, R. Jahn, *Molecular anatomy of a trafficking organelle*. Cell, 2006. **127**(4): p. 831-846.

## References

---

106. S. Wittig, M.G., M. Barth, ..., R. Jahn, C. Schmidt, *Cross-linking mass spectrometry uncovers protein interactions and functional assemblies in synaptic vesicle membranes*. Nat. Commun., 2021. **12**(858).
107. N. A. Lakomek, H.Y., R. Jahn, A. Perez-Lara, *Structural dynamics and transient lipid binding of synaptobrevin-2 tune SNARE assembly and membrane fusion*. PNAS, 2019. **116**(18): p. 8699-8708.
108. J. Hazzard, T.C.S., J. Rizo, *NMR analysis of the structure of synaptobrevin and of its interaction with syntaxin*. J. Biomol. NMR, 1999. **14**: p. 203-207.
109. K. D. Brewer, W.L., B. E. Horne, J. Rizo, *Reluctance to membrane binding enables accessibility of the synaptobrevin SNARE motif for SNARE complex formation*. Proc. Natl Acad. Sci. USA, 2011. **108**: p. 12723-12728.
110. J. F. Ellena, B.L., M. Wiktor, A. Stein, D. S. Cafiso, R. Jahn, L. K. Tamm, *Dynamic structure of lipid-bound synaptobrevin suggests a nucleation-propagation mechanism for trans-SNARE complex formation*. Proc. Natl. Acad. Sci. U.S.A., 2009. **106**: p. 20306-20311.
111. B. Liang, D.D., J. F. Ellena, L. K. Tamm, D. S. Cafiso, *The SNARE Motif of Synaptobrevin Exhibits an Aqueous-Interfacial Partitioning That Is Modulated by Membrane Curvature*. Biochemistry, 2014. **53**(9): p. 1485-1494.
112. J. Han, K.P., D. Bruns, R. A. Bockmann, *Synaptobrevin transmembrane domain determines the structure and dynamics of the SNARE motif and the linker region*. Biochem. Biophys. Acta, 2016. **1858**(4): p. 855-865.
113. Y. Xu, F.Z., Z. Su, J. A. McNew, Y. K. Shin, *Hemifusion in SNARE-mediated membrane fusion*. Nat. Struct. Mol. Biol., 2005. **12**(5): p. 417-422.
114. E. Fdez, M.M.-S., M. Beard, P. Woodman, S. Hilfiker, *Transmembrane-domain determinants for SNARE-mediated membrane fusion*. J. Cell Sci., 2010. **123**(14): p. 1473-1280.
115. S. S. Rathore, Y.L., H. Yu, ..., M. H. B. Stowell, J. Shen, *Intracellular Vesicle Fusion Requires a Membrane-Destabilizing Peptide Located at the Juxtamembrane Region of the v-SNARE*. Cell Rep., 2019. **29**(13): p. 4583-4592.
116. J. A. McNew, T.W., F. Parlati, R. J. Johnston, T. J. Melia, T. H. Söllner, J. E. Rothman, *Close is not enough: SNARE-dependent membrane fusion requires an active mechanism that transduces force to membrane anchors*. J. Cell. Biol., 2000. **150**(1): p. 105-117.
117. J. Hesselbarth, C.S., *Disorder-to-order transition of synaptobrevin-2: Tracing the conformational diversity of a synaptic SNARE protein*. J. Struct. Biol., 2021. **214**(1): p. 107824.
118. Gundersen, C.B., *A membrane-fusion model that exploits a  $\beta$ -to- $\alpha$  transition in the hydrophobic domains of syntaxin 1A and synaptobrevin 2*. Int. J. Mol. Sci., 2017. **18**(7): p. 1582.
119. L. N. Carpp, L.F.C., S. G. Shanks, A. Boyd, N. J. Bryant, *The Sec1p/Munc18 protein Vps45p binds its cognate SNARE proteins via two distinct modes*. J. Cell Biol., 2006. **173**(6): p. 927-936.
120. C. Yan, J.J., Y. Yang, X. Geng, W. Dong, *The function of VAMP2 in mediating membrane fusion: An overview*. Front. Mol. Neurosci., 2022. **16**: p. 1-15.
121. T. L. Rodkey, S.L., M. Barry, J. A. McNew, *Munc18a scaffolds SNARE assembly to promote membrane fusion*. Mol. Biol. Cell., 2008. **19**(12): p. 5422-5434.

## References

---

122. R. W. Baker, P.D.J., M. Zick, B. P. Phillips, W. T. Wickner, F. M. Hughson, *A direct role for the Sec1/Munc18-family protein Vps33 as a template for SNARE assembly*. *Science*, 2015. **349**(6252): p. 1111-1114.
123. S. Wang, Y.L., J. Gong, S. Ye, X. Yang, R. Zhang, C. Ma, *Munc18 and Munc13 serve as a functional template to orchestrate neuronal SNARE complex assembly*. *Nat. Commun.*, 2019. **10**(1).
124. T. André, J.C., P. Brenner, ..., M. Verhage, T. H. Söllner, *The Interaction of Munc18-1 Helix 11 and 12 with the Central Region of the VAMP2 SNARE Motif Is Essential for SNARE Templating and Synaptic Transmission*. *eNeuro*, 2020. **7**(6): p. 1-15.
125. A. Munch, G.H.K., J. R. T. van Weering, ..., T. H. Söllner, M. Verhage, J. B. Sørensen, *Extension of Helix 12 in Munc18-1 Induces Vesicle Priming*. *J. Neurosci.*, 2016. **36**(26): p. 6881-6891.
126. D. Parisotto, M.P., A. Scheutzow, ..., I. Sining, T. H. Söllner, *An extended helical conformation in domain 3a of Munc18-1 provides a template for SNARE (soluble N-ethylmaleimide-sensitive factor attachment protein receptor) complex assembly*. *J. Biol. Chem.*, 2014. **289**(14): p. 9639-9650.
127. E. Sitarska, J.X., S. Park, ..., S. Sugita, J. Rizo, *Autoinhibition of Munc18-1 modulates synaptobrevin binding and helps to enable Munc13-dependent regulation of membrane fusion*. *eLife*, 2017. **6**(e24278).
128. C. Ma, L.S., A. B. Seven, Y. Xu, J. Rizo, *Reconstitution of the vital functions of Munc18 and Munc13 in neurotransmitter release*. *Science*, 2013. **339**(6118): p. 421-425.
129. T. Shu, H.J., J. E. Rothman, Y. Zhang, *Munc13-1 MUN domain and Munc18-1 cooperatively chaperone SNARE assembly through a tetrameric complex*. *Proc. Natl Acad. Sci. USA*, 2020. **117**(2): p. 1036-1041.
130. K. P. Stepien, J.R., *Synaptotagmin-1-, Munc18-1-, and Munc13-1-dependent liposome fusion with a few neuronal SNAREs*. *Proc. Natl Acad. Sci. USA*, 2021. **118**(4).
131. E. A. Prinslow, K.P.S., Y. Z. Pan, J. Xu, J. Rizo, *Multiple factors maintain assembled trans-SNARE complexes in the presence of NSF and  $\alpha$ SNAP*. *eLife*, 2019(8:e38880).
132. Rizo, J., *Mechanism of neurotransmitter release coming into focus*. *Protein Science*, 2018. **27**(8): p. 1364-1391.
133. R. F. Toonen, M.V., *Munc18-1 in secretion: lonely Munc joins SNARE team and takes control*. *Trends in Neurosciences*, 2007. **30**(11): p. 564-572.
134. M. Cote, M.M.M., A. Burgess, ..., A. Fischer, G. de Saint Basile, *Munc18-2 deficiency causes familial hemophagocytic lymphohistiocytosis type 5 and impairs cytotoxic granule exocytosis in patient NK cells*. *J. Clin. Invest.*, 2009. **119**(12): p. 3765-3773.
135. J. L. Jewell, E.O., D. C. Thurmond, *Exocytosis mechanisms underlying insulin release and glucose uptake: conserved roles for Munc18c and syntaxin 4*. *Am. J. Physiol. Regul. Integr. Comp. Physiol.*, 2010. **298**: p. 517-531.
136. M. Pons-Vizcarra, J.K., B. Tawfik, J. B. Sørensen, J. R. T. van Weering, M. Verhage, *MUNC18-1 regulates the submembrane F-actin network, independently of syntaxin1 targeting, via hydrophobicity in  $\beta$ -sheet 10*. *J. Cell Sci.*, 2019. **132**(23).
137. J. K. Archbold, A.E.W., S.-H. Hu, B. M. Collins, J. L. Martin, *SNARE-ing the structures of Sec1/Munc18 proteins*. *Curr. Opin. Struc. Biol.*, 2014. **29**: p. 44-51.



## References

138. R. Kasula, Y.J.C., A. T. Bademosi, ..., A. Papadopoulos, F. A. Meunier, *The Munc18-1 domain 3a hinge-loop controls syntaxin-1A nanodomain assembly and engagement with the SNARE complex during secretory vesicle priming*. J. Cell Biol., 2016. **214**: p. 847-858.
139. G. A. Han, N.T.M., N. M. Saw, L. Li, L. Han, F. A. Meunier, B. M. Collins, S. Sugita, *Munc18-1 domain-1 controls vesicle docking and secretion by interacting with syntaxin-1 and chaperoning it to the plasma membrane*. Mol. Biol. Cell., 2011. **22**(21): p. 4134-4149.
140. P. Burkhardt, D.A.H., W. I. Weis, D. Fasshauer, *Munc18a controls SNARE assembly through its interaction with the syntaxin N-peptide*. EMBO J., 2008. **27**: p. 923-933.
141. X. Wang, J.G., L. Zhu, S. Wang, X. Yang, Y. Xu, X. Yang, C. Ma, *Munc13 activates the Munc18-1/syntaxin-1 complex and enables Munc18-1 to prime SNARE assembly*. EMBO J., 2020. **39**(16).
142. Y. Xu, L.S., J. Rizo, *Binding of Munc18-1 to synaptobrevin and the SNARE four-helix bundle*. Biochemistry, 2010. **49**: p. 1568-1576.
143. A. T. Brunger, U.B.C., Y. Lai, J. Leitz, K. I. White, Q. Zhou, *The pre-synaptic fusion machinery*. Curr. Opin. Cell Biol., 2019. **54**: p. 179-188.
144. S. Lee, J.S., Y. Jung, H. Son, J. Shin, C. Jeong, S.-H. Kweon, Y.-K. Shin, *Munc18-1 induces conformational changes of syntaxin-1 in multiple intermediates for SNARE assembly*. Sci. Rep., 2020. **10**(11623).
145. C. Ma, Y.X., J. Rizo, *Munc13 mediates the transition from the closed syntaxin-Munc18 complex to the SNARE complex*. Nat. Struct. Mol. Biol., 2011. **18**: p. 5442-549.
146. F. Tang, D.X., L. Chen, H. Gao, X. Li, *Role of Munc18-1 in the biological functions and pathogenesis of neurological disorders*. Mol. Med. Rep., 2021. **23**(3): p. 198.
147. A. Orock, S.L., F. Deak, *Munc18-1 haploinsufficiency impairs learning and memory by reduced synaptic vesicular release in a model of Ohtahara syndrome*. Mol. Cell Neurosci., 2018. **88**: p. 33-42.
148. B. P. Grone, M.M., K. R. Hamling, ..., M. Patel, S. C. Baraban, *Epilepsy, behavioral abnormalities, and physiological comorbidities in syntaxin-binding protein 1 (STXBP1) mutant Zebrafish*. PLOS One, 2016. **11**(3): p. e0151148.
149. L. Ortego-Moreno, B.G.G., A. Verdu, ..., J. M. Serratosa, R. Guerrero-Lopez, *Novel mutation in STXBP1 gene in a patient with non-lesional Ohtahara syndrome*. Neurologia, 2016. **31**(8): p. 523-527.
150. M. Meijer, T.C., R. F. Toonen, M. Vergage, *Synaptic Effects of Munc18-1 Alternative Splicing in Excitatory Hippocampal Neurons*. PLOS One, 2018. **13**(4): p. e0195470.
151. I. Augustin, C.R., T. C. Südhof, N. Brose, *Munc13-1 is essential for fusion competence of glutamatergic synaptic vesicles*. Nature, 1999. **400**: p. 457-461.
152. Brenner, S., *The Genetics of Caenorhabditis Elegans*. Genetics, 1974. **77**(1): p. 71-94.
153. H.-T. Chou, D.D., M. G. Chambers, K. M. Reinisch, T. Walz, *CATCHR, HOPS and CORVET tethering complexes share a similar architecture*. Nat. Struct. Mol. Biol., 2016. **23**: p. 761-763.
154. C. Santana-Molina, F.G., S. P. Devos, *Homology and Modular Evolution of CATCHR at the Origin of the Eukaryotic Endomembrane System*. Genome Biology and Evolution, 2021. **13**(7): p. evab125.

## References

---

155. M. Camacho, B.Q., T. Trimbuch, ..., Josep Rizo, Christian Rosenmund, *Control of neurotransmitter release by two distinct membrane-binding faces of the Munc13-1 C1C2B region*. eLife, 2021. **10**(e72030).
156. A. Betz, P.T., H. J. Junge, ..., C. Rosenmund, J. Rettig, N. Brose, *Functional interaction of the active zone proteins Munc13-1 and RIM1 in synaptic vesicle priming*. Neuron, 2001. **30**: p. 183-196.
157. M. Camacho, J.B., T. Trimbuch, ..., I. Dulubova, M. Abo-Rady, J. Rizo, C. Rosenmund, *Heterodimerization of Munc13 C2A domain with RIM regulates synaptic vesicle docking and priming*. Nat. Commun., 2017. **10**(8): p. 15293.
158. L. Deng, P.S.K., W. Xu, T. C. Südhof, *RIM proteins activate vesicle priming by reversing autoinhibitory homodimerization of Munc13*. Neuron, 2011. **69**: p. 317-331.
159. J. Lu, M.M., H. Dai, T. C. Südhof, D. R. Tomchick, J. Rizo, *Structural Basis for a Munc13-1 homodimer to Munc13-1/RIM heterodimer switch*. PLOS Biology, 2006. **4**(e192).
160. H. J. Junge, J.S.R., O. Jahn, ..., C. Rosenmund, N. Brose, *Calmodulin and Munc13 form a Ca<sup>2+</sup> sensor/effector complex that controls short-term synaptic plasticity*. Cell, 2004. **118**: p. 389-401.
161. J. Basu, A.B., N. Brose, C. Rosenmund, *Munc13-1 C1 domain activation lowers the energy barrier for synaptic vesicle fusion*. J. Neurosci., 2007. **27**: p. 1200-1210.
162. O.-H. Shin, J.L., J.-S. Rhee, D. R. Tomchick, ..., J. Rizo, C. Rosenmund, *Munc13 C2B domain is an activity-dependent Ca<sup>2+</sup> regulator of synaptic exocytosis*. Nat. Struct. Mol. Biol., 2010. **17**: p. 280-288.
163. B. Quade, M.C., X. Zhao, ..., C. Rosenmund, J. Rizo, *Membrane bridging by Munc13-1 is crucial for neurotransmitter release*. eLife, 2019. **8**(e42806).
164. J. Xu, M.C., V. Esser, ..., C. Ma, D. R. Tomchick, C. Rosenmund, J. Rizo, *Mechanistic insight into neurotransmitter release and presynaptic plasticity from the crystal structure of Munc13-1 C<sub>1</sub>-C<sub>2</sub>B-MUN*. eLife, 2017. **6**(e22567).
165. X. Liu, A.B.S., V. Esser, ..., C. Ma, C. Rosenmund, J. Rizo, *Functional synergy between the Munc13 C-terminal C1 and C2 domains*. eLife, 2016. **5**(e13696).
166. A. Betz, M.O., F. Benseler, N. Brose, *Direct interaction of the rat unc-13 homologue Munc13-1 with the N terminus of syntaxin*. J. Biol. Chem., 1997. **272**: p. 2520-2526.
167. X. Yang, S.W., Y. Sheng, ..., J. Rizo, R. Zhang, T. Xu, C. Ma, *Syntaxin Opening by the MUN Domain Underlies the Function of Munc13 in Synaptic Vesicle Priming*. Nat. Struct. Mol. Biol., 2015. **22**(7): p. 547-554.
168. Y. Lai, U.B.C., J. Leitz, ..., J. S. Rhee, A. T. Brunger, *Molecular Mechanisms of Synaptic Vesicle Priming by Munc13 and Munc18*. Neuron, 2017. **95**(3): p. 591-607.
169. H. Stamberger, M.N., M. H. Willemsen, ..., R. S. Möller, S. Weckhuysen, *STXBP1 encephalopathy - A neurodevelopmental disorder including epilepsy*. Neurology, 2016. **86**(10).
170. A. G. Engel, D.S., X.-M. Shen, M. Milone, C. M. Harper, *Loss of MUNC13-1 function causes microcephaly, cortical hyperexcitability, and fatal myasthenia*. Neurol. Genet., 2016. **2**(5).
171. M. Verhage, J.B.S., *SNAREopathies: Diversity in Mechanisms and Symptoms*. Neuron, 2020. **107**(1): p. 22-37.

## References

---

172. Kullmann, D.M., *Neurological channelopathies*. Annu. Rev. Neurosci., 2010. **33**: p. 161-172.
173. Grant, S.G., *Synaptopathies: diseases of the synaptome*. Curr. Opin. Neurobiol., 2012. **22**: p. 522-529.
174. Y. J. Chai, E.S., V. M. Tomatis, ..., B. M. Collins, Y. Gambin, F. A. Meunier, *Munc18-1 is a molecular chaperone for  $\alpha$ -synuclein, controlling its self-replicating aggregation*. J. Cell. Biol., 2016. **214**(6): p. 705-718.
175. N. G. L. Guiberson, A.P., D. Abramov, ..., J. S. Dittman, J. Burre, *Mechanism-based rescue of Munc18-1 dysfunction in varied encephalopathies by chemical chaperones*. Nature Communications, 2018. **9**(3986).
176. V. Salpietro, N.T.M., I. Llano-Rivas, ..., J. E. Rothman, S. S. Krishnakumar, H. Houlden, *Mutations in the Neuronal Vesicular SNARE VAMP2 Affect Synaptic Membrane Fusion and Impair Human Neurodevelopment*. Am. J. Hum. Genet., 2019. **104**(4): p. 721-730.
177. A. A. Rebane, B.W., L. Ma, ..., S. Krishnakurma, J. E. Rothman, Y. Zhang, *Two Disease-Causing SNAP-25B Mutations Selectively Impair SNARE C-terminal Assembly*. J. Mol. Biol., 2018. **430**(4): p. 479-490.
178. G. Vardar, F.G., X. J. Schmitt, P. Rautenstrauch, T. Trimbuch, J. Schubert, H. Lerche, C. Rosenmund, C. Freund, *Epilepsy-causing STX1B mutations translate altered protein functions into distinct phenotypes in mouse neurons*. Brain, 2020. **143**(7): p. 2119-2138.
179. Y.-J. Wu, R.T., M. Arancillo, ..., L. Tabares, C. Rosenmund, *Syntaxin 1B is important for mouse postnatal survival and proper synaptic function at the mouse neuromuscular junctions*. J. Neurophysiol., 2015. **114**(4): p. 2404-2417.
180. G. Vardar, S.C., M. Arancillo, Y.-J. Wu, T. Trimbuch, C. Rosenmund, *Distinct Functions of Syntaxin-1 in Neuronal Maintenance, Synaptic Vesicle Docking, and Fusion in Mouse Neurons*. J. Neurosci., 2016. **36**(30): p. 7911-7924.
181. J. Schubert, A.S., M. Langlois, ..., EruoEPINOMICS RES Consortium, H. Lerche, *Mutations in STX1B, encoding a presynaptic protein, cause fever-associated epilepsy syndromes*. Nature Genetics, 2014. **46**: p. 1327-1332.
182. S. Wolking, P.M., D. Mei, ..., H. Lerche, J. Schubert, *Clinical spectrum of STX1B-related epileptic disorders*. Neurology, 2019. **92**: p. 1238-1249.
183. K. M. Fiest, K.M.S., S. Wiebe, ..., D. L. Lorenzetti, N. Jetté, *Prevalence and incidence of epilepsy: A systematic review and meta-analysis of international studies*. Neurology, 2017. **88**(13): p. 296-303.
184. R. D. Thijs, R.S., T. J. O'Brien, J. W. Sander, *Epilepsy in adults*. The Lancet, 2019. **393**(10172): p. 689-701.
185. Staley, K., *Molecular mechanisms of epilepsy*. Nature neuroscience, 2015. **18**(3): p. 367-372.
186. Scharfman, H.E., *The Neurobiology of Epilepsy*. Current neurology and neuroscience reports, 2007. **7**(4): p. 348-354.
187. C. E. Stafstrom, E.H.K., *Epileptic Encephalopathy in Infants and Children*. Epilepsy Currents, 2016. **16**(4): p. 230-279.
188. C. A. Ellis, S.P., S. F. Berkovic, *Epilepsy genetics: clinical impacts and biological insights*. The Lancet Neurology, 2020. **19**(1): p. 93-100.

## References

---

189. C. E. Stafstrom, L.C., *Seizures and Epilepsy: An Overview for Neuroscientists*. Cold Spring Harbor perspectives in medicine, 2015. **5**(6).
190. A. Pitkänen, K.L., *Molecular and cellular basis of epileptogenesis in symptomatic epilepsy*. *Epilepsy Behav.* , 2009. **14**(1): p. 16-25.
191. B. J. Vorderwülbecke, B.W., Y. Weber, M. Holtkamp, *Genetic generalized epilepsies in adults — challenging assumptions and dogmas*. *Nature Reviews Neurology*, 2022. **18**: p. 71-83.
192. S. Khan, R.A.B., *Epileptic Encephalopathies: An Overview*. *Epilepsy Res. Treat.*, 2012. **2012**(403592).
193. Witkowska, A., *Study of SNARE-mediated membrane fusion with a novel single vesicle fusion assay*, in *School of Science*. 2016, Georg-August University. p. 1-148.
194. P. Atkins, J.d.P., *Elements of Physical Chemistry*. 4 ed. 2005: Oxford University Press.
195. K. Nakanishi, N.B., R. Woody, *Circular dichroism principles and applications*. 1994: VCH.
196. V. Hall, A.N., E. Hines, A. Rodgers, *Elucidating protein secondary structure with circular dichroism and a neural network*. *Journal of Computational Chemistry*, 2013. **34**(32): p. 2774-2786.
197. L. Whitmore, B.A.W., *Protein secondary structure analyses from circular dichroism spectroscopy: methods and reference databases*. *Biopolymers*, 2008. **89**(5): p. 392-400.
198. Greenfield, N.J., *Using circular dichroism spectra to estimate protein secondary structure*. *Nature Protocols*, 2006. **1**(6): p. 2876-2890.
199. V. Hall, A.N., A. Rodgers, *SSNN, a method for neural network protein secondary structure fitting using circular dichroism data*. *Analytical Methods*, 2014. **7**(17): p. 6721-6726.
200. Snyder, R.A., *Circular dichroism - Circularly polarised*. 2010.
201. CommonsWiki, F., *Effect of a circular dichroism on a left- or right-handed circularly polarized wave*. 2006.
202. Y. Wei, A.A.T., R. A. Latour, *Protein Helical Structure Determination Using CD Spectroscopy for Solutions with Strong Background Absorbance from 190-230 nm*. *Biochim Biophys Acta*, 2014. **1844**(12): p. 2331-2337.
203. T. Weber, B.V.Z., J. A. McNew, ..., T. H. Söllner, J. E. Rothman, *SNAREpins: minimal machinery for membrane fusion*. *Cell*, 1998. **92**: p. 759-772.
204. D. K. Struck, D.H., R. E. Pagano, *Use of resonance energy transfer to monitor membrane fusion*. *Biochemistry*, 1981. **20**: p. 4093-4099.
205. G. A. Gibson, M.L.L., *Phospholipid vesicle fusion monitored by fluorescence energy transfer*. *Biochemical and Biophysical Research Communications*, 1979. **88**: p. 135-140.
206. G. Krainer, S.K., *Single-experiment displacement assay for quantifying high-affinity binding by isothermal titration calorimetry*. Vol. 76. 2015: Elsevier Methods.
207. E. Freire, O.L.M., M. Straume, *Isothermal titration calorimetry*. *Analytical Chemistry*, 1990. **62**(18).
208. J.-P. E. Grolier, J.M.d.R., *Isothermal titration calorimetry: A thermodynamic interpretation of measurements*. *The Journal of Chemical Thermodynamics*, 2012. **55**: p. 193-202.

## References

---

209. TA-Instruments *Quick Start: Isothermal Titration Calorimetry (ITC)*. 2016. 1-5.
210. V. K. Srivastava, R.Y., *Isothermal titration calorimetry*. Data Processing Handbook for Complex Biological Data Sources. 2019: Academic Press.
211. Caulton, S., *ITC thermogram with  $K_a$ , the reciprocal of  $K_d$ ; stoichiometry; and enthalpy labelled*. 2019.
212. Microcal-Inc. *VP-ITC Instruction Manual*. 2001. 1-107.
213. AB, G.H.B.-S., *MicroCal iTC200 System MicroCal Auto-iTC200 System*. 2011.
214. Pascal, S.M., *NMR Primer: An HSQC-Based Approach*. 2008, Charlton, Chichester, UK: IM-Publications.
215. Gerth, F., *Regulation of a single SH3 domain in ITSN1 modulates its function in the synaptic vesicle cycle*, F.U. Berlin, Editor. 2016: Berlin.
216. Hahn, E.L., *Nuclear induction due to free Larmor precession*. Phys. Rev., 1950. **77**(1): p. 297-298.
217. Wüthrich, K., *The way to NMR structures of proteins*. Nature Structural Biology, 2001. **8**(11): p. 923-925.
218. Sticht, J., *Introduction to protein NMR spectroscopy*. 2023, Freie Universität Berlin. p. 1-62.
219. W. F. Vranken, W.B., T. J. Stevens, ..., J. Ionides, E. D. Laue, *The CCPN data model for NMR spectroscopy: development of a software pipeline*. Proteins, 2005. **59**: p. 687-696.
220. S. P. Skinner, R.H.F., W. Boucher, T. J. Ragan, L. G. Mureddu, G. W. Vuister, *CcpNmr AnalysisAssign: a flexible platform for integrated NMR analysis*. Journal of Biomolecular NMR, 2016. **66**(2): p. 111-124.
221. Z. Liu, S.C., D. R. Gallie, R. R. Julian, *Exploring the Mechanism of Selective Noncovalent Adduct Protein Probing Mass Spectrometry Utilizing Site-Directed Mutagenesis To Examine Ubiquitin*. Anal. Chem., 2008. **80**(10): p. 3846-3852.
222. Pitt, J.J., *Principles and Applications of Liquid Chromatography–Mass Spectrometry in Clinical Biochemistry*. Clin. Biochem. Rev, 2009. **30**(1): p. 19-34.
223. Niessen, W.M.A., *Liquid Chromatography-Mass Spectrometry*. 3 ed. 2006: Boca Raton: CRC Taylor & Francis.
224. L. Konermann, E.A., A. D. Rodriguez, S. Vahidi, *Unraveling the Mechanism of Electrospray Ionization*. Anal. Chem., 2013(85): p. 2-9.
225. C. S. Ho, C.W.K.L., M. H. M. Chan, R. C. K. Cheung, L. K. Law, L. C. W. Lit, K. F. Ng, M. W. M. Suen, H. L. Tai, *Electrospray Ionisation Mass Spectrometry: Principles and Clinical Applications*. Clin. Biochem. Rev, 2003. **24**(1): p. 3-12.
226. R. A. Scheltema, J.-P.H., O. Lange, D. Hornburg, E. Denisov, E. Damoc, A. Kuehn, M. Mann, *The Q Exactive HF, a Benchtop Mass Spectrometer with a Pre-filter, High-performance Quadrupole and an Ultra-high-field Orbitrap Analyzer*. Mol. Cell. Proteomics, 2014. **13**(12): p. 3698-3708.
227. Thermo Scientific, *Thermo Scientific Q Exactive HF - Orbitrap LC-MS/MS System*. 2014.
228. E. de Hoffmann, V.S., *Mass Spectrometry: Principles and Applications*. 2 ed. 2003, Toronto: John Wiley & Sons, Ltd.

## References

---

229. J. V. Olsen, B.M., O. Lange, A. Makarov, S. Horning, M. Mann, *Higher-energy C-trap dissociation for peptide modification analysis*. Nat. Methods, 2007. **4**(9): p. 709-712.
230. J. Kurreck, J.W.E., F. Lottspeich, *Bioanalytik*. 4th Edition ed, ed. S. Spektrum. 2022.
231. Q. Hu, H.L., A. Makarov, M. Hardman, R. Graham Cooks, *The Orbitrap: a new mass spectrometer*. Journal of Mass Spectrometry, 2005. **40**(4): p. 430-443.
232. Rappsilber, J., *The beginning of a beautiful friendship: crosslinking/mass spectrometry and modelling of proteins and multi-protein complexes*. J Struct Biol, 2011. **173**: p. 530-540.
233. Z. A. Chen, A.J., L. Fischer, C. Buchen, S. Tahir, T. Kamenski, ..., P. Cramer, J. Rappsilber, *Architecture of the RNA polymerase II-TFIIF complex revealed by cross-linking and mass spectrometry*. EMBO J., 2010. **29**: p. 717-726.
234. O. Rinner, J.S., T. Walzthoeni, L. N. Mueller, M. Beck, A. Schmidt, M. Mueller, R. Aebersold, *Identification of cross-linked peptides from large sequence databases*. Nat. Methods, 2008. **5**: p. 315-318.
235. H. Zhang, X.T., G. R. Munske, N. Tolic, G. A. Anderson, J. E. Bruce, *Identification of protein-protein interactions and topologies in living cells with chemical cross-linking and mass spectrometry*. Mol. Cell. Proteomics, 2009. **8**: p. 409-420.
236. M. A. Gonzalez-Lozano, F.K., P. F. Sullivan, J. Protze, G. Krause, M. Verhage, K. W. Li, F. Liu, A. B. Smit, *Stitching the synapse: Cross-linking mass spectrometry into resolving synaptic protein interactions*. Sci. Adv., 2020. **6**(eaax5783).
237. F. Liu, P.L., B. M. Rabbitts, R. S. Balaban, A. J R. Heck, *The interactome of intact mitochondria by cross-linking mass spectrometry provides evidence for coexisting respiratory supercomplexes*. Mol. Cell. Proteomics, 2018. **17**(2): p. 216-232.
238. A. Kao, C.-L.C., D. Vellucci, ..., P. Baldi, S. D. Rychnovsky, L. Huang, *Development of a Novel Cross-linking Strategy for Fast and Accurate Identification of Cross-linked Peptides of Protein Complexes*. Mol. Cell. Proteomics, 2011. **10**(1).
239. M. Q. Müller, F.D., C. H. Ihling, M. Schäfer, A. Sinz, *Cleavable Cross-Linker for Protein Structure Analysis: Reliable Identification of Cross-Linking Products by Tandem MS*. Anal. Chem., 2010. **82**(16): p. 6958-6968.
240. A. Sinz, C.A., D. Chorev, M. Sharon, *Chemical cross-linking and native mass spectrometry: A fruitful combination for structural biology*. Protein Science, 2015. **24**(8): p. 1193-1209.
241. Scientific, T., *MS-Cleavable Corsslinkers, Catalog Number A33545, A35459*. 2017.
242. F. Liu, P.L., R. Scheltema, R. Viner, A. J R. Heck, *Optimized fragmentation schemes and data analysis strategies for proteome-wide cross-link identification*. Nature Communications, 2017. **8**(15473).
243. J. Rappsilber, M.M., Y. Ishihama, *Protocol for micro-purification, enrichment, pre-fractionation and storage of peptides for proteomics using StageTips*. Nature Protocols, 2007. **2**: p. 1896-1906.
244. Kawakami, K., *Tol2: a versatile gene transfer vector in vertebrates*. Genome Biology, 2007. **8**.
245. C. N. Pace, J.M.S., *A Helix Propensity Scale Based on Experimental Studies of Peptides and Proteins*. Biophysical Journal, 1998. **75**: p. 422-427.

## References

---

246. M. Schiffer, A.B.E., *Use of helical wheels to represent the structures of proteins and to identify segments with helical potential*. Biophysical Journal, 1967. **7**(2): p. 121-135.
247. Richardson, J.S., *The anatomy and taxonomy of protein structure*. Advances in Protein Chemistry, 1981. **34**: p. 167-339.
248. H. Reiersen, A.R.R., *The hunchback and its neighbours: proline as an environmental modulator*. Trends in Biochemical Science, 2001. **26**(11): p. 679-684.
249. Witkowska, A., *Reconstitution of synaptic vesicle exocytosis - Method Course Presentation*. 2017.
250. K. Aoyagi, T.S., M. Umeda, ..., S. Terakawa, M. Takahashi, *The activation of exocytotic sites by the formation of phosphatidylinositol 4,5-bisphosphate microdomains at syntaxin clusters*. J. Biol. Chem., 2005. **280**(17): p. 17346-17352.
251. Y. Park, J.M.H., G. van den Bogaart, ..., Dietmar Riedel, Reinhard Jahn, *Controlling synaptotagmin activity by electrostatic screening*. Nat. Struct. Mol. Biol., 2013. **19**(10): p. 991-997.
252. Greenfield, N.J., *Using circular dichroism collected as a function of temperature to determine the thermodynamics of protein unfolding and binding interactions*. Nature Protocols, 2006. **1**: p. 2527-2535.
253. Huhmann, S., *Stabilization of peptides by site-specific incorporation of fluorinated amino acids: Model studies and the development of fluorinated, peptide-based HIV-1 fusion inhibitors*, in *Department of Biology, Chemistry and Pharmacy*. 2018, Freie Universität Berlin: Berlin.
254. K. Gawel, M.L., T. Martins, W. van der Ent, E. Tiraboschi, M. Jacmin, A. D. Crawford, C. V. Esguerra, *Seizing the moment: Zebrafish epilepsy models*. Neuroscience & Biobehavioral Reviews, 2020. **116**: p. 1-20.
255. K. Howe, M.D.C., C. F. Torroja, ..., H. Roest Crolius, J. Rogers, D. L. Stemple, *The zebrafish reference genome sequence and its relationship to the human genome*. Nature, 2016. **496**: p. 498-503.
256. T. Afrikanova, A.-S.K.S., O. E. M. Buenafe, R. Clinckers, I. Smolders, P. A. M. de Witte, A. D. Crawford, C. V. Esguerra, *Validation of the zebrafish pentylene tetrazol seizure model: locomotor versus electrographic responses to antiepileptic drugs*. PLOS One, 2013. **8**(e54166).
257. A. Brenet, R.H.-A., J. Somkhit, C. Yanicostas, N. Soussi-Yanicostas, *Defective Excitatory/Inhibitory synaptic balance and increased neuron apoptosis in a zebrafish model of dravet syndrome*. Cells, 2019. **8**.
258. M. T. Dinday, S.C.B., *Large-scale phenotype-based antiepileptic drug screening in a zebrafish model of dravet syndrome*. eNeuro, 2015. **2**.
259. E. A. Naumann, A.R.K., D. A. Prober, A. F. Schier, F. Engert, *Monitoring neural activity with bioluminescence during natural behavior*. Nat. Neurosci., 2010. **13**: p. 513-520.
260. E. Tiraboschi, S.M., W. van der Ent, K. Grzyb, K. Gawel, M. L. Cordero-Maldonado, S. K. Poovathingal, S. Heintz, S. V. Satheesh, J. Brattespe, J. Xu, M. Suster, A. Skupin, C.V. Esguerra, *New insights into the early mechanisms of epileptogenesis in a zebrafish model of Dravet syndrome*. Epilepsia, 2020. **61**(3): p. 549-560.
261. M. Schiavina, L.B., T. Bolognesi, ..., R. Pieratelli, I. C. Felli, *Intrinsically disordered proteins studied by NMR spectroscopy*. JMRO, 2024. **18**.

## References

---

262. S. J. Koo, S.M., D. Puchkov, ..., H. Oschkinat, V. Haucke, *SNRE motif-mediated sorting of synaptobrevin by endocytic adaptor clathrin assembly lymphoid myeloid leukemia (CALM) and AP180 at synapses*. PNAS, 2011. **108**(33): p. 13540-13545.
263. J. Rizo, M.K.R., K. H. Gardner, *Enlightening molecular mechanisms through study of protein interactions*. JMCB, 2012. **4**(5): p. 270-283.
264. J. Jiao, M.H., S. A. Port, ..., T. J. Eisemann, F. M. Hughson, Y. Zhang, *Munc18-1 catalyzes neuronal SNARE assembly by templating SNARE association*. eLife, 2018. **7**(e41771).
265. Sinz, A., *Chemical cross-linking and mass spectrometry to map three-dimensional protein structures and protein-protein interactions*. Mass Spectrom Rev, 2006. **25**: p. 663-682.
266. T. Walzthoeni, A.L., F. Stengel, R. Aebersold, *Mass spectrometry supported determination of protein complex structure*. Curr.Opin Struc Biol, 2013. **23**: p. 252-260.
267. F. Liu, A.J.R.H., *Interrogating the architecture of protein assemblies and protein interaction networks by cross-linking mass spectrometry*. Curr. Opin. Struc. Biol., 2015. **35**: p. 100-108.
268. Leibniz-fmp.de. <https://leibniz-fmp.de/research/research-section/structural-biology/fan-liu-mass-spectrometry>.
269. BioSupaMol-MS-FUBerlin.de. [https://www.biosupramol.de/en/Methoden/\\_Dokumente/Methoden\\_Massenspektrometrie\\_1.html](https://www.biosupramol.de/en/Methoden/_Dokumente/Methoden_Massenspektrometrie_1.html).
270. Sinz, A., *The advancement of chemical cross-linking and mass spectrometry for structural proteomics: from single proteins to protein interaction networks*. Expert Review of Proteomics, 2014. **11**(6): p. 733-743.
271. Kelleher, N.L., *Top-down proteomics*. Analytical Chemistry, 2004. **76**(11): p. 196-203.
272. Sinz, A., *Mass spectrometry-based structural proteomics*. European Journal of Mass Spectrometry, 2006. **12**(2): p. 69-79.
273. Zubarev, R., *Mass spectrometric analysis of cross-linking and posttranslational modification of proteins*. Methods in Molecular Biology, 2004. **251**: p. 375-386.
274. F. Liu, A.J.R.H., *Chemical cross-linking and mass spectrometry for protein-protein interaction studies: a review*. Analytical and Bioanalytical Chemistry, 2015. **407**(10): p. 2417-2423.
275. B. Schilling, R.H.R., B.W. Gibson, X. Guo, M.M. Young, *MS2Assign, automated assignment and nomenclature of tandem mass spectra of chemically crosslinked peptides*. J. Am. Soc. Mass Spectrom., 2003. **14**: p. 834-850.
276. P. Singh, S.A.S., A. Scherl, C. Holman, R. A. Pfuetzner, T. J. Larson Freeman, S. I. Miller, P. Hernandez, R. D. Appel, D. R. Goodlett, *Characterization of protein cross-links via mass spectrometry and an open-modification search strategy*. Anal Chem, 2008. **80**: p. 8799-8806.
277. F. Chu, P.R.B., A. L. Burlingame, R. J. Chalkley, *Finding chimeras: a bioinformatics strategy for identification of cross-linked peptides*. Mol. Cell. Proteomics, 2010. **9**: p. 25-31.
278. S. McIlwain, P.D., P. Singh, D. R. Goodlett, W. S. Noble, *Detecting cross-linked peptides by searching against a database of cross-linked peptide pairs*. J. Proteome Res., 2010. **9**: p. 2488-2495.



## References

---

279. H. Xu, P.H.H., L. Zhang, M. D. Tsai, M. A. Freitas, *Database search algorithm for identification of intact cross-links in proteins and peptides using tandem mass spectrometry*. J. Proteome Res., 2010. **9**: p. 3384-3393.
280. M. Götze, C.I., C. H. Ihling, A. Sinz, *A Simple Cross-Linking/Mass Spectrometry Workflow for Studying System-wide Protein Interactions*. Anal. Chem., 2019. **91**: p. 10236–10244.
281. F. Liu, D.T.S.R., H. Post, A. J. R. Heck, *Proteome-wide profiling of protein assemblies by cross-linking mass spectrometry*. Nat. Methods, 2015. **12**: p. 1179-1184.
282. C. H. Ihling, P.S., C. Iacobucci, C. Hage, M. Götze, M. Schäfer, A. Sinz, *The Isotope-Labeled, MS-Cleavable Cross-Linker Disuccinimidyl Dibutyric Urea for Improved Cross-Linking/Mass Spectrometry Studies*. J. Am. Soc. Mass Spectrom., 2019. **31**(2): p. 183-189.
283. M. J. Trnka, P.R.B., P. J. J. Robinson, A. L. Burlingame, R. J. Chalkley, *Matching Cross-linked Peptide Spectra: Only as Good as the Worse Identification*. Mol. Cell. Proteomics, 2014. **13**(12): p. 420-434.
284. Sinz, A., *Divide and conquer: cleavable cross-linkers to study protein conformation and protein–protein interactions*. Analytical and Bioanalytical Chemistry, 2017. **409**: p. 33-44.
285. C. Iacobucci, M.G.C.H.I., ..., R. Schmidt, A. Sinz, *A crosslinking/mass spectrometry workflow based on MS-cleavable crosslinkers and the MeroX software for studying protein structures and protein-protein interactions*. Nature Protocols, 2018. **13**(12): p. 2864-2889.
286. C. Arlt, C.H.I., A. Sinz, *Structure of full-length p53 tumor suppressor probed by chemical cross-linking and mass spectrometry*. Proteomics, 2015. **15**(16): p. 2746-2755.
287. E. D. Merkley, S.R., A. Kahraman, R. P. Hafen, V. Daggett, J. N. Adkins, *Distance restraints from crosslinking mass spectrometry: Mining a molecular dynamics simulation database to evaluate lysine–lysine distances*. Prot. Sci., 2014. **23**(6): p. 747-759.
288. C. W. Combe, L.F., J. Rappsilber, *xiNET: Cross-link Network Maps With Residue Resolution*. Mol. Cell. Proteomics, 2015. **14**: p. 1137-1147.
289. A. Barozet, K.M., M. Vaisset, C. Zanon, P. Fauret, T. Simeon, J. Cortes, *MoMA-LoopSampler: a web server to exhaustively sample protein loop conformations*. Bioinformatics, 2022. **38**(2): p. 552-553.
290. X. Wang, J.G., L. Zhu, H. Chen, Z. Jin, X. Mo, S. Wang, X. Yang, C. Ma, *Identification of residues critical for the extension of Munc18-1 domain 3a*. BMC Biology, 2023. **21**(158).
291. Berg, J.M., *Stryer Biochemie*. Vol. 6. 2007: Spektrum Akademischer Verlag.
292. Werk, T.J., *Structural and functional investigation of the orchestrated SNARE-complex formation*, in *Department of Chemistry and Biochemistry*. 2024, Freie Universität Berlin: Berlin, Germany.
293. A. Salazar Lazaro, T.T., G. Vardar, C. Rosenmund, *The stability of the primed pool of synaptic vesicles and the clamping of spontaneous neurotransmitter release rely on the integrity of the C-terminal half of the SNARE domain of syntaxin-1A*. eLife, 2024. **12**(RP90775).
294. Rizo, J., *Molecular Mechanisms Underlying Neurotransmitter Release*. Annual Review of Biophysics, 2022. **51**: p. 377-408.
295. D. Fasshauer, M.M., *A Transient N-terminal Interaction of SNAP-25 and Syntaxin Nucleates SNARE Assembly*. J. Biol. Chem., 2004. **279**(9): p. 7613-7621.

## References

---

296. S. Jakhanwal, C.-T.-L., H. Urlaub, R. Jahn, *An activated Q-SNARE/SM protein complex as a possible intermediate in SNARE assembly*. EMBO J., 2017. **36**: p. 1788-1802.
297. J. Abramson, J.A., J. Dunger, ..., M. Jaderberg, D. Hassabis, J. M. Jumper, *Accurate structure prediction of biomolecular interactions with AlphaFold 3*. Nature, 2024. **630**: p. 493-500.
298. J. E. Richmond, R.M.W., E. M. Jorgensen, *An open form of syntaxin bypasses the requirement for UNC-13 in vesicle priming*. Nature, 2001. **4**(12): p. 338-341.
299. S. Park, N.-R.B., B. Yu, R. Wong, E. Sitarska, ..., S. Gao, J. Rizo, S. Sugita, *UNC-18 and Tomosyn Antagonistically Control Synaptic Vesicle Priming Downstream of UNC-13 in Caenorhabditis elegans*. J. Neurosci., 2017. **37**(36): p. 8797-8815.
300. S. H. Gerber, J.-C.R., S.-W. Min, X. Liu, H. de Wit, I. Dulubova, A. C. Meyer, J. Rizo, M Arancillo, R. E. Hammer, M. Verhage, C. Rosenmund, T. C. Südhof, *Conformational switch of syntaxin-1 controls synaptic vesicle fusion*. Science, 2008. **321**(5895): p. 1507-1510.
301. J. E. Ladbury, B.Z.C., *Sensing the heat: the application of isothermal titration calorimetry to thermodynamic studies of biomolecular interaction*. Chemistry & Biology, 1996. **3**(10): p. 791-801.
302. S. Leavitt, E.F., *Direct measurement of protein binding energetics by isothermal titration calorimetry*. Current Opinion in Structural Biology, 2001. **11**(5): p. 560-566.
303. Cooper, A., *Thermodynamic analysis of biomolecular interactions*. Curr. Opin. Chem. Biol., 1999. **3**(5): p. 557-563.
304. M. S. de Abreu, R.G., A. C. V. V. Giacomini, ..., M. O. Parker, A. V. Kalueff, *Zebrafish as a Model of Neurodevelopmental Disorders*. Neuroscience, 2020. **445**(3-11).
305. K. Gawel, N.S.B., A. Michalak, C. V. Esguerra, *A critical review of zebrafish schizophrenia models: time for validation?* Neurosci. Biobehav. Rev., 2019. **107**: p. 6-22.
306. C. Sakai, S.I., E. J. Hoffman, *Zebrafish models of neurodevelopmental disorders: past, present, and future*. Front. Mol. Neurosci., 2018. **11**: p. 294.
307. M. D'Amora, A.G., M. Marchese, ..., F. Angelis, F. S. Giorgi, *Zebrafish as an Innovative Tool for Epilepsy Modeling: State of the Art and Potential Future Directions*. Int. J. Mol. Sci., 2023. **24**(9).
308. G. Streisinger, C.W., N. Dower, D. Knauber, F. Singer, *Production of clones of homozygous diploid zebra fish (Brachydanio rerio)*. Nature, 1981. **291**: p. 293-296.
309. S. Rinkwitz, P.M., T.S. Becker, *Zebrafish: An integrative system for neurogenomics and neurosciences*. Prog. Neurobiol., 2011. **93**: p. 231-243.
310. T.S. Becker, S.R., *Zebrafish as a genomics model for human neurological and polygenic disorders*. Dev. Neurobiol., 2012. **72**: p. 415-428.
311. V. M. Bedell, Y.W., J. M. Campbell, ..., K. J. Clark, J. J. Essner, S. C. Ekker, *In vivo genome editing using a high-efficiency TALEN system*. Nature, 2012. **491**(7422): p. 114-118.
312. W. Y. Hwang, Y.F., D. Reyon, ..., R. T. Peterson, J.-R. J. Yeh, J. K. Joung, *Efficient genome editing in zebrafish using a CRISPR-Cas system*. Nat. Biotechnol., 2013. **31**(3): p. 227-229.
313. T.-Y. Choi, T.-I.C., Y.-R. Lee, S.-K. Choe, C.-H. Kim, *Zebrafish as an animal model for biomedical research*. Exp. Mol. Med., 2021. **53**: p. 310-317.

## References

---

314. O. Cozzolino, F.S., E. Paoli, F. Trovato, F.M. Santorelli, G.M. Ratto, M. Marchese, *Evolution of Epileptiform Activity in Zebrafish by Statistical-Based Integration of Electrophysiology and 2-Photon Ca<sup>2+</sup> Imaging*. *Cells*, 2020. **9**: p. 769.
315. S.-J. Cho, E.P., A. Baker, A.Y. Reid, *Age bias in zebrafish models of epilepsy: What can we learn from old fish?* *Front. Cell Dev. Biol.*, 2020. **8**(573303).
316. M. L. Suster, H.K., A. Urasaki, K. Asakawa, K. Kwakami, *Transgenesis in Zebrafish with the Tol2 Transposon System*. *Transgenesis Techniques. Methods in Molecular Biology*. Vol. 561. 2009: Springer Protocols, Humana Press.
317. K. J. Clark, M.D.U., K. J. Skuster, S. C. Ekker, *Transgenic Zebrafish Using Transposable Elements*. *Methods Cell Biol.*, 2011. **104**: p. 137-149.
318. Navarro, M.M. *CRISPR/Cas9 vs. Tol2 Techniques for Zebrafish Genomic Manipulation - Evaluating Methods for Precision and Efficiency in Genetic Engineering*. *Genetics* 2024; Available from: <https://www.zeclinics.com/blog/comparison-of-crispr-cas9-and-tol2-transposase-systems/>.
319. J. Bessa, J.J.T., E. de la Calle Mustiene, A. Fernandez-Minan, ..., Fernando Casares, J. L. Gomez-Skarmeta, *Zebrafish enhancer detection (ZED) vector: A new tool to facilitate transgenesis and the functional analysis of cis-regulatory regions in zebrafish*. *Developmental Dynamics*, 2009. **238**(9): p. 2409-2417.
320. D. Y. R. Stainier, E.R., N. D. Lawson, ..., N. Mochizuki, P. Panula, C. B. Moens, *Guidelines for morpholino use in zebrafish*. *PLOS Genetics*, 2017. **13**(10): p. e1007000.
321. S. Knafo, K.F., A. Prendergast, ..., O. Thouvenin, H. Pascal-Moussellard, C. Wyart, *Mechanosensory neurons control the timing of spinal microcircuit selection during locomotion*. *eLife*, 2017. **6**(e25260).
322. F. A. Issa, G.O.B., P. Kettunen, A. Sagasti, D. L Glanzman, D. M. Papazian, *Neural circuit activity in freely behaving zebrafish (Danio rerio)*. *J. Exp. Biol.*, 2011. **214**(6): p. 1028-1038.
323. D. W. Pfaff, N.D.V., J. L. Rubenstein, *Post-Synaptic Potentials and Action Potentials: Membrane Potentials*. 3rd ed. *Neuroscience in the 21st Century - From Basic to Clinical*. 2016, New York: Springer Nature.
324. A. N. Shore, S.C., W. F. Tobin, ..., M. J. Boland, W. N. Frankel, M. C. Weston, *Reduced GABAergic Neuron Excitability, Altered Synaptic Connectivity, and Seizures in a KCNT1 Gain-of-Function Mouse Model of Childhood Epilepsy*. *Cell Rep.*, 2020. **33**(4).
325. A. C.-H. Ng, M.C., M. H. Scantlebury, J. P. Appendino, *Channelopathies in epilepsy: an overview of clinical presentations, pathogenic mechanisms, and therapeutic insights*. *Journal of Neurology*, 2024. **271**: p. 3063-3094.
326. H. C. A. Lammertse, A.A.v.B., M. Iacomino, R. F. Toonen, P. Striano, A. Gambardella, M. Verhage, F. Zara, *Homozygous STXBP1 variant causes encephalopathy and gain-of-function in synaptic transmission*. *Brain*, 2020. **143**(2): p. 441-451.
327. J. A. McNew, F.P., R. Fukuda, ..., T. H. Söllner, J. E. Rothman, *Compartmental specificity of cellular membrane fusion encoded in SNARE proteins*. *Nature*, 2000. **407**: p. 153-159.
328. T. Liu, W.C.T., A. Bhalla, E. R. Chapman, J. C. Weisshaar, *SNARE-Driven, 25-Millisecond Vesicle Fusion In Vitro*. *Biophysical Journal*, 2005. **89**: p. 2458-2472.
329. X. Liu, A.B.S., J. Xu, V. Esser, ..., C. Ma, J. Rizo, *Simultaneous lipid and content mixing assays for in vitro reconstitution studies of synaptic vesicle fusion*. *Nature Protocols*, 2017. **12**: p. 2014-2028.

## References

---

330. A. Reklós, *Investigation of the Influence of Epilepsy Related Stx1b Mutants E210K and L221P on the SNARE Complex Formation Machinery via biochemical and biophysical methods and assays.*, in *Department of Chemistry and Biochemistry*. 2024, Freie Universität Berlin: Berlin. p. 74.
331. B. Yang, M.S., L. C. Gonzalez, R. H. Scheller, *nSec1 binds a closed conformation of syntaxin1A*. *J. Cell Biol.*, 2000. **148**: p. 247-252.
332. X. Chen, J.L., I. Dulubova, J. Rizo, *NMR Analysis of the Closed Conformation of Syntaxin-1*. *J. Biol. NMR*, 2008. **41**(1): p. 43-54.
333. D. A. Gell, A.H.K., J.P. Mackay, *NMR Spectroscopy in the Analysis of Protein-Protein Interactions*. *Modern Magnetic Resonance*, ed. G. Webb. 2017: Springer.
334. Parella, T. *Labeling Level - Deuterated Protein, Advantages vs Drawbacks*. 2008.
335. J. Angulo, P.M.N., *STD-NMR: application to transient interactions between biomolecules - a quantitative approach*. *Eur. Biophys. J.*, 2011. **40**: p. 1357-1369.
336. M. Matzinger, A.V., M. Madalinski, F. Müller, F. Stanek, K. Mechtler, *Mimicked synthetic ribosomal protein complex for benchmarking crosslinking mass spectrometry workflows*. *Nat. Comm.*, 2022. **13**(3975).
337. S. Azari, B.X., M. Zhang, L- Peng, *Preprocessing Tandem Mass Spectra Using Genetic Programming for Peptide Identification*. *J. Am. Soc. Mass Spectrom.*, 2019. **30**: p. 1294-1307.
338. P. Stefanowicz, A.K., Z. Szewczuk, *Amino Acids, Peptides and Proteins*, ed. F.H. M. Ryadnov. Vol. 40. 2015: The Royal Society of Chemistry.
339. S. Kalkhof, A.S., *Chances and pitfalls of chemical cross-linking with amine-reactive N-hydroxysuccinimide esters*. *Anal. Bioanal. Chem.*, 2008. **392**: p. 305-312.
340. G. Mattson, E.C., S. Desai, G. Nielander, M. D, Savage, S. Morgensen *A practical approach to crosslinking*. *Mol. Biol. Rep.*, 1993. **17**: p. 167-183.
341. P. Giansanti, L.T., T. Y. Low, A. J. R. Heck, *Six alternative proteases for mass spectrometry based proteomics beyond trypsin*. *Nature Protocols*, 2016. **11**(5): p. 993-1006.
342. S. Madler, M.S., J. Robinson, R. Zenobi, *Does chemical cross-linking with NHS esters reflect the chemical equilibrium of protein-protein noncovalent interactions in solution?* *J. Am. Soc. Mass Spectrom.*, 2010. **21**: p. 1775-1783.
343. O. Klykov, B.S., S. Pekras, D. Fasci, A. J. R. Heck, R. A. Scheltema, *Efficient and robust proteome-wide approaches for crosslinking mass spectrometry*. *Nature Protocols*, 2018. **13**(12): p. 2964-2990.
344. C. H. Ihling, L.P., M. Kipping, A. Sinz, *Cross-Linking/Mass Spectrometry Combined with Ion Mobility on a timsTOF Pro Instrument for Structural Proteomics*. *Analytical Chemistry*, 2021. **93**(33): p. 11442-11450.
345. Y.-H. Ding, S.-B.F., S. Li, B.-Y. Feng, N. Gao, K. Ye, S.-M. He, M.-Q. Dong, *Increasing the Depth of Mass-Spectrometry-Based Structural Analysis of Protein Complexes through the Use of Multiple Cross-Linkers*. *Analytical Chemistry*, 2016. **88**(8): p. 4461-4469.
346. Z. A. Chen, J.R., *Protein structure and dynamics by cross-linking mass spectrometry*. *Curr. Opin. Struc. Biol.*, 2023. **80**(102599).

## References

---

347. L. Piersimoni, P.L.K., C. Arlt. A. Sinz, *Cross-Linking Mass Spectrometry for Investigating Protein Conformations and Protein-Protein Interactions-A Method for AllSeasons*. Chem. Rev., 2022. **122**: p. 7500-7531.
348. A. Maiolica, D.C., D. Borsotti, L. Sennels, C. Ciferri, C. Tarricone, A. Musacchio, J. Rappsilber, *Structural analysis of multiprotein complexes by cross-linking, mass spectrometry, and database searching*. Mol. Cell. Proteomics, 2007. **6**: p. 2200-2211.
349. UniProt.org. <https://www.uniprot.org/>.



## IV. List of Publications

Miriam Bertazzon, Almudena Hurtado-Pico, Carlos Plaza-Sirvent, Marc Schuster, Marco Preußner, Benno Kuroпка, Fan Kiu, Andor Zenon Amandus Kristen, **Xiao Jakob Schmitt**, Benjamin König, Miguel Álvaro-Benito, Esam T. Abualrous, Gesa I. Albert, Stefanie Kliche, Florian Heyd, Ingo Schmitz, Christian Freund. **The nuclear GYF protein CD2BP2/U5-52K is required for T cell homeostasis**, 2024; *Frontiers in Immunology*, 15, 1415839.

Fabio Lolicato, Julia P. Steringer, Roberto Saleppico, Daniel Beyer, Jaime Fernandez-Sobaberas, Sebastian Unger, Steffen Klein, Petra Riegerová, Sabine Wegehingel, Hans-Michael Müller, **Xiao Jakob Schmitt**, Shreyas Kaptan, Christian Freund, Martin Hof, Radek Šachl, Petr Chlanda, Ilpo Vattulainen, Walter Nickel. **Disulfide bridge-dependent dimerization triggers FGF2 membrane translocation into the extracellular space**, 2024; *eLife*, 12, RP88579.

Gülçin Vardar\*, Fabian Gerth\*, **Xiao Jakob Schmitt**, Pia Rautenstrauch, Thorsten Trimbuch, Julian Schubert, Holger Lerche, Christian Rosenmund, Christian Freund. **Epilepsy-causing STX1B mutations translate altered protein functions into distinct phenotypes in mouse neurons**, 2020; *Brain*, 143 (7): 2119-2138.

(\*These authors contributed equally to this work)

Fabian Gerth, Maria Jäpel, Jana Sticht, Benno Kuroпка, **Xiao Jakob Schmitt**, Jan H. Driller, Bernhard Loll, Markus C. Wahl, Kevin Pagel, Volker Haucke, Christian Freund. **Exon Inclusion Modulates Conformation Plasticity and Autoinhibition of the Intersectin 1 SH3A Domain**, 2019; *Structure*, 27 (6): 977-987.

Melanie Göth, Frederik Lermyte\*, **Xiao Jakob Schmitt\***, Stephan Warnke, Gert von Helden, Frank Sobott, Kevin Pagel. **Gas-Phase microsolvation of ubiquitin: investigation of crown ether complexation sites using ion mobility-mass spectrometry**, 2016; *The Analyst*, 141 (19): 5502-5510. (\*These authors contributed equally to this work)

## **V. Curriculum Vitae**

*Der Lebenslauf ist in der Online-Version aus Gründen des Datenschutzes nicht enthalten.*



*Der Lebenslauf ist in der Online-Version aus Gründen des Datenschutzes nicht enthalten.*

